



**New routes to enhance the efficiency of biomass  
torrefaction and gasification processes**  
[Potentials for valorization of lignocellulosic biomass and mining  
residues]

**Thèse**

**Amin Sarvaramini**

**Doctorat en génie chimique  
Philosophiae Doctor (Ph.D)**

Québec, Canada

© Amin Sarvaramini, 2014



## Résumé

L'objectif de la recherche proposée dans cette thèse est d'apporter une meilleure compréhension au mécanisme de la torréfaction de la biomasse et de proposer des méthodes pratiques afin d'améliorer l'efficacité de ce processus. Quant au mécanisme, la torréfaction de deux échantillons de biomasse lignocellulosique des forêts du Québec (le faux-tremble et le bouleau) et leurs constituants principaux tels que la lignine, la cellulose et l'hémicellulose est étudiée en détail en utilisant différentes techniques expérimentales et un modèle cinétique a été développé pour décrire la cinétique de leur torréfaction. Notre étude sur le mécanisme et la cinétique de torréfaction de la biomasse révèle également une faible vitesse de torréfaction de la biomasse, ce qui nous a motivés à proposer et développer une nouvelle méthode de torréfaction impliquant des liquides ioniques dans le but de stimuler la vitesse de torréfaction de la biomasse.

Bien que la torréfaction améliore les propriétés physicochimiques de la biomasse en tant que combustible, la production d'hydrocarbures oxygénés (sous forme de volatils) de la biomasse lors de la torréfaction réduit son énergie globale. Dans le but de récupérer l'énergie des volatils, une nouvelle combinaison de la torréfaction de la biomasse et de la combustion des volatils dans une boucle chimique de combustion (*Chemical Looping Combustion*) a été étudiée dans cette thèse. À cet effet, les minéraux ultramafiques abondants et préalablement broyés, largement disponibles dans la province de Québec, ont été testés en tant que transporteurs solides d'oxygène conduisant à près de 96% de conversion des volatils à 700°C dans un réacteur CLC.

Comme travail supplémentaire, nous étions également intéressé à explorer l'application potentielle des résidus miniers contenant une quantité considérable de fer pour le craquage catalytique de goudrons produits pendant les processus de gazéification de la biomasse. À cet effet, le potentiel de deux résidus miniers et des minéraux renfermant du fer obtenus de diverses activités minières au Québec a été comparé à celui de l'olivine (connu comme minéral actif pour le craquage du goudron).



## **Abstract**

The aim of the proposed research was to provide a better understanding of the mechanisms of biomass torrefaction and to propose practical methods to improve the efficiency of this process. As for the mechanism, torrefaction of two woody biomass samples from Quebec forests (aspen and birch) and their main constituents, i.e., lignin, cellulose and hemicellulose is studied in details using different experimental techniques and a kinetic model is developed for their torrefaction. Our studies on the mechanism and kinetics of biomass torrefaction also revealed the slow rate of biomass torrefaction which motivated us to propose and develop a new ionic-liquid assisted torrefaction process with the aim of increasing the rate of biomass torrefaction.

Although torrefaction improves the physicochemical properties of biomass fuel, release of oxygenated hydrocarbons (in the form of volatiles) from biomass reduces its overall energy. To recover volatiles energy, a new combination of biomass torrefaction and chemical looping volatiles combustion was studied. In this regard, the already comminuted, abundant and cheap iron and magnesium bearing silicate minerals found widely in the form of mining residues in the province of Quebec were tested as solid oxygen carrier and up to 96% of volatiles conversion at 700°C was achieved in CLC reactor.

As a supplementary work, we were also interested to explore the potential of mining residues containing sizeable quantities of iron for catalytic cracking of tar released during the gasification of biomass. For this purpose, iron-bearing mining residues and minerals obtained from the mining activities in Quebec were evaluated comparatively to olivine (known as an active mineral for tar cracking) for benzene cracking in simulated syngas. It was found that chrysotile showed up to four-fold increase in benzene and methane conversion than olivine.



## Table of contents

Résumé.....	iii
Abstract.....	v
List of tables.....	x
List of figures .....	xii
Acknowledgements.....	xviii
Foreword.....	xx
Chapter 1 : Introduction and objectives.....	1
A) Background.....	1
B) Literature review.....	4
B.1. Biomass thermochemical conversion and importance of pre-treatment.....	4
B.2. Application of minerals in thermochemical biomass conversion .....	21
C) Objectives, scope and outline of the project.....	47
D) References .....	53
Chapter 2 : Dry torrefaction of biomass and of its constitutive components - Characterization of torrefied products and torrefaction kinetics using the distributed activation energy model.....	59
2.1. Introduction.....	61
2.2. Experimental.....	63
2.3. Kinetic modeling.....	66
2.4. Results and discussion .....	68
2.4.1. Biomass torrefaction.....	68
2.4.2. Kinetic modeling of torrefaction.....	77
2.5. Conclusion .....	86
2.6. References.....	87
Chapter 3 : Torrefaction of ionic-liquid impregnated lignocellulosic biomass and its comparison to dry torrefaction.....	91
3.1. Introduction.....	93
3.2. Experimental.....	95
3.2.1. Materials .....	95
3.2.2. Weight loss and volatiles via thermogravimetry & mass spectrometry analysis.....	96
3.2.3. Fixed-bed torrefaction setup .....	96
3.2.4. Characterization of solids .....	98
3.3. Results & discussion.....	99
3.3.1. IL and dry torrefaction, TG-MS studies.....	99
3.3.2. IL and dry biomass torrefaction, fixed-bed studies.....	107

3.3.3. IL thermal stability under torrefaction conditions.....	112
3.4. Conclusion.....	115
3.5. References .....	116
Chapter 4 : Biomass torrefaction and CO <sub>2</sub> capture using mining wastes - A new approach for reducing greenhouse gas emissions of co-firing plants .....	119
4.1. Introduction .....	121
4.2. Experimental .....	123
4.2.1. Materials preparation.....	123
4.2.2. Experimental assembly .....	124
4.3. Results and discussion.....	127
4.3.1. Analysis of torrefaction products .....	127
4.3.2. Carbonation-free torrefaction .....	128
4.3.3. Coupled torrefaction-carbonation .....	131
4.3.4. Origin of residue carbonation activity.....	133
4.3.5. Effect of CO and CH <sub>4</sub> on residue carbonation .....	136
4.3.6. Effect of temperature on residue carbonation .....	137
4.4. Conclusion.....	140
4.5. References .....	141
Chapter 5 : Integrated biomass torrefaction - chemical looping combustion as a method to recover torrefaction volatiles energy.....	145
5.2. Experimental .....	149
5.2.1. Materials.....	149
5.2.2. Experimental setup.....	149
5.3. Results and discussion.....	153
5.3.1. Torrefied solid produced in torrefaction-CLC closed assembly .....	153
5.3.2. Gases released in torrefaction-CLC closed assembly .....	154
5.3.3. Long term stability .....	160
5.3.4. Effect of torrefaction environment on properties of torrefied solid product .....	161
5.4. Conclusion.....	167
Chapter 6 : Fe/Mg silicate mining residues as solid oxygen carriers for chemical looping combustion of torrefaction volatiles.....	171
6.1. Introduction .....	173
6.2. Experimental .....	175
6.2.1. Materials characterization and preparation .....	175
6.2.2. Experimental setup.....	176
6.3. Results and discussions .....	178
6.3.1. RMR characterization .....	178

6.3.2. Biomass torrefaction - RMR CLC .....	181
6.3.3. Biomass torrefaction - RMR CLC - carbonation.....	187
6.4. Conclusion .....	190
6.5. References.....	191
Chapter 7 : Mössbauer spectroscopy & catalytic reaction studies of chrysotile-catalyzed steam reforming of benzene.....	195
7.1. Introduction.....	197
7.2. Experimental.....	198
7.3. Results & discussion.....	202
7.3.1. X-ray powder diffraction patterns.....	202
7.3.2. <sup>57</sup> Fe Mössbauer spectroscopy .....	203
7.3.3. Temperature-programmed reduction .....	206
7.3.4. Reaction tests .....	208
7.4. Conclusion .....	214
7.5. References.....	215
Chapter 8 : Catalytic oxygenless steam cracking of syngas-containing benzene model tar compound over natural Fe-bearing silicate minerals.....	219
8.1. Introduction.....	221
8.2. Experimental section.....	222
8.3. Results & discussion.....	226
8.3.1. Catalyst characterization.....	226
8.3.2. Comparison of RMR, chrysotile and olivine activity.....	234
8.3.3. Parametric study of chrysotile activity .....	236
8.4. Conclusion .....	244
8.4. References.....	245
Chapter 9 : Conclusion and future work.....	249
9.1. Key contributions.....	249
9.2. Suggested future works.....	249

## List of Tables

Table 1-1: Approximate composition in mass percentage of different biomass species [5].....	4
Table 1-2: Some tar compounds in different classes of tar [68] .....	38
Table 1-3: Summary of activity of some synthesized catalysts tested by different research groups.....	42
Table 2-1 : Proximate analysis in mass % of cellulose, xylan, lignin, birch and aspen wood ....	64
Table 2-2: Ultimate analysis, O/C and H/C mole ratio, mass yield, high heating value, energy yield and energy density of as received and torrefied cellulose, xylan, lignin, birch and aspen.	65
Table 2-3: Optimum values of parameters for the torrefaction kinetic models of cellulose, xylan, lignin, birch and aspen.....	78
Figure 3-1: Schematics of fixed-bed reactor setup used for biomass torrefaction .....	97
Table 3-2 . Ultimate analysis, mass yield (dry basis) and high heating value of raw, and dry and ionic liquid ([Emim][OTf] <sub>s</sub> ) torrefied aspen, birch and sawdust at different residence time and temperatures. ....	109
Table 3-3 : Ultimate moisture uptake of raw, dry and ionic liquid ([Emim][OTf] <sub>s</sub> ) torrefied aspen, birch and sawdust at different residence time and temperatures after 4-day exposure of samples in saturated stream of 30°C. ....	112
Table 3-4: Decomposition rate (mass%/h) of different ionic liquids tested in this study at different operating conditions .....	113
Table 4-1 . Ultimate analysis (wt%), mass yield, higher heating value and energy yield of as-received and torrefied birch.....	127
Table 5-1. Ultimate analysis, mass yield, higher heating value and energy yield of as received and torrefied birch. ....	153
Table 5-2. Ultimate analysis, mass yield, higher heating value and energy yield of torrefied birch at different residence time and temperatures and under N <sub>2</sub> and water/CO <sub>2</sub> atmospheres.	162
Table 6-1. Wt % of main constitutive elements of RMR (Raglan mine, Québec) <i>via</i> XRF analysis.....	175
Table 6-2. Isomer shift ( $\delta$ ), quadrupole splitting ( $\Delta$ ), hyperfine field ( $B_{hf}$ ) and relative areas of the components used to fit the as-received and calcined RMR and used RMR in five oxidation/reduction cycles.....	181
Table 6-3: Ultimate analysis, mass yield and energy yield of as-received and torrefied birch.	182
Table 7-1: Wt % of analytes constitutive of raw chrysotile (Thetford Mines, Québec) and olivine (Greenland) <sup>a</sup> Lost on ignition .....	199

Table 7-2: Isomer shift ( $\delta$ ), quadrupole splitting ( $\Delta$ ), hyperfine field ( $B_{hf}$ ) and relative areas of the components used to fit the chrysotile and olivine spectra shown in Figure 7-2.....	204
Table 7-3: Catalyst calcination pre-treatment and various steam-reforming operating conditions, products' yields and benzene conversion over chrysotile and olivine .....	209
Table 8-1. Wt % of main constitutive elements of RMR (Raglan mine residues, Québec), chrysotile (Thetford Mines, Québec) and olivine (Greenland).....	223
Table 8-2. Isomer shift ( $\delta$ ), quadrupole splitting ( $\Delta$ ), hyperfine field ( $B_{hf}$ ) and relative areas of the components used to fit the spectra of the as-received RMR (Raglan mine residues, Québec), chrysotile (Thetford Mines, Québec) and olivine .....	230
Table 8-3. Isomer shift ( $\delta$ ), quadrupole splitting ( $\Delta$ ), hyperfine field ( $B_{hf}$ ) and relative areas of the components used to fit the spectra of calcined RMR, chrysotile and olivine for 2h at 900°C .....	231

## List of figures

Figure 1-1: Chemical structure of cellulose [4].....	5
Figure 1-2: Main components of hemicellulose [4] .....	5
Figure 1-3: <i>p</i> -coumaryl, coniferyl and sinapyl structures [4].....	6
Figure 1-4: The evolution of H/C versus O/C of torrefied biomass [21] .....	13
Figure 1-5: Schematic of The two step kinetic model used by Prins et al. [28].....	17
Figure 1-6: Schematic of the kinetic mechanism used by Repellin et al. [27].....	18
Figure 1-7: Some commonly used ionic liquid systems [32].....	20
Figure 1-8: Dissolution mechanism of cellulose in [C <sub>4</sub> MIM][Cl] [37].....	21
Figure 1-9: Effect of pH on the dissolution of diopside at 25 °C [52] .....	28
Figure 1-10: Effect of temperature on the dissolution of mineral fiber in a 4 M formic acid [53] .....	28
Figure 1-11: Schematic of silica gel layer formation [54].....	29
Figure 1-12: Dominant species of dissolved CO <sub>2</sub> in function of pH.....	29
Figure 1-13: TG analysis of MgO samples during 10 days in humid environment: (a) low concentrations of CO <sub>2</sub> ; (b) High CO <sub>2</sub> concentration (◇)T= 0°C; (□)T= 20°C; (Δ)T= 40°C; (----) theoretical Mg(OH) <sub>2</sub> ; (.....) theoretical MgCO <sub>3</sub> ·3H <sub>2</sub> O [55].....	30
Figure 1-14: Distribution of the four tar component classes as a function of temperature [67]..	37
Figure 1-15: XPS spectra of olivine for two binding energy regions [87] .....	46
Figure 2-1: Mass yield, weight loss derivative and differential thermal analysis of cellulose, xylan, lignin, birch and aspen wood decomposed in thermogravimetric analyzer at 5°C/min heating rate until 300°C.....	69
Figure 2-2 : FTIR spectra of as-received and torrefied cellulose, xylan and lignin samples .....	71
Figure 2-3: Humidity uptake of the as-received and torrefied cellulose, xylan, lignin, birch and aspen wood at 25 °C during 5 intervals of 48 h .....	72
Figure 2-4: TG derived profile of volatile release vs. time for xylan torrefaction and DAEM simulated profiles of xylan torrefaction .....	78
Figure 2-5: TG derived profile of volatile release versus time for lignin torrefaction and the DAEM simulated profiles of lignin torrefaction .....	79
Figure 2-6: TG derived profile of volatile release versus time for cellulose torrefaction and the DAEM simulated profiles of cellulose torrefaction .....	80
Figure 2-7: Distributions of activation energies for xylan, cellulose and lignin .....	81

Figure 2-8: TG derived profile of volatile release versus time for birch torrefaction and the simulated profiles using optimized $c_i$ values .....	82
Figure 2-9: TG derived profile of volatile release versus time for aspen torrefaction and the simulated trends using optimized $c_i$ values .....	83
Figure 2-10: TG derived profile of volatile release versus time for birch torrefaction and the results of its simulated profiles using the actual chemical composition of birch.....	84
Figure 2-11: TG derived profile of volatile release versus time for aspen torrefaction and the results of its simulated profiles using the actual chemical composition of aspen.....	85
Table 3-1: Proximate analysis in mass % of sawdust, birch and aspen wood .....	95
Figure 3-2 : Mass loss profile of cellulose ionic liquid and dry torrefaction .....	100
Figure 3-3 : MS positive ion current ( $m/z= 44$ , $CO_2$ ) during cellulose ionic liquid and dry torrefaction.....	101
Figure 3-4. MS positive ion current ( $m/z= 18$ , $H_2O$ ) during cellulose liquid and dry torrefaction .....	102
Figure 3-5. Mass loss profile of xylan ionic liquid and dry torrefaction.....	103
Figure 3-6. Mass loss profile of lignin ionic liquid and dry torrefaction .....	104
Figure 3-7. Mass loss profile of aspen ionic liquid and dry torrefaction .....	105
Figure 3-8. Mass loss profile of birch wood ionic liquid and dry torrefaction .....	106
Figure 3-9. Mass loss profile of sawdust ionic liquid and dry torrefaction.....	107
Figure 3-10: Solid mass yield of torrefied aspen, birch and sawdust (1) dry torrefaction (2) ionic liquid ([Emim][OTf]S) torrefaction .....	108
Figure 3-11: Energy density of torrefied aspen, birch and sawdust (1) dry torrefaction (2) ionic liquid ([Emim][OTf]S) torrefaction .....	110
Figure 3-12: Energy yield of torrefied aspen, birch and sawdust (1) dry torrefaction (2) ionic liquid ([Emim][OTf]S) torrefaction .....	111
Figure 4-1. Schematic of experimental torrefaction-carbonation assembly. (1) K-type thermocouple (2) stainless steel mesh (3) birch sample holder (4) induction coil (5) stainless steel torrefaction reactor (6) pyrometer (7) induction power supply (8) $CO_2$ probe (9) hygrometer-thermocouple (10) carbonation upper compartment (11) electrical fan (12) gate (13) stainless steel filter (14) TDR probe (15) pH probe (16) residue bed holder (17) carbonation lower compartment (18) peristaltic pump (19) micro-GC (20) mass flowmeters.....	125
Figure 4-2. Time evolution of accumulated (left y-scale) and captured (right y-scale) $CO_2$ during birch dry torrefaction at $260^\circ C$ . The marginal differences in $CO_2$ compositions in upper (empty symbols) and lower (filled symbols) compartments is worthy of notice. ....	129

Figure 4-3. Time evolution of accumulated CO during a) dry birch torrefaction b) IL-impregnated birch torrefaction. Time evolution of CO/ CO <sub>2</sub> mole ratio during c) dry birch torrefaction d) IL-impregnated birch torrefaction .....	130
Figure 4-4. Time evolution of accumulated (left y-scale) and captured (right y-scale) CO <sub>2</sub> of the torrefaction of IL-impregnated birch at 260°C. Differences in CO <sub>2</sub> compositions in upper (empty symbols) and lower (filled symbols) compartments reveal strong carbonation reactivity of residues .....	132
Figure 4-5. pH profiles versus time during a) dry birch torrefaction b) IL-impregnated birch torrefaction .....	134
Figure 4-6. Profiles of ionic conductivity and liquid saturation versus time during a) dry birch torrefaction b) IL-impregnated birch torrefaction .....	135
Figure 4-7. Effect of CO and methane content on CO <sub>2</sub> instantaneous concentration and amount of captured CO <sub>2</sub> using NMR .....	137
Figure 4-8. Effect of temperature on accumulated and captured CO <sub>2</sub> versus time during dry birch torrefaction in the presence of NMR (liquid saturation □ = 50 %) .....	138
Figure 5-1. The schematic of experimental torrefaction-chemical looping combustion assembly: (1) K type thermocouple (2) stainless steel mesh (3) birch sample (4) induction coil (5) stainless steel torrefaction reactor (6) pyrometer (7) induction heater power supply (8) chemical looping combustion reactor (9) electric heater (10) iron/iron oxide fixed bed (11) CLC shortcut line (12) CO <sub>2</sub> infrared detector used during iron oxide regeneration(13) cold trap (14) peristaltic pump (15) micro GC (16) mass flow meters.....	150
Figure 5-2. CO <sub>2</sub> accumulation profiles during the torrefaction of 500 mg of birch at 260°C (a) and 300°C (b) for different combustion temperatures in the torrefaction-CLC assembly. ....	154
Figure 5-3. CO accumulation profiles during the torrefaction of 500 mg of birch at 260°C (a) and 300°C (b) for different combustion temperatures in the torrefaction-CLC assembly. ....	156
Figure 5-4. H <sub>2</sub> accumulation profiles during the torrefaction of 500 mg of birch at 260°C (a) and 300°C (b) for different combustion temperatures in the torrefaction-CLC assembly. ....	157
Figure 5-5. CH <sub>4</sub> accumulation profiles during the torrefaction of 500 mg of birch at 260°C (a) and 300°C (b) for different combustion temperatures in the torrefaction-CLC assembly. ....	158
Figure 5-6. Profile of CO <sub>2</sub> production and oxygen consumption during five cycles of torrefaction/combustion and oxidation/regeneration of iron oxides. Torrefaction and CLC temperatures were, respectively, 260°C and 600°C. Red triangle = % released carbon converted to CO <sub>2</sub> . Purple diamond = O <sub>2</sub> concentration exiting CLC reactor during oxidation/regeneration. Initial O <sub>2</sub> concentration during oxidation was 6 mol% for N <sub>2</sub> flow-rate of 200 mL/min. Y1= produced CO <sub>2</sub> /total released carbon (mol/mol%), Y2 = oxygen concentration (mole%). ....	159
Figure 5-7. Gas products' distribution as a function of time during the reduction and oxidation steps of iron oxide at 600°C with acetic acid model torrefaction volatile. Acetic acid concentration during reduction was 1.6 mol.% and N <sub>2</sub> flow-rate was 100 mL/min, initial O <sub>2</sub> concentration during oxidation was 6 mol% and N <sub>2</sub> flow-rate was 200 mL/min. ....	160

Figure 5-8. Mass yield of birch wood torrefied at 260 °C and 300 °C in the thermogravimetric analyzer and under N <sub>2</sub> and CO <sub>2</sub> atmospheres.....	163
Figure 5-9. EMC of raw and torrefied birch under water/CO <sub>2</sub> and N <sub>2</sub> environments. The relative humidity (H <sub>R</sub> ) prevailing for each salt solution is shown on x axis, lines show trends. ....	164
Figure 5-10. Weight-based particle size distribution of ground raw and torrefied birch under water/CO <sub>2</sub> and N <sub>2</sub> environments. ....	166
Figure 6-1. Schematic of the experimental torrefaction-chemical looping-carbonation assembly: (1) K type thermocouple (2) stainless steel mesh (3) birch sample (4) induction coil (5) stainless steel torrefaction reactor (6) pyrometer (7) induction heater power supply (8) chemical looping combustion reactor (9) electric heater (10) fixed bed of RMR solid oxygen carrier (11) three way valve (12) carbonation column (13) carbonation fixed-bed of RMR spent residue (14) cold trap (15) peristaltic pump (16) micro GC (17) mass flow meters.....	177
Figure 6-2 . X-ray powder diffraction patterns of (a) as-received RMR; (b) RMR calcined under air at 700°C; (c) calcined RMR used during five oxidation/reduction cycles at 700°C. (●) chrysotile and lizardite, (▪) hematite, (○) chlorite, (x) forsterite, (*) magnetite.....	179
Figure 6-3 . CO <sub>2</sub> accumulation profile in the assembly during torrefaction of 500 mg of birch at 260°C (a) and 300°C (b) for different CLC temperatures.....	183
Figure 6-4. CO accumulation profiles in the assembly during torrefaction of 500 mg of birch at 260°C (a) and 300°C (b) for different CLC temperatures.....	184
Figure 6-5. CH <sub>4</sub> accumulation profiles in the assembly during torrefaction of 500 mg of birch at 260°C (a) and 300°C (b) for different CLC temperatures.....	185
Figure 6-6. H <sub>2</sub> accumulation profiles in the assembly during torrefaction of 500 mg of birch at 260°C (a) and 300°C (b) for different CLC temperatures.....	186
Figure 6-7. Profiles of CO <sub>2</sub> production and oxygen consumption during five cycles of torrefaction/combustion and oxidation /regeneration of RMR. Temperatures of torrefaction and CLC reactors were 260°C and 700°C, respectively. Blue circles are mol% of released carbon converted to CO <sub>2</sub> and accumulated in assembly. Purple diamonds are mol% of oxygen exiting CLC reactor during oxidation/regeneration step. Initial oxygen mol% during oxidation step was 6 mol% and nitrogen flow-rate 200 mL/min. Y1: produced CO <sub>2</sub> /total released carbon (mol/mol%), Y2: oxygen concentration (mol%).....	187
Figure 6-8. Accumulated and captured CO <sub>2</sub> versus time during dry birch torrefaction at 260°C in the presence of RMR carbonation bed at different temperatures.....	188
Figure 7-1. X-ray powder diffraction patterns of (a) raw chrysotile (b) chrysotile calcined with air at 900 °C (c) raw olivine (d) olivine calcined with air at 900 °C. (●) chrysotile, (◇) magnetite, (▪) forsterite, (□) enstatite, (○) hematite, (x) brucite, (*) olivine, (+) serpentine impurities in olivine. ....	202
Figure 7-2. Room-temperature <sup>57</sup> Fe Mössbauer spectra of (a) raw chrysotile. (b) chrysotile calcined for 2 h in air at 900°C. (c) chrysotile calcined for 2 h in N <sub>2</sub> at 900°C (d) raw olivine. (e) olivine calcined for 2 h in air at 900°C. ....	205

Figure 7-3. Hydrogen consumption rates (in mol(H <sub>2</sub> )/g <sub>cat</sub> /s) as a function of ramp temperature in temperature-programmed reduction tests of native and calcined chrysotile and olivine samples.	207
Figure 7-4. Activity tests of chrysotile during long-term runs (22 h) with cyclic benzene steam reforming between 800-900 °C, S/C =1.05, GHSV= 28.4 m <sup>3</sup> /(kg <sub>cat</sub> . h).	211
Figure 7-5. Transmission electron microscopy (TEM) images of (a) raw olivine, (b) olivine calcined for 2 h in air at 900°C, (c) olivine calcined for 10 h in air at 900°C, (d) chrysotile calcined for 2 h in air at 900°C.	212
Figure 8-1. Schematic of experimental setup used for measuring the catalytic activity of RMR, chrysotile and olivine for benzene cracking in a simulated syngas.	224
Figure 8-2. X-ray powder diffraction patterns of (a) as-received RMR (b) RMR calcined under air at 900 °C. (●) chrysotile and lizardite, (▪) maghemite, (○) enstatite, (x) forsterite, (*) magnetite, (+) hematite	227
Figure 8-3. TG monitoring of RMR and chrysotile weight loss during calcination at 50°C heating rate	228
Figure 8-4. MS monitoring of positive ion currents (a) m/z= 18 (H <sub>2</sub> O) for chrysotile (b) m/z= 18 (H <sub>2</sub> O) for RMR, (c) m/z= 44 (CO <sub>2</sub> ) for chrysotile and (d) m/z= 44 (CO <sub>2</sub> ) for RMR, during air calcination at 50 °C heating rate in TG	229
Figure 8-5. Hydrogen consumption rates (in mol(H <sub>2</sub> )/g <sub>Fe</sub> /s) as a function of ramp temperature in temperature-programmed reduction tests of calcined RMR, chrysotile and olivine samples	233
Figure 8-6. Transmission electron microscopy (TEM) images taken of (a) calcined RMR for 2 h at 900 °C (b) calcined chrysotile for 2 h at 900 °C (c) raw olivine (d) calcined olivine for 2 h at 900 °C (e) calcined olivine for 10 h at 900°C	234
Figure 8-7. Comparison of Benzene and methane conversion by RMR, chrysotile and olivine at two different syngas concentrations	236
Figure 8-8. (a) CO and CO <sub>2</sub> concentration profile by passing mixtures of CO/CO <sub>2</sub> /N <sub>2</sub> through a reduced bed of chrysotile at 800 °C (b) benzene and methane conversion by chrysotile versus CO <sub>2</sub> concentration in C <sub>6</sub> H <sub>6</sub> /CH <sub>4</sub> /CO/CO <sub>2</sub> /N <sub>2</sub> mixture (c) benzene and methane conversion by chrysotile versus CO/CO <sub>2</sub> mole ratio in C <sub>6</sub> H <sub>6</sub> /CH <sub>4</sub> /CO/CO <sub>2</sub> /N <sub>2</sub> mixture (d) coke formation on chrysotile versus CO <sub>2</sub> concentration in C <sub>6</sub> H <sub>6</sub> /CH <sub>4</sub> /CO/CO <sub>2</sub> /N <sub>2</sub> mixture (e) coke formation on chrysotile versus CO/CO <sub>2</sub> concentration in C <sub>6</sub> H <sub>6</sub> /CH <sub>4</sub> /CO/CO <sub>2</sub> /N <sub>2</sub> mixture.	238
Figure 8-9. (a) H <sub>2</sub> production by passing mixtures of CO/CO <sub>2</sub> /N <sub>2</sub> through a reduced bed of chrysotile at 800 °C (b) benzene and methane conversion by chrysotile versus H <sub>2</sub> O concentration in C <sub>6</sub> H <sub>6</sub> /CH <sub>4</sub> /H <sub>2</sub> O/N <sub>2</sub> mixture (c) coke formation on chrysotile versus H <sub>2</sub> O concentration in C <sub>6</sub> H <sub>6</sub> /CH <sub>4</sub> /H <sub>2</sub> O/N <sub>2</sub> mixture (d) benzene and methane conversion by chrysotile versus H <sub>2</sub> /H <sub>2</sub> O mole ratio in C <sub>6</sub> H <sub>6</sub> /CH <sub>4</sub> /H <sub>2</sub> /H <sub>2</sub> O/N <sub>2</sub> mixture (e) coke formation on chrysotile versus H <sub>2</sub> /H <sub>2</sub> O mole ratio in C <sub>6</sub> H <sub>6</sub> /CH <sub>4</sub> /H <sub>2</sub> /H <sub>2</sub> O/N <sub>2</sub> mixture (f) benzene and methane conversion by chrysotile versus CH <sub>4</sub> concentration in C <sub>6</sub> H <sub>6</sub> /CH <sub>4</sub> /H <sub>2</sub> O/N <sub>2</sub> mixture.	240
Figure 8-10: (a) benzene and methane conversion by chrysotile at 800 °C versus H <sub>2</sub> concentration (b) benzene and methane conversion by chrysotile at 800 °C versus CO and H <sub>2</sub>	

concentration (c) coke formation on the surface of chrysotile at 800 °C versus CO and H<sub>2</sub>  
concentrations ..... 243

## **Acknowledgements**

This thesis would not have been possible without the support and patience of my family, friends and advisor.

Hereby I would like to express my deepest thanks to my advisor, Professor Faïçal Larachi who always encouraged me and gave me more confidence and strength during my PhD study at Laval University. I was very lucky to get a chance to have you as my advisor and work with you. Thank you for all your kind support and guidance.

My great gratitude goes to my brother, Erfan, who was always there for me and helped me a lot through the dilemmas.

My sincere appreciations to the chemical engineering department technical staff (in Pavillon Adrien Pouliot), Jérôme Noël, Marc Lavoie, Jean-Nicolas Ouellet, Michel Lafrance and Anne Bourassa for their help and supports during this research project.

My sincere gratefulness to all my friends and my colleagues, especially Dr. Mohsen Hamidipour, Dr. Pouya Hajiani, Dr. Hojjat Mahi and Ali Faridkhou for their friendship and support. I would like to have special thanks to my friend Ali Faridkhou who helped me a lot during my PhD for editing my texts and my papers.

Finally, I acknowledge the financial support of Natural Sciences and Engineering Research Council of Canada (NSERC) and the Canada Research Chair “Green processes for cleaner and sustainable energy”.



## Foreword

This PhD thesis includes nine chapters. Except for the first and last chapters which are respectively the introduction to the thesis and conclusion of the research work, each one of the chapters represents an article published in, or submitted to, scientific journals. These articles are listed below.

[1] **Sarvaramini, A.**, Assima, G.P., Larachi, F. Dry torrefaction of biomass – Torrefied products and torrefaction kinetics using the distributed activation energy model. *Chemical Engineering Journal*. 2013. p. 498-507.

[2] **Sarvaramini, A.**, Gravel, O., Larachi, F. Torrefaction of ionic-liquid impregnated lignocellulosic biomass and its comparison to dry torrefaction. *Fuel*. 2013;103:814-26.

[3] **Sarvaramini, A.**, Assima, G.P., Beaudoin, G., Larachi, F. Biomass torrefaction and CO<sub>2</sub> capture using mining wastes- A new approach for reducing greenhouse gas emissions of co-firing plants. *Fuel*. 2014;115:749-57.

[4] **Sarvaramini, A.**, Larachi, F. Integrated biomass torrefaction-chemical looping combustion as a method to recover torrefaction volatiles energy. *Fuel*. 2014;116:158-67.

[5] **Sarvaramini, A.**, Larachi, F. Mossbauer spectroscopy and catalytic reaction studies of chrysotile-catalyzed steam reforming of benzene. *Journal of Physical Chemistry C*. 2011;115:6841-8.

[6] **Sarvaramini, A.**, Larachi, F. Catalytic oxygenless steam cracking of syngas-containing benzene model tar compound over natural Fe-bearing silicate minerals. *Fuel*. 2012;97:741-50.

[7] **Sarvaramini, A.**, Larachi, F. Fe/Mg silicate mining residues as solid oxygen carriers for chemical looping combustion of torrefaction volatiles. Submitted to *Energy and Fuels*.

The research papers are organized on my own and reviewed by my supervisor, Prof. Faïçal Larachi who directed and provided expertise in designing experiments and handling data analysis during my research work.

Mr Olivier Gravel, co-author of the paper entitled, “Torrefaction of ionic-liquid impregnated lignocellulosic biomass and its comparison to dry torrefaction”, helped me

to prepare the necessary instruments for the ionic liquid assisted torrefaction experiments and he was also involved in performing the experiments in the lab.

Dr. Gnouyaro Palla Assima, co-author of the papers entitled “Dry torrefaction of biomass – Torrefied products and torrefaction kinetics using the distributed activation energy model” and “Biomass torrefaction and CO<sub>2</sub> capture using mining wastes- A new approach for reducing greenhouse gas emissions of co-firing plants” assisted me to perform the diverse experiments required for the papers and I also used his expertise on mineral carbonation field. He was also involved in analysis of the experimental results and helped me to revise the manuscripts. In this regard, Prof George Beaudoin, (co-supervisor of Dr. Gnouyaro Palla Assima, and also co-author of the published work) from the department of Geology and Geological Engineering of Laval University, provided us with the mineral samples required for the carbonation experiments and also helped in manuscript revision thanks to his fruitful suggestions.

Some of the research findings were also presented in the following conferences:

**Sarvaramini, A.**, Larachi, F. Chrysotile for catalytic cracking in biomass steam gasification - Kinetics & catalyst characterization of model-tar compound, CAMURE 8 & ISMR 7, Naantali, Finland, 2011.

**Sarvaramini, A.**, Larachi, F. Catalytic cracking of gasification tar by Fe-bearing silicate minerals, presented at the 3rd CGCC Annual Meeting, Université Laval, Quebec, Canada, 2011.

Hasib-ur-Rahman, M., Bouteldja, H., Khan Wardag, A.N., **Sarvaramini, A.**, Assima, G.P., Siaj, M., Larachi, F. Advances towards adept biomass gasification and efficient carbon dioxide capture processes, CQMF 4th Annual Symposium at Duchesnay, Quebec, Canada, 2011.

**Sarvaramini, A.**, Gravel, O., Larachi, F. Torrefaction of ionic-liquid impregnated lignocellulosic biomass and its comparison to dry torrefaction, presented at the 4rd CGCC Annual Meeting, Université de Montréal, Montréal, Canada, 2012.



## **Chapter 1 : Introduction and objectives**

### **A) Background**

The worldwide energy demand is increasing constantly due to fast growth in population and industrialization. Although many efforts are made to increase the energy efficiency of different industrial sectors, the economic and population growth rate results in energy request growth of 1.2% per year [1]. Presently, the major part of world's energy is provided by conventional energy sources, e.g., coal, natural gas and oil. However, these fossil energy sources are facing some problems. First, fossil fuel resources are limited and fossil fuel reserves are getting depleted. Second, energy extraction from fossil fuels is polluting the environment. As an example, the global increase in greenhouse gas emissions due to the burning of fossil fuels is increasingly objectified as a menace to world climate. Consequently, the increased worldwide energy requirement coupled with climate change issues and the rising cost of fossil fuels are pressing factors for exploration of alternative energy sources that are cheap, renewable and harmless to the environment. As a result, new green technologies that are harvesting energy from renewable resources such as solar, wind, hydroelectric and biomass are developed and improved to reduce the dependency to fossil fuels. Among the portfolio of renewable sources for energy production, biomass has this advantage to produce solid, liquid and gaseous fuels through different thermal and chemical processes.

Biomass is carbon neutral resource whose life cycle is considered as the fourth energy source in the world after coal, oil and natural gas [2]. Presently, renewable biomass resources are playing an important role in the worldwide energy production and it is estimated that around 14% of world's energy is provided by biomass resources through their conversion to heat, electricity, transportation fuels and chemicals [2]. Some of the main advantages of biomass as energy source are listed below [2]:

- Biomass is a renewable, sustainable and relatively environmentally friendly energy source.
- Biomass is CO<sub>2</sub> neutral energy source and its consumption does not increase the CO<sub>2</sub> level of atmosphere.
- The sulfur content of biomass is normally low leading to less SO<sub>2</sub> emissions to the environment.

- The mineral content of biomass lower than in coal leads to less ash production.
- Biomass is considered as an abundant energy source in comparison with the fossil fuels.

Biomass could be provided through different sources. The three main sources of biomass for energy production are as below [2]:

- Agricultural production wastes and crop residues, etc.
- Forest residues;
- Energy crops comprising low-cost plants grown especially for biofuel production. Energy crops could be categorized as woody and herbaceous plants.

In the recent years, the use of forest residues as a source of bioenergy in Canada has found a considerable interest [3]. This interest arises from the fact that Canada has a large potential forest bioenergy because of its vast area of managed forests (more than  $2 \cdot 10^6 \text{ km}^2$ ) and its large wood supply (annual allowable cut of  $250 \cdot 10^6 \text{ m}^3$ ) compared to its relatively small population (34 million inhabitants) [3]. In Canada, the potential of forest bioenergy to meet the energy requirements of its population is high compared to other countries: approximately  $8 \text{ m}^3$  of wood per capita are harvested annually in Canada, which places the country third behind Finland ( $14 \text{ m}^3$ ) and Sweden ( $9 \text{ m}^3$ ) [3]. There are three main sources of forest residues in Canada such as (i) primary residues which are the by-products of conventional forest management, such as biomass from thinning and harvesting residues (ii) secondary residues which comprise by-products of industrial processes, such as bark, sawdust and (iii) tertiary residues which are by-products of demolition, construction and packaging processes. Among the mentioned products, the primary products are considered as the largest potential stable source of bioenergy for Canada.

Due to the fluctuations in the price of different fossil fuels and the environmental costs associated with the use of fossil fuels, the government of Québec also adopted an Action Plan in 2009 for the valorization of the huge forest biomass resources of the province. The total annual available forest residue in the province of Québec is estimated to be around 6.4 million dry tonnes per year. Almost 3.5 million of the forest residue is in the form of trunks and the rest in the form of branches. According to the scenario adopted by the Québec Government until 2016, around 22% of the mentioned forest biomass source could be used annually to produce energy and chemicals through

industrial transformation technologies such as combustion, gasification and pyrolysis. It is estimated that by using this approach, it would be possible to replace the equivalent of 10.2 petajoules of oil by forest biomass energy, which represents 1.4 % of the predicted oil consumption in the energy strategy of Quebec in 2016.

In addition to the huge biomass resources, Québec has also large deposits of different minerals such as gold, silver, nickel, copper and iron ores. The mining industry, including the primary mineral processing segment, makes a significant contribution to the economy of Québec. On 2009 and 2010, Québec ranked first among the Canadian provinces, ahead of Ontario for the first time, in terms of metal mineral production. In addition, Québec also extracts different types of non-metallic minerals such as chrysotile, graphite, ilmenite, mica, a silica, and peat. The vast mining activities in Québec have led to the accumulation of huge amounts of ultramafic mining tailings and residues containing significant amount of Mg, Si and Fe. Two examples of such mine tailings are the waste residues of Black Lake (Thetford Mines, Québec) and the Dumont Nickel Mines (25 km north-west of Amos, Québec). The Black Lake mine residues extend over an area of 1.7 km<sup>2</sup> and have a height of 130 m leading to a huge store of ca. 2 billion metric tons of chrysotile mining residues (CMR) accumulated in southern Québec. The accumulated residues in Dumont Nickel Mines are also estimated to attain ca. one billion tonnes. Due to the presence of valuable metals such as magnesium and iron in the structure of cheap, abundant and already crushed residues, several attempts are being explored to use these materials in thermochemical conversion processes. For example, sequestration of CO<sub>2</sub> produced during the thermochemical fuel conversion by means of the magnesium leached from the residue structure is one of the foreseen applications.

Applying the mentioned potential of mining residues in biomass thermochemical conversion processes could have some interesting applications for the biomass energy sector. One of the main objectives of the present thesis is therefore to investigate new routes to valorize mining residues in thermochemical conversion processes. The focus of this study was more on the implementation of this potential in biomass torrefaction and gasification processes. Torrefaction is a pre-requisite step for using the forest residue in thermochemical processes such as gasification. The forest residue could contain a wide variety of biomass types with different humidity levels and

physicochemical properties. Consequently, forest biomass residues should be pretreated to make them amenable for thermochemical conversion processes.

## **B) Literature review**

This section is divided into two sub-sections. In the first sub-section, the thermochemical biomass conversion route is introduced and different types of biomass pre-treatments as pre requisite steps for efficient thermochemical biomass conversion are discussed. Torrefaction as one of the main pre-treatment routes is discussed in detail in the first sub-section. The second sub-section is devoted to review some existing applications of cheap and abundant minerals and mining residues in thermochemical processes.

### **B.1. Biomass thermochemical conversion and importance of pre-treatment**

#### **B.1.1. Lignocellulosic biomass composition**

Wood and other plant biomass are composite materials constructed from oxygen-containing organic polymers. The presence of large amounts of oxygen in plant carbohydrate polymers is the main difference between biomass and fossil fuels which leads to some differences in the pyrolytic chemistry of biomass from other fossil fuels. High-molecular weight carbohydrate polymers and oligomers (65-75%) and lignin (18-35%) are the major components of biomass. Small amount of low-molecular weight materials mostly organic extractives and inorganic minerals are also present in wood (usually 4-10%) [4]. Consequently, the major constituents of biomass are cellulose, hemicelluloses, lignin, organic extractives and inorganic minerals. The weight percent of cellulose, hemicellulose, and lignin varies in different biomass species as can be observed in Table 1-1.

**Table 1-1:** Approximate composition in mass percentage of different biomass species [5]

<b>Species</b>	<b>Mineral</b>	<b>Extractable</b>	<b>Lignin</b>	<b>Hemicellulose</b>	<b>Cellulose</b>
<b>Softwood</b>	0.4	2.1	27.8	24	41
<b>Hardwood</b>	0.3	3.1	19.5	35	39
<b>Wheat straw</b>	6.6	11.1	16.7	28.2	39
<b>Rice straw</b>	16.1	17.9	11.9	24.5	30.2

Cellulose is the most abundant component present in wood and almost 40-50 wt % of dry wood is made of cellulose. Cellulose is a polymer of D-glucose monomers (i.e., a

polysaccharide) which are bound together by ether-type linkages called glycosidic bonds (Figure 1-1). Glucose anhydride, formed via removal of water from each glucose, is polymerized into long cellulose chains that contain 5000-10000 glucose units [4]. The basic repeating unit of cellulose polymer consists of two glucose anhydride units, called cellobiose unit. The principal physical characteristic of cellulose is its extreme insolubility. It can only be dissolved by hydrolysis in the form of sugars using strong mineral acids or enzymes. Cellulose is degraded at temperatures in the range of 240 to 350°C and the pyrolysis of cellulose leads to the production of anhydrocellulose and levoglucosan [4].

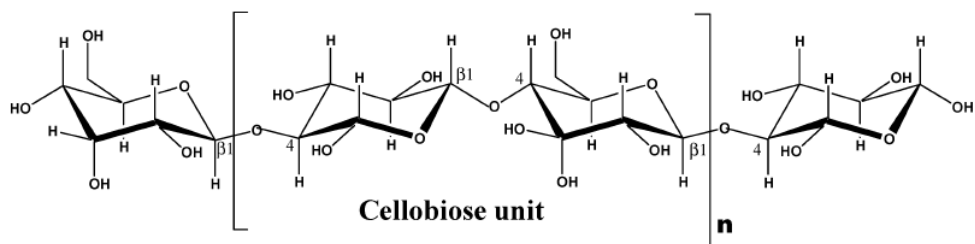


**Figure 1-1:** Chemical structure of cellulose [4]

Hemicellulose is the second major wood chemical constituent which is also known as polyose. Hemicellulose is a mixture of various polymerized mono-saccharides such as glucose, mannose, galactose, xylose, arabinose, 4-*O*-methyl glucuronic acid and galacturonic acid residues (Figure 1-2). Hemicellulose has lower molecular weight than cellulose. The number of repeating saccharide monomers is only 150 which, compared to the number of repeating units in cellulose (5000-10000) is low. Hemicellulose decomposes at lower temperatures (200-260°C) than cellulose [4].

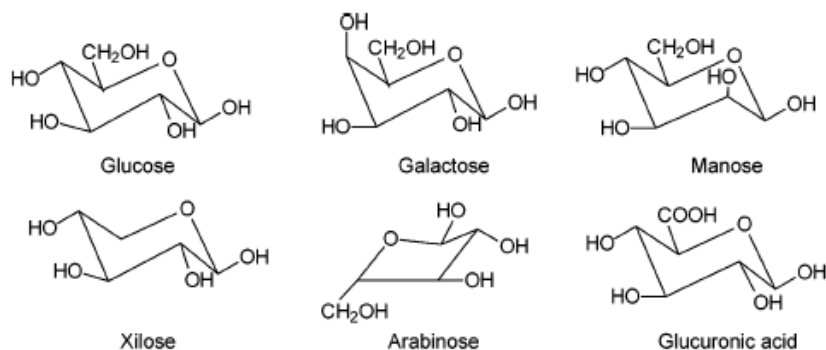


**Figure 1-2:** Main components of hemicellulose [4]

The third major component of wood is lignin. About 23-33 wt % of softwoods and 16-25 wt % of hardwoods are composed of lignin [4]. Lignin is a highly branched, polyphenolic substance that consists of an irregular array of variously bonded “hydroxy-” and “methoxy-” phenylpropane units. The three general monomeric phenylpropane units exhibit *p*-coumaryl, coniferyl, and sinapyl structures (Figure 1-3). Hardwood and softwood lignin have different structures. Guaiacyl lignin, which is found mainly in softwoods, results from the polymerization of a higher fraction of coniferyl phenylpropane units. Guaiacyl-syringyl lignin, which is typically found in many hardwoods, is a copolymer of both coniferyl and sinapyl phenylpropane units where the fraction of sinapyl units is higher than that in softwood lignins [4]. Lignin pyrolysis yields phenols via the cleavage of ether and carbon-carbon linkages.

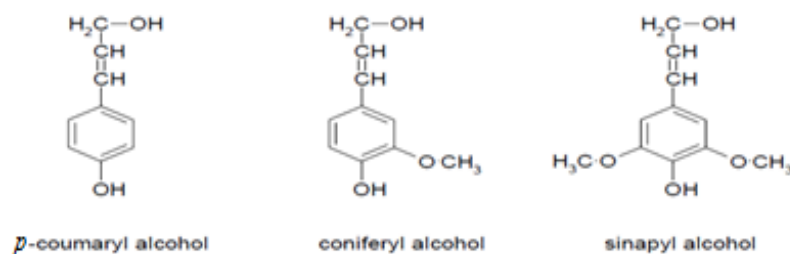


**Figure 1-3:** *p*-coumaryl, coniferyl and sinapyl structures [4]

Organic extractives and inorganics are the fourth and fifth constituents of wood. Organic extractives can be extracted from wood with polar solvents (such as water, methylene chloride, or alcohol) or nonpolar solvents (such as toluene or hexane). Example extractives include fats, waxes, alkaloids, proteins, phenolics, simple sugars, pectins, mucilages, gums, resins, terpenes, starches, glycosides, saponins, and essential oils [6]. The inorganic constituents or ashes represent less than 1wt% of the wood but, as shown in Table 1-1, they are much higher in herbaceous biomass. Ash is mainly composed of oxides of calcium, potassium, sodium, magnesium, silicone and iron. Oxides of calcium are the most abundant constituents of ash [6]. Traces of heavy metals could be also present in wood ashes.

### **B.1.2. Thermochemical biomass conversion; technologies and challenges**

Biomass fuels could be converted to energy via different routes. The two most widely known routes for biomass conversion are thermochemical and biochemical. Thermochemical conversion methods have some advantageous over biochemical routes

such as their flexibility regarding the feedstock and production of a wider range of end products. Combustion, pyrolysis and gasification are the three biomass thermochemical conversion routes for energy production. Combustion burns biomass at temperatures ranging from 800-1000°C and in the presence of excess oxygen to produce heat and electricity. Combustion can be considered as a well-established industrial technology and combustion systems are available in the domestic and industrial scales. Pyrolysis is a thermochemical conversion of biological material under an inert atmosphere to produce solid (char), liquid (bio-oil), and permanent gases. Biomass pyrolysis processes are divided into three subgroups: slow pyrolysis, fast pyrolysis and flash pyrolysis. Slow pyrolysis is performed at temperatures around 500°C while the heating rate of biomass is kept low ( $<1^{\circ}\text{C s}^{-1}$ ) leading to the production of larger amounts of char than volatiles [7]. This process has always been used by mankind for production of charcoals [7]. Fast pyrolysis uses much faster heating rates ( $10\text{-}200^{\circ}\text{C s}^{-1}$ ) and could produce larger amounts of liquid and gases. Fast pyrolysis is different from traditional pyrolysis where charcoal is the desired product, mainly because the primary goal in this process is to produce liquid fuels in replacement (or back-up) of crude oil. In the fast pyrolysis biomass is subjected to higher heating rates than slow pyrolysis while its residence time in the reactor is short. Flash pyrolysis is considered as an improved version of fast pyrolysis in which biomass is subjected to heating rates exceeding  $1000^{\circ}\text{C s}^{-1}$  [7]. The process applies very high heating rate for biomass pyrolysis while the biomass residence time in the reactor is around a few seconds. Flash pyrolysis leads to the production of higher amounts of bio-oils than the other two pyrolysis routes. However, bio-oil cannot be used directly in internal combustion engines and should be upgraded to meet the necessary specifications of combustion engine fuels. In contrast to pyrolysis, biomass gasification is performed under a partially oxidizing atmosphere. In this process solid biomass is converted to synthesis gas at temperatures varying from 600°C to 1000°C. The synthesis gas consists of  $\text{H}_2$  and  $\text{CO}$  as the desired gasification products and some other gases such as  $\text{CO}_2$ , water,  $\text{CH}_4$  along with some heavy hydrocarbons called tar. Separation and elimination of tar from the syngas account for a significant portion of fuel production costs [8]. Consequently, different configurations of gasifiers with diverse operating conditions have been already developed to minimize in-situ tar production and consequently to reduce the cost of the cleanup step. A tar free synthesis gas produced during gasification can be used for different purposes to produce a broad range of chemicals and transportation fuels.

Application of raw biomass in thermochemical processes is reported to cause several inconveniences. Some of the inconveniences are listed below:

- The bio-oil derived from raw biomass is difficult to burn in diesel engines due to its difficult ignition (due to low heating value and high water content), corrosiveness (presence of acids), and coking (due to the existence of thermally unstable components) [9].
- Low energy density of raw biomass due to its large moisture and oxygen content is known to cause flame instabilities in the combustion chambers [10].
- Raw biomass contains variable amount of moisture. The unprocessed wood could contain up to 50% of humidity. This variable humidity content of wood could afflict the conversion efficiency in thermochemical processes and as a result an adjustment in the thermochemical process is always required.
- Several thermochemical conversion processes such as fast pyrolysis for bio-oil production require small or fine biomass particles. However, the rigidity and mechanical strength of biomass structure attributed to the long crystalline cellulose fibers intertwined with non-crystalline hemicellulose results in higher grinding energy requirements and reduces grinding efficiency of bio-energy units [11].
- The presence of alkali metals in bio-oil catalyzes the polymerization reactions in bio-oil leading to its instability and causing some changes in its physical and chemical properties. Furthermore, the ash present in the synthesis gas or vapors derived from pyrolysis could be deposited in turbines and combustion engines [12]. Biomass ash could also induce some agglomeration problems in the gasifiers.
- Raw biomass has low flowability and fluidization properties which lead to some difficulties in feeding biomass into fluidized bed pyrolysis and gasification units [13].
- The high moisture content of biomass expedites its degradation due to fungal attacks and consequently the storage of raw biomass before thermal conversion is too often problematic.
- Low conversion of cellulose in fast pyrolysis due to the presence of lignin surrounding hemicellulose and cellulose and the crosslinking with the

carbohydrate polymers reducing the susceptibility of cellulose to pyrolysis degradation [14-16].

- The transportation and handling of biomass to the thermal conversion units is expensive due to its low energy density [17].

The mentioned inconveniences associated with thermochemical biomass conversion necessitate some biomass pre-treatment steps to improve its properties before thermal conversion. Several pre-treatment methods have been already applied on biomass to enhance its quality prior to its thermal conversion. Pre-treatment techniques could be divided into three subgroups: 1) biomass torrefaction which is a thermal process to remove oxygen from the raw biomass and to increase its energy density in a non-oxidizing environment. 2) Biomass pre-treatment with some solvents such as dilute acids to disrupt the lignin structure and to remove the inorganics from biomass and 3) biomass pre-treatment using fungi to enhance lignin destruction and to improve the pyrolysis properties of biomass.

### **B.1.3. Torrefaction**

#### **B.1.3.1. Principles and mechanism of torrefaction**

Torrefaction is a biomass thermal pre-treatment performed at temperatures ranging from 200-300°C to upgrade the biomass quality and to reduce some of the biomass inconveniences such as its low heating value and energy density, high moisture content, low combustion efficiency and high grinding energy requirements. The solid products obtained from torrefaction have some advantageous properties such as (1) higher energy density and heating value (2) reduced transport cost due to reduced humidity of the biomass (3) higher resistivity of torrefied biomass to fungal attack due to the hydrophobic nature it gains during torrefaction (4) reduced grinding energy requirement of torrefied biomass due to the breakup of some polymeric chains.

Depending on the torrefaction temperature and biomass residence time in the torrefaction reactor, hemicellulose, cellulose and lignin content of biomass are partly decomposed. The decomposition of biomass during torrefaction leads to the release of some condensable and non-condensable gases. In a typical biomass torrefaction process, around 30 weight percent of biomass is released to the gas phase in the form of humidity, some oxygenated hydrocarbons and other gases. However, the gas phase only removes ca. 10 percent of biomass energy leading to solid products with higher energy

density than the initial raw biomass. Torrefaction is normally performed at atmospheric pressure and in a non-oxidizing environment.

Numerous reactions could take place during torrefaction due to the degradation of the polymeric structures in the biomass. The torrefaction reactions are complex and exposing a thorough mechanism for torrefaction is not possible. A simplified mechanism presented by Bergman et al. [18] is normally used to explain the evolution of biomass with temperature during torrefaction. According to Bergman et al. [18] a general mechanism for biomass torrefaction consists of five steps which are dependent on the torrefaction temperature and type of biomass. These steps are as follows:

1-Drying

2-Glass transition/softening

3-Depolymerization and recondensation

4-Limited devolatilization and carbonization

5-Extensive devolatilization and carbonization

The first step in biomass torrefaction is drying in which biomass loses humidity. Biomass drying is normally performed at temperatures below 120°C in which biomass is considered as non-reactive and the chemical structure of cellulose, hemicellulose and lignin remains unaltered in this step. By increasing the biomass temperature above 120°C, lignin softening occurs. The third step in biomass torrefaction is depolymerisation. Biomass depolymerisation happens at temperatures ranging from 150°C to 200°C leading to the breakage of some hydrogen and carbon bonds, and formation and condensation of some short chain polymers in the solid structure. However, biomass devolatilization starts at temperatures higher than 200°C leading to a disruption of intermolecular and intramolecular hydrogen bonds, and C–C and C–O bonds in biomass resulting in a release of some oxygenated compounds such as alcohols, carboxylic acids, aldehydes, ethers, and some permanent gases as CO, CO<sub>2</sub> and CH<sub>4</sub>. In the case where the torrefaction temperature is lower than 250°C, hemicellulose is mostly decomposed while the decomposition of cellulose and lignin are limited. However, by increasing the torrefaction temperature up to 300°C all the biomass compounds are involved in devolatilization.

### **B.1.3.2. Torrefaction products**

The biomass torrefaction products could be classified into solid and volatiles. Several operating parameters such as torrefaction temperature and biomass residence time in torrefaction reactor as well as the physical and chemical properties of biomass could affect the amount of solid and volatiles produced during torrefaction. The solid product consists of a gamut of intact polymers from less reactive fractions that are not likely to take part in the torrefaction reaction to various products resulting from it. The latter include oligomers produced due to depolymerisation, short chain organics condensed in the lattice of torrefied biomass, char and mineral components present in the original biomass. Volatiles normally account for 30-40 wt% of the torrefaction products and could encompass 10-20 % of total initial biomass energy. The presence of some low-caloric value oxygenated compounds in the volatiles is the main reason for its low energy content. Furthermore, partial elimination of oxygen from biomass and its release into the gas phase leads to the formation of solid products with higher energy density.

The volatiles released during biomass torrefaction consist of a condensable fraction and a non-condensable part. Prins et al. [19] investigated the yield and composition of volatiles which were released from the torrefaction of two deciduous wood types (beech and willow) and a coniferous wood (larch) torrefied at temperatures ranging from 230°C to 300°C. The main condensable products released from their samples were water, acetic acid and formic acid while small quantities of methanol, lactic acid, furfural, hydroxyl acetone and phenol were also produced. The yield of each compound is dependent on the type of biomass and torrefaction temperature. However, in general the amount of volatiles released from the deciduous wood (particularly, methanol and acetic acid) was higher than those of coniferous wood. The main condensable products obtained from the torrefaction of their samples were similar to those obtained during the torrefaction of xylan leading to this conclusion that the oxygenated hydrocarbons are more abundantly produced during hemicellulose decomposition. The presence of acetoxy and methoxy groups in hemicellulose and their breakage during torrefaction could lead to the formation of formic acid and methanol. CO<sub>2</sub> is the main non-condensable gas produced during torrefaction. CO<sub>2</sub> production during torrefaction is explained by the decomposition of carboxyl acid groups of the biomass. Beside CO<sub>2</sub>, CO and very small amounts of hydrogen and methane were also detected. Bergman et al. [18] also studied the products of torrefaction of three different wood samples such as

willow, woodcutting and demolition wood torrefied at temperatures ranging from 250°C to 300 °C and for residence times ranging from 7 to 30 min. They reported that the yield of volatiles produced during torrefaction is strongly dependent on the torrefaction temperature, time and biomass properties. They divided the condensable products into three sub-groups. The first one was reaction water produced due to biomass dehydroxylation and decomposition. The second sub-group consists of organics produced during biomass decomposition such as acids, alcohols, furans and ketones. The last sub-group was composed of lipids which are not really the reaction products and are present in the original biomass in the form of waxes and fatty acids.

### **B.1.3.3. Properties of torrefied biomass**

**Energy density** Torrefaction leads to some significant changes in proximate and elemental composition of biomass making it a more suitable fuel for energy production. In recent years, many papers and reports have been published showing the improvement in energy density of biomass thanks to torrefaction. In general, torrefaction reduces the moisture and volatile content of biomass. During this process the carbon content of biomass increases due to the charring of biomass as well as the cracking of volatiles while biomass hydrogen and oxygen content is decreasing. The formation of CO, CO<sub>2</sub>, water and oxygenated hydrocarbons which have less energy density than biomass leads to the formation of solid products with higher energy density. Patel et al. [20] studied the torrefaction of cotton stalk, prosopis and sugarcane bagasse at 300°C for one hour and they observed 27-41% of improvement in high heating value of the samples. The torrefied samples had less humidity and volatiles content with the higher fixed carbon than the raw samples (9-24%). Similar observations were reported in the study of Bridgeman et al. [21] on the torrefaction of reed canary grass, wheat straw and willow at temperatures ranging from 230 to 290°C and 30 min residence time. Increasing the torrefaction temperature improved the samples carbon content while the concentration of hydrogen and oxygen decreased. The torrefied sample at 290°C during 30 min showed 10-20 % increase in their carbon content compared to the raw samples while oxygen and hydrogen contents of the torrefied samples were 3-26% and 7-18% less than those of the raw samples, respectively. They also plotted the oxygen-to-carbon and hydrogen-to-carbon ratios on the Van Krevelen diagram as observed in Figure 1-4. As is illustrated, the change in elementary composition of torrefied biomass moves towards lignite on the Van Krevelen plot.

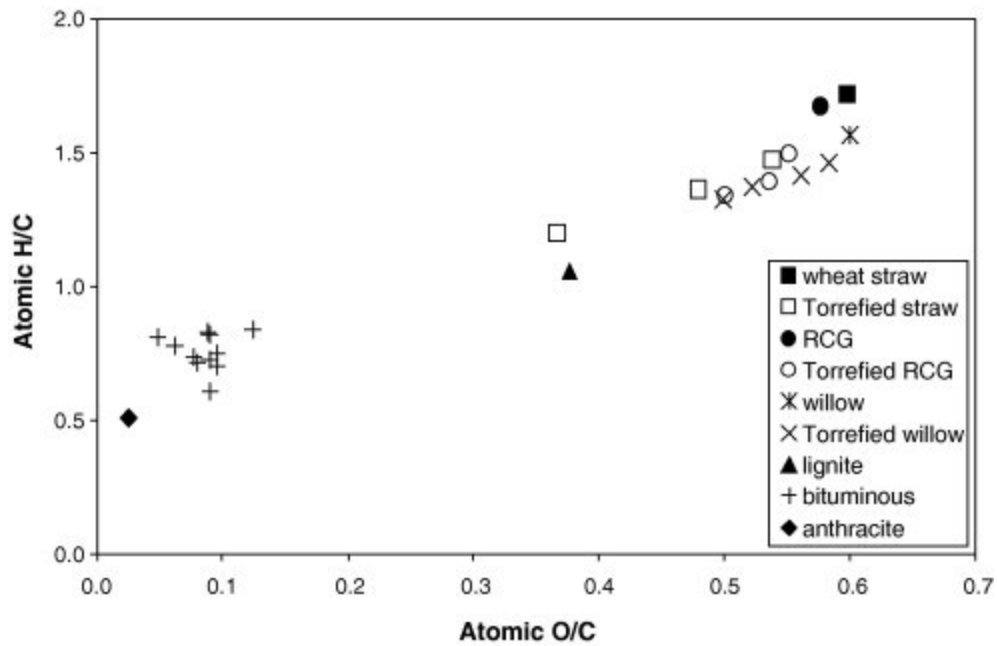


**Figure 1-4:** The evolution of H/C versus O/C of torrefied biomass [21]

**Biomass grindability** Torrefaction improves the grindability of biomass. The improved grindability of torrefied biomass could increase the efficiency of co-firing and entrained flow gasification processes in which pulverized biomass is required. Torrefaction leads to partial depolymerization/ decomposition of cellulose and hemicellulose which reduces the fibers length and mechanical stability of biomass and as a result improves its grindability [13,22,23]. The torrefied biomass is more brittle leading to the reduced grinding energy requirements than that of raw biomass.

Phanphanich et al. [22] torrefied pine wood samples at temperatures ranging from 225 to 300°C during 30 min and they investigated the effect of torrefaction on the grindability and grinding energy requirements of pine wood and some logging residues using a laboratory heavy duty knife mill. The specific grinding energy of raw samples was ca. 237 kWh/t while torrefaction reduced considerably the grinding energy of pine wood and logging residues. Up to 90% reduction in the grinding energy requirement of pine chips was observed after torrefaction at 300°C. The specific grinding energy of torrefied sample at 300°C compared well with wheat straw, corn, and switch grass and similar to the energy needed to grind coal. Their study also showed the presence of a negative linear correlation between the torrefaction temperature and biomass grinding energy. Increasing the torrefaction temperature decreased considerably the grinding energy of pine wood leading to the grinding energies close to that of coal.

The effect of torrefaction temperature and duration on the grinding energy and particle size distribution of beech and spruce chips was investigated by Repellin et al. [23] using knife and rotary mill instruments. The results of their study showed that the fine grinding of raw wood requires a high amount of energy contributing to almost one sixth of its high heating value. However a high reduction in the grinding energy requirement of birch and spruce was observed due to torrefaction. Almost 90% of the energy required for grinding of raw spruce and beech woods could be saved by torrefaction at 280°C. The mechanism controlling grinding properties of the biomass samples could be explained in two steps. The first step which is taking place at temperatures lower than 200°C is mainly attributed to the dehydration and lignin physical transformation leading to the shrinkage of the lignocellulosic material and formation of some cracks on the biomass sample which improves its grindability. This step has a strong influence on the grindability of the wood samples. The second step begins with thermal decomposition of wood at temperatures higher than 200°C which leads to progressive embrittlement and degradation of wood cell walls. By increasing the decomposition temperature of spruce and birch and as a result increasing the decomposition extent of the sample, a considerable reduction in grinding energy was observed.

**Humidity uptake** The equilibrium moisture content (EMC) of biomass affects transportation cost, storage and overall economy of bio-fuel production. The equilibrium moisture content is established when humidity content of biomass sample is in equilibrium with the relative humidity of the surrounding environment at a given relative humidity, temperature and pressure.

The main mechanism for water adsorption on biomass is water binding to the polar sites of biomass such as hydroxyl and carboxyl groups. Torrefaction leads to the cleavage of some of these polar groups and formation of some nonpolar structures. As a result, the number of biomass active sites for humidity adsorption is decreasing leading to reduced water uptake of torrefied biomass. Hemicellulose is known as one of the main biomass compounds having active hydroxyl groups for humidity adsorption [24]. However, depending on the temperature of biomass torrefaction process, hemicellulose is decomposed and it loses some of its hydroxyl groups leading to samples with reduced water humidity uptake. Medic et al. [25] investigated the equilibrium moisture content of raw and torrefied corn stover biomass samples at temperatures ranging from 10 to

40°C. The corn samples were torrefied at temperatures between 200°C to 300°C and their equilibrium moisture content was obtained at five different relative humidities of the surrounding atmosphere. Considerable decrease in the equilibrium moisture content of torrefied corn stover was observed compared to the raw sample. It is also observed that by increasing the torrefaction temperature the equilibrium moisture content of corn stover was decreasing.

Acharjee et al. [26] used a static desiccator technique to measure the equilibrium moisture content of raw and torrefied pine wood samples exposed to constant relative humidities maintained by saturated salt solutions. At low relative humidities, equilibrium moisture content increases rapidly with relative humidity followed by a period of more gradual increase and then at high relative humidities the EMC increases quite rapidly. Torrefaction affected EMC of pine wood and the torrefied pine wood samples showed more hydrophobic properties than the raw pine samples. Almost 50% reduction in the EMC of pine wood after torrefaction at 300°C was observed. Acharjee et al. [26] also studied the effect of torrefaction on bonded and non-bonded water. In the case of raw pine wood, the dominant mechanism of water uptake at low relative humidity ( $HR < 20\%$ ) was adsorption through formation of strong bonds with the biomass network leading to the formation of bonded water. However, at HR above 20% the fraction of bonded water was almost constant and it was independent of relative humidity showing that biomass is fully saturated with water. However, after torrefaction biomass showed less bonded water representing a significant change in its structure. Increasing the torrefaction temperature also led to a pronounced reduction of bonded water resulting in the formation of less hydrophilic samples. However, the results of their study showed that the content of non-bonded water was independent of the thermal treatment.

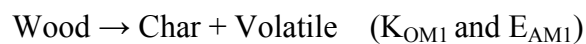
**Combustion properties** Bridgeman et al. [21] investigated the combustion properties of torrefied willow, red canary grass and wheat straw and concluded that torrefaction modifies the combustion of volatiles released from the biomass and it occurs over a shorter temperature range. The torrefied biomass also produced 10-65% higher heat of combustion (depending on the torrefaction conditions) due to its higher char content. They also investigated the combustion properties of torrefied willow under high heating rate and high temperature by suspending the particles in a methane air flame and its

further combustion. Torrefaction reduced the required time for burning of the volatiles released from willow decomposition in the combustion stage, however, the time of char burnout increased for the torrefied willow. By combining both stages of volatile and char combustion, they concluded that the required time for complete combustion of torrefied willow increased due to the higher char content of torrefied sample. However, they found that the ignition time for volatile and char combustion of the torrefied willow was reduced.

#### **B.1.3.4. Kinetic modeling of biomass torrefaction**

A few kinetic models have thus far been developed to explain the weight loss of biomass during torrefaction. The kinetic models applied for biomass torrefaction mostly originate from models developed for biomass pyrolysis as the torrefaction reactions are the same as those taking place at the early stages of pyrolysis. Due to the complexity of the reactions involved in the torrefaction process, the simplified models were applied in the literature for biomass torrefaction which are mostly based on the decomposition of the main constituents of biomass such as hemicellulose, lignin and cellulose. The decomposition of these components is considered to produce some lump products referred to as solid char, condensable and non-condensable gases.

Repellin et al. [27] applied a simple one-step model to describe the kinetics of beech and spruce mass loss during torrefaction at temperatures ranging from 160°C to 300°C. The model considers that the decomposition of wood leads to the production of char and volatiles and the wood, char and volatiles are pseudo-components whose compositions are not well defined. This model has only two parameters,  $K_{OM1}$  and  $E_{AM1}$ .



Using this model the obtained pre-exponential factor ( $K_{OM1}$ ) for spruce and beech torrefaction was  $1.02 \cdot 10^5 \text{ s}^{-1}$  and  $2.88 \cdot 10^5 \text{ s}^{-1}$ , respectively. The lower pre-exponential factor obtained for spruce than for beech was expected since hardwoods exhibit higher activity than softwoods. The activation energies obtained for spruce and beech were also comparable (92.0 kJ/mol). In general, this model featured a good estimation of the rate of spruce and beech mass loss during torrefaction.

Prins et al. [28] used a two-step kinetic model developed by Di Blasi and Lanzetta [29] to explain the mass loss of willow torrefied at the temperature ranges from 270°C to 300°C (Figure 1-5). The model considers that biomass is torrefied in two consecutive steps and each step consists of two parallel reactions leading to the formation of solids and volatiles.

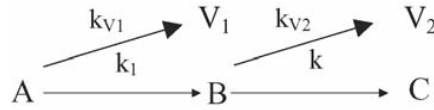


**Figure 1-5:** schematic of The two step kinetic model used by Prins et al. [28]

The solid yield for each step in this model is given by:

$$y_1 = \frac{k_1}{k_1 + k_{v1}}$$

$$y_2 = \frac{k_2}{k_2 + k_{v2}}$$

Where  $y_1$  is the solid yield of the first intermediate and  $y_2$  is the yield of char product. The results obtained by Prins et al. [28] showed that the rate of the two reactions in the first stage is considerably higher than those of the second stage. The first reaction step is considered to be representative of the reactions of xylan decomposition. The second reaction step was in accordance with the decomposition of the rest of willow constituents such as cellulose and lignin. The two-step reaction model had a good agreement with the experimental results of willow yield at 280-300°C, however, the model could not fit the experimental torrefaction weight loss at 270°C.

Repellin et al. [27] also fitted mass loss profiles of torrefied willow using a model developed by Rousset et al. [30] for xylan thermal decomposition. This model considers thermal decomposition of wood as a superposition of thermal decomposition of lignin, cellulose and hemicellulose in proportion to their content in wood [27]. According to this model, lignin is converted to char and volatile products in a single step reaction (Figure 1-6). The cellulose decomposition in the torrefaction conditions is assumed to take place in a one-step two-parallel reaction in which cellulose is decomposed into tar, volatiles and char, and finally hemicellulose decomposition proceeds according to the model developed by Di Blasi and Lanzetta in two steps as just explained above. This

model had some good predictive power of the weight loss profile of spruce and beech. However, the model predicted that spruce reacts more than beech which is in disagreement with experimental observations.

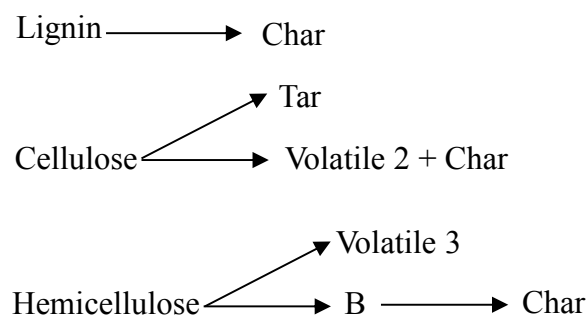


**Figure 1-6:** Schematic of the kinetic mechanism used by Repellin et al. [27]

#### **B.1.4. Biomass pre-treatment using solvents**

Biomass pre-treatment using solvents prior to thermochemical conversion is considered as one of the methods to promote thermochemical reactions and upgrade oil contents derived from biomass pyrolysis. Biomass pre-treatment using solvents could modify biomass chemical structure or selectively remove lignocellulosic components leading to its improved thermochemical properties. In this regard, different types of solvents such as acids (HCl, HF, H<sub>3</sub>PO<sub>4</sub>) alkaline pre-treatment and liquid hot water have been already used for biomass pre-treatment. Das et al. [12] studied the vacuum pyrolysis of ash free sugar bagasse pre-treated by HCl, HF and water. Pre-treatment of bagasse with water, dilute HCl and HF solutions showed a remarkable change in the distribution of pyrolysis products. Pre-treatment of bagasse with mild HF solution removed its ash content completely. Furthermore, 69% increase in the yield of bio-oil produced through pyrolysis of pre-treated bagasse with HF was observed. Dobele et al. [15] studied the effect of pre-treatment of microcrystalline cellulose, recycle kraft pulp and birch wood sawdust using phosphoric acid on the release of levoglucosan and levoglucosenone during fast pyrolysis. The results of the study showed a threefold increase in the yield of levoglucosan and levoglucosenone after cellulose treatment with phosphoric acid. The acid causes depolymerisation and dehydration of all types of cellulosic materials leading to an increased yield of bio-oil produced during fast pyrolysis. Acid pre-treatment of birch wood sawdust also increased the yield of levoglucosan and levoglucosenone production due to reduction of the protecting effect of lignin which limits the

susceptibility of cellulose to pyrolysis degradation. Misson et al. [16] also studied the effect of chemical pre-treatment using different alkali solvents (NaOH, H<sub>2</sub>O<sub>2</sub> and Ca(OH)<sub>2</sub>) on the degradation of lignin content of palm fruit bunches. Spectrophotometric analyses showed that consecutive addition of NaOH and H<sub>2</sub>O<sub>2</sub> decomposed almost all the lignin content of palm fruit bunches. The degradation of lignin using this pre-treatment led to an enhanced pyrolysis of their sample. Up to 90 wt% phenolic yield was obtained during catalytic pyrolysis of pretreated sample.

Although acid pre-treatment of biomass favors dehydration, inter- and intramolecular bond breakage in cellulose chains and could destroy the lignin structure which results in higher yields of bio-oil, corrosiveness of most acids as well as their volatility which leads to poisonous releases [16] limits their application for biomass pre-treatment. Unlike acids, which are objected for their environmental concerns, green solvents such as ionic liquids are environmentally friendly as they have shown their potential to provide interactions with cellulose and lignin. Yet, studies on the potential of ionic liquids for biomass pre-treatment prior to thermo-chemical conversion have not been subjected to investigation.

Ionic liquids (ILs) are considered as a group of organic salts with melting point usually lower than 100°C. Most of the ILs are composed of an organic cation and inorganic anion. The sizes of cation and anion are normally large leading to a low melting point of ILs. Ionic liquids have some interesting properties which make them interesting solvents for chemical processes. Among these properties one can cite their high thermal stability, low toxicity and negligible vapor pressure. Due to these properties, ionic liquids have received considerable importance as solvents to replace highly volatile organic solvents in a wide variety of chemical processes [31]. Different properties of ionic liquids such as their melting point, viscosity, hydrophobicity and thermal stability depend on the type of anion and cation involved in the ILs structure. Different types of ILs with different properties suitable for a desired chemical process could be synthesized by making some changes in the structure of the anions or cations. Some of the commonly used cations and anions which have been frequently employed as solvents are shown in Figure 1-7.

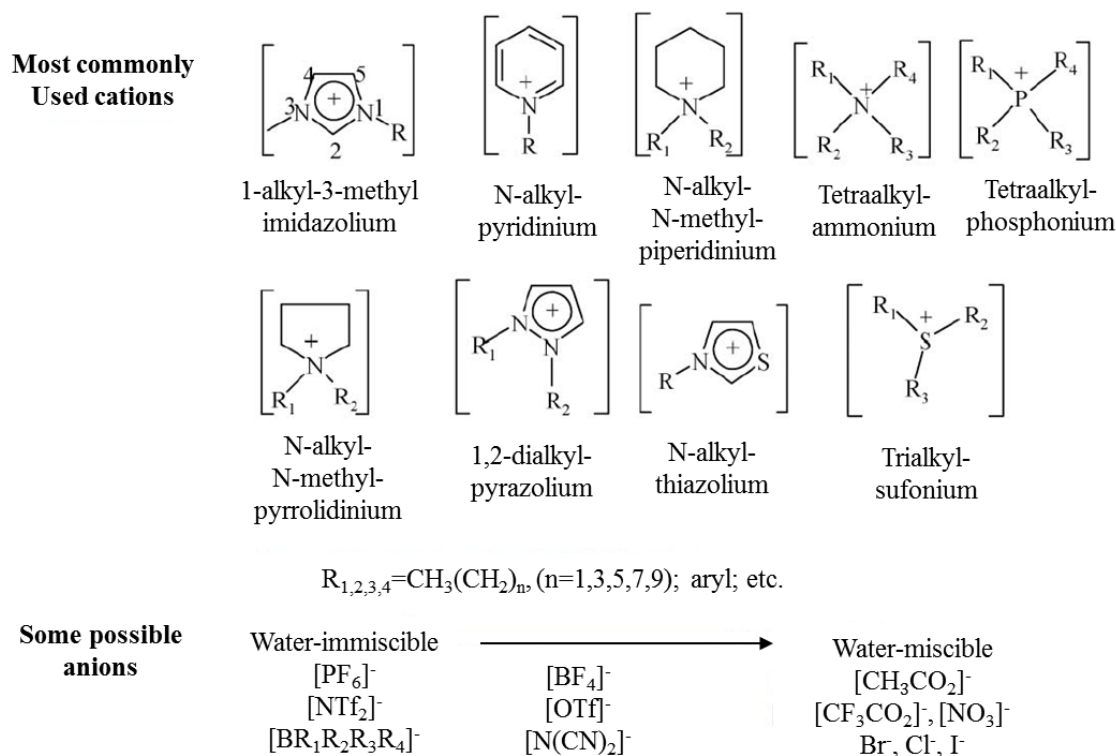


**Figure 1-7:** some commonly used ionic liquid systems [32]

Ionic liquids have been widely used as solvents for the fractionation of biomass [33, 34]. Different types of ILs having ability to dissolve specified biomass components such as cellulose and lignin or the whole biomass have been already identified [35]. Ionic liquids containing a variety of cations such as imidazolium, pyridinium and pyrrolidinium based cations, choline, tetrabutylammonium, tetrabutylphosphonium ions, and different anions, e.g., halogens, formates, acetates, amides, imides, thiocyanates, phosphates, sulfates, sulfonates, have been identified as powerful ions for biomass dissolution [35]. The main parameters affecting the dissolution of lignocellulosic materials in ionic liquids are the size and shape of ILs, their polar characteristics and their ability to form hydrogen bonds with the hydroxyl groups of lignocellulosic materials [35]. In general, the ability of ILs for biomass dissolution reduces as the cation size alongside its alkyl branching is increased which will in turn hamper the hydrogen bonding formation [35]. Zhang et al. [34] reported that 1-allyl-3-methylimidazolium cation, [AMIM], is more powerful in cellulose dissolution than 1-butyl-3-methylimidazolium [BMIM] due to its smaller size. Figure 1-8 shows a schematic of the mechanism of cellulose dissolution in ILs. Anions and cations of ILs could set hydrogen bonding with the hydroxyl groups in the lignocellulosic material

leading to the disruption of hydrogen bonding in the biomass polymeric structure and dissolution of biomass [36]. Zhang et al. [36] concluded that ionic liquids dissolving cellulose meet the following aspects 1) the anion is a good hydrogen bond acceptor 2) the cation should be a moderate hydrogen bond donator 3) the size of cation should not be too large.

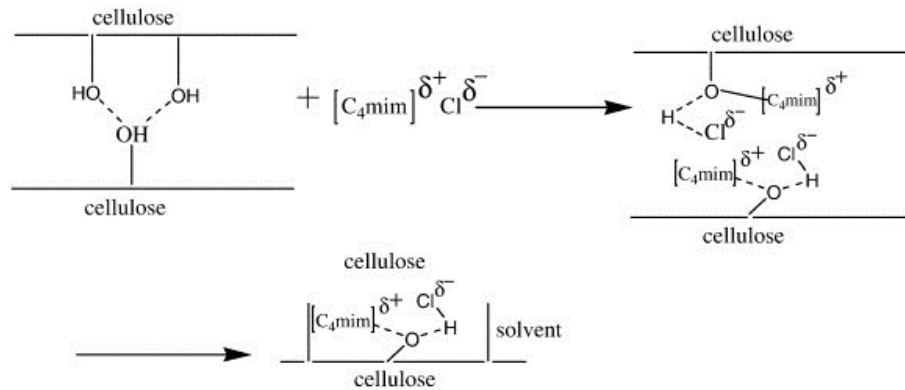


**Figure 1-8:** Dissolution mechanism of cellulose in [C<sub>4</sub>MIM][Cl] [37]

### B.1.5. Biomass pre-treatment using fungi

Fungal pre-treatment has been widely used in bioethanol production and in the pulping industries [38]. However, very limited publications investigating the effect of fungal treatment on the pyrolysis and gasification of biomass could be found. Zeng et al. [38] studied the effects of white-rot and brown-rot fungal pre-treatment on the chemical composition and thermochemical conversion of corn stover. The degradation of lignin and amorphous regions of cellulose was observed due to the pre-treatment by the mentioned fungi. This bio-treatment enhanced the thermal decomposition of corn stover leading to 55% increase in bio-oil production.

### B.2. Application of minerals in thermochemical biomass conversion

In this section, we review three main applications of minerals and mining residues in thermochemical processes. Different types of cheap and abundant minerals and mining residues have been used as a medium for CO<sub>2</sub> sequestration, as a solid oxygen carrier aiming for the combustion of a fuel in chemical looping combustion reactor and as a cheap catalyst for cracking tar in gasification reactors.

## **B.2.1. Application of minerals in CO<sub>2</sub> sequestration**

### **B.2.1.1. Principles of CO<sub>2</sub> sequestration by minerals**

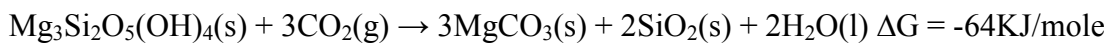
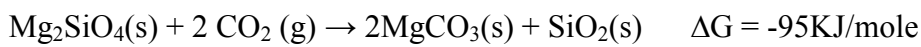
CO<sub>2</sub> is known as a major greenhouse gas due to its large emission from the fossil fuel based plants. Due to the increased consumption of fossil fuels, it is essential to reduce emissions of CO<sub>2</sub> in order to stabilize its level in the atmosphere. For this purpose, several methods have been suggested and studied to capture and sequester carbon dioxide. 1) CO<sub>2</sub> could be injected to the high depth of oceans to form carbonic acid (H<sub>2</sub>CO<sub>3</sub>). The carbonic acid is then dissociated to solvated protons and bicarbonate ions. Although this method has been widely studied [39, 40], there are some uncertainties about the environmental consequences of this practice due to its effect on reduction of pH of the ocean waters. 2) Carbon dioxide could be stored in geological formations in which the temperature and pressure are high enough to keep carbon dioxide in a supercritical state [41]. Carbon dioxide could be stored between geological layers; however, the main concern about this type of storage is a risk of CO<sub>2</sub> leakages in the reservoir. 3) CO<sub>2</sub> sequestration through mineral carbonation which leads to the formation of some stable carbonate minerals such as calcite (CaCO<sub>3</sub>) and magnesite (MgCO<sub>3</sub>). This method could be practiced in-situ or ex-situ. The in-situ mineral carbonation consists of CO<sub>2</sub> injection into underground reservoirs to react with metal oxides and to form stable carbonates. Ex-situ mineral carbonation is an aboveground carbonation of natural minerals and industrial alkaline wastes performed in one-single pot or in a series of reactors. The ex situ carbonation takes advantage of already available mined ores, mining tailings and wastes especially those consisting of mafic/ultramafic rocks due to their high Mg contents.

Mg and Ca are considered as the most suitable elements for carbonation mostly due to their abundance in the nature. Mg and Ca could be found in different minerals and mining wastes mainly in the form of silicate minerals. Silicate minerals are widely found in mafic and ultramafic rocks which are considered as the most suitable sources of Mg due to their abundance and occurrence as large deposits at numerous locations in the world. CO<sub>2</sub> could be reacted with magnesium and calcium oxides according to the following reactions:



These reactions' products are magnesite and calcite where both above reactions are exothermic. However, in nature, magnesium and calcium are usually found in the form of natural silicates and the direct carbonation of magnesium and calcium oxide is not common. Meanwhile magnesium silicates are more attractive for carbonation than calcium silicates due to the higher concentration of Mg found in magnesium silicates (21-25 wt%) versus calcium in calcium silicates (9-12 wt%) [42].

Considerable amounts of Mg could be found in silicate minerals such as olivine ( $\text{Mg}_2\text{SiO}_4$ ) and serpentines ( $\text{Mg}_3\text{Si}_2\text{O}_5(\text{OH})_4$ ). The overall carbonation reactions of olivine and serpentine could be written as below:



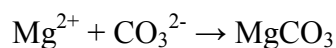
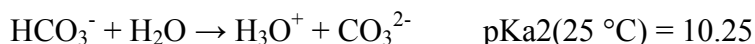
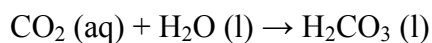
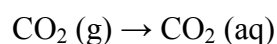
The type of solid carbonates produced during carbonation depends on several parameters such as temperature, pressure and liquid saturation. Different types of carbonates observed due to the carbonation of magnesium silicates are  $\text{MgCO}_3$  (magnesite),  $\text{MgCO}_3 \cdot 3\text{H}_2\text{O}$  (nesquehonite),  $4\text{MgCO}_3 \cdot \text{Mg}(\text{OH})_2 \cdot 4\text{H}_2\text{O}$  (hydromagnesite) and  $4\text{MgCO}_3 \cdot \text{Mg}(\text{OH})_2 \cdot 5\text{H}_2\text{O}$  (dypingite) [43].

Ex-situ mineral carbonation can be achieved through different processes. These could be divided into two main routes. The first route is called direct carbonation in which carbonation is performed in a single reactor under dry or wet conditions. The second route consists of carbonation in which more than one single reactor is required. In these processes, Mg is extracted in a separate reactor and then it is carbonated and precipitated in subsequent reactors.

### **B.2.1.2 Direct mineral carbonation**

Direct carbonation could be considered as the simplest approach for the carbonation of minerals. In this route, minerals rich in Mg/Ca are carbonated directly at specified temperature and pressure while Mg/Ca extraction and carbonation occur simultaneously in one single reactor. Direct mineral carbonation experiments have been performed in dry or aqueous conditions and a wide range of temperature and pressure has been also tested [44-46].

As for the atmospheric pressure and ambient temperature carbonation of magnesium silicates found in ultramafic mining residues, rather comprehensive investigations of Assima et al. [44, 45] addressed a wide range of parameters such as pore liquid saturation and watering schemes, residue size and mineralogy and gas composition on the rate of residue carbonation [45]. The mining residues studied in their work mainly consisted of chrysotile, lizardite, brucite and magnetite. According to their results, the rate of CO<sub>2</sub> uptake by dry residue subjected to dry CO<sub>2</sub> flow was very low. However, addition of water to the bed boosted the rate of carbonation. The residues having 30-50% of water pore saturation showed an improved activity for carbonation. The observed CO<sub>2</sub> sequestration was related to the carbonation of native brucite content of the samples along with the carbonation of coarser magnesium silicate particles (chrysotile and lizardite). Dissolution of brucite in water releases Mg which promptly reacts with dissolved CO<sub>2</sub>. In addition, water is also destabilizing the structure of chrysotile, leading to Mg dissolution from the outwardly-oriented chrysotile octahedral layers which then react with CO<sub>2</sub> to produce magnesium carbonates. The following steps are proposed to take place during serpentine carbonation:



According to Assima et al. [44], the extent of residue carbonation is limited due to the formation of some silica and iron oxides passivating layers which reduce accessibility of reactants to the reactive surface of residue and consequently reduce Mg leaching and carbonation [44]. However, regular watering of residues could slow down the densification of silica gel passivation layer leading to higher carbonation extent. The best magnesium carbonate conversion efficiency was obtained by adding an amount of water equal to 12.5% of the pore volume once every 24h for 4 days resulting in nearly 22 mg of CO<sub>2</sub> captured per gram of residue [44].

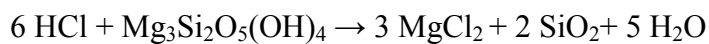
Direct carbonation of chrysotile at high temperatures (300-1200°C) and in dry and humid environments was comprehensively studied by Larachi et al. [47]. The results of

their study showed that the rate of chrysotile direct carbonation at different temperatures was slow which could be attributed to the incompatibility between CO<sub>2</sub> van der Waals molecular diameter and the narrow octahedral lattice parameters of chrysotile structure. However, humid carbonation was found to enhance conversion of chrysotile and formation of hydromagnesite. The highest chrysotile carbonation in their study was obtained for carbonation reactions performed at 375°C in a moist atmosphere. It was estimated that in this condition, almost 2.5% of the total brucitic Mg in chrysotile was carbonated. Although the partial carbonation of chrysotile was thermodynamically favorable, formation of some passivation hydromagnesite layer over the chrysotile surface could be the reason for its low carbonation activity. In another work, Larachi et al. [48] showed that the activity of chrysotile for direct carbonation could be enhanced by applying some residue pre-treatments. Exposing partially dehydroxylated chrysotile samples (*meta*-chrysotile) to a CO<sub>2</sub>/steam mixture led to significant carbonation of Mg in *meta*-chrysotile. Carbonation of steam mediated *meta*-chrysotile at 130°C led to the conversion of almost 70% of magnesium of *meta*-chrysotile to magnesium carbonates which are the highest CO<sub>2</sub> uptake ever reported for magnesium silicates direct carbonation. However, the main disadvantage of this thermal pre-treatment is the high temperature required for the dehydroxylation of chrysotile which occasions some heat penalties to the process.

In order to increase the rate of carbonation, O'Connor et al. [49] developed a process in which the carbonation of olivine was performed in a slurry reactor and supercritical CO<sub>2</sub> to produce magnesite. In this process, CO<sub>2</sub> is first dissolved in water leading to the release of H<sup>+</sup> and HCO<sub>3</sub><sup>-</sup>. The H<sup>+</sup> could hydrolyze the olivine leading to the release of Mg<sup>2+</sup> which could subsequently react with HCO<sub>3</sub><sup>-</sup> to form solid carbonates. However, according to the results published by this group, the rate of olivine carbonation at ambient temperature and supercritical CO<sub>2</sub> pressure is low. Nevertheless, at elevated temperatures and pressures and in a mixed slurry reactor significant conversion of olivine to carbonates was observed. The extent of olivine carbonation at 185°C and CO<sub>2</sub> partial pressure of 11.6 MPa was around 90% showing the important effect of temperature on the rate of carbonation in the studied process.

### B.2.1.3. Indirect carbonation

If mineral carbonation is performed in several steps the process is termed indirect carbonation. Such a process mainly consists of two steps. The first step is about Mg extraction from the minerals under sufficiently acidic pH. The second step is a carbonation of extracted Mg and its further precipitation in the form of magnesium carbonates. The rate of carbonation of minerals is normally enhanced using additives. Different types of acids such as hydrochloric, nitric and acetic acids have been already tested in mineral carbonation to enhance the rate of Mg leaching and consequently improve the rate of carbonation. Lackner et al. [50] developed a method for the carbonation of Mg silicates through extraction of Mg using hydrochloric acid. Serpentine could be dissolved rapidly in hydrochloric acid leading to the formation of magnesium chloride and silica gel [50]:



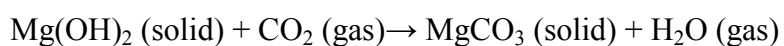
One advantage of using HCl to extract Mg is the ease of regeneration of this acid. Excess HCl and water could be boiled and further heating of the mixture to 150°C could lead to the decomposition of magnesium chloride and regeneration of hydrochloric acid [50]:



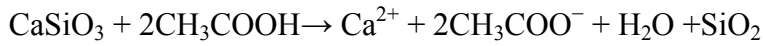
Solution of Mg(OH)Cl<sub>2</sub> in water leads to the formation of solid brucite as follow [50]:



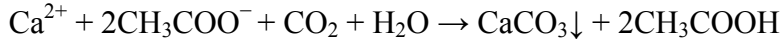
The produced brucite could be later separated and carbonated according to the following reaction [50]:



However, this process could be costly due to the consumption of some hydrochloric acid which requires some make up as well as energy for water evaporation, not to mention HCl highly corrosive character and costly burden it puts on the selection of the reactor materials. Consequently, Kakizawa et al. [51] proposed to use acetic acid to overcome HCl problems. The proposed process consisted of two steps. The first step was the extraction of calcium ions by acetic acid from calcium silicate as:



Further injection of CO<sub>2</sub> could lead to the precipitation of calcium carbonate from the solution of calcium ions;



In this process, acetic acid used in the extraction step could be recovered during carbonate precipitation. Consequently, no acid is consumed in the combined process. A feasibility study was also performed by Kakizawa et al. [51] who showed that the total energy consumption of carbonation in a 100 MW thermal power plant would represent some 20.4 % of energy consumed in CO<sub>2</sub> disposal the consequence of which is a reduction of total efficiency of thermal plant from 40 to 32%. The calculated cost for CO<sub>2</sub> disposal was also about US\$200/tonne carbon under the assumption that all the energy consumption would be supplied by electricity priced at US\$0.18/kWh [51].

#### **B.2.1.4. Mechanism of magnesium silicate carbonation in close to ambient conditions**

Three important steps are taking place during the silicate minerals carbonation 1) dissolution of metals 2) dissolution of CO<sub>2</sub> and 3) precipitation of carbonates.

**Dissolution of metals** Several parameters such as pH, temperature and surface evolution with time could have important effects on the dissolution rate of magnesium silicates. Acids proved to enhance Mg leaching from the magnesium silicates. In acidic conditions, the magnesium silicates are dissociated faster leading to the release of Mg and other minor elements such as Fe and Ca. In fact, the presence of protons could make the structure of magnesium silicate fragile favoring leaching of Mg and other metals according to the following reactions:

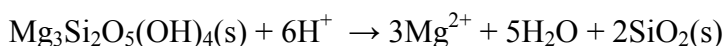
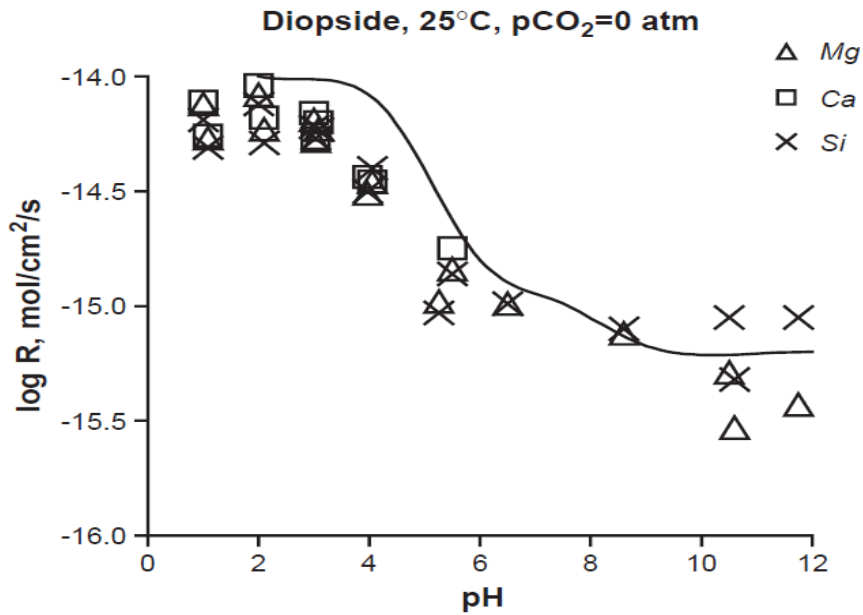
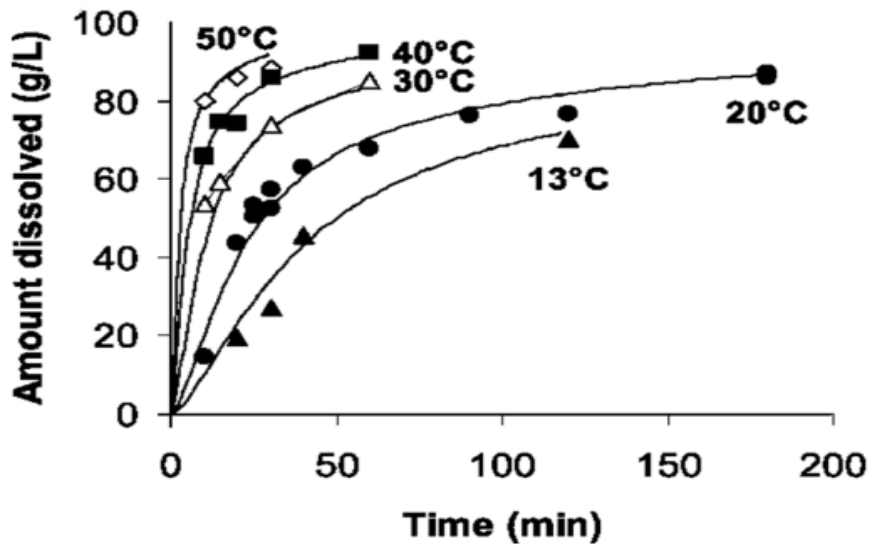


Figure 1-9 also shows the effect of pH on the extent of Ca, Mg and Fe leaching from diopside at 25°C. As can be observed in this Figure, the lower the pH the higher the amount leached metals.



**Figure 1-9:** Effect of pH on the dissolution of diopside at 25 °C [52]

Medium temperature also has an important effect on the rate of metal leaching from the magnesium silicates. Increasing temperature has been shown to improve the rate of dissolution of metals as seen in Figure 1-10.



**Figure 1-10:** Effect of temperature on the dissolution of mineral fiber in a 4 M formic acid [53]

Another important parameter affecting the rate of metal dissolution from magnesium silicates is surface passivation. As dissolution progresses, the surface of particles may become increasingly covered by new solid products limiting diffusion of the leaching agents and acting as a barrier to prevent criss-crossing of the soluble species such as the release of Mg into the carbonation environment. Among these products, the formation

of a dense silica passivation layer is worth mentioning which reduces the rate of carbonation of magnesium silicates. This layer is mainly formed due to the polymerization of the silicate layer in the serpentines. Figure 1-11 shows how the polymerization and densification of silanol could prevent the dissolution of the rest of particle.

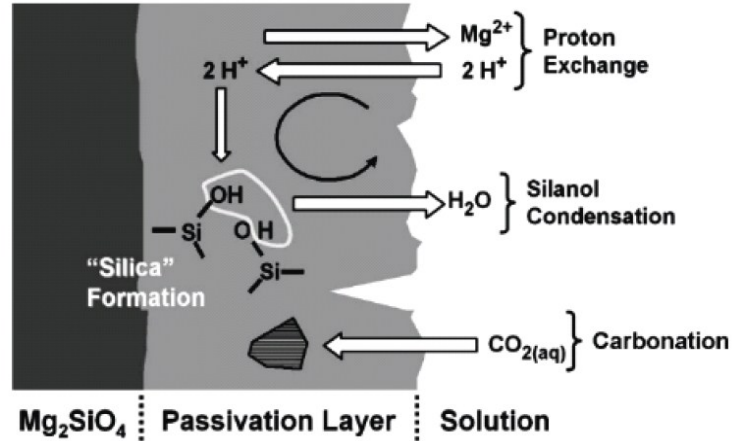


Figure 1-11: schematic of silica gel layer formation [54]

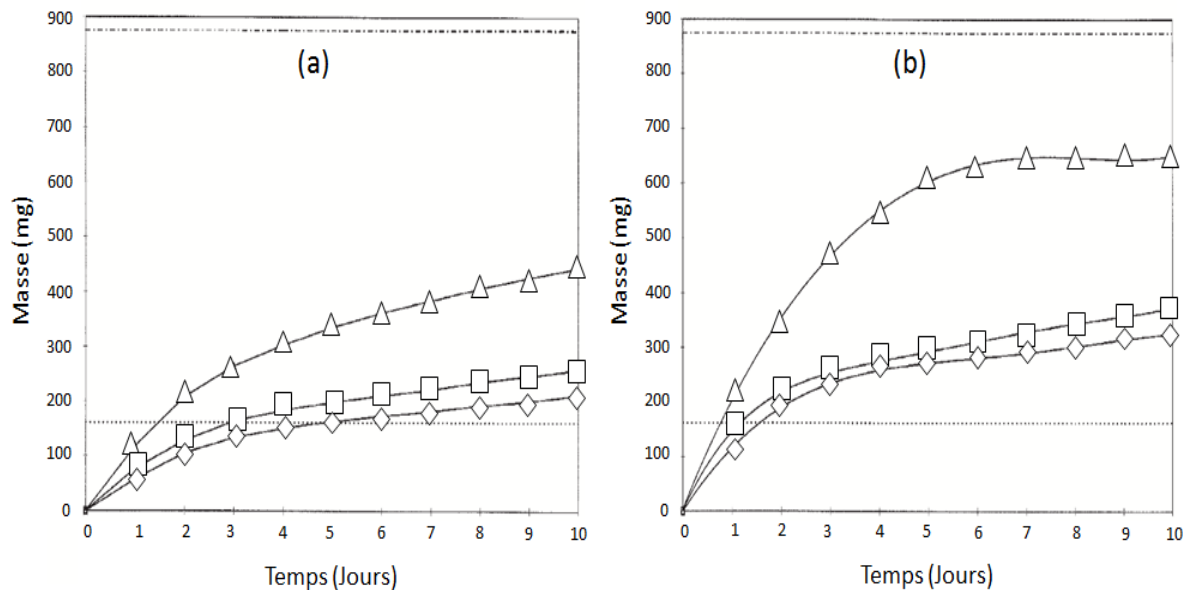
**Carbonate precipitation** The simultaneous presence of  $Mg^{2+}$  and  $CO_3^{2-}$  is necessary for the precipitation of magnesium carbonates. Precipitation is favored when the dominant  $CO_2$  species in the aqueous phase is in the form of  $CO_3^{2-}$ . Figure 1-12 shows the  $CO_2$  equilibrium in water at ambient conditions. As can be observed, carbonate ions are predominant for pH higher than 10.3 at 25°C whereby the formation of magnesium carbonates is highly favored. However, precipitation of magnesium carbonates starts at pH around 8-8.5. At this pH, the  $CO_3^{2-}$  ions coexist with  $HCO_3^-$  ions. Contrary to magnesium leaching in acidic media, precipitation of magnesium carbonates necessitates a basic medium.



Figure 1-12: Dominant species of dissolved  $CO_2$  in function of pH

Temperature is also another important parameter which could affect the rate of carbonate precipitation. Although increasing temperature reduces the solubility of  $CO_2$  in water, its effect on the rate of precipitation is positive. Figure 1-13 shows the results of experiments performed by Dheilily et al. [55] on the carbonation of  $Mg(OH)_2$  at

temperatures ranging from 10-40°C. As can be observed, temperature increases the rate of magnesium carbonate formation. In addition, the type of magnesium carbonates formed at different temperatures was also changing showing the effect of temperature on the carbonate species produced during carbonation. Nesquehonite is mostly formed at temperatures less than to 20°C while at 40°C carbonation leads to formation of hydromagnesite, giorgiosite and nesquehonite.



**Figure 1-13:** TG analysis of MgO samples during 10 days in humid environment: (a) low concentrations of CO<sub>2</sub>; (b) High CO<sub>2</sub> concentration (◇)T= 0°C; (□)T= 20°C; (Δ)T= 40°C; (----) theoretical Mg(OH)<sub>2</sub>; (.....) theoretical MgCO<sub>3</sub>·3H<sub>2</sub>O [55]

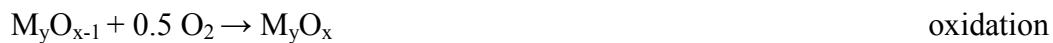
## B.2.2. Application of minerals in chemical looping combustion

### B.2.2.1. Chemical looping combustion principles

The concept of chemical looping combustion (CLC) was first introduced in 1954 to produce pure carbon dioxide [56]. However, renewed interest for studying and applying this concept was initiated again in the 1990's due to the increased concerns about greenhouse gas emissions which favored drives for separation and sequestration of CO<sub>2</sub> in the combustion plants. Presently a number of processes are available to separate CO<sub>2</sub> from flue gas for its subsequent sequestration. Among these, the oxy-fuel combustion is worthy of mention which burns fuel in a combustor with pure oxygen obtained from a cryogenic N<sub>2</sub> process or the post combustion separation in which CO<sub>2</sub> is separated from flue gas using different approaches such as amine physical absorption, membrane and molecular sieves separation [57, 58]. However, these approaches may be expensive and

hamper overall efficiency of combustion with as a consequence an impact on the pricing of electricity generation. Considering this factor, chemical looping combustion could represent a less expensive solution for production of pure CO<sub>2</sub> in the combustion units.

In general, a continuous CLC process could be achieved by using two interconnected fluidized bed reactors [59]. The solid oxygen carrier is oxidized in an air reactor in which a stream of air is flowing. The exit gas from the air reactor is N<sub>2</sub> with a very low amount of unreacted oxygen and some carbon dioxide released from burning of deposited carbon on metal oxide which could be sent to the atmosphere. The hot solid oxygen carrier is then transferred to the fuel fluidized bed reactor in which the fuel is burned due to the contact with the metal oxide leading to a nitrogen free stream. In the presence of an efficient solid oxide oxygen carrier the products from the fuel reactor are CO<sub>2</sub> and water. Water could be separated from the stream through condensation and high-concentration CO<sub>2</sub> streams could be obtained. The reduced metal could be then transferred to the air reactor for re-oxidation. The main oxidation/reduction reactions taking place in CLC reactors are [59]:



The total amount of heat released from the two oxidation and reduction processes is the same as for a normal combustion where the fuel is burned in a direct contact with oxygen. However, the heat released from each of the reactors is dependent on the type of solid oxygen carrier [60].

Although most of the researches on chemical looping combustion is concentrated on the combustion of gaseous fuels, the chemical looping concept has been also used for the gasification of solid fuels such as coal, coke and biomass [61]. Direct contact of volatiles released from solid fuels with oxygen carrier could lead to a partial combustion of tar compounds stimulating the synthesis gas yield of the gasification process. However, partial gasification of solid char using solid oxygen carriers is not efficient and char should be gasified either by steam or oxygen [61].

### **B.2.2.2. Oxygen carriers in chemical looping combustion**

Selection of a suitable solid oxygen carrier for a chemical looping combustion process is an important criterion. The most important characteristics of an oxygen carrier is its reactivity in reduction and oxidation cycles [57]. A highly active solid oxygen carrier could completely burn a fuel in the reduction cycle. A solid oxygen carrier should have some other characteristics such as [57] : 1) being stable under successive reduction and oxidation cycles at high temperature 2) having suitable fluidization characteristics 3) being resistant to carbon deposition 4) being resistant to agglomeration at CLC high temperatures 5) having high mechanical strength.

Different metal oxides have been already tested as potential solid oxygen carrier candidates for chemical looping combustion. Some studies have revealed that  $\text{Mn}_2\text{O}_3/\text{Mn}_3\text{O}_4$ ,  $\text{CuO}/\text{Cu}_2\text{O}$ ,  $\text{Fe}_2\text{O}_3/\text{Fe}_3\text{O}_4$  and  $\text{NiO}/\text{Ni}$  oxygen carriers are active enough to burn methane and some other fuels to  $\text{CO}_2$  almost completely [57]. Metal oxides are generally combined with porous supports which provide high surface area for reaction, mechanical strength and attrition resistance [60]. Different types of materials such as porous  $\text{Al}_2\text{O}_3$ ,  $\text{ZrO}_2$ ,  $\text{SiO}_2$  and  $\text{TiO}_2$  have been already tested as inert supports for the metal oxide oxygen carriers. Selection of a suitable support for a special reaction is dependent on the metal oxide selected for the process. Adanez et al. [60] investigated the activity and mechanical resistance of 240 potential oxygen carrier samples for chemical looping methane combustion. The samples were prepared using four inorganic oxides such as  $\text{CuO}$ ,  $\text{Fe}_2\text{O}_3$ ,  $\text{MnO}_2$  and  $\text{NiO}$  and five different inert materials such as  $\text{Al}_2\text{O}_3$ ,  $\text{ZrO}_2$ ,  $\text{SiO}_2$ ,  $\text{TiO}_2$  and sepiolite ( $\text{Mg}_4\text{Si}_6\text{O}_{15}(\text{OH})_2 \cdot 6\text{H}_2\text{O}$ ) by mechanical mixing. The results of their study showed that the mechanical strength of oxygen carriers depends on the type of metal oxide and its concentration, the inert used as a binder and the sintering temperature [60].  $\text{SiO}_2$  and  $\text{TiO}_2$  were the best supports for nickel, copper and manganese oxides in terms of mechanical strength while mechanical stability of iron oxide oxygen carrier supported on  $\text{Al}_2\text{O}_3$ ,  $\text{TiO}_2$  and  $\text{ZrO}_2$  was high enough provided the samples were sintered at temperatures higher than  $1100^\circ\text{C}$  [60]. In terms of reactivity, copper and iron oxide showed superior activity to manganese oxides for methane combustion. The activity of nickel oxides for methane burning was also very high. However, the formation of considerable carbon deposits at the end of reduction process on the surface of the nickel oxide oxygen carriers was remarkable [60].

### **B.2.2.3. Natural minerals as solid oxygen carrier**

In recent years, research on application of natural minerals as low cost oxygen carriers for chemical looping combustion has found considerable interest. Application of low price natural minerals could be interesting where combustion of solid fuels with oxygen carrier is performed. The presence of high amount of minerals and ash content in solid fuels and consequently the required discharge of ash from combustion reactors could reduce the lifetime of oxygen carriers [62]. Ash could be mixed with solid oxygen carrier and separation of the two could be difficult. Furthermore some ash fouling reactions could decrease the lifetime of oxygen carrier [62]. Consequently, low-cost natural minerals could be an option to replace expensive synthesized solid oxygen carriers.

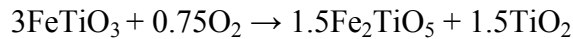
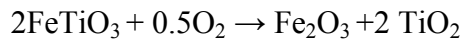
Linderholm et al. [62] studied chemical looping combustion of pet coke in a 10 kW reactor system using two different minerals such as Mn ores and ilmenite as oxygen carriers. The batch of Mn ores used in their study had complex mineralogy including oxides, hydroxides, carbonates, silicates and amorphous manganese oxides ( $\text{MnO}_2$ ). The use of Mn ore as oxygen carrier significantly enhanced the rate of coke gasification which was almost four times faster than that in the presence of ilmenite [62]. The remaining char yield from the coke gasification in the presence of Mn ores was about 6% which was considerably lower than that in the presence of ilmenite (30%)[62]. However, the mechanical stability of Mn ores was lesser than ilmenite's [62].

Huang et al. [63] studied the possibility of synthesis gas production through biomass direct chemical looping with natural hematite as an oxygen carrier. The natural hematite contained around 89.5wt % of  $\text{Fe}_2\text{O}_3$ , 6.8 wt% of  $\text{SiO}_2$ , 1.3% of  $\text{Al}_2\text{O}_3$  and some other impurities. Gasification in their study was performed in a fluidized-bed reactor in which natural hematite was put in contact with solid biomass at 840°C. The efficiency of natural hematite for biomass gasification was also benchmarked with that of  $\text{SiO}_2$  which could be considered as an inert oxide. The result of the study showed that natural hematite has a potential to be used as solid oxygen carrier in biomass gasification [63]. The high activity and availability of oxygen on the surface of natural hematite led to the formation of considerable amounts of  $\text{CO}_2$  at the beginning of gasification cycle which is not a desirable product for gasification [63]. However, after a few minutes the concentration of  $\text{CO}_2$  declined at the expense of increased concentrations of CO and  $\text{H}_2$ .

Hematite could increase the yield of syngas production through secondary burning of tar compounds produced during gasification [63]. Furthermore, the solid contact between oxygen carrier and char led to increased gas yield, carbon conversion and gasification efficiency showing that natural hematite particles as oxygen carrier could provide lattice oxygen as gasifying agent for biomass gasification. However, the successive operation of hematite for twenty oxidation-reduction cycles revealed some attrition of the oxygen carrier leading to reduced activity of natural hematite for partial gasification of tar compounds formed during pine gasification. The observed attrition could be related to the possible shrinkage of hematite particle due to the internal phase changes during gasification leading to the loss of oxygen carrier through entrainment out of the reactor by the fluidizing gas [63].

Tian et al. [64] tested the feasibility of using eight copper oxide and iron oxide natural ores, three CuO ores (chrysocolla, limonite, malachite) and five Fe<sub>2</sub>O<sub>3</sub> ores (hematite, ilmenite, limonite, magnetite and taconite) for combustion of coal and methane using a thermogravimetric method (TGA) and bench scale fixed-bed flow reactor. They found that most of the ores could supply oxygen for direct coal combustion at 700-100°C. However, their combustion and re-oxidation performances were worse than pure CuO or Fe<sub>2</sub>O<sub>3</sub> due to the low active species concentrations in the ores [64]. They also found that in methane CLC process, CuO ores showed faster reaction rates than Fe<sub>2</sub>O<sub>3</sub>-based ores but Fe<sub>2</sub>O<sub>3</sub> ores had greater oxygen transfer capacity [64]. Chrysocolla, hematite and limonite showed excellent performance in long duration CLC experiments performed in TGA and fixed-bed reactor though high attrition was detected in the case of chrysocolla [64].

One of the minerals studied widely as a solid oxygen carrier in chemical looping combustion is ilmenite. This mineral has been widely investigated as solid oxygen carrier due to its low cost, good fluidizability, high melting point and low fine production in CLC reactors [62]. Ilmenite is a weakly magnetic titanium iron oxide mineral (FeTiO<sub>3</sub>). The natural ilmenite ores are mainly composed of FeTiO<sub>3</sub>; however, some rutile (TiO<sub>2</sub>) and hematite (Fe<sub>2</sub>O<sub>3</sub>) compounds could be also found in the ores. Ilmenite is activated through pre-oxidation at around 950°C which leads to the formation of hematite and pseudo-brookite (Fe<sub>2</sub>TiO<sub>5</sub>) as the active solid oxygen carriers.



Leion et al. [61] tested pre-oxidized ilmenite as solid oxygen carrier for the steam gasification of petroleum coke and different types of coal in a fluidized bed reactor. The activity of ilmenite for the gasification of the solid fuel was also compared with that of a synthesized  $\text{Fe}_2\text{O}_3/\text{MgAl}_2\text{O}_4$  solid oxygen carrier. The results of their study showed that the rate of solid fuel gasification was two times higher in the presence of ilmenite as solid oxygen carrier and natural ilmenite was as active as the synthesized  $\text{Fe}_2\text{O}_3/\text{MgAl}_2\text{O}_4$  for the gasification of different tested fuels. Although ilmenite particles were tested at temperatures as high as  $1000^\circ\text{C}$ , minor agglomeration was observed. Leion et al. [61] also studied the activity of ilmenite for the combustion of methane and synthesis gas in a fluidized bed reactor. They concluded that ilmenite helps attaining high conversions of carbon monoxide and hydrogen while activity for methane burning was moderate. The tested ilmenite during 37 redox cycles showed no decrease in activity while it also showed good mechanical stability and fluidization behavior. Limited defluidization of ilmenite particles was detected when the oxygen carrier was in a highly reduced state which is not an expected condition in CLC operation.

### **B.2.3. Application of minerals in tar cracking**

#### **B.2.3.1. Tar formation in the gasification reactors**

Biomass gasification consists of a thermochemical conversion of solid biomass to produce synthesis gas. Biomass is gasified when it heated at high temperature ( $600^\circ\text{C}$ - $1000^\circ\text{C}$ ) in the presence of a gasifying agent, such as air, oxygen, steam,  $\text{CO}_2$ , or mixtures of thereof. During gasification, carbon monoxide ( $\text{CO}$ ), hydrogen ( $\text{H}_2$ ), carbon dioxide ( $\text{CO}_2$ ), methane ( $\text{CH}_4$ ), tars (benzene-like and other aromatic hydrocarbons), hydrogen sulfide ( $\text{H}_2\text{S}$ ), residual solids, and traces of  $\text{HCN}$ ,  $\text{NH}_3$ , and  $\text{HCl}$  are produced. Inorganic materials such as Al, P, Ca, Mg, Si, Na which are present in biomass also may be detected in the gas stream depending on the biomass feedstock, operating conditions of gasifier and gasifying agent. The quality of synthesis gas depends on the choice of gasifying agent. Based on it and on the way heat is provided to gasification, gasifiers can be divided into two main groups: directly-heated gasifiers in which oxygen, air or

mixtures thereof with steam are used as gasifying agent and indirectly-heated gasifiers which use pure steam as gasifying agent.

One of the main hurdles in commercial gasification processes is the formation and presence of tars in syngas. Tars are as the condensable fraction of the organic gasification products that are heavier than benzene and mainly consist of aromatics. Tars can be condensed in filters, pipes and other equipment, they also are coke precursors leading to catalyst deactivation as well as they may damage turbines and engines. Removing tar from syngas can be carried out by several methods, such as physical separation, thermal and catalytic cracking. Catalytic cracking of tar into syngas is an efficient tar conversion method and can be performed either during gasification by placing catalysts directly in the gasification reactor or after gasification in a secondary reactor.

Tars are formed during gasification in a series of complex reactions. The formation of tar is strongly dependent on reaction conditions. By increasing reaction temperature, secondary reactions of tar occur in the gas phase thus converting oxygenated tar compounds into light hydrocarbons, aromatics, oxygenates and olefins which could subsequently form heavier hydrocarbons and larger polyaromatics [65,66]. Three major product classes have been identified as a result of thermal gas phase reactions of tar [67]. The primary products found at temperatures in the range 400-700°C consist of oxygenated compounds. Cellulose derived products such as levoglucosan, hydroxyacetaldehyde and furfurals, analogous hemicellulose derived products and lignin derived methoxyphenols are among the primary products. Secondary products could be distinguished from primary products in the temperature range of 700-850°C. In this range, the decomposition of oxygenated compounds in the primary gas such as levoglucosan is compensated by the formation of CO and CO<sub>2</sub> and light hydrocarbons, e.g., ethane, ethylene, propylene and also single-ring aromatics such as furan, benzene, toluene and phenol. Tertiary products consist of polynuclear aromatics which form at high temperatures 850-1000°C. Release of different classes of tar compounds at different temperatures is shown in Figure 1-14. A brief list of different compounds of three different tars classes proposed by Morf et al. [68] is also presented in Table 1-2. As seen in this Table, several compounds appear in the second and in one of the other

two classes as well. This suggests the evolutionary development and the loose boundaries between the three classes.

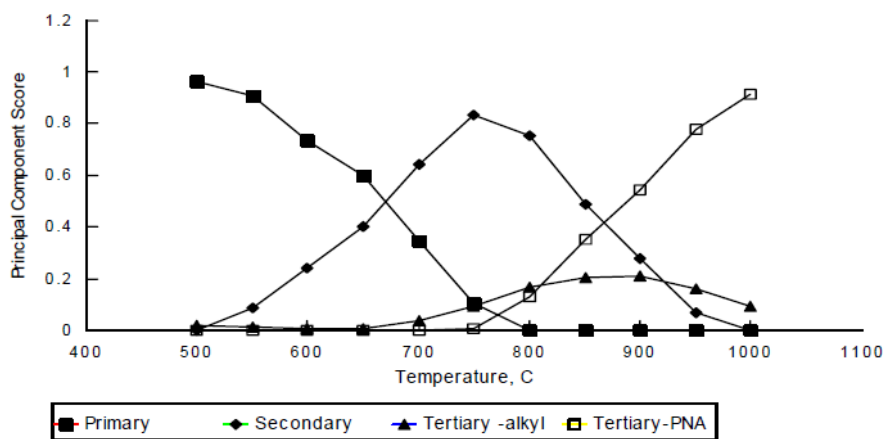


**Figure 1-14:** Distribution of the four tar component classes as a function of temperature [67]

**Table 1-2:** Some tar compounds in different classes of tar [68]

Tar compound class	Compound type	Compound name
Primary tar compounds	Acids	Acetic acid; Propionic acid; Butyric acid
	Ketones	Acetol
	Phenols	Phenol; 2,3-dimethylphenol; 2,4/2,5 dimethylphenol; 2,6 dimethylphenol; 3,4 dimethylphenol; 3,5 dimethylphenol
	Guaiacols	Guaiacol; 4-methylguaiacol
	Furans	Furfural; furfural alcohol; 5-methylfurfural
Secondary tar compounds	Phenols	Phenol; <i>o</i> -Cresol; <i>p</i> -Cresol; <i>m</i> -Cresol
	Mono-aromatic hydrocarbons	<i>p</i> -Xylene; <i>o</i> -Xylene, <i>m</i> -Xylene
Secondary/tertiary tar	Mono-aromatic hydrocarbons	Benzene; Ethylbenzene; $\alpha$ -Methylstyrene; 3&2-Methylstyrene; 4-Methylstyrene; 2-Ethyltoluene; 3-Ethyltoluene; 4-Ethyltoluene;
	Miscellaneous hydrocarbons	2,3-Benzofurans; Biphenyl; Indene; Dibenzofurann;
	Methyl derivatives of aromatics	2-Methylnaphtalene; 1-Methylnaphtalene; Toluene
Tertiary tar compounds	PAH: 2 rings	Acenaphthylene; Acenaphcene; Fluorene; Naphthalene
	3 rings	Phenanthrene; Anthracene; Fluoranthene; Pyrene
	4 rings	Benzanthracene; Chrysene; Benzacephenanthrylene; Benzofluoranthene;
	5 rings	Benzopyrene; Perylene; Dibenzoanthracene;
	6 rings	Indenopyrene; Benzoperylene

### **B.2.3.2. Gasification processes and tar production**

Introduction of biomass solid particles into gasifiers leads to their thermal decomposition and production of synthesis gas. Particles first undergo a pyrolysis step starting as low as 200°C. Primary volatiles released during this step depend on the prevailing heating rate. Primary volatiles can react with the gasifying agent (dioxygen or/and steam) or can be cracked to produce secondary and tertiary tar products. Operating conditions such as temperature and pressure, type of contact between biomass and gasifying agent, size of biomass, heating rate increase of particle temperature, etc. are well known to affect the syngas composition, amount and composition of tar and also gasification efficiency.

Industrial gasifiers for syngas production could be divided into three main groups: entrained flow gasifiers, moving bed or fixed bed gasifiers and fluidized bed gasifiers. In the following, the main aspects of these gasifiers are briefly summarized.

In entrained-flow gasifiers, the fine fuel particles (<100 µm) are fed concurrently with a mixture of oxygen and steam. Due to the high gasification temperature, ash in the fuel particle melts and is removed as liquid slag. Entrained flow gasifiers are of the slagging type with temperatures above ash melting point (1200-1600°C). Due to such high temperatures, primary tar is destructed in the gasifier. Entrained flow gasifiers are considered as the cleanest gasifiers due to the very low level of tar in the produced gas, a synthesis of the highest quality with low tar and methane contents.

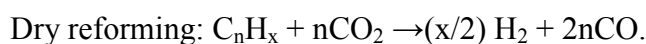
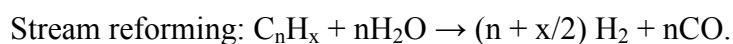
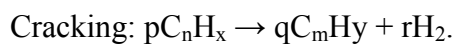
In a fixed or moving bed gasifier, the gasification medium flows through a fixed bed of solid fuel particles. Depending on flow direction of the gasifying agent through the bed, this group of gasifiers could be divided into two main sub-groups: updraft (gas medium flows upward and counter current with fuel) and downdraft (gas medium flows downward and concurrent with fuel). In updraft gasifiers, air/oxygen/steam contact fuel particles on a grate and generate gas temperatures of 1000-1400°C [67]. This hot gas rises through the down-coming biomass, pyrolyzing it at lower temperatures and drying it. These gasifiers can be used for different sizes of biomass and fuel. However, the level of tar in the outlet gas is very high (50 g/Nm<sup>3</sup>) [67]. In downdraft gasifiers, air/oxygen and fuel enter the reaction zone from above and burn most of the tars to pyrolyze fuel, in a process called "flaming pyrolysis". The flame temperatures are 1000-

1400°C, but the flame occurs in the interstices of the pyrolyzing particles whose temperatures are 500-700°C, so that about 0.1% of the primary tars are converted to secondary tars and the rest are burned to supply energy for pyrolysis and char gasification [67]. The low tar levels of downdraft gasifiers make them more suitable for applications which require clean gas. Typically, in downdraft gasifiers the tar loading is less than 1 g/ Nm<sup>3</sup> [67].

In a fluidized bed gasifier, air/ steam and fuel are mixed in a hot bed of granular solids such as sand. Due to the intense gas-solid mixing in a fluidized bed, the different gasification zones such as drying, pyrolysis, oxidation and reduction cannot be distinguished and the temperature is uniform all over the bed. In a typical fluidized bed gasifier, the solid fuel particles are brought into contact with a controlled supply of oxygen and steam. The tar level in a fluidized bed gasifier is intermediate between updraft and downdraft (10 g/ Nm<sup>3</sup>) gasifiers and the tar is mostly composed of secondary and tertiary tars [67].

### **B.2.3.3. Catalytic cracking of tar**

Catalytic cracking of tar is an efficient method for tar removal from the synthesis gas. Despite the physical and thermal methods for tar separation such as filtering, use of liquid scrubbers and thermal cracking which impose heat penalty to the process and produce water waste, catalytic gas conditioning does not produce waste, it can be performed at the same temperature as that of gasifier and it converts tar to syngas which increases the process efficiency. Catalysts for tar cracking can be placed inside gasifiers for example in fluidized bed gasifiers as a fluidization medium, or they can be used in secondary reactors after the main gasifier to convert tar. Several reactions can occur in a secondary catalytic reactor downstream of the gasifier. The most important reactions are as follows [69]:



Carbon formation:  $C_nH_x \rightarrow nC + (x/2) H_2$ .

In above reactions,  $C_nH_x$  represents tar and  $C_mH_y$  hydrocarbons with smaller C number than tar.

Catalysts for tar cracking could be divided into two main groups; synthesized catalysts and minerals. Synthesized catalysts are very active and able to crack stable aromatics such as benzene, toluene and naphthalene. Naturally occurring catalysts are virtually non-expensive as opposed to synthesized catalysts. However, they may not be as active as often temperatures required for tar cracking are higher.

**Synthesized catalysts** Synthesized catalysts for tar cracking are mainly composed of three phases: 1) an active catalytic phase for tar cracking which could be some metallic elements such as Ni, Pt and Rh. Although Rh and Pt have shown high reforming activity, their cost limits their use for large-scale applications. Because of costly noble metal catalysts, studies have more focused on Ni-based catalysts; 2) high surface area supports that facilitate dispersion of active phase. A variety of supports such as  $ZrO_2$ ,  $TiO_2$ ,  $CeO_2$ , MgO, combined MgO and alumina, zeolites and other supports have been already tested for synthesized catalysts and 3) a promoter, which increases activity and/or stability. Transition metals and alkali metals are among the potential elements as promoter for the tar cracking. Table 1-3 summarizes different synthesized catalysts developed and tested for biomass tar cracking.

**Table 1-3:** Summary of activity of some synthesized catalysts tested by different research groups

Catalyst tested	Operating conditions and feed characteristics	Results and findings	Reference
M-CeO <sub>2</sub> -SiO <sub>2</sub> (M: Rh, Pd, Pt, Ru, Ni)  Loading of M= $1.2 \times 10^{-4}$ mol/ g-catalyst	<b>Tar:</b> Produced in the reactor from cedar wood <b>Reactor:</b> tar produced in a primary fixed bed and passed through the fluidized bed of catalyst <b>Reagent environment:</b> Tar, synthesis gas and O <sub>2</sub> in N <sub>2</sub> <b>Temperature:</b> 823-923 K <b>Biomass feed rate:</b> 150 g/min <b>Weight of Catalyst bed:</b> 3 g <b>Equivalent ratio:</b> 0.25	Order of activity of catalyst for tar cracking at 823 K: Rh > Pt > Pd > Ni= Ru  Order of activity of catalyst for tar cracking at 923 K: Rh > Ni > Pd > Pt > Ru	[70]
Co/MgO and Ni/MgO  12 wt% of Co on Co/MgO 4-36 wt% of Ni on Ni/MgO	<b>Tar :</b> Naphthalene as a model tar compound <b>Reactor:</b> Fixed bed of catalyst <b>Reagent environment:</b> Naphthalene and steam in N <sub>2</sub> <b>Temperature:</b> 1173K <b>Naphthalene flow rate:</b> 1 g/h <b>Weight of catalyst bed:</b> 1 g <b>Steam flow rate:</b> 0.9 g/h <b>N2 flow rate:</b> 20 ml/min <b>GHSV:</b> 3000 h <sup>-1</sup>	Activity of Co/MgO catalyst is higher than Ni/MgO catalyst	[71]
Ni/Support Support: Al <sub>2</sub> O <sub>3</sub> , ZrO <sub>2</sub> , TiO <sub>2</sub> , CeO <sub>2</sub> , MgO  12 wt% of Ni on the catalyst	<b>Tar:</b> Produced in the reactor from cedar wood <b>Reactor:</b> Tar produced in a primary fixed bed and passed through the fluidized bed of catalyst <b>Reagent environment:</b> Tar, synthesis gas and O <sub>2</sub> /steam in N <sub>2</sub> <b>Temperature:</b> 823-923 K <b>Biomass feed rate:</b> 150 g/min <b>Weight of catalyst bed:</b> 1 g <b>N2 flow rate:</b> 150 ml/min <b>Equivalent ratio:</b> 0.25 <b>Steam/C mole ratio:</b> 0.5	Order of activity of catalyst for tar cracking : Ni/Al <sub>2</sub> O <sub>3</sub> > Ni/ZrO <sub>2</sub> > Ni/TiO <sub>2</sub> > Ni/CeO <sub>2</sub> > Ni/MgO  Ni/CeO <sub>2</sub> produced less coke than others.	[72]
Rh/support (0.5 wt% Rh) Rh/Ce/support (0.5 wt% Rh with 1 wt% Ce) Support: 65 ppi $\alpha$ Al <sub>2</sub> O <sub>3</sub> foam monoliths (17 mm diameter and 1 cm length)	<b>Tar:</b> Benzene as a model tar compound <b>Reactor:</b> Fixed bed of foam monoliths <b>Reagent environment:</b> Benzene and steam in N <sub>2</sub> <b>Temperature:</b> 650-850 °C <b>Benzene concentration:</b> 2 mol% <b>Steam/C mole ratio:</b> 0.42-1.67 mol%	Rh/ $\alpha$ Al <sub>2</sub> O <sub>3</sub> catalyst showed high activity for the cracking of benzene.  Addition of Ce to the catalyst increased Rh dispersion and stability.	[73]

**Table 2-3:** Summary of activity of some synthesized catalysts tested by different research groups

Catalyst tested	Operating conditions and feed characteristics	Results and findings	Reference
<p>Ni/Al<sub>2</sub>O<sub>3</sub>  Ni/MgO-Al<sub>2</sub>O<sub>3</sub>  Ni/MgO-La<sub>2</sub>O<sub>3</sub>-Al<sub>2</sub>O<sub>3</sub>  Ni-Co/MgO-La<sub>2</sub>O<sub>3</sub>-Al<sub>2</sub>O<sub>3</sub>  Ni-Cr/MgO-La<sub>2</sub>O<sub>3</sub>-Al<sub>2</sub>O<sub>3</sub>  MgO-Al<sub>2</sub>O<sub>3</sub>  MgO-La<sub>2</sub>O<sub>3</sub>-Al<sub>2</sub>O<sub>3</sub>  NiO: 15 wt%  Mg/Ni: 1 mol% ; Ni/La: 8mol% ; Ni/Cr: 3 mol% ; Ni/Co: 3 mol%</p>	<p><b>Tar:</b> Bio-oil generated from poplar wood  <b>Reactor:</b> Fixed bed micro reactor  <b>Reagent environment:</b> Bio-oil and steam in argon and helium mixture  <b>Temperature:</b> 825-875 °C  <b>Oil feed rate:</b> 150 mg/min  <b>Steam/C mole ratio:</b> 4.92 mol%  <b>Space velocity:</b> 126000 h<sup>-1</sup></p>	<p>Ni-Co/MgO-La<sub>2</sub>O<sub>3</sub>-Al<sub>2</sub>O<sub>3</sub> and Ni-Cr/MgO-La<sub>2</sub>O<sub>3</sub>-Al<sub>2</sub>O<sub>3</sub> showed the highest activity for the cracking of bio-oil.  Addition of magnesium and lanthanum facilitated the consumption of surface carbon.    Addition of cobalt and chromium increased the catalyst stability.</p>	[74]
<p>Ni-WO<sub>3</sub>/MgO-CaO    NiO: 25 wt%  WO<sub>3</sub>: 0, 6, 12, 18, 23 wt%</p>	<p><b>Tar:</b> Toluene and naphthalene as model tar compounds  <b>Reactor:</b> Fixed bed reactor  <b>Reagent environment:</b> Naphthalene/ toluene in steam, CO<sub>2</sub>, H<sub>2</sub>, CO, H<sub>2</sub>S (0-500 ppm) and N<sub>2</sub>  <b>Temperature:</b> 800-850 °C  <b>Tar feed rate:</b> 20 g/m<sup>3</sup> of naphthalene and 60 g/m<sup>3</sup> of toluene  <b>Space velocity:</b> 14000 h<sup>-1</sup>  <b>Gas flow rate:</b> 2 LN-dry /min</p>	<p>Catalyst has a superior resistance to coking and sulfur poisoning    Addition of WO<sub>3</sub> improves the resistivity of catalyst to sulfur poisoning.</p>	[75]
<p>NiO/CaO,K<sub>2</sub>O/SiO<sub>2</sub>,Al<sub>2</sub>O<sub>3</sub>  NiO/CaO,K<sub>2</sub>O,FeOx/SiO<sub>2</sub>,Al<sub>2</sub>O<sub>3</sub></p>	<p><b>Tar:</b> Produced in the reactor from seed corn  <b>Reactor:</b> Tar produced in a fluidized bed gasifier is passed through the fixed bed of catalyst.  <b>Reagent environment:</b> Tar, synthesis gas and steam in N<sub>2</sub>  <b>Temperature:</b> 740-820 °C  <b>Weight of catalyst bed:</b> 22-24 g  <b>Space velocity (dry gas basis):</b> 1500-6000 h<sup>-1</sup>  <b>Steam/C mole ratio:</b> 4.5-6.5</p>	<p>Addition of potassium and calcium to the catalyst enhances the coke consumption on the surface of catalyst.</p>	[76]

**Mineral catalysts** Catalysts belonging to the class of minerals are available mainly from mining operations and can be used directly or with some physical treatments (such as heating). In general, mineral catalysts are relatively cheap compared to the synthetic homologs. Abu El-Rub et al. [77] classified mineral catalysts into four main groups: 1) calcined rocks which contain alkaline earth metal oxides such as calcite, magnesite and calcined dolomite; 2) Olivine which is found widely in Nature whose stoichiometric formula is  $(\text{Fe}_x\text{Mg}_{1-x})_2\text{SiO}_4$ ; 3) Clay minerals which mostly belong to kaolinite, montmorillonite, and illite groups and 4) Iron-rich ores.

Among these groups of mineral catalysts, calcined rocks and olivine have been widely studied in catalytic gas conditioning. Calcined rocks include calcined calcite, magnesite and calcined dolomites which contain alkaline earth metal oxides (CaO and/or MgO). Non-calcined forms of these materials refer to limestone ( $\text{CaCO}_3$ ), magnesium carbonate ( $\text{MgCO}_3$ ), and dolomite ( $\text{CaCO}_3\cdot\text{MgCO}_3$ ). These materials show catalytic activity for tar elimination when calcined. Calcination of dolomite involves decomposition of the carbonate mineral which eliminates  $\text{CO}_2$  to form MgO-CaO. Deep dolomite calcination occurs at 800 to 900°C which restricts the efficient use of this catalyst to high temperatures. Calcined dolomite also loses its tar conversion activity under conditions where  $\text{CO}_2$  partial pressure is higher than the equilibrium decomposition pressure of dolomite [78]. This is an important issue when dolomite is used in pressurized gasification. As the process pressure increases, the operating temperature of calcined dolomite reactor must be increased to maintain catalyst activity. Calcination also reduces dolomite surface area and makes it more friable [78]. Delgado et al. [79, 80] investigated the catalytic activity of calcined calcite, magnesite and calcined dolomite for the cracking of tar in secondary catalytic fixed beds. For this purpose, tar produced in a fluidized bed gasifier was flowed through a fixed bed of catalyst. Their results showed good calcined dolomite catalytic activity for tar cracking. When calcined dolomite was used as catalyst, tar in the produced gas was about 0.5 g/Nm<sup>3</sup>. In the case of calcined calcite and magnesite, tar content was about 1 and 3 g/Nm<sup>3</sup>, respectively, which was considerably lower than that produced in the presence of sand (10 g/Nm<sup>3</sup>) highlighting the good activity of calcined rocks.

Olivine mainly found in igneous rocks is the most abundant mineral in the Earth's upper mantle [81]. It is an orthosilicate with a formula of  $(\text{Fe}_x\text{Mg}_{1-x})_2\text{SiO}_4$  representing a complete solid solution of forsterite,  $\text{Mg}_2\text{SiO}_4$ , and fayalite,  $\text{Fe}_2\text{SiO}_4$  [82-84]. Olivine is a high attrition resistance material with mechanical strength comparable to sand's. Olivine is available in the market and the price of olivine is about 120 Euros per metric tonne [77]. Catalytic activity of olivine for cracking of biomass tar has been investigated by several groups. Rapagna et al. [85] investigated the catalytic activity of olivine in a fluidized bed biomass steam gasifier and they reported more than 90% reduction in the average tar content in the presence of olivine. The tar content of the produced gas was reduced from 43  $\text{g}/\text{Nm}^3$  to 2.43  $\text{g}/\text{Nm}^3$  by implementing olivine instead of sand as a bed material. Devi et al. [86, 87] also investigated the catalytic activity of olivine for cracking of tar produced in a fluidized bed gasifier. Tar was passed through a fixed bed of olivine and the composition and concentration of tar in the produced gas was measured. According to these results, 45% reduction in tar content was observed using olivine instead of sand as a bed material. The presence of iron species in olivine (4-7 wt% of olivine is iron) is considered to be the main reason for its tar cracking activity.

The effect of calcination temperature and calcination duration on the activity of olivine as a catalyst for cracking of naphthalene biomass model tar compound was investigated by Devi et al. [87]. Olivine samples from Norwegian ores with 7 wt.% of iron oxides were calcined at 900°C and for varying durations (1-20 h). A combination of X-ray photo electron spectroscopy (XPS), Mössbauer spectroscopy and temperature program reduction (TPR) was used to investigate the effect of calcination time. Surface analysis of pre-calcined olivine using XPS revealed the presence of Fe 2p and Fe 3p peaks on the pre-calcined sample (Figure 1-15) while the intensity of these peaks was much lower in the case of untreated olivine showing the extraction of iron from the structure of olivine due to the calcination. Mössbauer spectroscopy also confirmed the presence of Fe (III) oxides on the pre-calcined olivine (mostly in the form of  $\alpha\text{-Fe}_2\text{O}_3$ ). These results indicate that during calcination, segregation of iron occurs on the surface of olivine. The study's results also showed that calcination increased olive activity for the cracking of naphthalene. It is also mentioned that increasing the calcination time of olivine from 1 to 10 hours slightly increased the catalytic conversion of naphthalene (model tar compound) from 62 % to 69%.

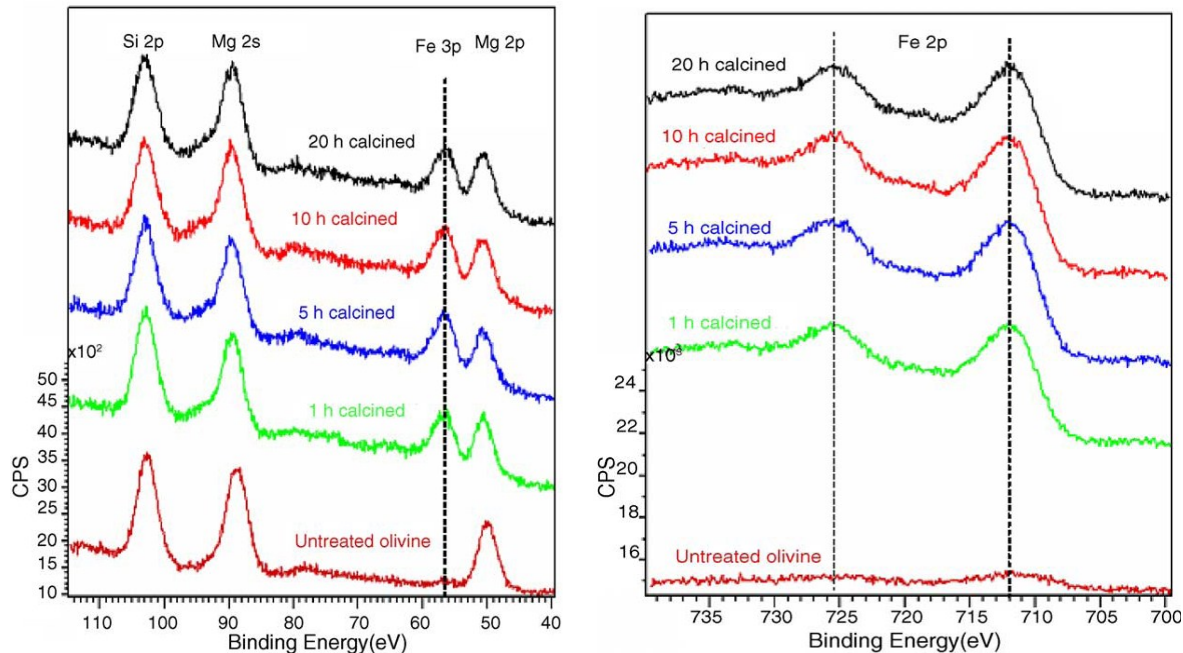


**Figure 1-15:** XPS spectra of olivine for two binding energy regions [87]

Due to the important role of iron on the catalytic properties of olivine, Swierczynski et al. [83] investigated the effect of oxidation and reduction (between 400-1400°C) of iron-bearing olivine (obtained from Austria mine, 7.1 wt% of iron) on the thermal transformation of  $\text{Fe}^{2+}$ . X-ray diffraction and Mössbauer spectroscopy of the initial olivine studied in their research revealed a system containing  $(\text{Mg}_{0.94}\text{Fe}_{0.06})_2\text{SiO}_4$  as the main phase, small quantities of  $\text{MgSiO}_3$ , and free iron oxides (3 wt% of iron) consisting of  $\text{MgFe}_2\text{O}_4$  and  $\alpha\text{-Fe}_2\text{O}_3$ . The presence of free iron oxides in their olivine sample was due to the pre-calcination of olivine in the mine to enhance its mechanical stability. Pre-calcined olivine was done at temperatures between 400°C and 1400°C to study the effect of calcination on the crystalline phase and structural modifications of olivine. The main olivine phase did not change during calcination. However, after calcination at 1100°C, the formation of a main reflection of  $\alpha\text{-Fe}_2\text{O}_3$  and a slight increase in intensity of the spinel phase was observed. The presence of iron oxides was explained by rejection of iron from the olivine structure caused by the oxidation of iron (II) to iron (III) accompanied by the formation of amorphous silica (not detected by XRD). Mössbauer spectroscopy also confirmed the presence of 83 wt% of iron in the oxide form at 1100°C while this value was

45 wt% for non-calcined olivine. According to these results, the following reaction takes place during olivine calcination:



### **C) Objectives, scope and outline of the project**

Biomass fuel will have a major impact in the future energy policy of Quebec province. The high reserves of biomass especially abundant forest residues could be a rather sustainable source of clean energy for the Province. Forest residues are composed of different varieties of biomass species with different physicochemical characteristics. Pre-treatment of forest residues before thermochemical conversion is a necessary step for energy production purposes. Although many works have been published on the torrefaction of different types of biomass and the properties of torrefaction products, studies on the improvement of biomass torrefaction efficiency are unusual. Different practical problems associated with biomass torrefaction such as slow rate of biomass torrefaction and its low efficiency have been already pinpointed. However, a few works can be found in the literature suggesting practical solutions. Furthermore, Québec is endowed with huge resources of mining residues rich in magnesium, silicon and iron which could be used in biomass thermochemical processes. Previous studies have shown that the minerals and mining residues could be used for different purposes such as CO<sub>2</sub> sequestration or/and solid oxygen carrier in the coal combustion and gasification units. However, their potential application in different areas of biomass thermal conversion has not been addressed thoroughly enough. In what follows, a number of research foundations have been established on biomass thermochemical conversion which are further investigated in this thesis;

- 1- Biomass torrefaction is considered as an important pre-treatment method to enhance the biomass fuel qualities. Many studies could be found in the literature about the torrefaction of different types of biomass fuels. However, the mechanism of biomass torrefaction, the evolution of chemical structure of main biomass compounds such as cellulose, hemicellulose and lignin and the change in their chemical composition during torrefaction is not well totally elucidated in the

literature. Furthermore, few studies have tried to develop a model for biomass torrefaction and models developed for a special biomass cannot be used for other biomass types. As an objective, in this thesis we studied the mechanism of biomass torrefaction in more details and we developed a kinetic model for the torrefaction of biomass to predict its rate of decomposition at different residence time and temperature.

- 2- Biomass torrefaction is a slow process requiring long residence time of biomass and large torrefaction units. Few works in the literature addressed the necessity to improve the rate of biomass torrefaction while conserving or improving the properties of solid products. Some green solvents such as ionic liquids have been already used for the fractionation of biomass; however, their potential in torrefaction was not tested before. Some types of ionic liquids are able to interact with the hydrogen bonds in biomass leading to the breakage of its polymeric structure and its fast decomposition. In addition to their interaction with biomass, their high thermal stability and low vapor pressure could be also appealing to assess their potential application in biomass torrefaction.
- 3- Co-firing of biomass with coal is one of the attractive options for energy production from biomass fuel in existing coal plants. However, co-firing of raw biomass and coal has encountered several technical difficulties. The high grinding energy, low energy density and low flowability and fluidization properties of biomass compared to those of coal lead to some practical problems for co-firing processes. Torrefaction is known as a pre-requisite step to improve the properties of biomass for co-firing. However, a considerable amount of carbon dioxide is released to the atmosphere during biomass torrefaction. Integration of biomass torrefaction with carbon capture and sequestration unit was not previously studied in the literature. Another objective of this thesis was to investigate the potential of coupling biomass torrefaction with a mining-residue carbonation unit. Torrefaction units could be built in local areas close to mining residue tailings to take advantage of abundant and cheap residues to sequester torrefaction CO<sub>2</sub> emissions. This could bring a major modification to the existing co-firing plants to reduce their CO<sub>2</sub> emission.
- 4- The required energy of torrefaction could be provided by burning the torrefaction

volatiles in an air combustor and by recirculating flue gas to the torrefaction reactor. However, the presence of residual oxygen in flue gas could reduce the torrefaction efficiency by burning biomass. The concept of chemical looping combustion of volatiles could be an interesting option for torrefaction technology to solve the issue of oxygen in flue gas. Therefore, as another objective of the thesis, combination of torrefaction and chemical looping combustion for burning torrefaction volatiles were subjected to investigation. The mining residues rich in iron could be suitable choices for solid oxygen carrier in the chemical looping combustion to burn the torrefaction volatiles.

- 5- Presence of considerable amount of iron in the structure of ultramafic mining residues could represent a potential of these materials as catalysts for cracking of tar produced during biomass torrefaction. To the best of our knowledge, the different synthesized catalyst produced and tested in different laboratories have so far not been used at an industrial scale due to the short lifetime of these costly catalysts in the gasification conditions. Production of high amounts of coke on the catalyst surface leads to fast catalyst regeneration requirement which considerably reduces their life. However, the use of cheap and abundant mining residues containing iron as a catalyst could be thought of as an option to reduce tar concentration and improve synthesis gas yield.

In the light of the abovementioned objectives, seven sections (Chapters 2-8) presenting the ideas, theoretical background and experimental results are provided in this thesis:

The **second** chapter in the thesis is devoted to the study of torrefaction of two biomass samples (aspen and birch) along with their main constituents, cellulose, hemicellulose and lignin. In the first part of the chapter, different biomass samples were torrefied at temperatures ranging from 240°C to 280°C representing mild and severe torrefaction conditions. The experiments were performed using either a thermogravimetric analyzer or a fixed bed. This part aimed at investigating the mechanism of cellulose, lignin and hemicellulose decomposition under mild and severe torrefaction conditions. In addition, the effect of torrefaction on energy density, energy yield, oxygen and hydrogen to carbon ratio of the samples and hydrophobicity was studied. In the second part of the chapter a kinetic model was developed for lignin, cellulose and hemicellulose torrefaction based on the

distributed activation energy model. The models developed for lignin, cellulose and hemicellulose were further used to build a kinetic model for aspen and birch torrefaction kinetics.

In the **third** chapter we proposed and studied a new ionic liquid (IL) assisted torrefaction route as an alternative to conventional dry torrefaction for enhancing the reaction rate and the quality of solid torrefaction products. Ionic liquid impregnated aspen, birch and sawdust were torrefied at 240 –280°C temperature range using [Emim][OTf], [Emim][BF<sub>4</sub>] and [Hmim][NTf<sub>2</sub>] ILs. To study the benefits of IL impregnated biomass, dry and IL torrefaction were compared in terms of mass yield, energy density, energy yield, hydrophobicity and ultimate moisture uptake of torrefied solid products using thermogravimetry and fixed-bed setups. The torrefaction of cellulose, hemicellulose and lignin IL impregnated samples was also studied in order to find the biomass components which are most affected by ionic liquids. Finally, the effect of biomass ash and minerals on the stability of ILs tested was also studied.

In chapter **four**, we proposed and studied a novel combination of biomass torrefaction and CO<sub>2</sub> sequestration at near ambient temperature using mining residues. Using this concept, CO<sub>2</sub> as one of the main gases evolved during torrefaction of lignocellulosic biomass could be trapped using cheap, abundant and already size-reduced mining residues resulting in a carbon-negative torrefaction process. Knowing that torrefaction is a prerequisite step to an efficient biomass/coal co-firing, further enhancement in the torrefaction process could reduce the overall CO<sub>2</sub> emissions of co-firing plants. To test the concept, carbonation potential of two types of ultramafic tailing residues obtained from the mining activities in Quebec province was evaluated by testing streams of CO<sub>2</sub> produced during dry and ionic-liquid torrefaction of birch wood. The study's aim specifically addressed the impact of carbonation temperature, residues pore water saturation, CO and methane composition of the evolving torrefaction gas on the carbonation rate of the mining residues.

In the **fifth** chapter, we presented a new concept of combined biomass torrefaction and chemical looping combustion (CLC) to recover the energy of volatiles released during torrefaction. The concept studied consists of burning torrefaction volatiles (composed of acid hydrocarbons, CO, CH<sub>4</sub> and H<sub>2</sub>) using iron oxide as a solid oxygen carrier in a CLC

reactor. The CLC hot flue gas stream consisting of CO<sub>2</sub> and water was recycled to the upstream torrefaction unit to transfer heat for the torrefaction of the solid biomass particles. Birch wood was torrefied at a temperature range of 260°C and 300°C and the resulting volatiles were burned over iron oxide solid oxygen carriers at 400-600°C converting volatile carbon into CO<sub>2</sub>. Oxygen carrier stability for burning torrefaction volatiles and oxygen depletion during CLC were also studied. Also, the buildup of CO<sub>2</sub> and water vapor in the recirculating torrefaction gas and their incidence on the properties of torrefied solid product were quantified in terms of mass and energy yields, equilibrium moisture content and grindability of the torrefied birch wood. The concept developed in this chapter has two main advantages over existing processes in which the torrefaction volatiles are directly burned with air in a combustor. First, the hot flue gas being O<sub>2</sub>-deprived will present no risk of burning biomass during torrefaction. Second, preliminary condensation and separation of water from the CLC flue gas will lead to a pure CO<sub>2</sub> stream which could be captured *via* physical or chemical solvents in a conventional gas-liquid scrubber or directly sequestered in mining residues via dry or wet carbonation.

The **sixth** chapter as a continuation of chapter five where the potential of a mining residue obtained from the Raglan mines was explored as a solid oxygen carrier for burning the torrefaction volatiles in a chemical looping combustion reactor. The mining residue studied had a considerable iron content (around 17.3 wt %) which could represent an appealing solid oxygen carrier. In this regard, birch wood samples were torrefied in a separate torrefaction reactor and the volatiles were routed to the CLC reactor loaded with the calcined mining residue to evaluate its efficiency for burning the volatiles. The solid oxygen carrier was also characterized to study the change in its crystalline structure as well as transformation of its iron oxidation state and coordination as a result of pre-calcination and application in the CLC reactor. The possibility of ambient pressure and temperature carbonation using mining residues in CLC reactor was also investigated in the chapter.

In chapter **seven** we studied the potential of chrysotile found in mine and milling residue heaps from Southern Quebec as a tar cracking catalyst for biomass steam gasification. Presence of ca. 6 wt % of iron oxides in chrysotile residues was electing it as a potential catalyst for tar cracking. We tested the steam-reforming activity of chrysotile for cracking

benzene (model tar compound) at various temperatures, gas hourly space velocities, and catalyst pre-treatments. The activity of air-calcined chrysotile was also compared with that of olivine catalyst with nearly equal iron content. Several characterisation techniques such as Mössbauer spectroscopy, temperature programmed reduction, X-ray diffraction spectroscopy and transmission electron microscopy was also used to study different coordination and oxidation states of iron as an active metal for tar cracking.

The **eighth** chapter is a continuation of chapter seven in which we studied the catalytic activity of two mining residue samples from chrysotile and nickel mines for cracking of benzene as a biomass model tar compound. The activities of the two catalysts were compared to that of olivine. The effect of different concentrations of synthesis gas such as H<sub>2</sub>O, CO, CO<sub>2</sub>, CH<sub>4</sub> and H<sub>2</sub> on the activity of chrysotile samples was also studied in this chapter. Different characterisation techniques such as Mössbauer spectroscopy, temperature programmed reduction, X-ray diffraction spectroscopy and transmission electron microscopy also helped interpreting the different catalytic activities of the three different minerals tested.

## D) References

- [1] Vers la valorisation de la biomasse forestiere, un plan d'action. Government of Quebec; 2009.
- [2] Saxena RC, Adhikari DK, Goyal HB. Biomass-based energy fuel through biochemical routes: A review. *Renewable & Sustainable Energy Reviews*. 2009;13:167-78.
- [3] Pare D, Bernier P, Thiffault E, Titus BD. The potential of forest biomass as an energy supply for Canada. *Forestry Chronicle*. 2011;87:71-6.
- [4] Mohan D, Pittman CU, Jr., Steele PH. Pyrolysis of wood/biomass for bio-oil: A critical review. *Energy & Fuels*. 2006;20:848-89.
- [5] Shafizadeh F. Introduction to pyrolysis of biomass. *Journal of Analytical and Applied Pyrolysis*. 1982;3:283-305.
- [6] de Sousa LCR. Gasification of wood, urban wastewood (Altholz) and other wastes in a fluidised bed reactor 2001.
- [7] Bahng M-K, Mukarakate C, Robichaud DJ, Nimlos MR. Current technologies for analysis of biomass thermochemical processing: A review. *Analytica Chimica Acta*. 2009;651:117-38.
- [8] Baldwin RM, Magrini-Baira KA, Nimlos MR, Pepiot P, Donohoe BS, Hensley JE, et al. Current research on thermochemical conversion of biomass at the National Renewable Energy Laboratory. *Applied Catalysis B-Environmental*. 2012;115:320-9.
- [9] Huber GW, Iborra S, Corma A. Synthesis of transportation fuels from biomass: Chemistry, catalysts, and engineering. *Chemical Reviews*. 2006;106:4044-98.
- [10] Sami M, Annamalai K, Wooldridge M. Co-firing of coal and biomass fuel blends. *Progress in Energy and Combustion Science*. 2001;27:171-214.
- [11] van der Stelt MJC, Gerhauser H, Kiel JHA, Ptasiński KJ. Biomass upgrading by torrefaction for the production of biofuels: A review. *Biomass & Bioenergy*. 2011;35:3748-62.
- [12] Das P, Ganesh A, Wangikar P. Influence of pretreatment for deashing of sugarcane bagasse on pyrolysis products. *Biomass & Bioenergy*. 2004;27:445-57.
- [13] Li J, Brzdekiewicz A, Yang WH, Blasiak W. Co-firing based on biomass torrefaction in a pulverized coal boiler with aim of 100% fuel switching. *Applied Energy*. 2012;99:344-54.
- [14] Yu Y, Zeng Y, Zuo J, Ma F, Yang X, Zhang X, et al. Improving the conversion of biomass in catalytic fast pyrolysis via white-rot fungal pretreatment. *Bioresource Technology*. 2013;134:198-203.
- [15] Dobelev G, Dizhbite T, Rossinskaja G, Telysheva G, Mier D, Radtke S, et al. Pre-treatment of biomass with phosphoric acid prior to fast pyrolysis - A promising method for obtaining 1,6-anhydrosaccharides in high yields. *Journal of Analytical and Applied Pyrolysis*. 2003;68-9:197-211.
- [16] Misson M, Haron R, Fadhzir M, Kamaroddin A, Amin NAS. Pretreatment of empty palm fruit bunch for production of chemicals via catalytic pyrolysis. *Bioresource Technology*. 2009;100:2867-73.

- [17] Koppejan J, Sokhansanj S, Melin s, Madrali S. status overview of torrefaction technologies. IEA bioenergy task 32 report December 2012.
- [18] Bergman PC, Boersma AR, Zwart RWR, Kiel JHA. Torrefaction for biomass co-firing in existing coal-fired power stations (Biocoal). Energy Research Centre of the Netherlands 2005.
- [19] Prins MJ, Ptasiński KJ, Janssen F. Torrefaction of wood - Part 2. Analysis of products. Journal of Analytical and Applied Pyrolysis. 2006;77:35-40.
- [20] Patel B, Gami B, Bhimani H. Improved fuel characteristics of cotton stalk, prosopis and sugarcane bagasse through torrefaction. Energy for Sustainable Development. 2011;15:372-5.
- [21] Bridgeman TG, Jones JM, Shield I, Williams PT. Torrefaction of reed canary grass, wheat straw and willow to enhance solid fuel qualities and combustion properties. Fuel. 2008;87:844-56.
- [22] Phanphanich M, Mani S. Impact of torrefaction on the grindability and fuel characteristics of forest biomass. Bioresource Technology. 2011;102:1246-53.
- [23] Repellin V, Govin A, Rolland M, Guyonnet R. Energy requirement for fine grinding of torrefied wood. Biomass & Bioenergy. 2010;34:923-30.
- [24] Li H, Liu X, Legros R, Bi XT, Lim CJ, Sokhansanj S. Torrefaction of sawdust in a fluidized bed reactor. Bioresource Technology. 2012;103:453-8.
- [25] Medic D, Darr M, Shah A, Rahn S. Effect of torrefaction on water vapor adsorption properties and resistance to microbial degradation of corn stover. Energy & Fuels. 2012;26:2386-93.
- [26] Acharjee TC, Coronella CJ, Vasquez VR. Effect of thermal pretreatment on equilibrium moisture content of lignocellulosic biomass. Bioresource Technology. 2011;102:4849-54.
- [27] Repellin V, Govin A, Rolland M, Guyonnet R. Modelling anhydrous weight loss of wood chips during torrefaction in a pilot kiln. Biomass & Bioenergy. 2010;34:602-9.
- [28] Prins MJ, Ptasiński KJ, Janssen F. Torrefaction of wood - Part 1. Weight loss kinetics. Journal of Analytical and Applied Pyrolysis. 2006;77:28-34.
- [29] DiBlasi C, Lanzetta M. Intrinsic kinetics of isothermal xylan degradation in inert atmosphere. Journal of Analytical and Applied Pyrolysis. 1997;40-1:287-303.
- [30] Rousset P, Turner I, Donnot A, Perre P. The choice of a low-temperature pyrolysis model at the microscopic level for use in a macroscopic formulation. Annals of Forest Science. 2006;63:213-29.
- [31] Fredlake CP, Crosthwaite JM, Hert DG, Aki S, Brennecke JF. Thermophysical properties of imidazolium-based ionic liquids. Journal of Chemical and Engineering Data. 2004;49:954-64.
- [32] Plechkova NV, Seddon KR. Applications of ionic liquids in the chemical industry. Chemical Society Reviews. 2008;37:123-50.
- [33] Li B, Asikkala J, Filpponen I, Argyropoulos DS. Factors affecting wood dissolution and regeneration of ionic liquids. Industrial & Engineering Chemistry Research. 2010;49:2477-84.

- [34] Zhang H, Wu J, Zhang J, He JS. 1-Allyl-3-methylimidazolium chloride room temperature ionic liquid: A new and powerful nonderivatizing solvent for cellulose. *Macromolecules*. 2005;38:8272-7.
- [35] Maki-Arvela P, Anugwom I, Virtanen P, Sjöholm R, Mikkola JP. Dissolution of lignocellulosic materials and its constituents using ionic liquids-A review. *Industrial Crops and Products*. 2010;32:175-201.
- [36] Zhang J, Zhang H, Wu J, Zhang J, He J, Xiang J. NMR spectroscopic studies of cellobiose solvation in EmimAc aimed to understand the dissolution mechanism of cellulose in ionic liquids. *Physical Chemistry Chemical Physics*. 2010;12:1941-7.
- [37] Feng L, Chen Z-I. Research progress on dissolution and functional modification of cellulose in ionic liquids. *Journal of Molecular Liquids*. 2008;142:1-5.
- [38] Zeng Y, Yang X, Yu H, Zhang X, Ma F. Comparative studies on thermochemical characterization of corn stover pretreated by white-rot and brown-rot fungi. *Journal of Agricultural and Food Chemistry*. 2011;59:9965-71.
- [39] Yang H, Xu Z, Fan M, Gupta R, Slimane RB, Bland AE, et al. Progress in carbon dioxide separation and capture: A review. *Journal of Environmental Sciences-China*. 2008;20:14-27.
- [40] Voormeij DA, Simandl GJ. Geological, ocean, and mineral CO<sub>2</sub> sequestration options: A technical review. *Geoscience Canada*. 2004;31:11-22.
- [41] Cole DR, Chialvo AA, Rother G, Vlcek L, Cummings PT. Supercritical fluid behavior at nanoscale interfaces: Implications for CO<sub>2</sub> sequestration in geologic formations. *Philosophical Magazine*. 2010;90:2339-63.
- [42] Chouinard S. Valorisation des résidus de serpentine par extraction du magnésium au moyen de procédés hydrométallurgiques. Rapport de Mémoire. Université du Québec. Institut National de la Recherche Scientifique. Centre Eau, Terre et Environnement. 2006.
- [43] Wilson SA, Raudsepp M, Dipple GM. Verifying and quantifying carbon fixation in minerals from serpentine-rich mine tailings using the Rietveld method with X-ray powder diffraction data. *American Mineralogist*. 2006;91:1331-41.
- [44] Assima GP, Larachi F, Beaudoin G, Molson J. CO<sub>2</sub> Sequestration in chrysotile mining residues-implication of watering and passivation under environmental conditions. *Industrial & Engineering Chemistry Research*. 2012;51:8726-34.
- [45] P. Assima G, Larachi F, Beaudoin G, Molson J. Dynamics of carbon dioxide uptake in chrysotile mining residues- effect of mineralogy and liquid saturation. *International Journal of Greenhouse Gas Control*. 2013;12:124-35.
- [46] Pronost J, Beaudoin G, Lemieux JM, Hebert R, Constantin M, Marcouiller S, et al. CO<sub>2</sub>-depleted warm air venting from chrysotile milling waste (Thetford Mines, Canada): Evidence for in-situ carbon capture from the atmosphere. *Geology*. 2012;40:275-8.
- [47] Larachi F, Daldoul I, Beaudoin G. Fixation of CO<sub>2</sub> by chrysotile in low-pressure dry and moist carbonation: Ex-situ and in-situ characterizations. *Geochimica Et Cosmochimica Acta*. 2010;74:3051-75.

- [48] Larachi F, Gravel JP, Grandjean BPA, Beaudoin G. Role of steam, hydrogen and pretreatment in chrysotile gas-solid carbonation: Opportunities for pre-combustion CO<sub>2</sub> capture. *International Journal of Greenhouse Gas Control*. 2012;6:69-76.
- [49] O'Connor WK, Dahlin DC, Turner PC, Walters R. Carbon dioxide sequestration by ex-situ mineral carbonation. Second annual Dixy Lee Ray memorial symposium, American society of mechanical engineering. Washington D.C.1999.
- [50] Lackner KS, Wendt CH, Butt DP, Joyce EL, Sharp DH. Carbon-dioxide disposal in carbonate minerals. *Energy*. 1995;20:1153-70.
- [51] Kakizawa M, Yamasaki A, Yanagisawa Y. A new CO<sub>2</sub> disposal process via artificial weathering of calcium silicate accelerated by acetic acid. *Energy*. 2001;26:341-54.
- [52] Golubev SV, Pokrovsky OS, Schott J. Experimental determination of the effect of dissolved CO<sub>2</sub> on the dissolution kinetics of Mg and Ca silicates at 25 degrees C. *Chemical Geology*. 2005;217:227-38.
- [53] Grenman H, Ramirez F, Eraenen K, Waerna J, Salmi T, Murzin DY. Dissolution of mineral fiber in a formic acid solution: kinetics, modeling, and gelation of the resulting sol. *Industrial & Engineering Chemistry Research*. 2008;47:9834-41.
- [54] McKelvy MJ, Chizmeshya AVG, Squires KD, Carpenter RW, Béarat H. A novel approach to mineral carbonation: Enhancing carbonation while avoiding mineral pre-treatment process cost. Arizona State University, Center for Solid State Science, Science and Engineering of Materials Graduate Program, and Department of Mechanical and Aerospace Engineering 2005.
- [55] Dheilily RM, Sebaibi Y, Tudo J, Queneudec M. Importance of the presence of magnesia in limestone storage: Carbonation of magnesium oxide and magnesium hydroxide. *Canadian Journal of Chemistry-Revue Canadienne De Chimie*. 1998;76:1188-96.
- [56] Chiu P-C, Ku Y. Chemical Looping Process - A novel technology for inherent CO<sub>2</sub> capture. *Aerosol and Air Quality Research*. 2012;12:1421-32.
- [57] Hossain MM, de Lasa HI. Chemical-looping combustion (CLC) for inherent CO<sub>2</sub> separations-a review. *Chemical Engineering Science*. 2008;63:4433-51.
- [58] Hasib-ur-Rahman M, Siaj M, Larachi F. Ionic liquids for CO<sub>2</sub> capture-development and progress. *Chemical Engineering and Processing*. 2010;49:313-22.
- [59] Abad A, Adanez J, Cuadrat A, Garcia-Labiano F, Gayan P, de Diego LF. Kinetics of redox reactions of ilmenite for chemical-looping combustion. *Chemical Engineering Science*. 2011;66:689-702.
- [60] Adanez J, de Diego LF, Garcia-Labiano F, Gayan P, Abad A, Palacios JM. Selection of oxygen carriers for chemical-looping combustion. *Energy & Fuels*. 2004;18:371-7.
- [61] Leion H, Lyngfelt A, Johansson M, Jerndal E, Mattisson T. The use of ilmenite as an oxygen carrier in chemical-looping combustion. *Chemical Engineering Research & Design*. 2008;86:1017-26.

- [62] Linderholm C, Lyngfelt A, Dueso C. Chemical-looping combustion of solid fuels in a 10 kW reactor system using natural minerals as oxygen carrier. *Energy Procedia*. 2013;37:598-607.
- [63] Huang Z, He F, Feng YP, Zhao K, Zheng AQ, Chang S, et al. Synthesis gas production through biomass direct chemical looping conversion with natural hematite as an oxygen carrier. *Bioresource Technology*. 2013;140:138-45.
- [64] Tian HJ, Siriwardane R, Simonyi T, Poston J. Natural ores as oxygen carriers in chemical looping combustion. *Energy & Fuels*. 2013;27:4108-18.
- [65] Evans RJ, Milne TA. Molecular characterization of the pyrolysis of biomass .2. applications. *Energy & Fuels*. 1987;1:311-9.
- [66] Evans RJ, Milne TA. Molecular characterization of the pyrolysis of biomass .1. fundamentals. *Energy & Fuels*. 1987;1:123-37.
- [67] Milne TA, Evans RJ, Abatzoglou N. Biomass gasifier Tars: their nature, formation, and conversion. National Renewable Energy Laboratory, US department of energy; 1988.
- [68] Morf P, Hasler P, Nussbaumer T. Mechanisms and kinetics of homogeneous secondary reactions of tar from continuous pyrolysis of wood chips. *Fuel*. 2002;81:843-53.
- [69] Li C, Suzuki K. Tar property, analysis, reforming mechanism and model for biomass gasification-An overview. *Renewable & Sustainable Energy Reviews*. 2009;13:594-604.
- [70] Tomishige K, Miyazawa T, Asadullah M, Ito S, Kunimori K. Catalyst performance in reforming of tar derived from biomass over noble metal catalysts. *Green Chemistry*. 2003;5:399-403.
- [71] Furusawa T, Tsutsumi A. Comparison of Co/MgO and Ni/MgO catalysts for the steam reforming of naphthalene as a model compound of tar derived from biomass gasification. *Applied Catalysis a-General*. 2005;278:207-12.
- [72] Miyazawa T, Kimura T, Nishikawa J, Kado S, Kunimori K, Tomishige K. Catalytic performance of supported Ni catalysts in partial oxidation and steam reforming of tar derived from the pyrolysis of wood biomass. *Catalysis Today*. 2006;115:254-62.
- [73] Colby JL, Wang T, Schmidt LD. Steam reforming of benzene as a model for biomass-derived syngas tars over Rh-based catalysts. *Energy & Fuels*. 2010;24:1341-6.
- [74] Garcia L, French R, Czernik S, Chornet E. Catalytic steam reforming of bio-oils for the production of hydrogen: effects of catalyst composition. *Applied Catalysis a-General*. 2000;201:225-39.
- [75] Sato K, FujiMoto K. Development of new nickel based catalyst for tar reforming with superior resistance to sulfur poisoning and coking in biomass gasification. *Catalysis Communications*. 2007;8:1697-701.
- [76] Zhang JC, Wang YH, Ma RY, Wu DY. Characterization of alumina-supported Ni and Ni-Pd catalysts for partial oxidation and steam reforming of hydrocarbons. *Applied Catalysis a-General*. 2003;243:251-9.

- [77] Abu El-Rub Z, Bramer EA, Brem G. Review of catalysts for tar elimination in Biomass gasification processes. *Industrial & Engineering Chemistry Research*. 2004;43:6911-9.
- [78] Dayton D. A review of the literature on catalytic biomass tar destruction. NREL2002.
- [79] Delgado J, Aznar MP, Corella J. Calcined dolomite, magnesite, and calcite for cleaning hot gas from a fluidized bed biomass gasifier with steam: Life and usefulness. *Industrial & Engineering Chemistry Research*. 1996;35:3637-43.
- [80] Delgado J, Aznar MP, Corella J. Biomass gasification with steam in fluidized bed: Effectiveness of CaO, MgO, and CaO-MgO for hot raw gas cleaning. *Industrial & Engineering Chemistry Research*. 1997;36:1535-43.
- [81] Wang D, Mookherjee M, Xu Y, Karato S-i. The effect of water on the electrical conductivity of olivine. *Nature*. 2006;443:977-80.
- [82] Swierczynski D, Courson C, Bedel L, Kiennemann A, Guille J. Characterization of Ni-Fe/MgO/olivine catalyst for fluidized bed steam gasification of biomass. *Chemistry of Materials*. 2006;18:4025-32.
- [83] Swierczynski D, Courson C, Bedel L, Kiennemann A, Vilminot S. Oxidation reduction behavior of iron-bearing olivines  $(\text{Fe}_x\text{Mg}_{1-x})_2\text{SiO}_4$  used as catalysts for biomass gasification. *Chemistry of Materials*. 2006;18:897-905.
- [84] Swierczynski D, Courson C, Kiennemann A. Study of steam reforming of toluene used as model compound of tar produced by biomass gasification. *Chemical Engineering and Processing*. 2008;47:508-13.
- [85] Rapagna S, Jand N, Kiennemann A, Foscolo PU. Steam-gasification of biomass in a fluidised-bed of olivine particles. *Biomass & Bioenergy*. 2000;19:187-97.
- [86] Devi L, Ptasiński KJ, Janssen F, van Paasen SVB, Bergman PCA, Kiel JHA. Catalytic decomposition of biomass tars: use of dolomite and untreated olivine. *Renewable Energy*. 2005;30:565-87.
- [87] Devi L, Craje M, Thune P, Ptasiński KJ, Janssen F. Olivine as tar removal catalyst for biomass gasifiers: Catalyst characterization. *Applied Catalysis a-General*. 2005;294:68-79.

## **Chapter 2 : Dry torrefaction of biomass and of its constitutive components - Characterization of torrefied products and torrefaction kinetics using the distributed activation energy model**

**Résumé** La torréfaction est un traitement thermique utilisé pour améliorer les propriétés de la biomasse en vue d'un stockage à long terme et une meilleure conversion thermo-chimique du bois. Le comportement cinétique de la torréfaction de deux échantillons de biomasse lignocellulosique (peuplier faux-tremble et le bouleau) et de leurs principaux constituants (cellulose, xylane (hémicellulose) et lignine) a été étudié en détail. Les matériaux ont été torréfiés dans un réacteur à lit fixe jusqu'à 280°C et ont été caractérisés après 15 min et 60 min de traitement en termes de densité et de rendement énergétiques, de teneurs en H, en O et en C, de reprise d'humidité et de spectres obtenus par spectroscopie infrarouge à transformée de Fourier (FTIR). Indépendamment de la sévérité de la torréfaction, l'hémicellulose était le constituant le plus réactif. Comparée à la cellulose torréfiée, la lignine présentait une activité considérable et une augmentation de sa valeur calorifique lors de la torréfaction sévère (280°C). L'augmentation de la valeur de calorifique de la cellulose torréfiée était également moins importante que celle de la lignine en raison de la perte d'énergie par la cellulose due à la production d'un composé du goudron. La production de composants volatils en fonction du temps à partir de cellulose, de xylane et de lignine a été mesurée par thermogravimétrie et modélisée pour chaque type de *lump* à l'aide d'un modèle d'énergie d'activation répartie et d'une fonction de distribution log-normale à trois paramètres. Le modèle décrit bien les données expérimentales de torréfaction du xylane et de la lignine tandis qu'il a montré une légère sous-estimation dans le cas de la torréfaction de la cellulose. Les modèles développés pour les *lumps* individuels ont été combinés en un méta-modèle pour appréhender la cinétique de torréfaction de la biomasse ligneuse réelle (peuplier faux-tremble et le bouleau) en supposant l'implication parallèle et indépendante de leur trois constituants, présents en diverses compositions. Le modèle reflétait assez fidèlement les données expérimentales de torréfaction des deux types de biomasse.

**Abstract** Torrefaction is a thermal treatment applied to improve biomass properties for long-term storage and thermochemical conversion of wood. The torrefaction kinetic behavior of two woody biomass samples (aspen and birch) and their individual constituents (cellulose, xylan -hemicellulose proxy- and lignin) was studied in detail. The materials were torrefied in a fixed-bed reactor up to 280 °C and were characterized after 15 min and 60 min treatments in terms of their energy density, energy yield, H, O and C contents, humidity uptake and FTIR vibrational spectra. Hemicellulose was found to be the most reactive biomass compound during torrefaction. The lignin subjected to the mild (240 °C) and severe torrefaction conditions (280 °C) also showed considerable activity in comparison with the torrefied cellulose. Contrary to cellulose, the severe condition torrefaction of lignin led to a major increase in its heating value. However, the increase in the heating value of severe condition torrefied cellulose is less significant than that of lignin due to the loss of cellulose energy through the production of tar compounds. The release of volatiles versus time for cellulose, xylan and lignin torrefaction reactions measured using a thermogravimetric method was also modeled for each lump by means of the distributed activation energy model and a three-parameter log-normal distribution function. The model was found to fit the experimental data for xylan and lignin torrefaction while it showed slight under-prediction in the case of cellulose torrefaction. The distributed activation energy models developed for the individual lumps were combined into a meta-model to apprehend the torrefaction kinetics of actual (aspen and birch) woody biomass by assuming parallel and independent involvement of their three constituents present under various compositions. The model was found to represent with very good agreement the experimental data of aspen and birch torrefaction.

## 2.1. Introduction

Environmental and economic constraints as well as resource scarcity is increasingly calling into question the classical fossil-energy driven development paradigm. In response, alternative solutions (such as non-edible biomass) are steadfastly climbing the ladder of the energy portfolio as potentially viable and perennial carbon neutral energy options [1, 2]. However, as a fuel lignocellulosic biomass is disadvantaged in terms of O/C ratio, caloric value and moisture content, to name its main handicaps [3]. In order to upgrade biomass to a higher quality fuel, thermal treatments such as torrefaction are required. The goal behind torrefaction is to eliminate oxygen in the form of low caloric value torrefaction gases, e.g., CO<sub>2</sub>, water and some organic acids, by exposing biomass to temperatures as high as 200-300°C [4-6]. In spite of the fact that *ca.* 30 wt. % of biomass is lost during torrefaction the recovered solid may retain up to 90% of the initial biomass energy content [3]. In comparison to the parent raw biomass, torrefied solid products should bear certain properties such as lower moisture content, lower O/C ratio, and higher energy density to make them suitable biofuels [4-6].

Different torrefaction processes, *e.g.*, dry torrefaction [4-6], wet torrefaction [7,8] and ionic-liquid assisted torrefaction [9] have been proposed to leverage the above biomass properties. Dry torrefaction consists of slow heating of biomass in an inert atmosphere from 200°C to 300°C [4-6,10]. During this treatment, the three main constituents of biomass, *i.e.*, hemicellulose, cellulose and lignin [11] decompose at different rates. Hemicellulose is the most sensitive lump to be affected by dry torrefaction unlike cellulose whose decomposition is the rate limiting step of torrefaction [12]. The rate of cellulose decomposition is stimulated by elevated torrefaction temperatures, though temperatures in excess of 300°C are not recommended due to the release of heavy tars which tendency is to reduce biomass energy density [12]. Impregnation of biomass with room-temperature ionic liquids enhanced the rate of cellulose torrefaction at temperatures lower than 300°C [9]. However, despite advantages showcased by ionic liquids, the solid products resulting from ionic-liquid torrefaction treatments still require further improvements such as energy yield which was found to be lesser compared to the dry-torrefaction analogs [9]. In addition, cost of ionic liquids should be factored in if such advanced approaches are to be sought for

commercial applications of biomass torrefaction [13]. Wet torrefaction or hydrothermal pretreatment of biomass performed in a pressurized liquid water up to 5 MPa and 260°C produces solids with energy density greater than that obtained from dry torrefaction [7,8]. Likewise, elevated pressures tend to reflect in increased operational costs also. Therefore, it is likely that dry torrefaction, because of its rustic character and low cost, will still encompass the majority of lignocellulosic biomass torrefaction units [14].

Several kinetic models have been proposed for biomass torrefaction in dry inert atmosphere which are mostly of pseudo-mechanistic nature where one or several pseudo-reactions are assumed for modeling biomass torrefaction [12,15,16]. We are of the opinion that the wide range of heterogeneous reactions taking place during torrefaction must call for more appropriate mathematical representations. These latter must be able to account for the distributed nature of the reactions across the biomass structure, *e.g.*, catalytic effects of the alkali metals, and the corresponding wide range of activation energies [17] which are not reflected in current models. We propose to evaluate the potential of the distributed activation energy model (DAEM) which is viewed as one of the most accurate approaches for modeling biomass pyrolysis [17]. The model assumes an infinite number of irreversible  $n^{\text{th}}$ -order parallel reactions with different activation energies occurring simultaneously and where the difference in activation energies is represented by a distribution function. The DAEM has been widely used to analyze complex reactions such as pyrolysis of various ranks of coal and other fuels [18-21]. Yet, and to the best of the authors' knowledge, the merit of using DAEM has not been assessed for representing biomass torrefaction kinetics.

This work, therefore, aims at studying the dry torrefaction properties and kinetics of the main biomass constituents, *i.e.*, xylan (hemicellulose proxy), cellulose and lignin, as well as two different hardwoods, *i.e.*, aspen and birch. Characterization experiments were designed such that they evaluate a number of properties which are of paramount importance in the field of biomass torrefaction and provide a rather consolidated study. To do so, the main biomass constituents, birch and aspen were torrefied under mild and severe torrefaction conditions and the contribution of each biomass constituents on the properties of torrefied biomass was analyzed by obtaining their heating value and energy yield. Major emphasis was put on lignin which is considered as an inert compound in some existing literature [22,

23] and thus its decomposition rate, heating value and energy density of torrefied lignin was compared with that of cellulose. The FTIR analysis performed on the raw and torrefied samples also helped us to have some deep understandings on the mechanism of cellulose, hemicellulose and lignin torrefaction. Moreover, the humidity uptake of each biomass constituents subjected to the mild and severe torrefaction condition was studied to investigate their role on the equilibrium moisture content of torrefied birch and aspen as biomass representative. Finally, a DAEM kinetic model for the torrefaction of each constituent, separately, and for both hardwood samples is formulated. To achieve this, separate DAEM models are developed for each one of hemicellulose, cellulose and lignin lumps by monitoring their thermal decomposition rates versus time in a torrefaction environment using a thermogravimetric analyzer (TG). The quality of the models is judged both by their predictive power for actual wood samples using recombined kinetics from the constitutive wood lumps and actual torrefaction kinetics of aspen and birch samples.

## **2.2. Experimental**

Isothermal torrefaction studies were carried out using trembling aspen and birch, two abundant woody biomass samples from Québec forests (Canada), as well as powdered samples of cellulose (Avicel®PH-101), xylan (X0502) and lignin (37059-lignin, alkali), all three purchased from Sigma Aldrich. The proximate and ultimate analyses of the studied samples are summarized, respectively, in Tables 2-1 and 2-2. The birch and aspen samples were first grinded and then sieved to isolate particles finer than 500 µm. The samples were then torrefied in a fixed-bed torrefaction reactor. The bench scale biomass torrefaction unit consisted of a stainless steel (SS) fixed-bed reactor (ID. 34 mm, length 70 cm) placed inside an induction coil. For each one of the experiments, 300 mg of biomass was held atop of a steel grid located in the middle of a stainless steel tube to act as a support for the biomass bed. The reactor was heated through a 30 cm long coil connected to a 18 kW induction power supply for heating the stainless steel tube *via* an AC magnetic field then heating in turn the biomass layer through radiation and conduction. The biomass bed temperature was raised from the ambient to the target temperature (240°C and 280°C) in less than 10 s and then the samples were kept at the final temperature for specified time durations, 15 and 60 min, respectively. These torrefaction temperatures, *i.e.*, 240°C and

280°C were representatives of mild and severe torrefaction conditions, respectively [24]. The SS tube temperature was controlled by a fiber optic pyrometer connected to a temperature controller to meter the induction-heater power. Temperature was also measured through a K type thermocouple inserted in the center of the biomass bed. The difference in temperature between the bed and SS tube surface never exceeded 5°C in steady-state conditions. Volatiles forming in the reactor were directed towards a cold trap by sweeping the bed with a continuous N<sub>2</sub> flow (200 NmL/min).

**Table 2-1** : Proximate analysis in mass % of cellulose, xylan, lignin, birch and aspen wood

	Humidity	Volatile (dry basis)	Fixed carbon (dry basis)	Ash (dry basis)
Cellulose	3.4	93.1	6.9	<0.1
Xylan	8.5	74.2	24.7	1.1
Lignin	3.1	49.3	47.5	3.2
Birch	5.5	89.4	9.8	0.7
Aspen	4.8	87.5	12	0.5

The solid products obtained after torrefaction were further analyzed to quantify their properties after thermal treatment. The solid products were weighted to obtain their mass yield ( $Y_M = \text{\%mass solid product/mass feed}$ ) after torrefaction. The C, H, N, S contents of the samples were also measured using an elemental analyzer (Fisons EA 1108CHNS). All measurements were repeated twice and their averages were reported. The higher heating value (HHV) of the samples before and after torrefaction were determined using a relationship obtained by Channiwala et al. [25] based on carbon, hydrogen, oxygen, sulfur, nitrogen and ash content of biomass. The model developed in their work was tested for 225 samples and was shown to be applicable for estimation of the high heating values of torrefied biomass [26,27]:

$$\text{HHV (kJ/g)} = \{0.3491 \times \text{C}\} + \{1.1783 \times \text{H}\} + \{0.1005 \times \text{S}\} - \{0.1034 \times \text{O}\} - \{0.0151 \times \text{N}\} - \{0.0211 \times \text{Ash}\}$$

With C, H, S, O, N and Ash representing carbon, hydrogen, sulfur, oxygen, nitrogen and ash mass percentages, respectively. Using the solid product HHV, the energy density ( $e = \text{HHV solid product/HHV feed}$ ) and energy yield ( $Y_e = e \cdot Y_M$ ) of the solids were also obtained.

**Table 2-2:** Ultimate analysis, O/C and H/C mole ratio, mass yield, high heating value, energy yield and energy density of as received and torrefied cellulose, xylan, lignin, birch and aspen.

	C	H	N	S	O	O/C mole ratio	H/C mole ratio	Mass yield (%)	Energy Yield	HHV (kJ/g)	Energy density ratio
<b>Cellulose</b>											
Raw	42.8	6.4	0	0	50.8	0.89	1.81	.....	100	17.3	1
Torrefied at 240 °C	43.6	6.3	0	0	50.1	0.86	1.72	98.1	98.8	17.4	1.0
Torrefied at 280 °C	44.4	6.2	0	0	49.4	0.83	1.69	90.1	92.5	17.7	1.03
<b>Xylan</b>											
Raw	40.4	6.1	0	0	53.4	0.99	1.82	.....	100	15.5	1
Torrefied at 240 °C	56.7	4.4	0	0	38.9	0.51	0.92	54.5	71.2	20.2	1.31
Torrefied at 280 °C	60.4	4.1	0	0	35.5	0.44	0.81	41.2	56.0	21.0	1.36
<b>Lignin</b>											
Raw	63.7	6.0	0.90	2.29	27.2	0.32	1.13	.....	100	25.6	1
Torrefied at 240 °C	69.5	5.5	0.60	2.12	22.2	0.24	0.95	89.9	96.6	27.7	1.07
Torrefied at 280 °C	70.6	5.5	0.60	1.99	21.4	0.23	0.93	87.3	94.8	28.0	1.09
<b>Aspen</b>											
Raw	47.0	6.2	0.01	0	46.7	0.74	1.60	.....	100	18.9	1
Torrefied at 240 °C	50.0	6.1	0.02	0	43.9	0.66	1.46	86.4	91.6	20.0	1.06
Torrefied at 280 °C	51.6	5.9	0.02	0	42.50	0.62	1.36	78.5	84.90	20.4	1.08
<b>Birch</b>											
Raw	47.6	6.1	0.05	0	46.3	0.73	1.54	.....	100	18.9	1
Torrefied at 240 °C	51.0	6.0	0.06	0	43.0	0.63	1.40	86.2	92.3	20.2	1.07
Torrefied at 280 °C	52.9	5.7	0.09	0	41.4	0.59	1.28	74.5	81.5	20.6	1.09

To investigate the effect of torrefaction on the samples hydrophobicity, equilibrium moisture content (EMC) analysis was also performed on the torrefied samples. EMC of raw and torrefied biomass samples were obtained by putting 300 mg samples in a vapor-saturated environment controlled at 25°C. All the samples were oven-dried at 110°C overnight to remove the pre-existing humidity in the samples before EMC analysis. The

samples weight gain was measured after ten days which was estimated to be enough for the samples to reach moisture equilibrium uptake. Fourier transform infrared spectroscopy (FTIR) (Nicolet Magna 850 spectrometer, Thermo Scientific, Madison, WI) was also performed on the as-received and torrefied cellulose, xylan and lignin to study changes in their functional groups during torrefaction. The FTIR was equipped with high temperature Golden Gate ATR accessory.

For the derivation of the kinetic model for biomass torrefaction, isothermal torrefaction kinetics of all five substrates were performed in a thermogravimetric analyzer (TG) (Perkin Elmer Lab System Diamond TG-DTA) used to monitor the weight loss of the samples during torrefaction. TG is appropriate for developing kinetic models for steady-state (isothermal) or low-heating rate biomass torrefaction [28]. For this purpose, the samples were placed in an alumina ceramic holder forming a small bed with initial mass of 5-8 mg of woody biomass, lignin, cellulose, or xylan. The samples were first dried in TG at 120°C for 15 min and then heated up to the target temperature (240-290°C) with the maximum achievable heating rate (~200°C/min) under N<sub>2</sub> flow (200 NmL/min). The isothermal torrefaction of the samples was performed by maintaining the samples at the target temperature between 15 to 180 min while samples' mass was adjusted so that weight losses during torrefaction never dived below 30wt%.

### 2.3. Kinetic modeling

The total amount of volatiles released during torrefaction of xylan, lignin and cellulose were modeled separately using DEAM from the mass loss registered *via* TG. In this model, the decomposition of xylan, lignin and cellulose during torrefaction is considered to result from an infinite number of n<sup>th</sup>-order parallel reactions. For a particular i<sup>th</sup> reaction decomposition rate, one has:

$$\frac{d(V_i / V_i^*)}{(1 - V_i / V_i^*)^n} = k_i dt \quad (1)$$

where "i" may contribute to the decomposition of xylan, lignin and cellulose. In eq. (1), V<sub>i</sub> refers to the volatile contribution from reaction "i" during torrefaction of each biomass

model compound and  $V_i^*$  denotes the maximum volatile contribution to be released due to reaction "i". The rate constant of reaction "i" is expressed following an Arrhenius form as:

$$k_i = A_i \exp(-E_i / RT) \quad (2)$$

In which R is the universal gas constant,  $A_i$  is the frequency factor,  $E_i$  is the activation energy and T is the torrefaction temperature. Considering that the number of parallel reactions during the torrefaction of each compound is infinite, the maximum volatile contribution released by each reaction ( $V_i^*$ ) can be considered as a fraction of the total volatiles ( $V^*$ ) with activation energies between  $E_i$  and  $E_i + \delta E_i$ , i.e.,  $V_i^* = V^* f(E_i) \delta E_i$ . Consequently, the total volatiles evolved up to time instant t during torrefaction of each compounds could be expressed as follows [29]:

$$\frac{V^r}{V^*} = 1 - \frac{V}{V^*} = \int_0^\infty f(E) \left[ 1 - (1-n) \int_0^t A \exp(-E / RT) dt \right]^{1/1-n} dE \quad (3)$$

In eq.(3),  $f(E)$  is the distribution of activation energies ( $\int_0^\infty f(E) dE = 1$ ), V is the amount of volatiles evolved up to time t,  $V^*$  is the maximum volatile content of each compound and  $V^r$  is the residual compound volatile which is not released. In the special case where the order of the reaction is equal to one, eq.(3) reduces to:

$$\frac{V^r}{V^*} = 1 - \frac{V}{V^*} = \int_0^\infty f(E) e^{-\int_0^t A \exp(-E/RT) dt} dE \quad (4)$$

Several probability density functions such as Gaussian [18, 29], Weibull [30, 31] and Gamma [32] distributions have been tested for biomass pyrolysis. In the present study, the three -parameter log-normal distribution was used to model the distribution of activation energies of cellulose, xylan and lignin during torrefaction.

$$f(E) = \frac{1}{(E - E_0) \sqrt{2\pi\delta}} \exp\left(-\frac{(\ln(E - E_0) - \mu)^2}{2\sigma^2}\right), \quad E > E_0 \quad (5)$$

$$f(E) = 0 \quad 0 < E < E_0$$

Substituting  $f(E)$  in eqs.(3) and (4) by a log-normal distribution function leads to a double integral for which there is no analytical solution. Alternatively, numerical methods such as recursive adaptive Simpson quadrature technique available in MATLAB was used. There are five unknown parameters in the torrefaction DAEM for cellulose, lignin and xylan, *i.e.*,  $\mu$ ,  $\delta$  and  $E_0$  being the unknowns in the log-normal distribution and  $n$  and  $A$  associated with the order and frequency factor. These torrefaction kinetic parameters were obtained using a simulated annealing optimization technique. This technique is a derivative-free optimization method recommended for finding global optima for DAEM [33].

The DAEM developed for the isothermal torrefaction of cellulose; xylan and lignin could be employed to develop a kinetic model for the torrefaction of aspen and birch. It is assumed that the aspen and birch torrefaction is the result of torrefaction of their constitutive cellulose, xylan and lignin in a way that there is no interaction between components. Consequently, the following equation can be written to relate the torrefaction of aspen and birch at time  $t$  to the torrefaction of their main constituents.

$$\left(\frac{V}{V^*}\right)_{total} = \sum_{i=1}^3 c_i \left(\frac{V}{V^*}\right)_i \quad (6)$$

In eq.(6),  $c_i$  represents the contribution of each compound to the total volatiles release. Using the simulated annealing optimization technique, the optimum values of  $c_i$  which could fit the three component model to the experimental torrefaction data of aspen and birch could be obtained.

## 2.4. Results and discussion

### 2.4.1. Biomass torrefaction

**Lignin torrefaction** Lignin is a stable biopolymer which confers rigidity and strength to cellulose in the plant cell wall [34]. It consists of different proportions of guaiacyl (G), *p*-hydroxyphenyl (H) and syringyl (S) units which are inter-bonded irregularly through different types of linkages; the so-called  $\beta O_4$  linkage being the most frequent one [35-37]. Lignin resistance to decomposition depends on the type of linkages between its building units [36]. The aryl ether linkages (C–O–C) have low disassociation energy while the

biphenyl type linkages are more resistant to breakage [36]. Lignin decomposition takes place at temperatures as low as 150°C, earlier than xylan and cellulose though at quite a tepid rate (Figure 2-1). Lignin decomposition rate increases slowly with temperature until 300°C and reflects in a slight decrease in solids mass yield by increasing the torrefaction temperature (Table 2-2). For instance, lignin torrefaction at 240°C and 280 °C led, respectively, to 89.9% and 87.3% of dry mass yield. The lignin torrefaction is slightly exothermic as can be observed in Figure 2-1.

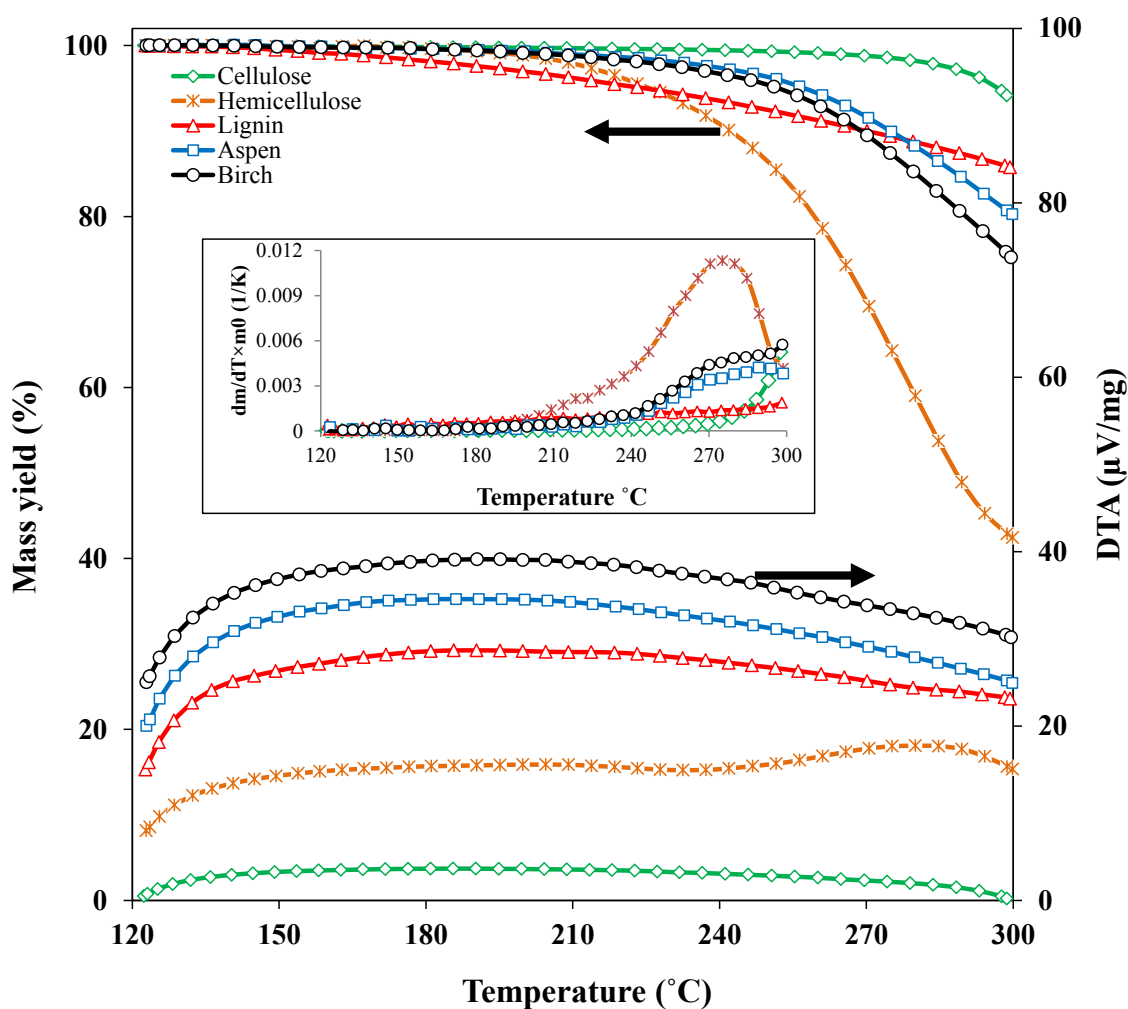


**Figure 2-1:** Mass yield, weight loss derivative and differential thermal analysis of cellulose, xylan, lignin, birch and aspen wood decomposed in thermogravimetric analyzer at 5°C/min heating rate until 300°C.

Torrefaction reduces the O/C and H/C atomic ratios in lignin (Table 2-2). As an example, these ratios are reduced from H/C = 1.12 and O/C = 0.32 in raw lignin to H/C = 0.93 and

O/C = 0.23 for lignin torrefied at 280°C. Also, these ratios are sensitive to torrefaction temperature such that the lignin carbon content increases with increasing the torrefaction temperature, whereas those of oxygen and hydrogen decrease. Reduction in O/C and H/C ratios can also be expected from the analysis of lignin decomposition volatiles at temperatures lower than 300°C. The release of H<sub>2</sub>O, CO<sub>2</sub>, formaldehyde and formic acid with higher O/C and H/C ratios than raw lignin, as a result of the cleavage of OH and carbon groups in the alkyl side chains, explains indeed these ratios' trends in torrefied lignin [36]. The energy density of torrefied lignin at 240°C and 280°C increases by 7 and 9 % (on a dry basis), respectively, due to the reduction in the oxygen content of lignin (Table 2-2). Considering that almost 3% of raw lignin consists of water, the energy density of torrefied lignin improves by *ca.* 10% with respect to that of untreated lignin. Lignin mass loss amounts to 13-17 % due to torrefaction treatment while almost 95% of its energy is preserved in the torrefied lignin product (Table 2-2). According to the van Krevelen diagram, raw lignin shares the fuel characteristics of low rank coals such as lignite or sub-bituminous coal [3].

Lignin FTIR spectra before and after torrefaction at 240°C and 280°C is shown in Figure 2-2. The aromatic nature of lignin due to the guaiacyl (G), *p*-hydroxyphenyl (H) and syringyl (S) units manifests in the vibrational range of 1400-1600 cm<sup>-1</sup> due to the C-C bonds in the aromatic structure [35]. Likewise, both aliphatic and phenolic hydroxyl groups, which prompt hydrogen bonding in the lignin polymeric structure, exhibit a broad hydroxyl peak in the 3200-3600 cm<sup>-1</sup> range [38]. Though torrefaction promotes lignin dehydroxylation and thus a reduction in the extent of hydrogen bonding, such changes are barely visible in terms of broadness and relative of OH vibrational peaks in the FTIR spectra of the torrefied lignin (Figure 2-2). Lignin torrefaction leads to a decrease in the peak intensities near 1035, 1205 and 1265 cm<sup>-1</sup> which are assigned to C-O bond deformations in methoxyl groups, C-O bond stretching in phenolic hydroxyl groups and C-O bond stretching in the ether aromatics, respectively [35].

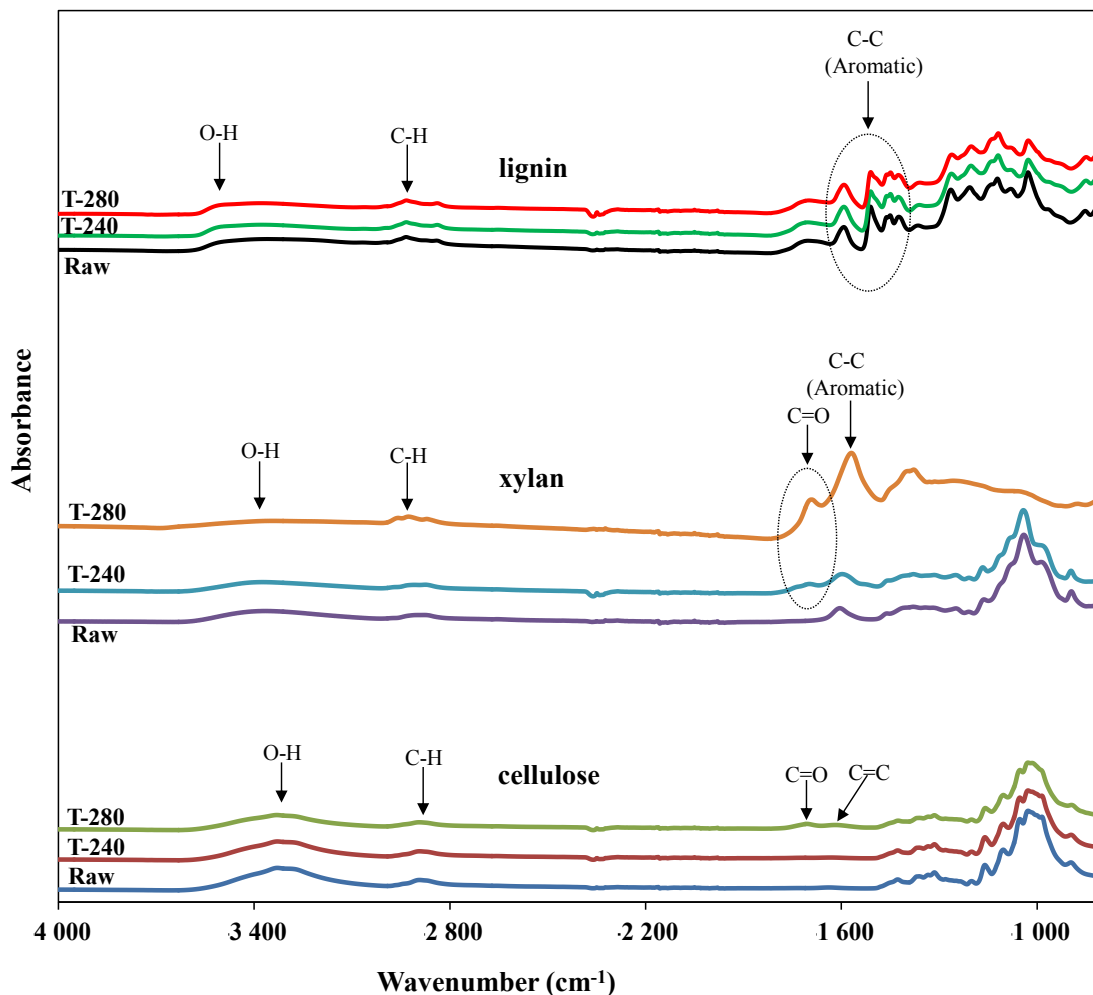


**Figure 2-2** : FTIR spectra of as-received and torrefied cellulose, xylan and lignin samples

Torrefaction reduces the equilibrium moisture content of lignin as well. The major mechanism for water adsorption on lignin is water physisorption *via* hydrogen bonds between water and the free hydroxyl groups in the lignin subunits [39]. Torrefaction also leads to a partial destruction of the free hydroxyl groups in the lignin. This translates in almost 40% reduction in equilibrium moisture uptake of treated lignin as shown in Figure 2-3. Increasing the torrefaction temperature could extend the lignin dehydroxylation causing less water uptake by lignin.

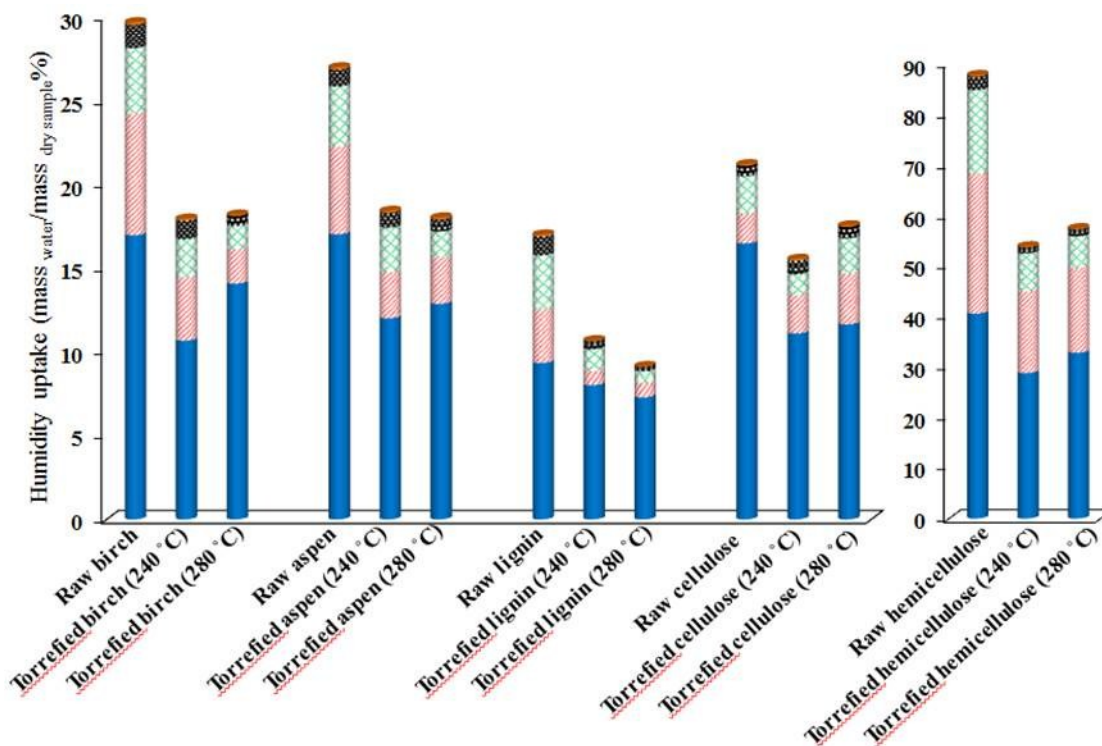


**Figure 2-3:** Humidity uptake of the as-received and torrefied cellulose, xylan, lignin, birch and aspen wood at 25 °C during 5 intervals of 48 h

**Cellulose torrefaction** Cellulose consists of linear chains of several hundreds to thousands of  $\beta$  (1→4) linked D-glucose units [40,41]. Cellulose decomposition commences around 260°C with a rate that increases with temperature (Figure 2-1). Similar to lignin, the torrefaction of cellulose is slightly exothermic. Torrefaction of cellulose at mild and severe conditions led to 1.9% and 9.9% mass reduction as can be seen in Table 2-2. The lower mass yield of torrefied cellulose at mild and severe conditions in comparison with lignin shows its lower rate of decomposition than lignin in the torrefaction temperature range. The mass reduction of mild condition torrefied cellulose is considerably lower than that of torrefied lignin at the same torrefaction conditions (1.9% and 10.1%, respectively). Although cellulose decomposition at mild condition torrefaction was low, a reduction in H/C and O/C ratios in cellulose was observed (Table 2-2). The mild torrefaction led to the reduction in the H/C and O/C ratios of cellulose from H/C = 1.81 and O/C = 0.89 in raw cellulose to H/C = 1.72 and O/C = 0.86 in the mild condition torrefied cellulose. The decrease in the H/C and O/C ratios of mild condition torrefied cellulose could be due to the

intra-molecular elimination of water from the torrefied cellulose. Due to the reduction in the O/C and H/C of torrefied cellulose, the energy density of mild condition torrefied cellulose was increased by 1%. In the case of severe condition torrefied cellulose; the mass yield of torrefied cellulose was more comparable with that of torrefied lignin in the same conditions (90.1% and 87.3 %, respectively, Table 2-2). However, the increase in the carbon content of torrefied lignin at the same conditions is quite higher than that of cellulose (10.8% and 3.7%, respectively). The same trend was also observed for the oxygen and hydrogen content of torrefied cellulose and lignin at severe torrefaction condition. The reduction in the oxygen and hydrogen content of severe condition torrefied cellulose were 2.75% and 3.13% while the oxygen and hydrogen content of lignin reduced by 21.3% and 8.3% respectively. These results indicate that the severe condition torrefaction of cellulose leads to the loss of some carbon in the form of tar. The release of tar could be the main reason for the small increase in the energy density of severe condition torrefied cellulose than lignin. Although some previous torrefaction studies [22,23] indicated that lignin is relatively inert under torrefaction conditions, these results reveal some activity which might not be neglected in comparison to that of cellulose at equal temperature and treatment time.

FTIR spectra of the as-received cellulose and the torrefied cellulose at 240°C and 280°C are shown in Figure 2-2. The changes in the FTIR spectrum of torrefied cellulose at 280°C (severe treatment) is more pronounced than that for 240°C (mild treatment). However, the cellulose main vibrational features are still perceptible after torrefaction. Cellulose torrefaction at 280°C leads to partial dehydroxylation reflecting in decreased intensities of the vibrational peak at 3200-3400  $\text{cm}^{-1}$  (O-H stretching) and 2850-2950  $\text{cm}^{-1}$  (C-H stretching). The FTIR spectrum of torrefied cellulose at 280°C pinpoints to the inception of two new peaks at 1620  $\text{cm}^{-1}$  and 1705  $\text{cm}^{-1}$  attributed, respectively, to unsaturated carbon-carbon (C=C) and carbonyl (C=O) stretching bonds. The dominant mechanism for cellulose decomposition at torrefaction temperatures below 300°C occurs *via* cellulose dehydration [42]. Intramolecular elimination of water from pyranose-ring C<sub>2</sub> and C<sub>3</sub> carbons leads to unsaturated pyranose rings (enol-anhydrocellulose) recognizable from the incipient vibrational peaks at 1705  $\text{cm}^{-1}$  as well as formation of ketone species (keto-anhydrocellulose) as revealed by 1620  $\text{cm}^{-1}$  peak [42]. However, at torrefaction temperatures over 250°C, in addition to dehydration reactions, cellulose degradation could

also cause the formation of some levoglucosan (tar), CO, CO<sub>2</sub> and some acid hydrocarbons [43]. Cellulose torrefaction favors loss of polar hydroxyl groups leading to thus to lesser water adsorption *via* hydrogen bonding. This is confirmed from Figure 2- 3 where nearly 30% reduction in equilibrium moisture content of torrefied cellulose was noted in comparison to moisture uptake of raw cellulose.

**Hemicellulose torrefaction** After cellulose, hemicellulose is the most abundant polysaccharide group in plant [44]. Depending on its source, it could contain different sugar monomers such as glucose, xylose, mannose, galactose, rhamnose and arabinose [45,46]. According to the type of sugar residues, hemicellulose species are grouped into four classes such as xylans, xyloglucans, and mannose and mixed-linkage  $\beta$ -glucans [47]. Each class could be also divided into several subgroups depending on the type and chemical nature of the side chains in their structure. Hardwood hemicellulose is mainly composed of xylan which has a linear polymeric skeleton form constituted of 1-4 linked  $\beta$ -xylano pyranosyl units which could be substituted by O-methyl-D-glucuronic acid residue [48]. The acetyl groups could also substitute the side chains in the xylanopyranosyl units [48,49].

Xylan decomposition initiates at temperatures around 200°C. This temperature is lower than that of cellulose but higher than that of lignin (Figure 2-1). The lack of crystallinity and lower polymerization degree of hemicellulose as compared to cellulose could lead to less thermal and chemical stability for hemicellulose [49]. The rate of xylan decomposition increases with temperature up to a maximum near 280°C (Figure 2-1). Therefore, temperatures lower than 300°C are suitable for xylan torrefaction. Xylan torrefaction under mild and severe conditions also led to mass losses, respectively, 45.5% and 58.8% (Table 2-2). These levels are considerably higher than those of lignin and cellulose for the same torrefaction conditions. It can be concluded that hemicellulose is the component most sensitive to torrefaction treatments. Xylan energy losses due to mild and severe torrefaction represent some 28.9% and 44.1%, respectively (Table 2-2). These loss percentages are lower than the corresponding mass loss percentages in the same conditions. The high oxygen concentration in xylan lowers its energy density and thus its higher heating value. However, torrefaction reduces oxygen concentration in xylan and eventually increases its energy density. The loss of oxygen from xylan upon torrefaction could also be the reason

for its slight exothermic decomposition (Figure 2-1). The H/C and O/C ratios decreased, respectively, from 1.82 and 0.99 in the as-received xylan to 0.92 and 0.51 (mild treatment) and to 0.81 and 0.44 (severe treatment). This was mirrored by an increase of 1.3% and 1.4% of energy density of torrefied xylan, respectively, for the mild and severe treatments.

The FTIR spectra of as-received and torrefied xylan are shown in Figure 2-2. It can be seen that xylan torrefaction at mild conditions could not complete the transformation xylan chemical structure. Xylan decomposition at temperatures lower than 250°C is known to be preceded by the release of water, CO, CO<sub>2</sub>, methanol, aldehyde type and acetic products [48]. The peak at 1690 cm<sup>-1</sup> assigned to carbonyl (C=O) functional groups in the torrefied xylan is a marker to follow the progress of xylan decomposition at 240°C. However, xylan torrefaction at 280°C (severe conditions) leads to major changes in xylan FTIR spectrum (Figure 2-2). Decomposition of xylan at 280°C is believed to lead to cleavage of glycosidic residues and release of furfurals, acids, water and other gases [48]. Peak intensities in the ranges 950-1200 cm<sup>-1</sup> (simple C-O bond stretching) and 3200-3600 cm<sup>-1</sup> (simple O-H bond stretching) decrease considerably upon treatment indicating a loss of these groups. This is unlike the intensity of C=O bond (1690 cm<sup>-1</sup>) which increased due to torrefaction at 280°C. Likewise, xylan carbonization during torrefaction and loss of hydrogen and oxygen led to the formation of aromatics (peaks at 1570 cm<sup>-1</sup>) as also confirmed by the spectral upward drift towards the large-wave number region [50].

Figure 2- 3 shows that the moisture uptake by as-received xylan is considerably larger than that of cellulose and lignin. In addition to the presence of polar hydroxyl and carboxyl groups, the amorphous structure of xylan enhances the adsorption of water in comparison with cellulose. Upon torrefaction treatment, dehydroxylation and decarboxylation of xylan could lead to a considerable decrease in equilibrium moisture content. The equilibrium moisture content of torrefied xylan at 240°C and 280°C is 38% and 35% less than that of non-treated xylan.

**Birch and aspen torrefaction** Thermal decomposition of aspen and birch, as shown in Figure 2-1, started at a temperature as low as 180°C likely *via* lignin decomposition. As discussed earlier, lignin decomposition took place at temperatures as low as 150°C. The rate of aspen and birch decomposition slightly increased from *ca.* 200°C after

decomposition of hemicellulose in birch and aspen was initiated, Figure 2-1. Torrefaction of aspen and birch also exhibits a similar exothermic behavior as expected from the individual exothermic behaviors of their constituents.

The results of elemental analysis as well as mass and energy yields of severe and mild torrefaction of aspen and birch are given in Table 2-2. The mild torrefaction of birch and aspen woods led to the respective mass yields of 86.2% and 86.4%. Increasing the torrefaction temperature also decreased the mass yield of torrefied birch and aspen to the respective values of 74.5 % and 78.5%. The considerable decrease in the mass yield of torrefied birch and aspen by increasing the torrefaction temperature was expected as the main constituents of birch and aspen such as cellulose, hemicellulose and lignin also showed the same trends due to the torrefaction. As can be observed in this Table, the H/C and O/C ratios of the torrefied birch and aspen reduced substantially due to the torrefaction at mild and severe conditions. These reductions in the H/C and O/C ratios of mild condition torrefied birch and aspen led to the 7% and 6% increase in their energy density ratio, respectively. Although birch and aspen are only losing around 14% of their mass, the increase in their energy density is significant. At severe torrefaction conditions, the weight loss of birch and aspen increases to 25.5% and 21.5%, respectively, but their energy density slightly increases about 9% and 7%, respectively, with respect to the non-treated wood samples. This trend could be explained due to the presence of high amount of cellulose in the structure of birch and aspen woods. Almost 58.9% and 51.2% of birch and aspen wood are composed of cellulose [51,52]. As it is observed during the torrefaction of cellulose; the severe condition torrefaction of cellulose leads to the release of some tar compounds such as levoglucosan [43] due to its rapid decomposition causing energy loss during torrefaction. Consequently, although the mass yields of severe condition torrefied birch and aspen woods are much lower than those of mild condition torrefied birch and aspen, the difference in their energy density is not that noticeable.

The equilibrium moisture content of torrefied aspen and birch is reduced by 30% due to torrefaction, Figure 2-3. This trend was expected from investigation of the individual biomass constituents. The loss of some biomass polar groups such as hydroxyl and carboxyl groups during torrefaction is the main reason for the observed behavior. The

equilibrium moisture content of the as-received aspen and birch was 30% and 26%, respectively. Torrefaction reduced its level to 17% for both wood samples. Torrefaction as a strategy to improve resistance to fungal colonization correlates with the reduction of equilibrium moisture content of the treated wood. Since fungal growth on lignocellulosic materials is strongly correlated to water uptake [53]. A significant wood decomposition was reported to occur above the wood fiber saturation point at 25-35% moisture content [54]. It should be mentioned that limited biomass decomposition due to fungal growth may also occur at moisture levels as low as 20% [55]. Certain types of fungi such as *Aspergillus* and *Penicillium* could grow at biomass moisture contents below 15% [56]. Hence, attenuation of microbiological activity in torrefied wood could facilitate its long-time storage.

#### **2.4.2. Kinetic modeling of torrefaction**

In the following section, first a DAEM was developed for the torrefaction of the individual components, xylan and lignin and cellulose. The DAEM parameters for each compound was optimized so that the model fits the TG mass loss profile for each compound versus time at three different torrefaction temperatures, 240°C, 260°C and 280°C. The DAEM optimal parameters for xylan, lignin and cellulose as gathered in Table 2-3. Furthermore, the DAEM was tested for predicting the TG mass loss profiles of torrefied xylan, lignin and cellulose versus time measured at 250°C, 270°C and 290°C. As shown in Figures 2-(4-6), the DEAM fits well the instantaneous of  $V^r/V^*$  obtained by TG experiments in the temperature range of 240-290°C, respectively, for xylan ( $r^2 = 0.99$ ), lignin ( $r^2 = 0.98$ ) and cellulose ( $r^2 = 0.94$ ). In the case of cellulose (Figure 2-6), the DAEM model slightly under-predicts the instantaneous  $V^r/V^*$  profiles at 250°C and 270°C while it shows small over-prediction at 280°C and 290°C. The optimum reaction orders for xylan, lignin and cellulose torrefaction reactions were 3, 2 and 1, respectively.

**Table 2-3:** Optimum values of parameters for the torrefaction kinetic models of cellulose, xylan, lignin, birch and aspen.

Biomass	$E_0$ (kJ/mol)	$\mu$ (kJ/mol)	$\delta$ (kJ/mol)	n	$A_0$ (min <sup>-1</sup> )	$c_1$	$c_2$	$c_3$	$r^2$
Xylan	89.8	3.76	0.05	3	$1.815 \times 10^{12}$	....	....	....	0.99
Lignin	56.3	5.01	0.26	2	$1.516 \times 10^{16}$	...	...	....	0.98
Cellulose	190.8	2.82	0.15	1	$3.804 \times 10^{17}$	...	...	....	0.94
Aspen	.....	.....	.....	.....	.....	0.534	0.235	0.231	0.97
Birch	.....	.....	.....	.....	.....	0.584	0.212	0.204	0.97

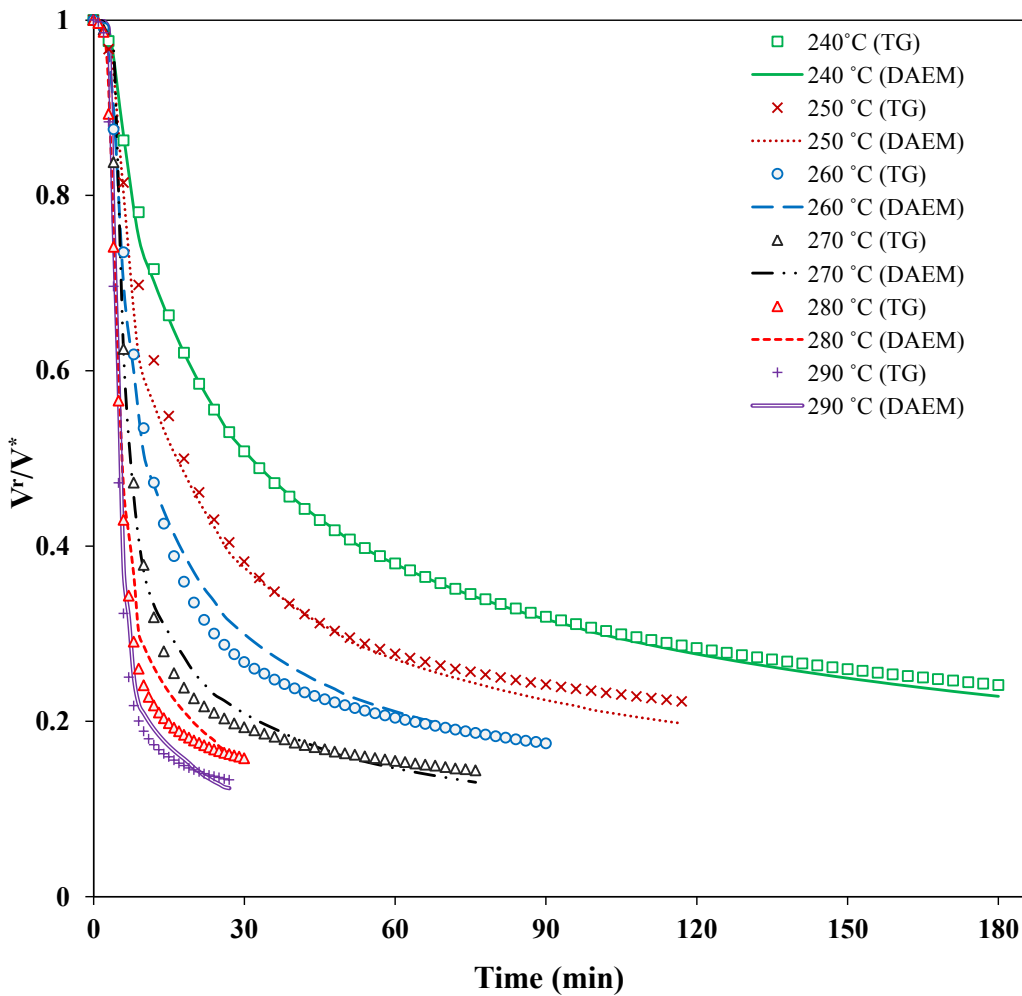


**Figure 2-4:** TG derived profile of volatile release vs. time for xylan torrefaction and DAEM simulated profiles of xylan torrefaction

Figure 2-7 shows the activation energy distribution of cellulose, xylan and lignin torrefaction reactions obtained using the log-normal distribution function. As can be seen, activation energy distributions of xylan, lignin and cellulose torrefaction reactions exhibit their respective maxima at 207 kJ/mol, 132 kJ/mol and 196 kJ/mol.

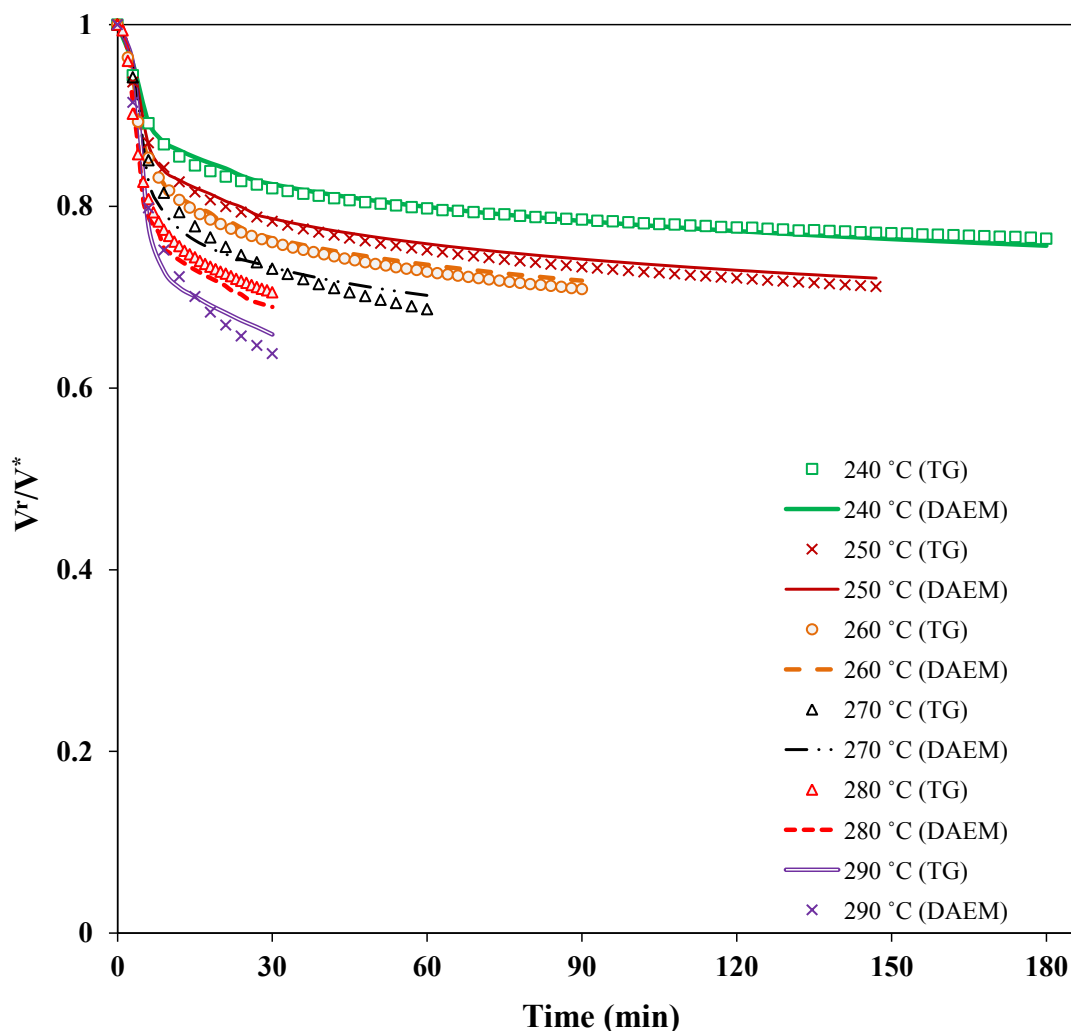


**Figure 2-5:** TG derived profile of volatile release versus time for lignin torrefaction and the DAEM simulated profiles of lignin torrefaction

In the case of cellulose and xylan, the activation energy distributions of the isothermal torrefaction reactions lie within the narrow ranges of 200-220 kJ/mol and 125-145 kJ/mol, respectively, showing that the parallel reactions involved in the cellulose and xylan torrefaction have close activation energies. Narrow ranges of activation energy distribution for non-isothermal pyrolysis of cellulose and hemicellulose have been already reported. Sonobe et al. [17] derived the distribution of activation energy for non-isothermal cellulose

pyrolysis at temperatures as high as 600°C and a narrow range of activation energy (180-190 kJ/mol) was reported with a maximum at 185 kJ/mol.

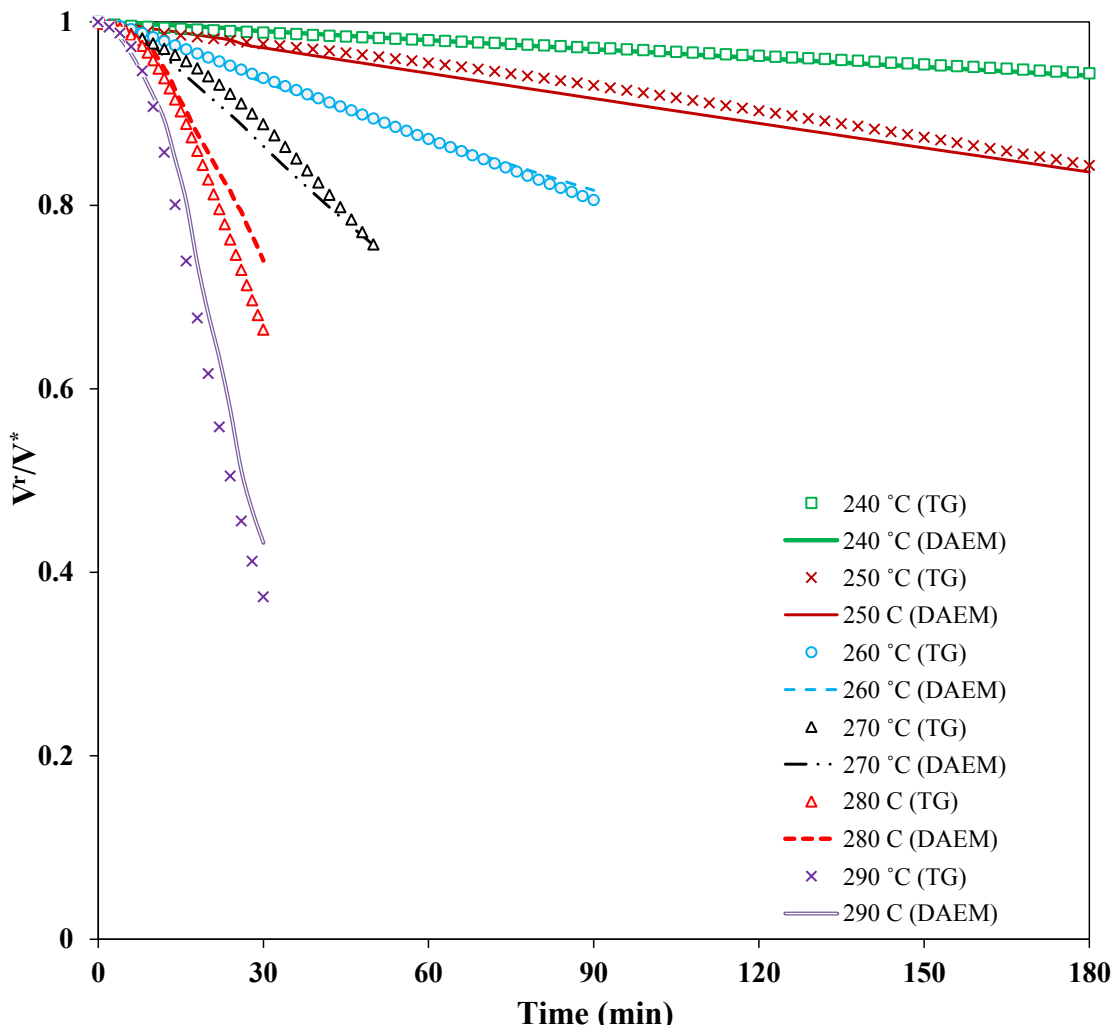


**Figure 2-6:** TG derived profile of volatile release versus time for cellulose torrefaction and the DAEM simulated profiles of cellulose torrefaction

Gasparovic et al. [57] also obtained an activation energy distribution for non-isothermal hemicellulose pyrolysis at temperatures as high as 500°C using Gaussian distribution functions. They stated that the activation energy of hemicellulose pyrolysis is distributed in a range of 124-142 kJ/mol with a maximum at 132.9 kJ/mol. The narrow range of activation energy distribution for cellulose and xylan parallel torrefaction reactions suggests that a distributed activation energy model for xylan and cellulose torrefaction might be regarded as equivalent to that in which only one single reaction represents the overall cellulose and xylan torrefaction.

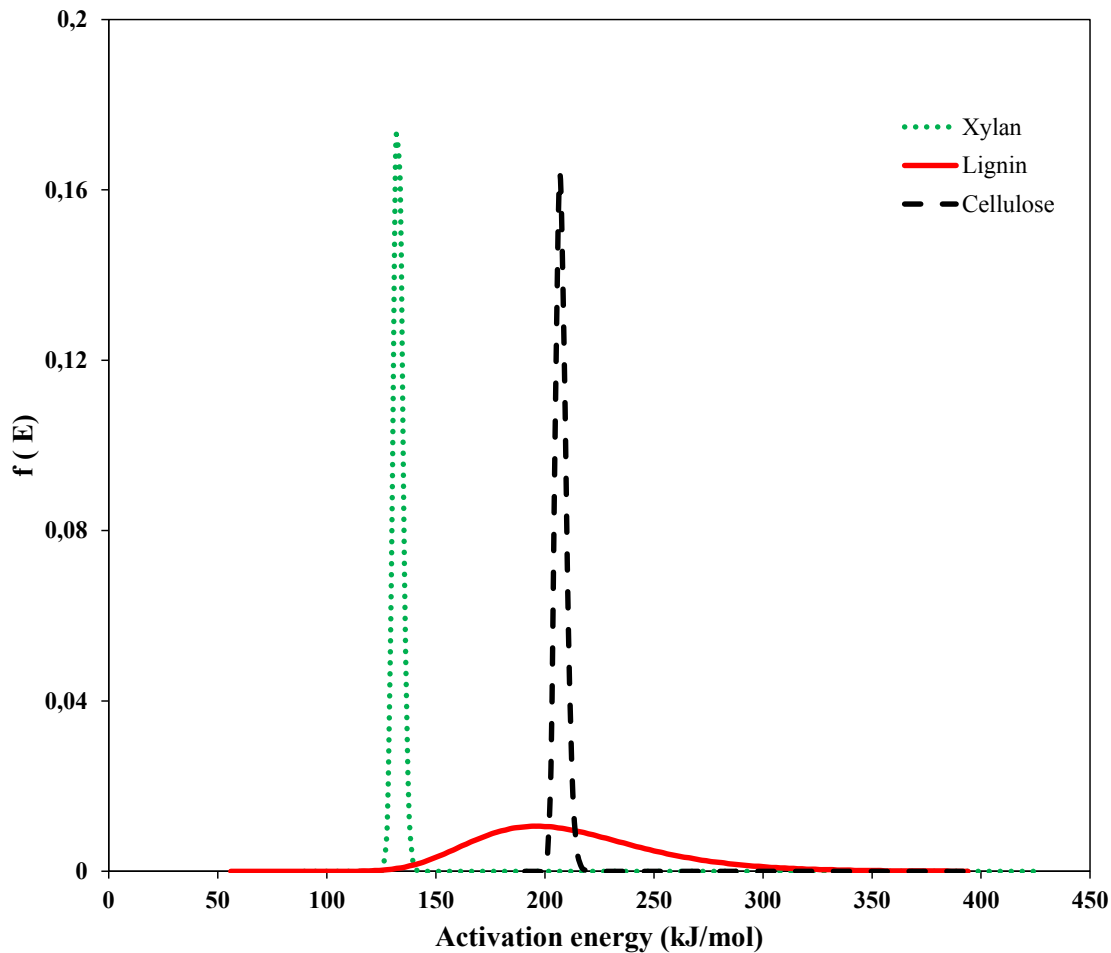


**Figure 2-7:** Distributions of activation energies for xylan, cellulose and lignin

In contrast to cellulose and xylan, the activation energy for the lignin torrefaction reactions is distributed widely in the range of 116- 384 kJ/mol. This is in accordance with the wide activation energy distribution of Alcell lignin pyrolysis (129-361 kJ/mol) reported by Ferdous et al. [58] and Mani et al. [33] also reported a wide range of activation energy for lignin pyrolysis (starting at around 100 kJ/mol) with maximum in the range of 158-170 kJ/mol. The broad activation energy revealed for lignin torrefaction could be due to the presence of various functional oxygen groups in the structure of lignin with different thermal stabilities leading to parallel reactions with broad activation energies. In addition, the presence of alkali and alkaline metals found in the structure of lignin could also catalyse some decomposition reactions during lignin torrefaction, shifting the activation energy distribution of lignin toward lower energies [17].

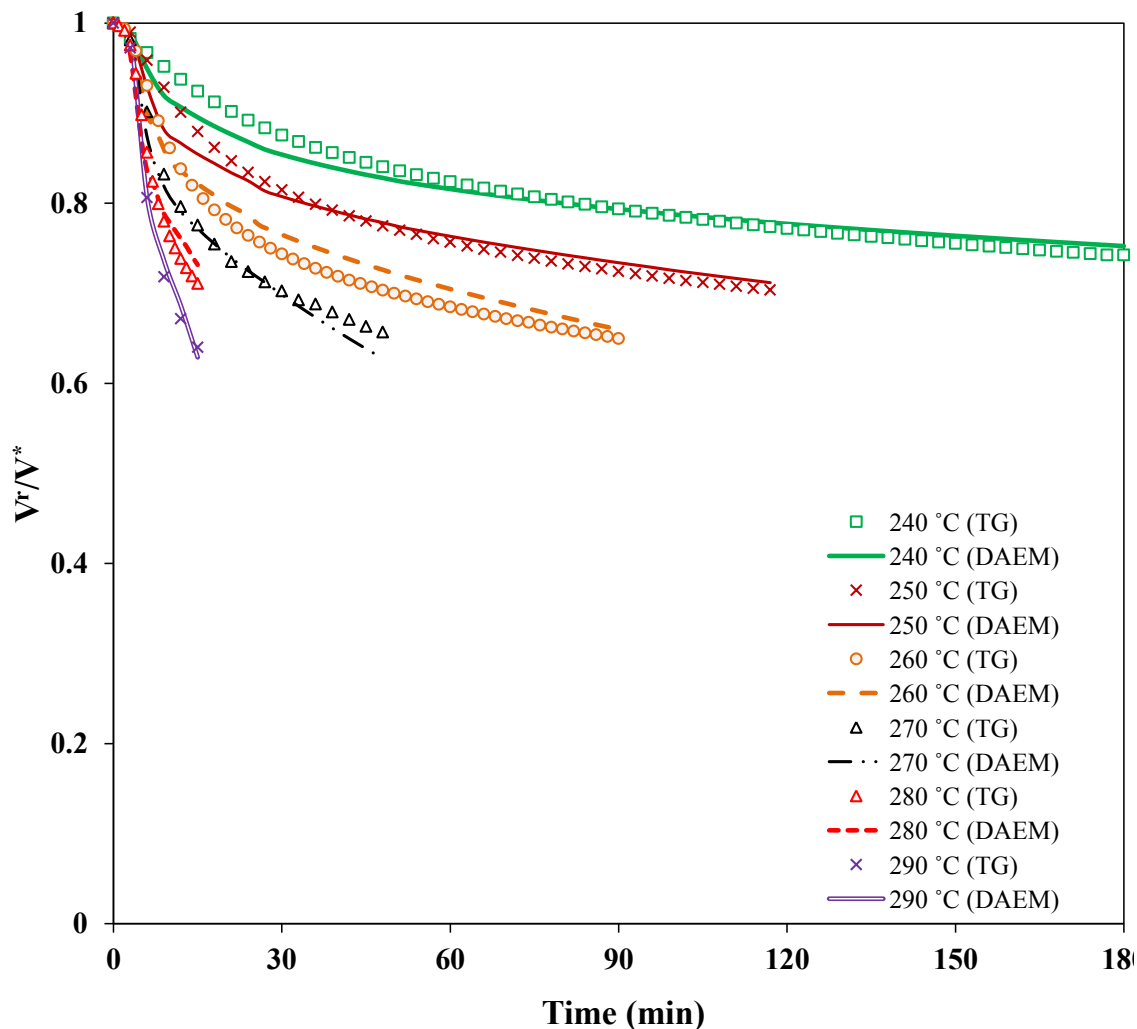


**Figure 2-8:** TG derived profile of volatile release versus time for birch torrefaction and the simulated profiles using optimized  $c_i$  values

To formulate a model for predicting the extent of torrefaction of aspen and birch, it was assumed that their torrefaction is the result of independent torrefaction of their cellulose, hemicellulose and lignin content. Using the optimized value found for the DEAM of cellulose, xylan and lignin torrefaction, the contribution of each compound ( $c_i$  in eq.(6)) was obtained so that the model best fits the TG derived  $V^r/V^*$  profile versus time at 240°C, 260°C and 280°C. These values were used to predict the profile of  $V^r/V^*$  versus time for the torrefied birch and aspen at 250°C, 270°C and 290°C. The model is in agreement with the experimental data within the temperature range from 240°C to 290°C as seen in Figures 2-8 and 2-9 ( $r^2 = 0.97$  for both aspen and birch torrefaction).

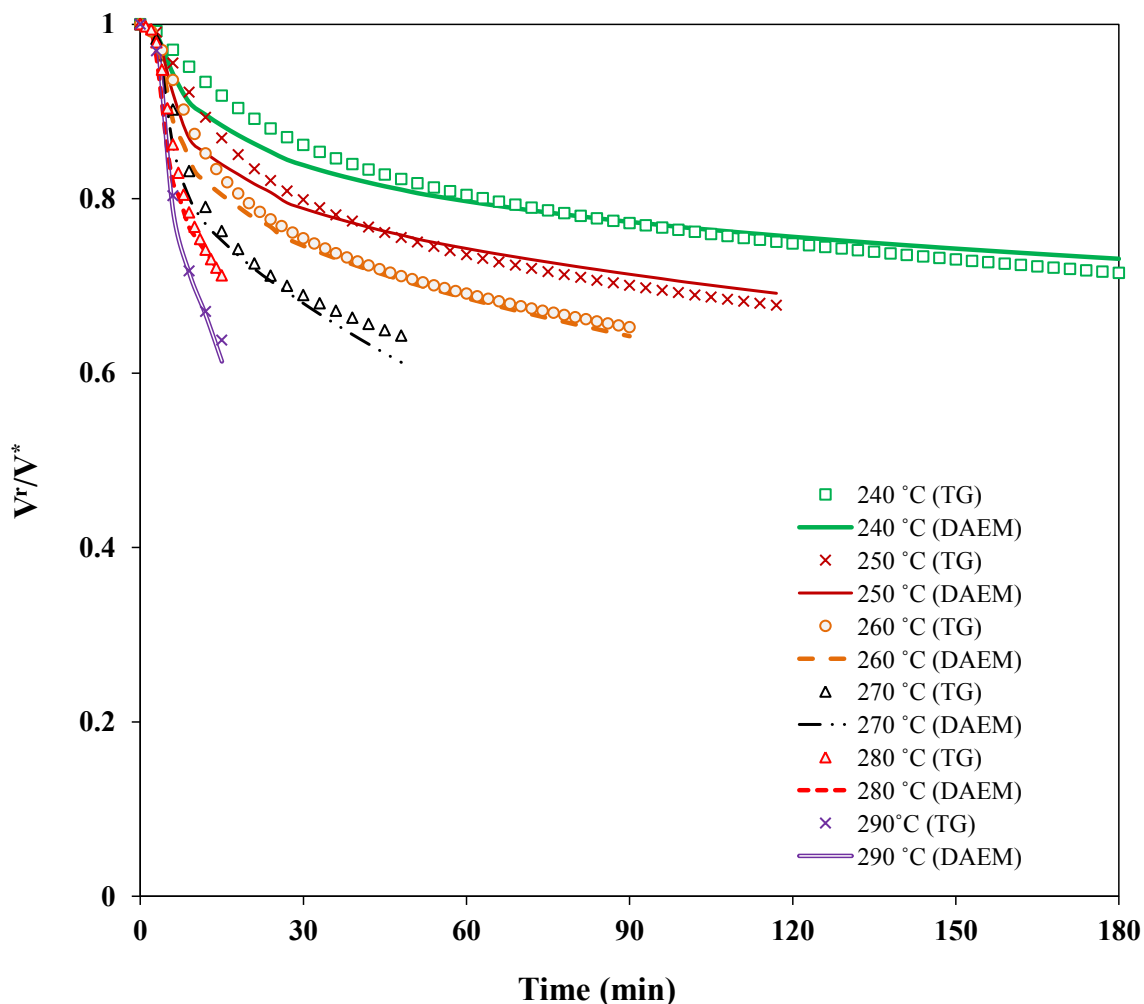


**Figure 2-9:** TG derived profile of volatile release versus time for aspen torrefaction and the simulated trends using optimized  $c_i$  values

The optimized values of cellulose, xylan and lignin contribution ( $c_i$ ) on the volatile release of birch during its torrefaction are 0.584, 0.212 and 0.204, respectively. In the case of aspen wood, the contributions of the abovementioned compounds in the volatile release during torrefaction are 0.534, 0.235 and 0.231, respectively. Note that birch is composed of almost 58.9% of cellulose, 20.3% of hemicellulose and 20.8% of lignin [51] (values normalized on ash- and extractives-free basis). The computed contributions of each compound ( $c_i$ ) on the volatile release of birch are close to the contributions of each compound in the chemical composition of birch wood. From this, it may be concluded that cellulose, xylan and lignin are decomposed independently during birch wood torrefaction and the presence of alkali and alkaline metals mostly found in the lignin structure do not affect the rate of cellulose and hemicellulose torrefaction.

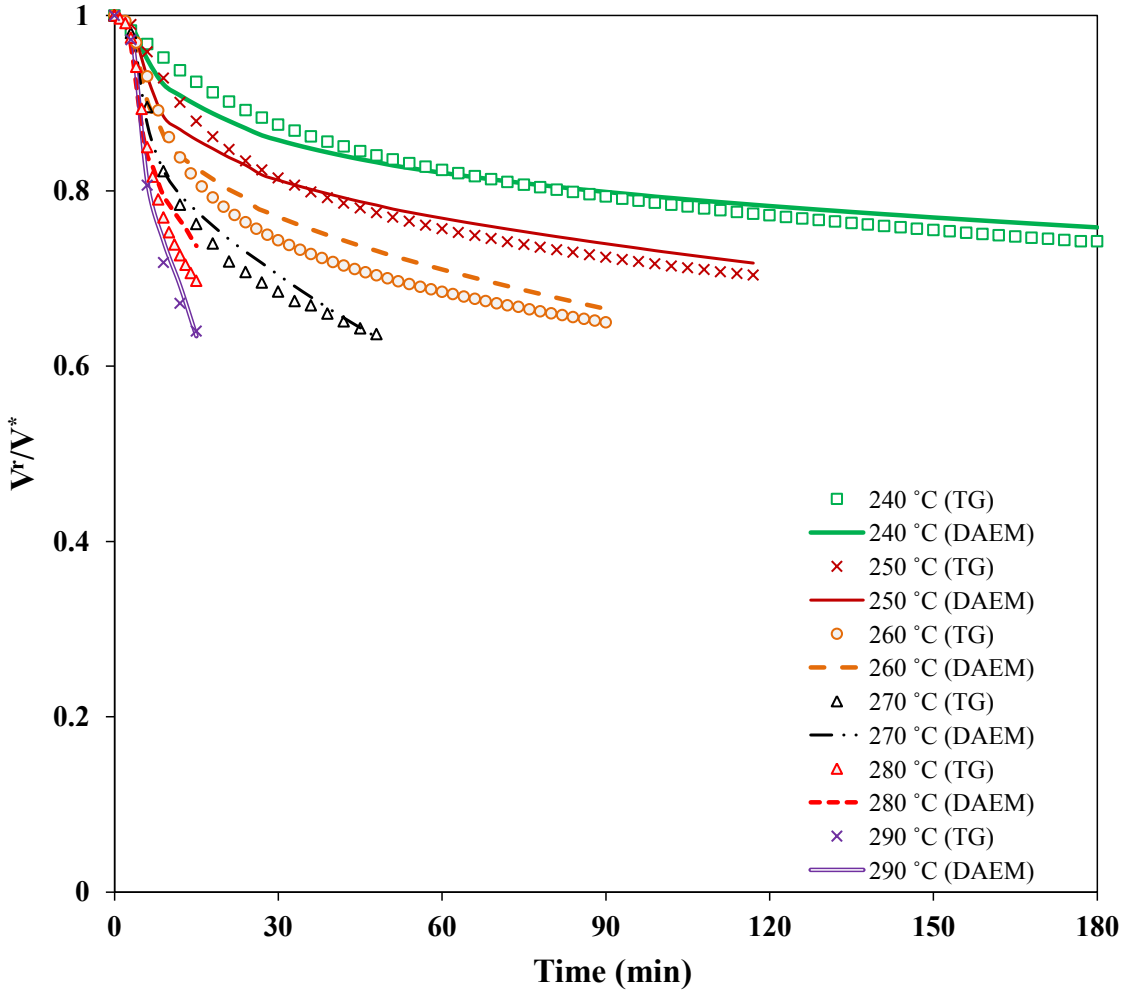


**Figure 2-10:** TG derived profile of volatile release versus time for birch torrefaction and the results of its simulated profiles using the actual chemical composition of birch

As can be seen in Figure 2-10, replacing  $c_i$  in eq. (6) with the chemical composition of birch could fit well the experimentally obtained trends of  $V^r/V^*$  versus time at temperatures from 240-290°C ( $r^2 = 0.97$ ). However, in the case of aspen wood, the calculated values of  $c_i$  for cellulose, xylan and lignin were respectively, 4, 15 and 8%, and different from their contributions in the chemical structure of aspen (51.2% of cellulose, 27.7% of hemicellulose and 21.1% of lignin [52]). Replacing  $c_i$  with the chemical composition of aspen leads to slight under-prediction of  $V^r/V^*$  versus time as shown in Figure 2-11 ( $r^2 = 0.92$ ). The difference between the chemical composition and the values obtained by the kinetic evaluation could be due to the effect of extractives decomposition on the torrefaction weight loss in the interrogated temperature range and/or to errors in the experimental techniques for obtaining the chemical composition of wood samples.

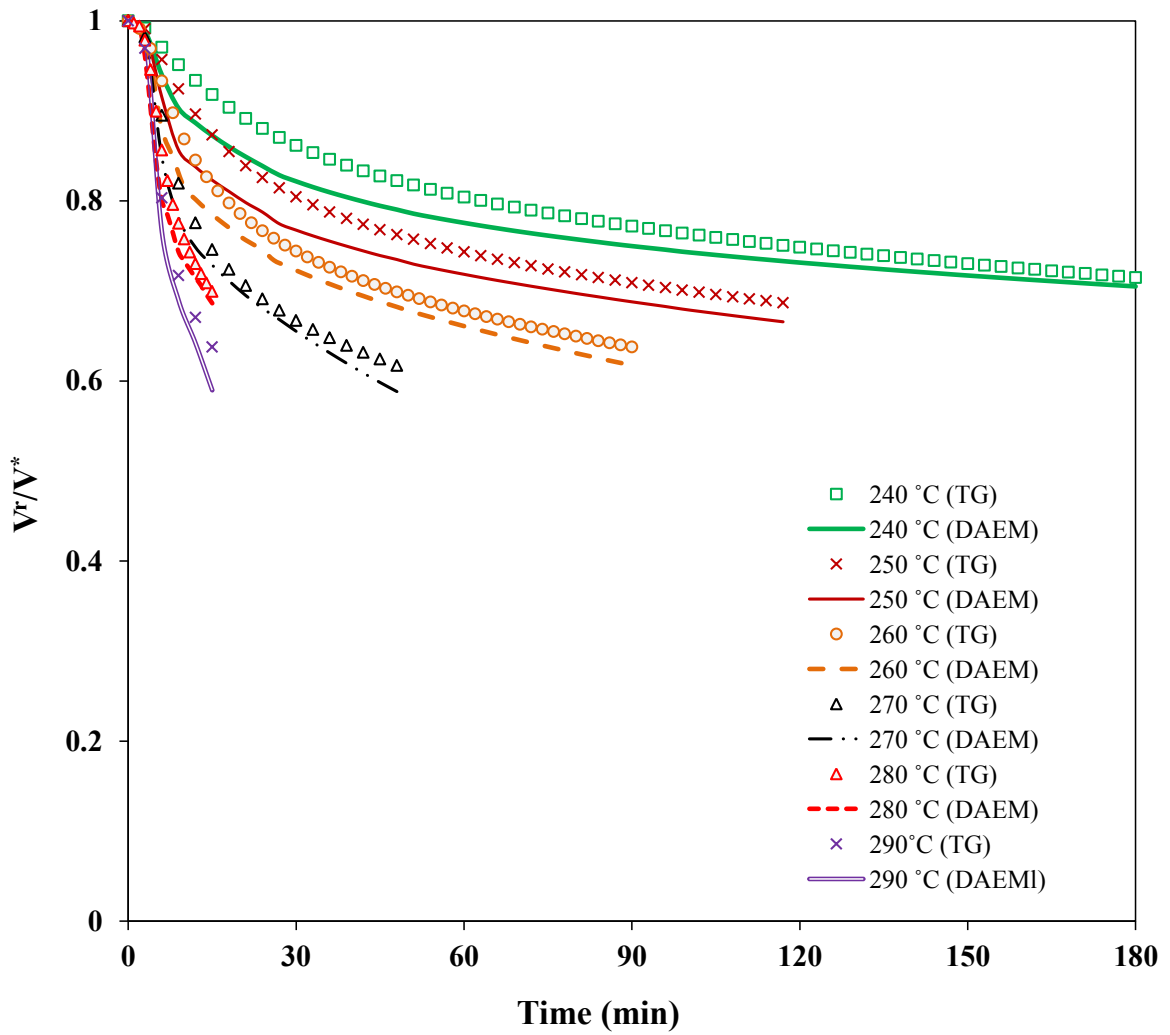


**Figure 2-11:** TG derived profile of volatile release versus time for aspen torrefaction and the results of its simulated profiles using the actual chemical composition of aspen

## 2.5. Conclusion

The torrefaction of two woody biomass samples (aspen and birch) and their main constituents (cellulose, xylan (representative of hemicellulose) and lignin) performed in a fixed-bed reactor showed that torrefaction improves the energy density of aspen and birch by reducing their oxygen and hydrogen content with respect to carbon in the solid residue. The equilibrium moisture content of birch and aspen and of their main constituents (cellulose, xylan and lignin) was reduced by about 30-40% due to torrefaction and was explained according to FTIR spectra to an ameliorated hydrophobicity upon torrefaction of the treated samples. Furthermore, the combined distributed activation energy model with a three-parameter log-normal distribution function could fit the experimental volatile release of xylan and lignin versus time while in the case of cellulose it exhibits some under-prediction. The distributed activation energy models developed for cellulose, xylan and lignin torrefaction could also be combined in three-parallel reaction meta-models for the kinetic description of aspen and birch torrefaction. The model could fit the experimental data of birch and aspen torrefaction in the mild and severe torrefaction conditions.

## 2.6. References

- [1] Berndes G, Hoogwijk M, van den Broek R. The contribution of biomass in the future global energy supply: a review of 17 studies. *Biomass & Bioenergy*. 2003;25:1-28.
- [2] Arena U, Di Gregorio F, Santonastasi M. A techno-economic comparison between two design configurations for a small scale, biomass-to-energy gasification based system. *Chemical Engineering Journal*. 2010;162:580-90.
- [3] van der Stelt MJC, Gerhauser H, Kiel JHA, Ptasinski KJ. Biomass upgrading by torrefaction for the production of biofuels: A review. *Biomass & Bioenergy*. 2011;35:3748-62.
- [4] Pimchuai A, Dutta A, Basu P. Torrefaction of agriculture residue to enhance combustible properties. *Energy & Fuels*. 2010;24:4638-45.
- [5] Deng J, Wang GJ, Kuang JH, Zhang YL, Luo YH. Pretreatment of agricultural residues for co-gasification via torrefaction. *Journal of Analytical and Applied Pyrolysis*. 2009;86:331-7.
- [6] Medic D, Darr M, Shah A, Potter B, Zimmerman J. Effects of torrefaction process parameters on biomass feedstock upgrading. *Fuel*. 2012;91:147-54.
- [7] Hoekman SK, Broch A, Robbins C. Hydrothermal carbonization (HTC) of lignocellulosic biomass. *Energy & Fuels*. 2011;25:1802-10.
- [8] Yan W, Hastings JT, Acharjee TC, Coronella CJ, Vasquez VR. Mass and energy balances of wet torrefaction of lignocellulosic biomass. *Energy & Fuels*. 2010;24:4738-42.
- [9] Sarvaramini A, Gravel O, Larachi F. Torrefaction of ionic-liquid impregnated lignocellulosic biomass and its comparison to dry torrefaction. *Fuel*. 2013;103:814-26.
- [10] Atienza-Martinez M, Fonts I, Abrego J, Ceamanos J, Gea G. Sewage sludge torrefaction in a fluidized bed reactor. *Chemical Engineering Journal*. 2013;222:534-45.
- [11] Yu J, Yao CB, Zeng X, Geng S, Dong L, Wang Y, et al. Biomass pyrolysis in a micro-fluidized bed reactor: Characterization and kinetics. *Chemical Engineering Journal*. 2011;168:839-47.
- [12] Prins MJ, Ptasinski KJ, Janssen F. Torrefaction of wood - Part 1. Weight loss kinetics. *Journal of Analytical and Applied Pyrolysis*. 2006;77:28-34.
- [13] Klein-Marcuschamer D, Simmons BA, Blanch HW. Techno-economic analysis of a lignocellulosic ethanol biorefinery with ionic liquid pre-treatment. *Biofuels Bioproducts & Biorefining-Biofpr*. 2011;5:562-9.
- [14] Chew JJ, Doshi V. Recent advances in biomass pretreatment - Torrefaction fundamentals and technology. *Renewable & Sustainable Energy Reviews*. 2011;15:4212-22.
- [15] Repellin V, Govin A, Rolland M, Guyonnet R. Modelling anhydrous weight loss of wood chips during torrefaction in a pilot kiln. *Biomass & Bioenergy*. 2010;34:602-9.

- [16] Ratte J, Fardet E, Mateos D, Hery JS. Mathematical modelling of a continuous biomass torrefaction reactor: TORSPYD (TM) column. *Biomass & Bioenergy*. 2011;35:3481-95.
- [17] Sonobe T, Worasuwanarak N. Kinetic analyses of biomass pyrolysis using the distributed activation energy model. *Fuel*. 2008;87:414-21.
- [18] Fiori L, Valbusa M, Lorenzi D, Fambri L. Modeling of the devolatilization kinetics during pyrolysis of grape residues. *Bioresource Technology*. 2012;103:389-97.
- [19] de Caprariis B, De Filippis P, Herce C, Verdone N. Double-Gaussian distributed activation energy model for coal devolatilization. *Energy & Fuels*. 2012;26:6153-9.
- [20] Liu XL, Pan G, Wang G, Wen Z. Mathematical model of lump coal falling in the freeboard zone of the COREX melter gasifier. *Energy & Fuels*. 2011;25:5729-35.
- [21] Tiwari P, Deo M. Detailed kinetic analysis of oil shale pyrolysis TGA data. *Aiche Journal*. 2012;58:505-15.
- [22] Meng JJ, Park J, Tilotta D, Park S. The effect of torrefaction on the chemistry of fast-pyrolysis bio-oil. *Bioresource Technology*. 2012;111:439-46.
- [23] Wang CW, Peng JH, Li H, Bi XTT, Legros R, Lim CJ, et al. Oxidative torrefaction of biomass residues and densification of torrefied sawdust to pellets. *Bioresource Technology*. 2013;127:318-25.
- [24] Chen WH, Hsu HC, Lu KM, Lee WJ, Lin TC. Thermal pretreatment of wood (Lauan) block by torrefaction and its influence on the properties of the biomass. *Energy*. 2011;36:3012-21.
- [25] Friedl A, Padouvas E, Rotter H, Varmuza K. Prediction of heating values of biomass fuel from elemental composition. *Analytica Chimica Acta*. 2005;544:191-8.
- [26] Bridgeman TG, Jones JM, Shield I, Williams PT. Torrefaction of reed canary grass, wheat straw and willow to enhance solid fuel qualities and combustion properties. *Fuel*. 2008;87:844-56.
- [27] Bridgeman TG, Jones JM, Williams A, Waldron DJ. An investigation of the grindability of two torrefied energy crops. *Fuel*. 2010;89:3911-8.
- [28] Radmanesh R, Courbariaux Y, Chaouki J, Guy C. A unified lumped approach in kinetic modeling of biomass pyrolysis. *Fuel*. 2006;85:1211-20.
- [29] Cai JM, Liu RH. New distributed activation energy model: Numerical solution and application to pyrolysis kinetics of some types of biomass. *Bioresource Technology*. 2008;99:2795-9.
- [30] Jankovic B. The comparative kinetic analysis of Acetocell and Lignoboost (R) lignin pyrolysis: The estimation of the distributed reactivity models. *Bioresource Technology*. 2011;102:9763-71.
- [31] Cai JM, Liu RH. Parametric study of the nonisothermal nth-order distributed activation energy model involved the Weibull distribution for biomass pyrolysis. *Journal of Thermal Analysis and Calorimetry*. 2007;89:971-5.

- [32] Jankovic B. Identification of the effective distribution function for determination of the distributed activation energy models using bayesian statistics: Application of isothermal thermogravimetric data. *International Journal of Chemical Kinetics*. 2010;42:641-58.
- [33] Mani T, Murugan P, Mahinpey N. Determination of distributed activation energy model kinetic parameters using simulated annealing optimization method for nonisothermal pyrolysis of lignin. *Industrial & Engineering Chemistry Research*. 2009;48:1464-7.
- [34] Saxena D, Stotzky G. Bt corn has a higher lignin content than non-Bt corn. *American Journal of Botany*. 2001;88:1704-6.
- [35] Liu Q, Wang SR, Zheng Y, Luo ZY, Cen KF. Mechanism study of wood lignin pyrolysis by using TG-FTIR analysis. *Journal of Analytical and Applied Pyrolysis*. 2008;82:170-7.
- [36] Pandey MP, Kim CS. Lignin depolymerization and conversion: A review of thermochemical methods. *Chemical Engineering & Technology*. 2011;34:29-41.
- [37] Pinkowska H, Wolak P, Zlocinska A. Hydrothermal decomposition of alkali lignin in sub- and supercritical water. *Chemical Engineering Journal*. 2012;187:410-4.
- [38] Kubo S, Kadla JF. Hydrogen bonding in lignin: A Fourier transform infrared model compound study. *Biomacromolecules*. 2005;6:2815-21.
- [39] Barrera-Garcia VD, Chassagne D, Paulin C, Raya J, Hirschinger J, Voiley A, et al. Interaction mechanisms between guaiacols and lignin: the conjugated double bond makes the difference. *Langmuir*. 2011;27:1038-43.
- [40] Saxena IM, Brown RM. Cellulose biosynthesis: Current views and evolving concepts. *Annals of Botany*. 2005;96:9-21.
- [41] Hoekstra E, Van Swaaij WPM, Kersten SRA, Hogendoorn KJA. Fast pyrolysis in a novel wire-mesh reactor: Decomposition of pine wood and model compounds. *Chemical Engineering Journal*. 2012;187:172-84.
- [42] Scheirs J, Camino G, Tumiatti W. Overview of water evolution during the thermal degradation of cellulose. *European Polymer Journal*. 2001;37:933-42.
- [43] Lin YC, Cho J, Tompsett GA, Westmoreland PR, Huber GW. Kinetics and mechanism of cellulose pyrolysis. *Journal of Physical Chemistry C*. 2009;113:20097-107.
- [44] Schadel C, Richter A, Blochl A, Hoch G. Hemicellulose concentration and composition in plant cell walls under extreme carbon source-sink imbalances. *Physiologia Plantarum*. 2010;139:241-55.
- [45] Peng F, Peng P, Xu F, Sun RC. Fractional purification and bioconversion of hemicelluloses. *Biotechnology Advances*. 2012;30:879-903.
- [46] Arslan Y, Takac S, Eken-Saracoglu N. Kinetic study of hemicellulosic sugar production from hazelnut shells. *Chemical Engineering Journal*. 2012;185:23-8.

- [47] Schadel C, Bochl A, Richter A, Hoch G. Quantification and monosaccharide composition of hemicelluloses from different plant functional types. *Plant Physiology and Biochemistry*. 2010;48:1-8.
- [48] Shen DK, Gu S, Bridgwater AV. Study on the pyrolytic behaviour of xylan-based hemicellulose using TG-FTIR and Py-GC-FTIR. *Journal of Analytical and Applied Pyrolysis*. 2010;87:199-206.
- [49] Spiridon I, Valentin P. Polysaccharides structural diversity and functional versatility. second ed 2004.
- [50] Sharma RK, Wooten JB, Baliga VL, Hajaligol MR. Characterization of chars from biomass-derived materials: pectin chars. *Fuel*. 2001;80:1825-36.
- [51] Li C, Zheng M, Wang A, Zhang T. On-pot catalytic hydrocracking of woody biomass into chemicals over supported carbide catalysts: simultaneous conversion of cellulose, hemicellulose and lignin. *Energy & Environmental Science*. 2011.
- [52] Chauvette G, Heitz M, Rubio M, Khorami J, Chornet E, Menard H. TG DTG as a rapid method for the characterization of solid residues derived from liquefaction of lignocellulosics. *Thermochimica Acta*. 1985;84:1-5.
- [53] Hoang CP, Kinney KA, Corsi RL, Szaniszló PJ. Resistance of green building materials to fungal growth. *International Biodeterioration & Biodegradation*. 2010;64:104-13.
- [54] Verma P, Dyckmans J, Militz H, Mai C. Determination of fungal activity in modified wood by means of micro-calorimetry and determination of total esterase activity. *Applied Microbiology and Biotechnology*. 2008;80:125-33.
- [55] Carll CG, Highley TL. Decay of wood and wood-based products above ground in buildings. *Journal of Testing and Evaluation*. 1999;27:150-8.
- [56] Sauer DB. Effects of fungal deterioration on grain - nutritional-value, toxicity, germination. *International Journal of Food Microbiology*. 1988;7:267-75.
- [57] Gasparovic L, Labovsky J, Markos J, Jelemensky L. Calculation of kinetic parameters of the thermal decomposition of wood by distributed activation energy model (DAEM). *Chemical and Biochemical Engineering Quarterly*. 2012;26:45-53.
- [58] Ferdous D, Dalai AK, Bej SK, Thring RW. Pyrolysis of lignins: Experimental and kinetics studies. *Energy & Fuels*. 2002;16:1405-12.

### **Chapter 3 : Torrefaction of ionic-liquid impregnated lignocellulosic biomass and its comparison to dry torrefaction**

**Résumé** La torréfaction de la biomasse lignocellulosique en tant que prétraitement dans le but d'augmenter la densité énergétique du produit est un prérequis pour plusieurs conversions thermochimiques. Dans cette optique, une voie de torréfaction de la biomasse lignocellulosique est proposée et étudiée en tant qu'alternative aux torréfactions sèches et humides dans l'objectif d'accélérer la vitesse de torréfaction et de potentiellement améliorer la qualité du produit solide torréfié. Des échantillons de bouleau, de tremble ainsi que de la sciure de bois ont été torréfiés entre 240 et 280°C après imprégnation par des liquides ioniques, soient [Emim][OTf], [Emim][BF<sub>4</sub>] et [Hmim][NTf<sub>2</sub>]. Afin de quantifier les bénéfices de la torréfaction utilisant ces liquides ioniques, ce mode de torréfaction a été comparé à une torréfaction sèche en termes de rendements massique et énergétique ainsi que de densité énergétique, d'hydrophobicité et de gain en humidité du produit solide torréfié. À temps de réaction et températures égaux, les vitesses de décomposition du bouleau, du tremble ainsi que de la sciure de bois imbibés de liquide ionique se sont avérées considérablement plus élevées que leurs homologues de la torréfaction sèche. Les liquides ioniques ont aussi mené à une augmentation de la densité énergétique des échantillons ainsi qu'à une plus grande hydrophobicité, se traduisant par une réduction de 40-45% dans leur gain et humidité ultime. Finalement, les résidus de cendre s'accumulant dans les liquides ioniques réutilisés après plusieurs cycles de torréfaction ont été investigués en tant que facteurs potentiellement responsables de la décomposition des liquides ioniques.

**Abstract** Torrefaction of woody biomass as a thermal pretreatment to increase biomass energy density is prerequisite to many thermochemical conversions. An ionic-liquid (IL) biomass torrefaction route was proposed and investigated as an alternative to conventional dry and wet torrefaction for enhancing the rate of biomass torrefaction and for potentially improving the quality of torrefied solid products. Ionic liquid-impregnated aspen, birch and sawdust were torrefied in the 240-280°C temperature range using [Emim][OTf], [Emim][BF<sub>4</sub>] and [Hmim][NTf<sub>2</sub>] ILs. To assess the benefits of IL impregnated biomass, dry and IL torrefaction were compared in terms of mass yield, energy density, energy yield, hydrophobicity and ultimate moisture uptake of torrefied solid products using thermogravimetry and fixed-bed setups. At equal reaction time and treatment temperature, the decomposition rates of birch, aspen and sawdust in ILs were considerably enhanced compared to their dry torrefaction counterparts. IL torrefaction led to increased energy density of treated aspen, birch and sawdust solids alike, whereas improved hydrophobicity of IL-torrefied solids translated in nearly 40-45% reduction of their ultimate moisture uptake. Finally, char and ash leftovers building up in spent ILs after repeated IL torrefaction cycles were specifically addressed as potential factors responsible for IL decomposition.

### 3.1. Introduction

Biomass as a carbon-neutral renewable energy source is increasingly receiving attention for the essential role it is anticipated to play in the world's energy [1]. However, raw biomass as a fuel features low calorific value and high oxygen-to-carbon ratio (O/C), and, being hygroscopic, high moisture besides producing smoke during combustion [2,3]. Dry and wet torrefaction of biomass are the thermal pretreatments often used to address these limitations to improve biomass properties [3, 4]. Dry torrefaction consists of slowly heating biomass in an inert atmosphere from 200°C to 300°C [5]. Wet torrefaction is a hydrothermal pretreatment wherein biomass is subjected to pressurized liquid water up to 5 MPa and 260°C for ca. 60 min [6, 7]. Both processes yield hydrophobic solid products with lower moisture content and O/C ratio, and higher energy density than raw biomass making them suitable biofuels [6-10]. Though at the expense of an elevated pressure, wet torrefaction produces solids with energy density greater than dry torrefaction [6]. To limit tar production and maximize energy for a given mass yield, dry biomass torrefaction requires capping temperatures below 300°C. Also, depending on biomass particle sizes, the residence time required for dry torrefaction varies widely, typically from 10 min for finely ground biomass particles to several hours for coarser bits thus all in all reflecting in large variability in reactor sizes [11].

The initial stage in biomass torrefaction involves hemicellulose decomposition which occurs extensively around 250-260°C [12]. But unlike hemicellulose, lignin and cellulose barely decompose below these temperatures contributing to a minor mass loss. The second stage in biomass torrefaction involves decomposition of cellulose which is less reactive than hemicellulose and rate-controlling below 300°C [11]. Water, CO and CO<sub>2</sub> evolve subsequent to the breakdown of hydrogen bonds within or between cellulose molecules resulting in a change in cellulose super-molecular structure shortening its length from 10<sup>4</sup> down to ca. 200 [13]. Increasing torrefaction temperature over 270°C positively affects the rate of cellulose decomposition [12].

Different classes of solvents such as mineral acids and ionic liquids have proved capable of disrupting the hydrogen bonds between the different polysaccharide chains. Solvent

exposure results in decreasing material compactness and in increasing sensitivity to hydrolysis of the carbohydrate fraction [14]. Such features are good omen for testing solvents to host biomass torrefaction. Doping cellulose with mineral acids such as H<sub>2</sub>SO<sub>4</sub>, HCl and HNO<sub>3</sub> is known to considerably increase the rate of cellulose decomposition and to lower the required decomposition temperature [15]. However, corrosiveness of most acids as well as their volatility, which leads to poisonous emanations [16] at elevated temperatures, make them unappealing for use in biomass torrefaction. Unlike mineral acids, room-temperature ionic liquids (ILs) feature very low vapor pressures, low flammability and high thermal stability [17,18]. ILs are also good heat-transfer media which may be a desirable characteristics to enhance heat transfer around the solid biomass [19]. Consequently the potential of ionic-liquids (ILs) to enhance the rate of biomass torrefaction and to improve the quality of torrefied solid products is interesting to be studied.

Torrefaction of three woody biomass varieties impregnated with three imidazolium-cation based ILs, namely, [Emim][OTf]: 1-ethyl-3-methyl imidazolium trifluoromethanesulfonate, [Emim][BF<sub>4</sub>]: 1-ethyl-3 methylimidazolium tetrafluoroborate and [Hmim][NTf<sub>2</sub>]: 1-hexyl-3-methylimidazolium bis(trifluoro methylsulfonyl)imide is studied in this work. These ILs were screened on the basis of biomass dissolution studies at *mild* temperatures which revealed these ionic liquids exhibit weak interactions with biomass [20] in addition to superior thermal stability at the tested torrefaction temperatures (240-280°C). Imidazolium halide-based ionic liquids, e.g., [Emim][Cl] or [Bmim][Cl], were not considered instead despite their featured superior biomass dissolving power. Too much stimulated biomass solubility by the high torrefaction temperatures was feared to do away with any residual biochar from recovery. Besides halide-bearing ILs showcase a low thermal stability and toxicity preventing their consideration for the present biomass torrefaction experiments [20-23]. [Emim][OTf] and [Emim][BF<sub>4</sub>] are hydrophilic and their onset decomposition temperature exceeds 400°C [24]. They also have shown ability to dissolve mono- and disaccharides such as glucose and sucrose [25] owing to hydrogen bond interactions via numerous carbohydrate hydroxyl groups [18]. However, dissolution in these ionic liquids of polysaccharides, such as cellulose, is low at mild temperature (up to 110°C) due to the presence of large non-coordinating anions and their relatively low hydrogen bond basicities [20]. Unlike [Emim][OTf] and [Emim][BF<sub>4</sub>], [Hmim][NTf<sub>2</sub>] is hydrophobic with onset

decomposition temperatures above 400°C [26]. [Hmim][NTf<sub>2</sub>] has large anion and cation sizes which makes it a poor solvent for cellulose and lignin dissolution [20].

## 3.2. Experimental

### 3.2.1. Materials

[Emim][OTf], [Emim][BF<sub>4</sub>] and [Hmim][NTf<sub>2</sub>] ionic liquids with 99% purity were purchased from Io-li-tech. Acidity tests using aqueous 10 vol% [Emim][OTf] mixtures led to pH = 2.5 revealed the presence of acidic residual impurities in the Io-li-tech ionic liquid. Such acidic impurities may enhance hydrogen bond breakup in the cellulose structure. Hence to distinguish the effects of acidic impurities and ionic liquid itself on biomass torrefaction, [Emim][OTf] free from acidic impurities was also purchased from Sigma Aldrich with purity >98 %. The Io-li-tech and Sigma ILs are designated as [Emim][OTf]<sub>i</sub> and [Emim][OTf]<sub>s</sub>.

Powdered samples of cellulose (Avicel®PH-101), xylan hemicellulose representative (X0502) and lignin (37059-lignin, alkali), purchased from Sigma Aldrich and three types of woody biomass (trembling aspen, birch and sawdust) were torrefied. The proximate analysis of sawdust, birch and aspen is given in Table 3-1.

**Table 3-1:** Proximate analysis in mass % of sawdust, birch and aspen wood

	Humidity	Volatile (dry basis)	Fixed carbon (dry basis)	Ash (dry basis)
Sawdust	5.3	79.6	16.1	4.3
Birch	5.5	89.4	9.8	0.7
Aspen	4.8	87.5	12	0.5

The sawdust was prepared using biomass pellets supplied from Enerkem Company (Québec). This sample was a mixture of different woody biomass residues which is used for gasification purposes. All the samples were first grinded and then sieved to isolate the 1-2 mm size of particles. Each biomass type was impregnated with each of the three ionic liquids. Impregnation of biomass with ionic liquid was carried out under mixing at 60°C to maximize ionic liquid absorption while preventing biomass dissolution [20]. The biomass samples were weighted regularly to estimate the amount of absorbed ionic liquid.

Absorption was dependent on the type of biomass and ionic liquid but was maximum with [Emim][OTf]<sub>1,5</sub>. The mass ratio of absorbed ionic liquid to biomass was in the range 1.5-2, 1.8-2.2 and 1.5-1.9 for birch, aspen and sawdust, respectively, whereas it was fixed to 2 for cellulose, xylan and lignin.

### **3.2.2. Weight loss and volatiles via thermogravimetry & mass spectrometry analysis**

A thermogravimetric analyzer (TG) (Perkin Elmer Lab System Diamond TGA-DTA) coupled with a quadrupole mass spectrometer (MS) (Thermostar Prisma QMS200, Pfeiffer Vacuum) was used to monitor the weight loss and volatiles released, and the temperature,  $T_s$ , at which biomass decomposition starts during IL and dry torrefaction. The samples first were dried in TG at 120°C for 30 min and then submitted to prograde heating at 5°C/min under N<sub>2</sub> flow (100 NmL/min) until 280°C where they were maintained for 60 min. The gases released from biomass decomposition were identified via MS. Special care was taken in choosing the sample containers to prevent corrosion by ionic liquids. Three different containers were tested, i.e., aluminum, alumina and platinum. Although aluminum was neutral to [Hmim][NTf<sub>2</sub>] and [Emim][OTf], a remarkable corrosion in the presence of [Emim][BF<sub>4</sub>] was observed. Aluminum catalyzed the decomposition of BF<sub>4</sub> anions especially in the acidic media leading to the formation of fluoroaluminate complexes [27]. The weight of aluminum container after contacting with [Emim][BF<sub>4</sub>] was lower than originally unveiling the corrosive nature of [Emim][BF<sub>4</sub>]. No change in the weight of alumina and platinum containers were observed in the presence of all three tested ionic liquids. Also, preliminary ionic liquid high-temperature degradation tests performed in both containers showed unchanged IL degradation rates. Consequently, alumina and platinum containers had no interaction with the tested ILs. Alumina pans owing to a higher capacity were chosen for the experiments.

### **3.2.3. Fixed-bed torrefaction setup**

As the amount of residual solid products recovered following TG analyses was too low for further quantifications, a fixed-bed torrefaction reactor was designed to obtain sufficient torrefied materials for complementary investigations on solid products. Furthermore, TG analysis revealed a more remarkable effect of [Emim][OTf] on the decomposition rate and

$T_s$  for birch, aspen and sawdust samples. Only this latter ionic liquid was tested for the fixed-bed reactor tests. The bench scale torrefaction unit (Figure 3-1) consisted of a stainless steel (SS) tube (ID. 34 mm, length 70 cm) placed inside an induction coil. A biomass sample 0.6 g in mass either impregnated with ionic liquid or not (dry torrefaction) was held atop of a steel grid located in the middle of the stainless steel tube to act as a support for the biomass bed. The reactor was heated through a 15 cm long coil connected to a 18 kW induction power supply for heating the stainless steel tube via AC magnetic field then heating in turn the biomass layer through radiation and conduction.

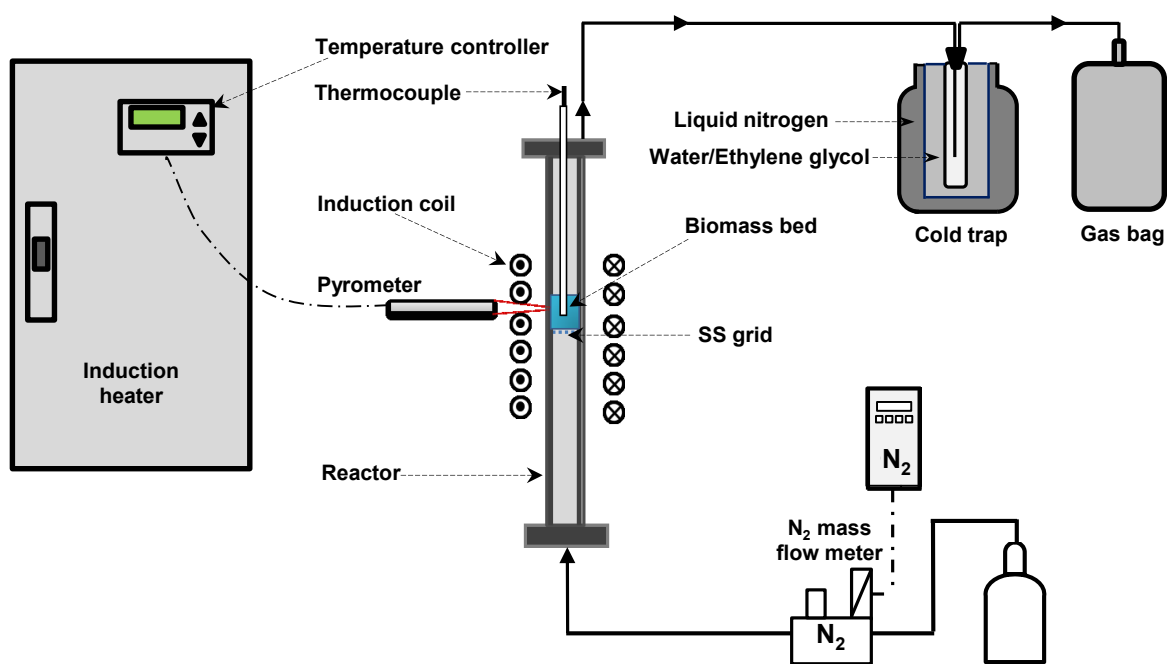


**Figure 3-1:** Schematics of fixed-bed reactor setup used for biomass torrefaction

The biomass bed temperature was raised from the ambient to the target temperature (240-280°C) in less than 10 s and then the samples were kept at final temperature for specified time duration (10-60 min). The SS tube temperature was controlled by a fiber optic pyrometer connected to a temperature controller to meter the induction-heater power. Temperature was also measured through a K type thermocouple inserted in the center of the biomass bed. The difference between the bed temperature and SS tube surface at steady state condition never exceeded 5°C. In order to keep the reactor environment inert and remove the volatiles from the reactor to the cold trap, a continuous flow (100 mL/min) of

N<sub>2</sub> passed through the bed. The cold trap consisted of a tube inserted inside a bigger one filled with a 70 mass % ethylene glycol aqueous solution. This was then placed inside a container full of liquid N<sub>2</sub>. The freezing point of this aqueous ethylene glycol solution allowed a minimal interior temperature of -55°C to be reached. This temperature was low enough to ensure maximum separation of condensable gases while sparing CO, CO<sub>2</sub> and methane which were transferred to a gas bag until the completion of the test.

#### 3.2.4. Characterization of solids

The torrefied biomass was removed from the steel grid, placed on a filter paper and washed for 30 min with approximately 200 mL of distilled water using vacuum filtration. The recovered solid was dried in an oven at 110°C for 12 h and then weighted to assess the total mass loss. The water and ionic liquid filtrate was once again filtered using syringe filters to remove the smaller solid impurities. The clear solution was subsequently transferred into a flask wherefrom water was evaporated under vacuum in a rotating evaporator with a 120°C Calflo AF bath. The ionic liquid leftover was then weighted.

Solid products from torrefaction were further analyzed to investigate their properties after thermal treatment. The C, H, N, S sample contents were measured using a Fisons EA 1108CHNS elemental analyzer. All measurements were duplicated and their average was reported. The higher heating value (HHV) of the samples before and after torrefaction was inferred using Friedl et al. [28] equation based on carbon, hydrogen and nitrogen content of biomass. This equation is considered enough robust for such estimations as it was derived on the basis of 122 biomass samples with less than 2 wt% error [29,30]:

$$\text{HHV (kJ/kg)} = 3.55 \cdot \text{C}^2 - 232 \cdot \text{C} - 2230 \cdot \text{H} + 51.2 \cdot \text{C} \cdot \text{H} + 131 \cdot \text{N} + 20600$$

where C, H and N represent carbon, hydrogen, and nitrogen mass %, respectively.

The effect of torrefaction treatments was evaluated in terms of hydrophobicity, ultimate moisture uptake,  $U_{\text{MU}}$ , i.e., percent mass water uptake on a dry biomass basis), and contact angle measurements. The ultimate moisture uptakes,  $U_{\text{MU}}$ , of raw and torrefied biomass samples were obtained by putting 300 mg of the samples in a vapor-saturated bath controlled at 30°C. To eliminate pre-existing moisture before  $U_{\text{MU}}$  measurements, all the

samples were dried overnight at 110°C. They then were placed in a bath for four days and their weight gain was measured after all the samples reached equilibrium. The water contact angles of raw and torrefied biomass were also measured using an optical contact angle analyzer (OCA 15 EC Plus, Dataphysics) using the sessile drop method. The system employed a high-resolution camera and specific software developed for OCA 15 EC Plus to capture and analyze the contact angle on very small and curved surfaces.

### **3.3. Results & discussion**

#### **3.3.1. IL and dry torrefaction, TG-MS studies**

IL and dry torrefaction of cellulose, hemicellulose and lignin individual components could shed insights on the mechanisms contributing to biomass torrefaction as these make up, respectively, 55-60 wt%, 20-25 wt% and 15-20 wt% of the biomass samples [31,32]. Moreover, pyrolysis kinetic studies have shown that the rate of biomass decomposition stems from parallel thermal decomposition of each model component [33]. Dry and IL torrefaction of cellulose, hemicellulose and lignin model compounds were performed in TG-MS to determine both  $T_s$  and weight loss profiles. A 2:1 IL-to-model component ratio was used in the latter torrefaction tests. The samples were dried in TG at 120°C for 30 min before their prograde heating at 5°C/min under 100 NmL/min N<sub>2</sub> flow until 280 °C where they were kept for 1 h.

##### **3.3.1.1 Torrefaction of model compounds**

Cellulose thermal decomposition for both IL and dry torrefaction is shown in Figure 3-2. Torrefaction of cellulose in [Emim][OTf]<sub>S</sub> and [Emim][OTf]<sub>I</sub> led to  $T_s$  of 190 and 220°C, respectively, while  $T_s$  for dry torrefaction was much higher at 260°C. The rate of thermal decomposition of cellulose was also markedly increased in [Emim][OTf]<sub>I</sub> and [Emim][BF<sub>4</sub>]. The time required for dry torrefaction of cellulose to reach 70% of solid product yield was 22 min. Under the applied heating program, this time was reduced to 8 and 10 min, respectively, for cellulose torrefied in [Emim][BF<sub>4</sub>] and [Emim][OTf]<sub>I</sub>. Cellulose torrefaction in [Emim][OTf]<sub>S</sub> featured a slower decomposition step leading to 28% mass loss and followed by a faster step contributing an additional 51%. Cellulose

torrefaction in [Hmim][NTf<sub>2</sub>], in comparison with dry torrefaction barely altered both the decomposition rate and T<sub>s</sub>. Such indifference can be attributed to [Hmim][NTf<sub>2</sub>] bulkier anions and cations resulting in less efficient interactions with cellulose as compared to [Emim][BF<sub>4</sub>] and [Emim][OTf].

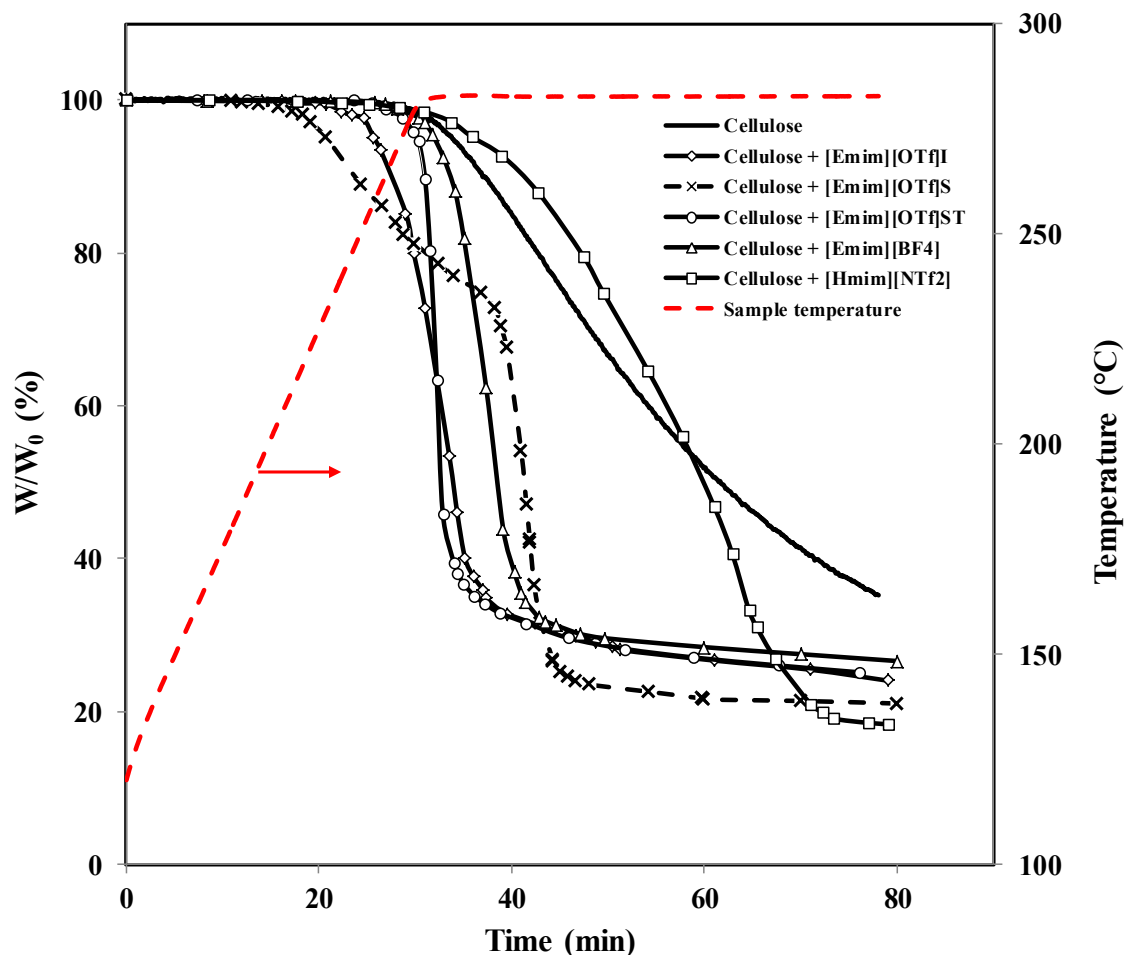


**Figure 3-2** : Mass loss profile of cellulose ionic liquid and dry torrefaction

Acceleration of cellulose torrefaction in [Emim][OTf]<sub>I,S</sub> and [Emim][BF<sub>4</sub>] was also corroborated via MS monitoring of CO<sub>2</sub> and H<sub>2</sub>O release accompanying mass losses. Figure 3-3 shows the evolution of CO<sub>2</sub> during IL and dry torrefaction of cellulose. Pure ionic liquids subjected to the same TG heating program released almost no CO<sub>2</sub>. Consequently, the detected CO<sub>2</sub> was plausibly arising from thermal decomposition of cellulose and not from ionic liquids. As observed, CO<sub>2</sub> was released at temperatures as low as 150°C for cellulose torrefied in [Emim][OTf]<sub>S</sub>. In both cases of [Emim][OTf]<sub>I</sub> and

[Emim][BF<sub>4</sub>], CO<sub>2</sub> release started near 200-210°C while the onset of CO<sub>2</sub> release for dry torrefaction of cellulose occurred at 260°C.

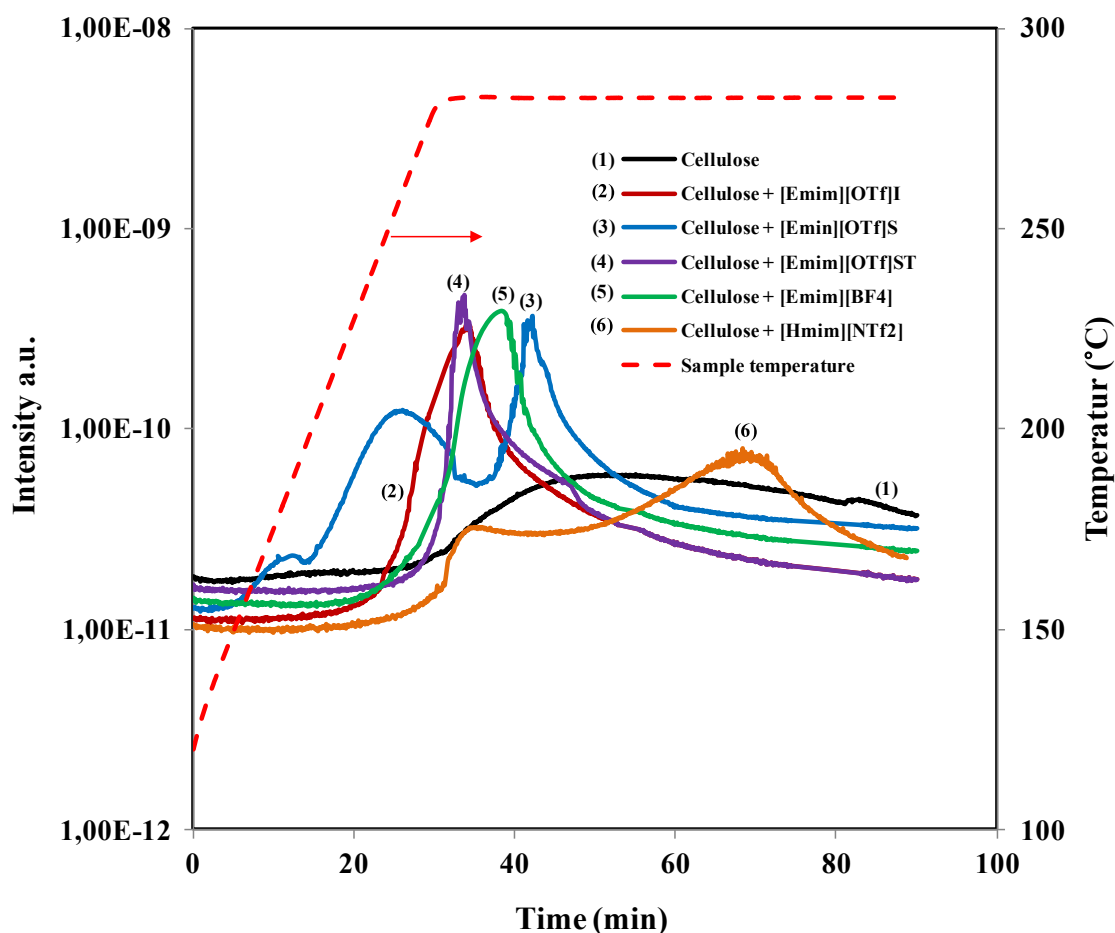
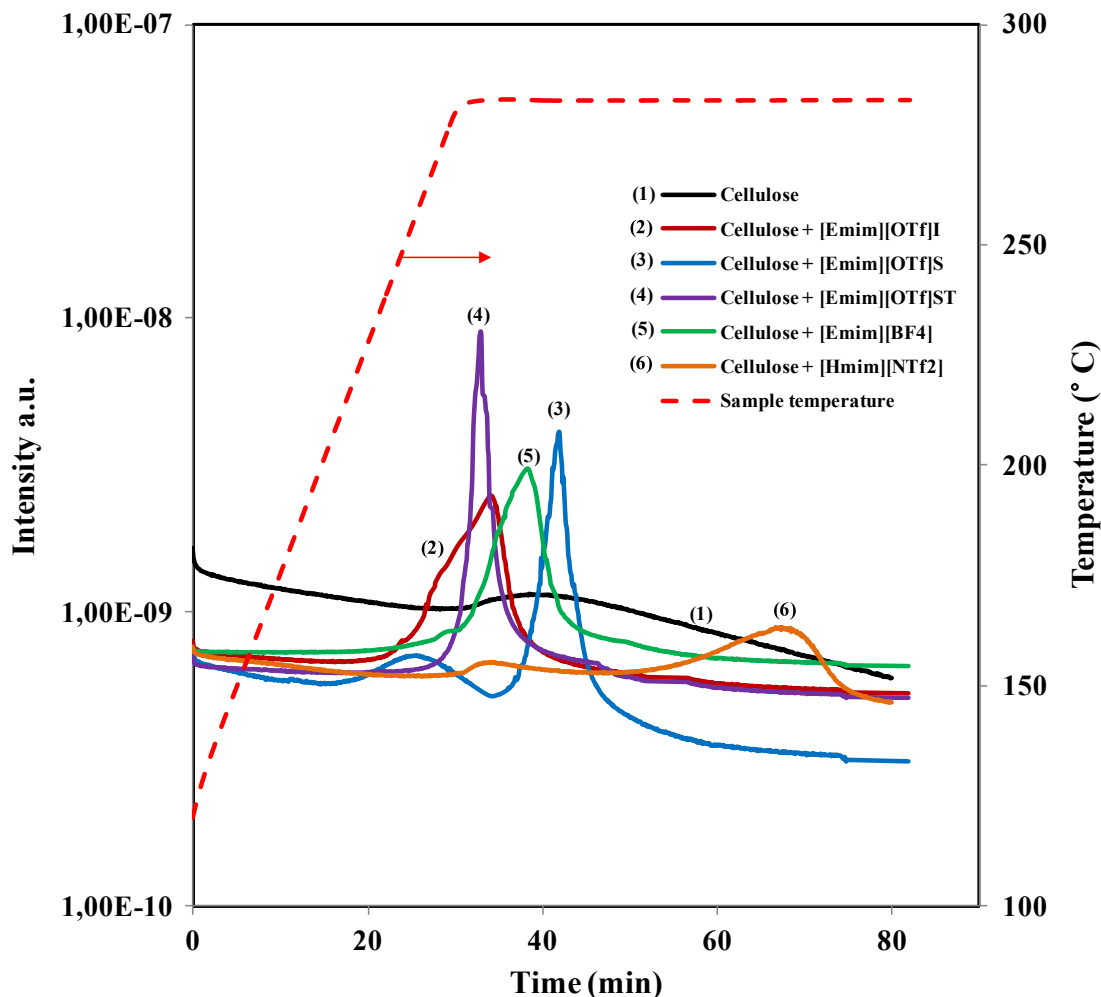


Figure 3-3 : MS positive ion current ( $m/z= 44$ , CO<sub>2</sub>) during cellulose ionic liquid and dry torrefaction

The rates of CO<sub>2</sub> release from cellulose in [Emim][OTf]<sub>I,S</sub> and [Emim][BF<sub>4</sub>] were rather sharp featuring more intense ion current peaks than for cellulose torrefied in [Hmim][NTf<sub>2</sub>] or in the dry mode. Ion currents corresponding to water released from cellulose also featured the same trend as CO<sub>2</sub>, Figure 3-4. Torrefaction of cellulose in [Emim][OTf]<sub>S,I</sub> and [Emim][BF<sub>4</sub>] drastically increased the amount of water released from cellulose. Water release also started at lower temperatures under [Emim][OTf]<sub>S,I</sub> and [Emim][BF<sub>4</sub>] cellulose torrefaction and unlike dry torrefaction.

To investigate how ionic liquids pre-exposed to elevated temperatures affect cellulose decomposition activity, [Emim][OTf]<sub>S</sub> was heated at 280°C for 48 h before it was

impregnated on cellulose. The heat-treated ionic liquid is referred to [Emim][OTf]<sub>ST</sub> and its effect on cellulose decomposition is shown in Figure 3-2. As seen, the rate of cellulose decomposition impregnated with [Emim][OTf]<sub>ST</sub> is as high as cellulose torrefied by [Emim][OTf]<sub>I</sub> and [Emim][BF<sub>4</sub>] while T<sub>S</sub> has shifted slowly toward higher temperatures. Heat treatment of [Emim][OTf]<sub>S</sub> caused its properties look like [Emim][OTf]<sub>I</sub> for cellulose decomposition.



**Figure 3-4.** MS positive ion current ( $m/z= 18, H_2O$ ) during cellulose liquid and dry torrefaction

Figure 3-5 shows xylan decomposition in dry and ionic-liquid torrefaction treatments. Xylan torrefaction in [Emim][OTf]<sub>S</sub> started at lower temperatures in comparison with the other ionic liquids or dry with dry torrefaction. However the rate of xylan decomposition did not change remarkably using the different ionic liquids. Ionic liquid torrefaction of xylan also led to more final decomposition than dry torrefaction, Figure 3-5. In contrast

with cellulose and xylan, ionic-liquid torrefaction of lignin had considerably lower effect on its  $T_s$ , Figure 3-6. The decomposition rate of lignin torrefied by ionic liquids also did not change significantly compared to dry torrefaction lignin. The small increase in the final decomposition of lignin is due to its torrefaction by [Emim][OTf]<sub>LS,ST</sub> and [Emim][BF<sub>4</sub>].

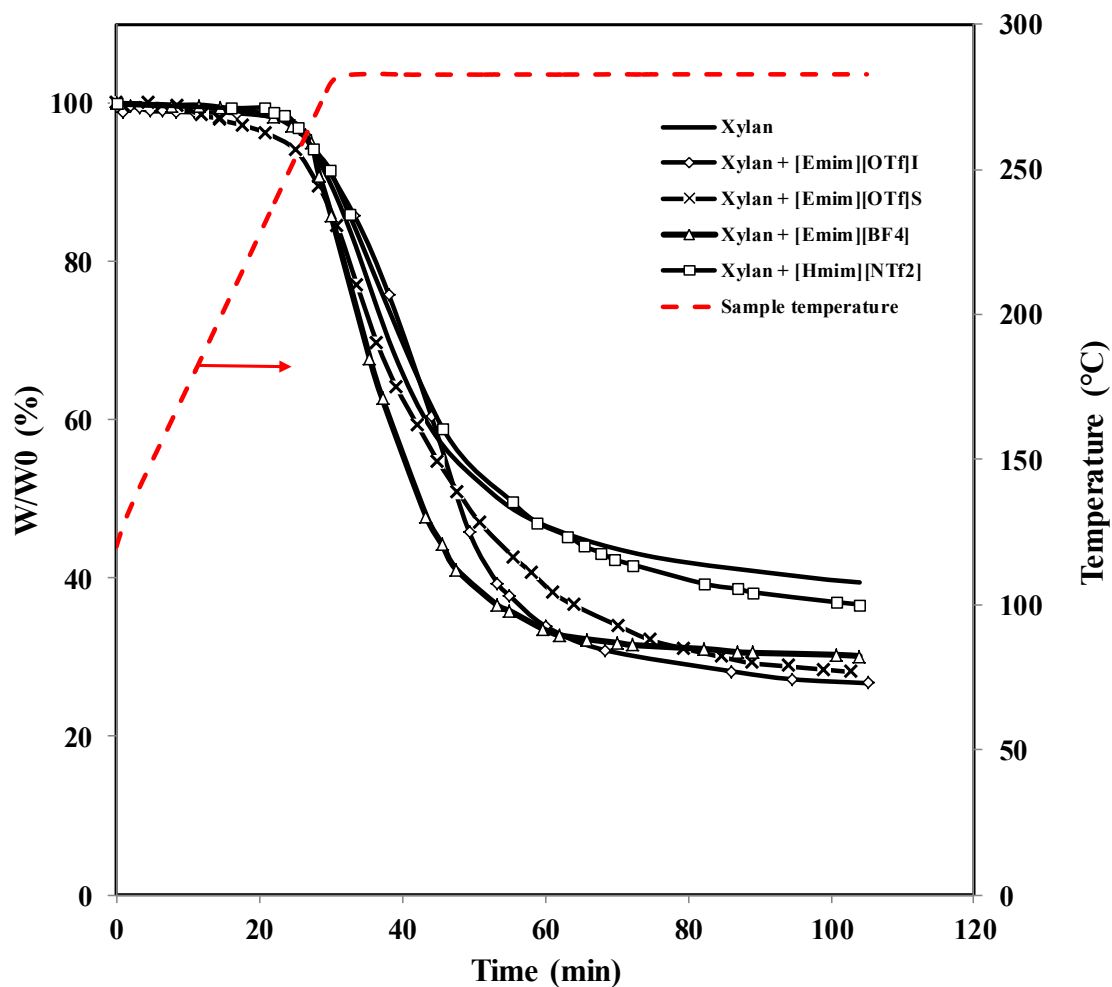


Figure 3-5. Mass loss profile of xylan ionic liquid and dry torrefaction

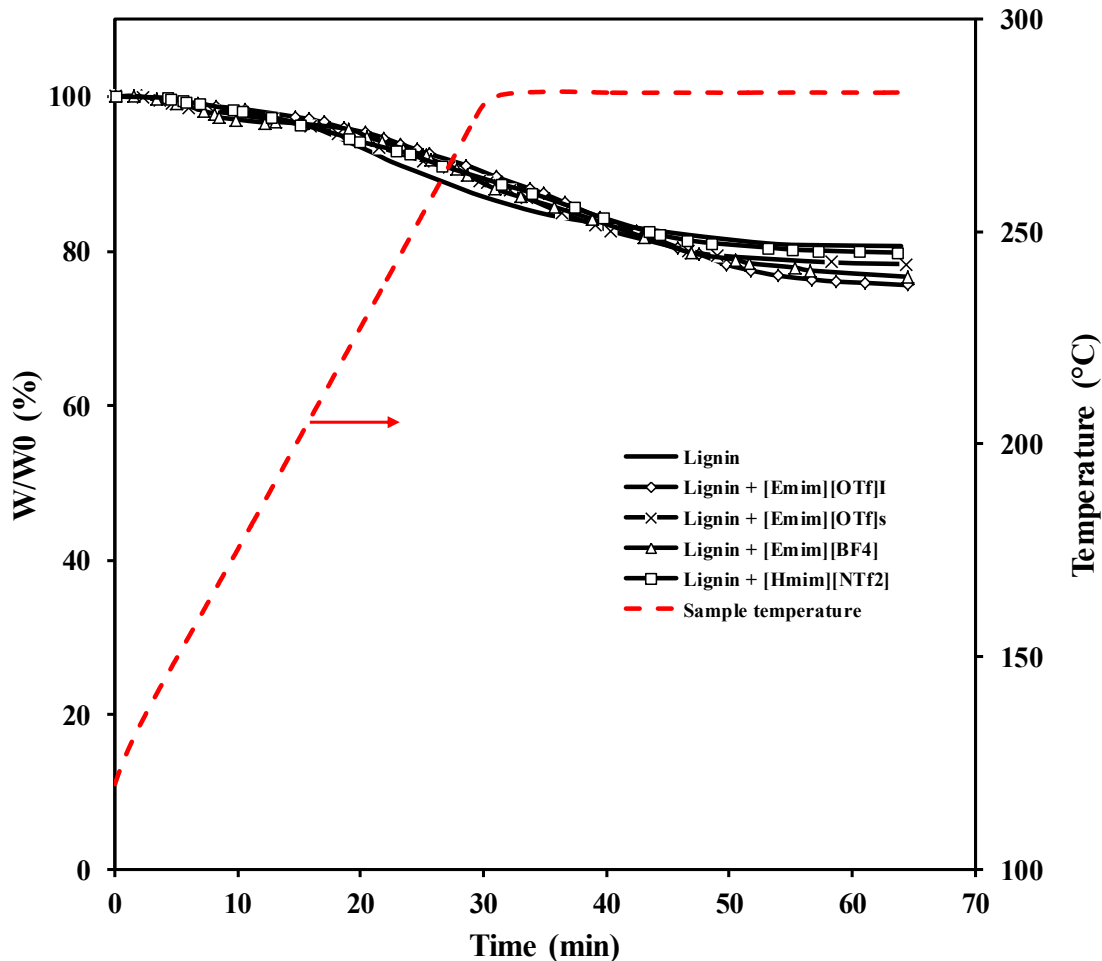
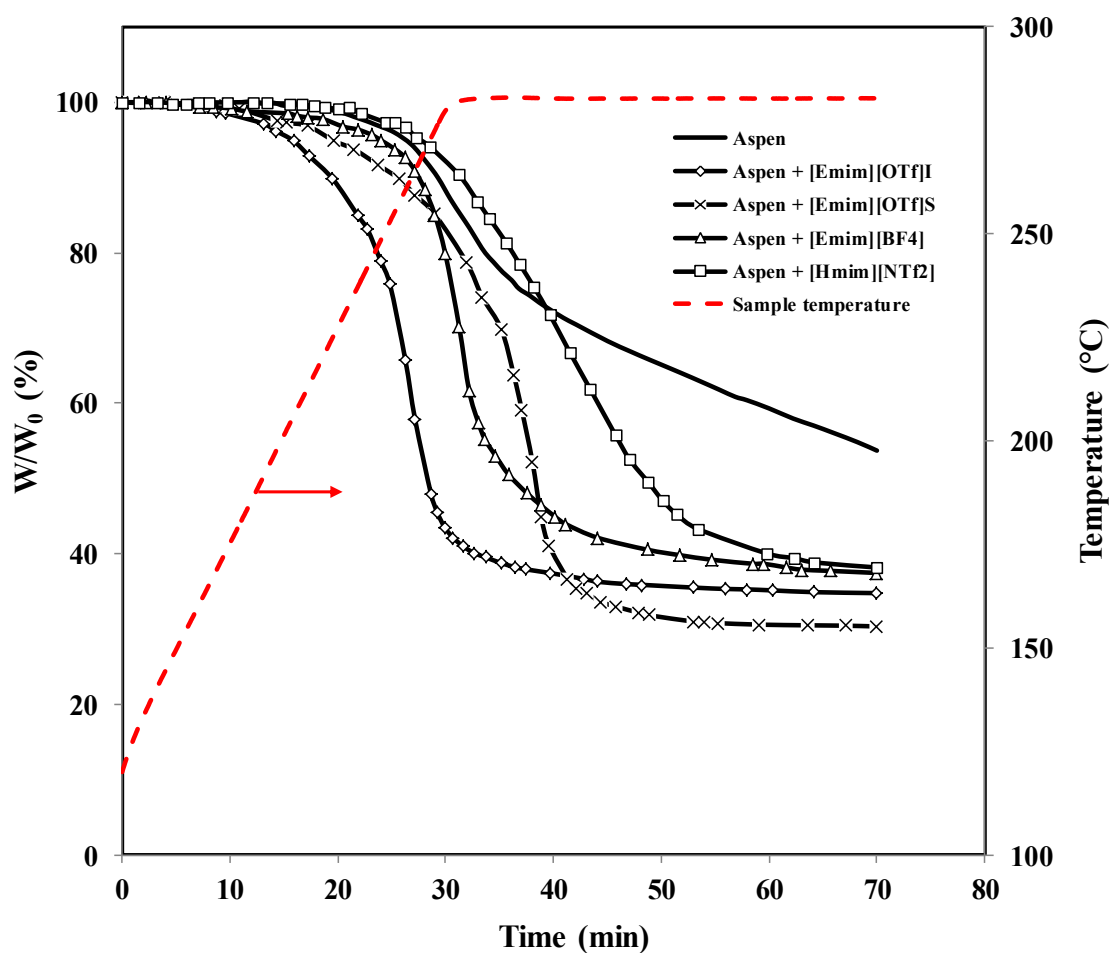


Figure 3-6. Mass loss profile of lignin ionic liquid and dry torrefaction

### 3.3.1.2 Torrefaction of woody biomass

IL and dry torrefaction of aspen, birch and sawdust was performed in TG-MS to obtain both  $T_s$  and weight loss profiles. Decomposition of aspen, birch and sawdust during IL torrefaction differs in trends from dry torrefied in accordance with the behaviors noted above for their constitutive model components. IL and dry torrefaction of aspen is shown in Figure 3-7 featuring an important decrease in  $T_s$  in presence of  $[\text{Emim}][\text{OTf}]_{\text{S,I}}$ . Decomposition of  $[\text{Emim}][\text{OTf}]_{\text{S,I}}$ -torrefied aspen started as low as 160 °C contrasting with  $T_s \sim 200^\circ\text{C}$  of dry torrefaction. The rate of aspen decomposition was also quite higher for  $[\text{Emim}][\text{OTf}]_{\text{S,I}}$  and  $[\text{Emim}][\text{BF}_4]$ -torrefied aspen compared to aspen dry torrefaction.  $[\text{Emim}][\text{OTf}]_{\text{I}}$  torrefaction outperformed that of  $[\text{Emim}][\text{OTf}]_{\text{S}}$  whereby the increased rate of aspen decomposition must have been due to the  $[\text{Emim}][\text{OTf}]_{\text{I}}$  acidic impurities.

Regardless of which IL is used, aspen torrefaction led to higher weight losses compared to dry torrefaction for the same contact times. The maximum aspen decomposition occurred with [Emim][OTf]<sub>s</sub>. Birch wood behaved nearly the same way as shown in Figure 3-8. Furthermore, T<sub>s</sub> for IL torrefaction of birch wood was lower than in dry torrefaction while birch wood decomposition rates were the slowest with [Hmim][NTf<sub>2</sub>]. Figure 3-9 compares the sawdust mass losses for IL and dry torrefaction. Contrary to dry torrefaction, higher decomposition rates as well as deeper weight losses are observed for sawdust torrefied in [Emim][OTf]<sub>l,s</sub> and [Emim][BF<sub>4</sub>]. Also, T<sub>s</sub> for [Emim][OTf]<sub>s,l</sub> and [Emim][BF<sub>4</sub>] torrefied sawdust was also lower compared to dry torrefaction of sawdust.



**Figure 3-7.** Mass loss profile of aspen ionic liquid and dry torrefaction

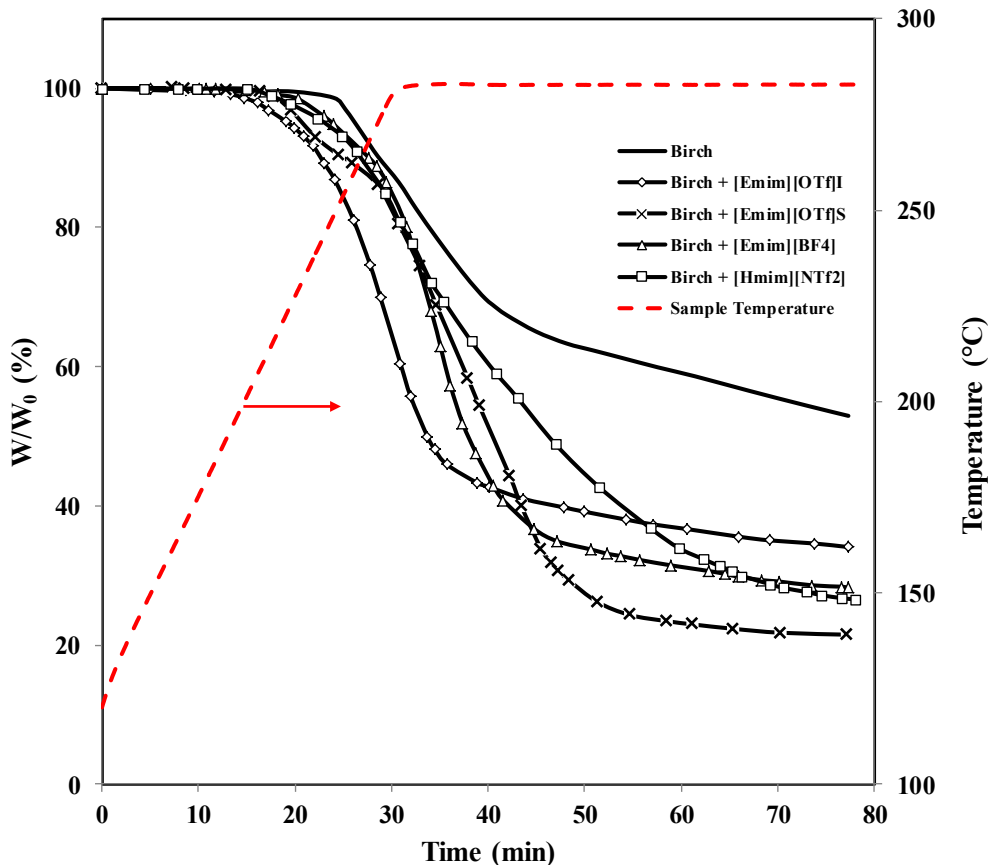


**Figure 3-8.** Mass loss profile of birch wood ionic liquid and dry torrefaction

As can be seen in the Figures 3-(7-9), the rate of decomposition of aspen, birch and sawdust could be considerably affected by the impregnation of the samples with the ionic liquids. Ionic liquids could effectively disrupt the extensive intra- and inter-molecular hydrogen bonding network in cellulose as well as intermolecular hydrogen bonding between cellulose and lignin leading to the higher decomposition rate of the mentioned biomass samples [16-18]. The interaction of ionic liquids with lignocellulosic biomass involves hydrogen bonding interactions between ionic liquid and biomass. Consequently the ionic liquids whose anions and cations have strong hydrogen bond accepting ability are more efficient in disrupting the cellulose structure [17,18,20]. As can be also observed in the Figures 3-(7-9), impregnated aspen, birch and sawdust by [Emim][OTf], [Emim][BF<sub>4</sub>] have considerably higher decomposition rate than that of by [Hmim][NTf<sub>2</sub>] impregnated samples. The cation size of [Hmim][NTf<sub>2</sub>] is larger than those of [Emim][OTf], [Emim][BF<sub>4</sub>]. Large cation size of [Hmim][NTf<sub>2</sub>] reduces its power for disrupting the

cellulose structure due to the less ability of large cations to form hydrogen bonds with cellulose [16-18]. Relatively small cations are often efficient in disrupting the hydrogen bonds of cellulose and when the alkyl chain length in the cation increases, as in the case of [Hmim][NTf<sub>2</sub>], the ability of ionic liquid to interact with lignocellulosic materials is decreasing [20]. However, additional experimental and theoretical studies are still needed to fully explain the effect of the nature of specific anions and cations on the torrefaction of biomass.

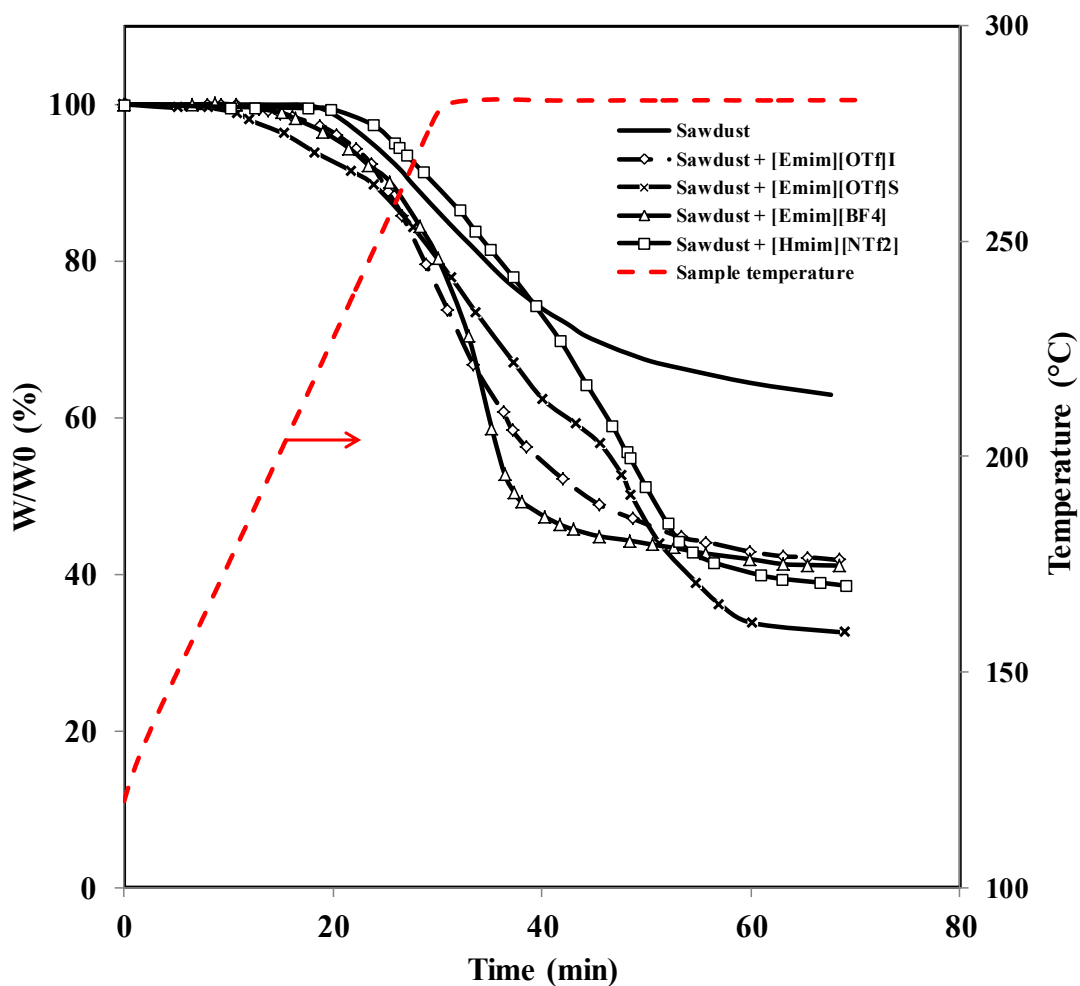


**Figure 3-9.** Mass loss profile of sawdust ionic liquid and dry torrefaction

### 3.3.2. IL and dry biomass torrefaction, fixed-bed studies

The previous TG tests showed that the activity of [Emim][OTf]-mediated TG torrefaction of aspen, birch and sawdust outperformed that from [Emim][BF<sub>4</sub>] and [Hmim][NTf<sub>2</sub>]. Also

the presence of acidic impurities in  $[\text{Emim}][\text{OTf}]_I$  were sensed to have some effects on the rate of decomposition of biomass. Consequently,  $[\text{Emim}][\text{OTf}]_S$  which is less prone to active impurities is chosen for the fixed-bed IL torrefaction of aspen, birch and sawdust. IL and dry torrefaction of aspen, birch and sawdust were performed at temperatures between 240-280°C for contact times ranging from 10 to 60 min. The solid biomass products obtained after dry and IL torrefaction of woody biomass were characterized in terms of mass yield ( $Y_M = \text{\%mass solid product/mass feed}$ ), energy density ( $e = \text{HHV solid product/HHV feed}$ ), energy yield ( $Y_e = e \cdot Y_M$ ), ultimate moisture uptake ( $U_{MU}$ ) and hydrophobicity.

Torrefaction of  $[\text{Emim}][\text{OTf}]_S$ -impregnated aspen, birch and sawdust led to brownish solids. The torrefied solid products after  $[\text{Emim}][\text{OTf}]_S$  and dry torrefaction of aspen, birch and sawdust are compared in Figure 3-10 in terms of their mass yields,  $Y_M$ , at different temperatures and contact times.

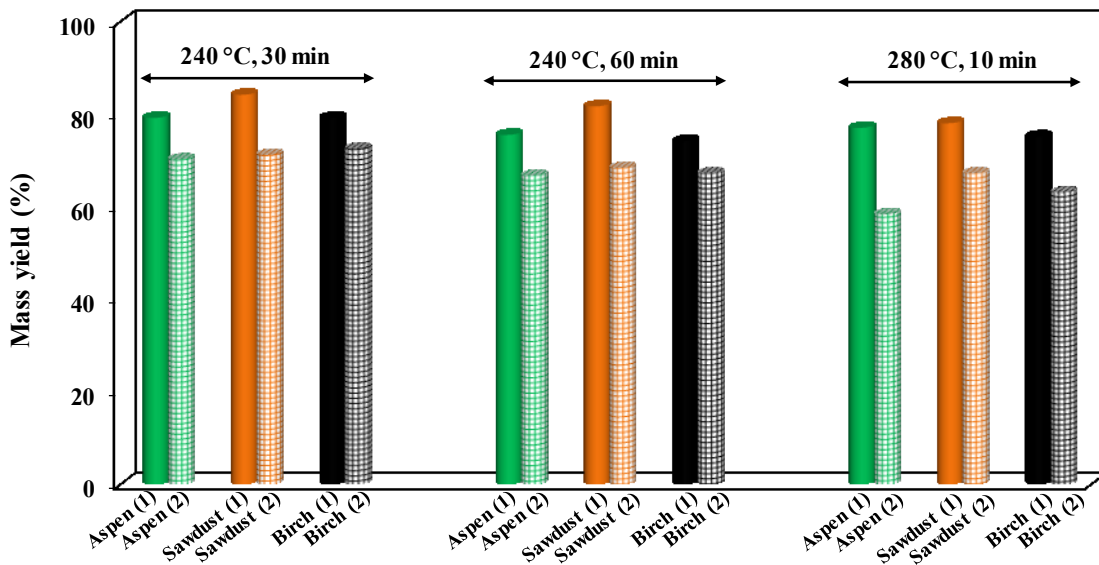


**Figure 3-10:** Solid mass yield of torrefied aspen, birch and sawdust (1) dry torrefaction (2) ionic liquid ( $[\text{Emim}][\text{OTf}]_S$ ) torrefaction

For any given biomass sample, IL-torrefied solids exhibit lower  $Y_M$ , in the 58-72% of initial weight, in comparison to those obtained in dry torrefaction, 74-84% of initial weight, everything else being kept constant. Also, irrespective of the type of torrefaction, a lower mass yield of aspen, birch and sawdust was scored as contact time and temperature

increased from 30 to 60 min and 240 to 280°C, respectively. These results are consistent with the increased decomposition rates of [Emim][OTf]<sub>s</sub>-impregnated aspen, sawdust and birch as unveiled from above TG analysis. It can be inferred that IL-torrefaction of biomass may reduce to a large extent the residence time required to reach a certain biomass mass yield during torrefaction. Results of elemental analysis of aspen, birch and sawdust before and after torrefaction are summarized in Table 3-2.

**Table 3-2** . Ultimate analysis, mass yield (dry basis) and high heating value of raw, and dry and ionic liquid ([Emim][OTf]<sub>s</sub>) torrefied aspen, birch and sawdust at different residence time and temperatures.

	Raw biomass	240 °C , 30 min		240 °C , 60min		280 °C , 10 min	
		dry	IL	Dry	IL	dry	IL
<b><i>Aspen</i></b>							
C (mass%)	48.5	50.2	51.5	50.5	51.8	51.8	51.5
H (mass%)	6.9	6.6	6.0	6.3	6.3	6.3	5.9
O (mass%)	44.4	43.2	42.1	43.1	41.6	42.0	42.1
N (mass%)	0.02	0.03	0.45	0.07	0.36	0	0.33
Mass yield (%)		79.2	70.2	75.5	66.7	77	58.3
C/O	1.19	1.16	1.22	1.17	1.25	1.23	1.22
HHV (kJ/kg)	19400	20100	20600	20200	20800	20700	20500
<b><i>Birch</i></b>							
C (mass%)	48.4	49.7	51.6	50.9	51.6	51.0	54.7
H (mass%)	6.9	6.6	5.8	6.4	6.4	6.3	5.0
O (mass%)	44.2	43.6	41.8	42.6	41.6	42.7	39.8
N (mass%)	0.06	0.09	0.42	0.08	0.40	0.06	0.44
Mass yield (%)		79.2	72.5	74.2	67.2	75.2	63.0
C/O	1.10	1.14	1.24	1.19	1.24	1.19	1.38
HHV (kJ/kg)	19400	19900	20600	20400	20800	20400	21500
<b><i>Sawdust</i></b>							
C (mass%)	48.9	51.7	51.5	53.3	53.5	52.0	58.3
H (mass%)	6.4	6.2	6.0	5.8	4.8	5.8	5.5
O (mass%)	42.7	42.0	42.1	40.7	41.0	42.1	35.4
N (mass%)	0.06	0.19	0.47	0.18	0.69	0.05	0.77
Mass yield (%)		84.2	71.2	81.7	68.3	78.0	67.2
C/O	1.15	1.23	1.22	1.31	1.30	1.23	1.64
HHV (kJ/kg)	19500	20700	20500	21300	20900	20700	23700

Dry and [Emim][OTf]<sub>S</sub> torrefaction of aspen, birch and sawdust led to an increase in C/O ratio translating in an increase in energy density subsequent to biomass torrefaction. As shown in Figure 3-11, the energy density,  $e$ , of aspen, birch and sawdust in all torrefied samples corresponding to Figure 3-10 conditions exceeds 1.0 for both IL and dry torrefaction of biomass. The higher energy density of torrefied biomass as compared to raw aspen, birch and sawdust would vouch for lower shipping costs and superior performance of coal co-fired power plants [34]. The energy density of [Emim][OTf]<sub>S</sub>-torrefied biomass was increased in the range 5-22% outperforming the  $e$  values corresponding to dry torrefaction which were limited between 3 and 9%.

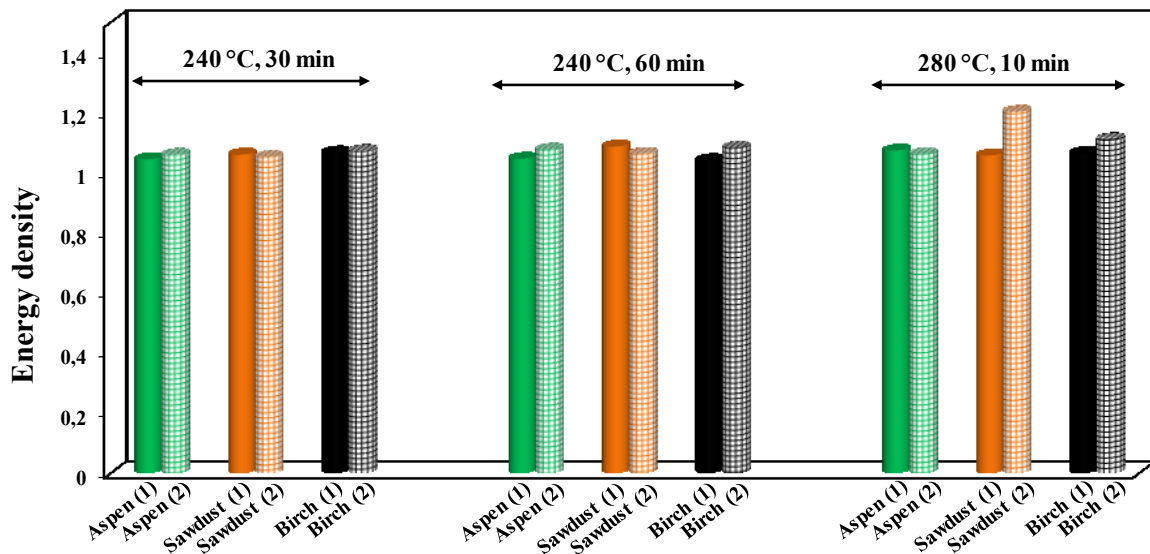


**Figure 3-11:** Energy density of torrefied aspen, birch and sawdust (1) dry torrefaction (2) ionic liquid ([Emim][OTf]<sub>S</sub>) torrefaction

Almost 90% of the non-condensable gases collected in the gas bag after cold trap were mostly composed of CO<sub>2</sub> for both [Emim][OTf]<sub>S</sub> and dry torrefaction of aspen, birch and sawdust while CO (7-8%) and methane (2-3) % were the other main constituents. In accordance with the ion current signals detected via MS, release of CO<sub>2</sub> and water during torrefaction could explain the increase in biomass C/O ratio and consequently leveraging of the heating value of the torrefied biomass samples, Table 3-2.

The energy yield,  $Y_e$ , of biomass torrefied with [Emim][OTf]<sub>S</sub> was below its dry torrefaction counterpart, everything else being kept constant. Figure 3-12 compares the

energy yield of IL torrefied aspen, birch and sawdust with dry torrefaction. This latter led to 1-25% higher energy yields than [Emim][OTf]<sub>S</sub>-torrefied biomass. These results can be explained by the fast decomposition of aspen, birch and sawdust cellulose during [Emim][OTf]<sub>S</sub> torrefaction which may release tar compounds that contributed to a reduction of  $Y_e$  of IL torrefied biomass.

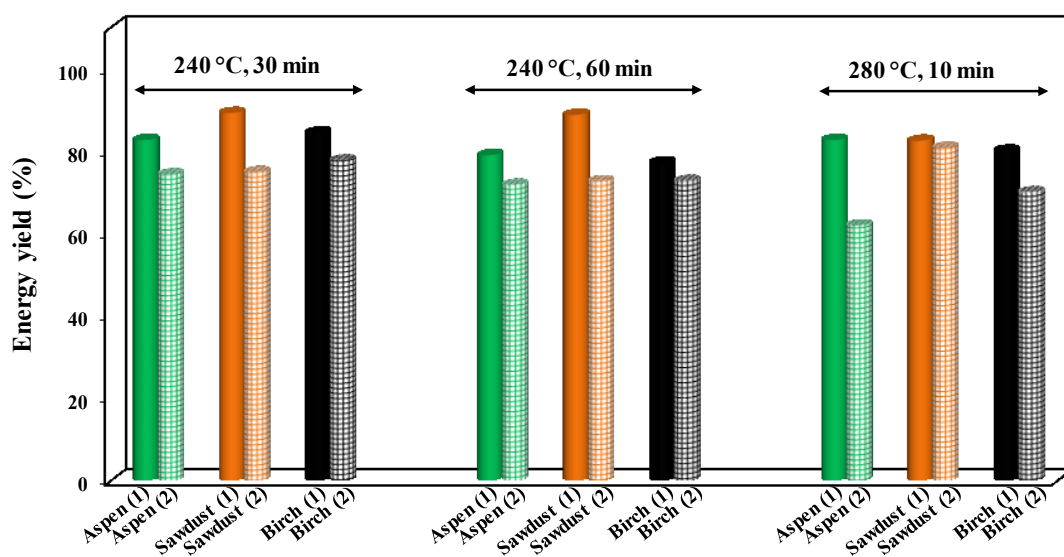


**Figure 3-12:** Energy yield of torrefied aspen, birch and sawdust (1) dry torrefaction (2) ionic liquid ([Emim][OTf]<sub>S</sub>) torrefaction

To assess hydrophobicity in the torrefied products,  $U_{MU}$  of solid products of [Emim][OTf]<sub>S</sub> and dry torrefaction of aspen, birch and sawdust were also measured. To eliminate biological activity and biomass deterioration during storage and to maintain lower transportation fees,  $U_{MU}$  has to be kept as low as possible [7]. As seen in Table 3-3,  $U_{MU}$  of solid products after [Emim][OTf]<sub>S</sub> and dry torrefaction of aspen, birch and sawdust were considerably lower than their  $U_{MU}$  before torrefaction. Moisture uptake occurs through hydrogen bond with the hydroxyl groups of the lignocellulosic cell wall components [7]. However, these hydroxyl groups by breaking during torrefaction yield more hydrophobic solids [7]. IL torrefaction led to 40-45% reduction in  $U_{MU}$  as compared to raw aspen, birch and sawdust. However, in most experiments, dry torrefaction led to solid products with  $U_{MU}$  lower than [Emim][OTf]<sub>S</sub> torrefaction. Increasing temperature of biomass torrefaction from 240 to 280°C improved hydrophobicity of aspen, birch and sawdust solid products.

Such increase in hydrophobicity of aspen, birch and sawdust after IL torrefaction was also confirmed from contact angle measurements. The contact angle for raw aspen, birch and sawdust were 83.3°, 82.2° and 75.25°, respectively. Correspondingly, contact angle of [Emim][OTf]<sub>s</sub>-torrefied aspen, birch and sawdust at 280°C increased to 92.85°, 92.75° and 90.65°.

**Table 3-3** : Ultimate moisture uptake of raw, dry and ionic liquid ([Emim][OTf]<sub>s</sub>) torrefied aspen, birch and sawdust at different residence time and temperatures after 4-day exposure of samples in saturated stream of 30°C.

	Raw biomass	240 °C , 30 min		240 °C , 60 min		280 °C , 10 min	
		dry	with IL	dry	with IL	dry	with IL
<i>Aspen</i>	24.8	15.5	17.4	15.7	16.7	14.1	14.3
<i>Birch</i>	23.9	15.3	16.1	14.0	16.7	15.4	13.4
<i>Sawdust</i>	22.6	15.6	16.3	15.6	15.9	13.6	13.5

### 3.3.3. IL thermal stability under torrefaction conditions

Investigating the contributory factors for long-term stability of ionic liquids as implemented for biomass torrefaction is important to check. Although the onset decomposition temperature of [Emim][BF<sub>4</sub>] [24], [Emim][OTf] [24] and [Hmim][NTf<sub>2</sub>] [26] as obtained from fast TG scanning is in excess of 400°C, other investigations have also revealed that decomposition of ILs may take place even at lower temperatures should they be employed over long-term periods [35]. Furthermore, production of some reactive gases during biomass thermal treatment as well as dissolution of biomass minerals may represent as many factors to catalyze ionic liquid decomposition [35]. Although imidazolium-based ionic liquids start to degrade, to some extent, at lower temperatures than those concluded from thermogravimetric analysis [36], long-term thermal stability of ionic liquid has been also studied via TG by several groups [35,37].

In this study, long term stability of ionic liquids is tested at 280°C using coupled TG-MS analysis. IL samples were dried in TG at 120°C for 30 min and then submitted to prograde heating at 5°C/min until 280°C. The samples were maintained overnight at this temperature to study their decomposition rate. The decomposition rate of as-received [Emim][OTf], [Emim][BF<sub>4</sub>] and [Hmim][NTf<sub>2</sub>] in a non-reactive gas environment (N<sub>2</sub>) is shown in the first entry of Table 3-4. Figure 3-13 also shows the TG trend of decomposition of the

mentioned ionic liquids. These data unveil some degradation at low temperature in accordance with the long-term thermal stability studies below 400°C. The decomposition rates of tested ILs follow the order: [Emim][BF<sub>4</sub>] > [Hmim][NTf<sub>2</sub>] > [Emim][OTf]. [Emim][OTf] from Sigma Aldrich had lower decomposition rate than that from ioli-tech as the acidic impurities present in the latter could prompt faster Emim cation decompositions [35].

**Table 3-4:** Decomposition rate (mass%/h) of different ionic liquids tested in this study at different operating conditions

	[Emim][BF <sub>4</sub> ]	[Hmim][NTf <sub>2</sub> ]	[Emim][OTf] <sub>s</sub>	[Emim][OTf] <sub>l</sub>
As-received IL	0.93	0.63	0.37	0.47
IL + 2 wt% ash	1.41	1.15	0.51	0.79
IL + 2 wt% ash + 2 wt% char	1.52	1.2	0.49	0.83

Thermal pretreatment of biomass at 280°C leads to the release of volatile and non-volatile gases such as organic acids, steam, CO<sub>2</sub>, CO, CH<sub>4</sub> and a small amount of hydrogen [38]. To investigate the sensitivity of IL decomposition to the presence of gases evolving during biomass thermal treatment, the non-reactive N<sub>2</sub> environment in the TG chamber was replaced by binary mixtures of 10%/90% CO<sub>2</sub>/N<sub>2</sub>, CO/N<sub>2</sub>, CH<sub>4</sub>/N<sub>2</sub>, H<sub>2</sub>O/N<sub>2</sub> and steam/N<sub>2</sub>. Although the decomposition rate of imidazolium based ionic liquids is reported to increase in the presence of air [35], our results showed no extensive changes in IL decomposition in response to changes in gas environments.

The effect of dissolution of minerals coexisting with biomass on the decomposition rate of the tested ionic liquids was also studied. Woody biomass contains some amounts of Si, Ca, K, Mg, P, Fe and Al [39] prone to dissolution in ILs during torrefaction. Dissolution of Fe, Au, Ag, Cu, Na and K, Mg and Ca in imidazolium-based ILs is known [40-42]. Mineral dissolution in ILs can be enhanced by elevated temperatures as in thermal treatment of biomass [40]. To investigate these effects on IL decomposition, ash was first produced after sawdust pyrolysis in the fixed bed at 800°C and N<sub>2</sub> environment and then burning the residual carbon for 4 h at 800°C. Addition of 2 wt% of ash to ionic liquid affected considerably its decomposition rate. The decomposition rate of the tested ILs (Table 3-4) increased by up to 100% and confirms the prejudice of minerals due to ash leftover. It is consistent with the reported boost on decomposition rate of 1-alkyl-3-methylimidazolium

triflates by amorphous and quartz silica [35],  $\text{BF}_4$  anions by calcium [27] and imidazolium ILs containing inorganic fluoride anions such as  $\text{PF}_6$  and  $\text{BF}_4$  by aluminum [22]. Switching in the presence of ash the  $\text{N}_2$  environment to gaseous mixtures to reflect the torrefaction evolving gases, i.e., 10%/90%  $\text{CO}_2/\text{N}_2$ ,  $\text{CO}/\text{N}_2$ ,  $\text{CH}_4/\text{N}_2$ ,  $\text{H}_2\text{O}/\text{N}_2$  and steam/ $\text{N}_2$ , had no boosting or neutralizing effect on IL decomposition.

Contacting between IL, solid biochar and ash on IL decomposition rate was also studied. Biochar was mixed with ash and IL in the proportions 2wt%/2 wt%/96 wt%, respectively. Special care was paid for char generation since contacting between IL and char may lead to the production of some volatiles from char itself. Consequently, char was generated by overnight pyrolysis of sawdust in TG at  $950^\circ\text{C}$  and under  $\text{N}_2$  environment after heating the biomass with the maximum rate achievable by TG ( $200^\circ\text{C}/\text{min}$ ) to extract the maximum volatiles from the sawdust. Addition of 2 wt% of char to the mixtures of ionic liquid and ash led to small increase in the decomposition rates of  $[\text{Emim}][\text{BF}_4]$ ,  $[\text{Hmim}][\text{NTf}_2]$  and  $[\text{Emim}][\text{OTf}]_1$  while it had no effect in case of  $[\text{Emim}][\text{OTf}]_s$ , see Table 3-4. As previously, switching from  $\text{N}_2$  to mixtures of 10%/90% of  $\text{CO}_2/\text{N}_2$ ,  $\text{CO}/\text{N}_2$ ,  $\text{CH}_4/\text{N}_2$ ,  $\text{H}_2\text{O}/\text{N}_2$  and steam/ $\text{N}_2$ , in the presence of ash and char at  $280^\circ\text{C}$  had no incremental effect due to gas on the decomposition rate of tested ionic liquids.

### 3.4. Conclusion

Torrefaction of cellulose, hemicellulose and lignin, and three different woody biomass varieties, namely, aspen, birch and sawdust impregnated with different ionic liquids, namely, [Emim][BF<sub>4</sub>], [Emim][OTf] and [Hmim][NTf<sub>2</sub>] was studied. The thermal decomposition rate of cellulose was found to increase considerably due to [Emim][OTf] and [Emim][BF<sub>4</sub>]. However, thermal decomposition of IL-torrefied xylan and lignin was comparable with dry torrefaction. For constant contact time and temperature, the decomposition rates of IL-impregnated birch, aspen and sawdust increased considerably compared to dry torrefaction. The efficiency of IL and dry torrefaction of aspen, birch and sawdust was compared in terms of mass yield, energy density, energy yield, hydrophobicity and ultimate moisture uptake of solid products. The energy density IL-torrefied biomass exceeded that of dry torrefaction. Conversely, plausibly ascribed to the release of heavy tars due to fast cellulose decomposition, the energy yield of IL-torrefied biomass was lower than dry torrefaction. Improvement in hydrophobicity of solid products from both IL and dry torrefaction was observed. This improvement led to nearly 40-45% reduction in ultimate moisture uptake of IL and dry torrefaction of aspen, birch and sawdust. Dissolution of minerals pre-existing in biomass have been shown to be detrimental in terms of prolonged exposures of ionic liquids and their possible degradation in the long run.

### 3.5. References

- [1] Berndes G, Hoogwijk M, van den Broek R. The contribution of biomass in the future global energy supply: a review of 17 studies. *Biomass & Bioenergy*. 2003;25:1-28.
- [2] Chen WH, Kuo PC. Torrefaction and co-torrefaction characterization of hemicellulose, cellulose and lignin as well as torrefaction of some basic constituents in biomass. *Energy*. 2011;36:803-11.
- [3] Pimchuai A, Dutta A, Basu P. Torrefaction of agriculture residue to enhance combustible properties. *Energy & Fuels*. 2010;24:4638-45.
- [4] Hoekman SK, Broch A, Robbins C. Hydrothermal carbonization (HTC) of lignocellulosic biomass. *Energy & Fuels*. 2011;25:1802-10.
- [5] Deng J, Wang GJ, Kuang JH, Zhang YL, Luo YH. Pretreatment of agricultural residues for co-gasification via torrefaction. *Journal of Analytical and Applied Pyrolysis*. 2009;86:331-7.
- [6] Yan W, Hastings JT, Acharjee TC, Coronella CJ, Vasquez VR. Mass and energy balances of wet torrefaction of lignocellulosic biomass. *Energy & Fuels*. 2010;24:4738-42.
- [7] Yan W, Acharjee TC, Coronella CJ, Vasquez VR. Thermal Pretreatment of lignocellulosic biomass. *Environmental Progress & Sustainable Energy*. 2009;28:435-40.
- [8] Medic D, Darr M, Shah A, Rahn S. Effect of torrefaction on water vapor adsorption properties and resistance to microbial degradation of corn stover. *Energy & Fuels*. 2012;26:2386-93.
- [9] Patel B, Gami B, Bhimani H. Improved fuel characteristics of cotton stalk, prosopis and sugarcane bagasse through torrefaction. *Energy for Sustainable Development*. 2011;15:372-5.
- [10] Chen WH, Cheng WY, Lu KM, Huang YP. An evaluation on improvement of pulverized biomass property for solid fuel through torrefaction. *Applied Energy*. 2011;88:3636-44.
- [11] Prins MJ, Ptasinski KJ, Janssen F. Torrefaction of wood - Part 1. Weight loss kinetics. *Journal of Analytical and Applied Pyrolysis*. 2006;77:28-34.
- [12] van der Stelt MJC, Gerhauser H, Kiel JHA, Ptasinski KJ. Biomass upgrading by torrefaction for the production of biofuels: A review. *Biomass & Bioenergy*. 2011;35:3748-62.
- [13] Wang S, Liu Q, Luo Z, Wen L, Can K. Mechanism study on cellulose pyrolysis using thermogravimetric analysis coupled with infrared spectroscopy. *Front Energy Power Eng China*. 2007;1:413-9.
- [14] Tadesse H, Luque R. Advances on biomass treatment using ionic liquids: An overview. *Energy & Environmental Science*. 2011;4:3913-29.
- [15] Julien S, Chornet E, Overend RP. Influence of acid pretreatment ( $H_2SO_4$ ,  $HCl$ ,  $HNO_3$ ) on reaction selectivity in the vacuum pyrolysis of cellulose. *Journal of Analytical and Applied Pyrolysis*. 1993;27:25-43.

- [16] Brodeur G, Yau E, Badal K, Collier J, Ramachandran KB, Ramakrishnan S. Chemical and physicochemical pretreatment of lignocellulosic biomass: a review. *Enzyme research*. 2011;2011:787532.
- [17] Li B, Asikkala J, Filpponen I, Argyropoulos DS. Factors affecting wood dissolution and regeneration of ionic liquids. *Industrial & Engineering Chemistry Research*. 2010;49:2477-84.
- [18] Zakrzewska ME, Bogel-Lukasik E, Bogel-Lukasik R. Solubility of carbohydrates in ionic liquids. *Energy & Fuels*. 2010;24:737-45.
- [19] Van Valkenburg ME, Vaughn RL, Williams M, Wilkes JS. Thermochemistry of ionic liquid heat-transfer fluids. *Thermochimica Acta*. 2005;425:181-8.
- [20] Maki-Arvela P, Anugwom I, Virtanen P, Sjöholm R, Mikkola JP. Dissolution of lignocellulosic materials and its constituents using ionic liquids-A review. *Industrial Crops and Products*. 2010;32:175-201.
- [21] Sun N, Rodriguez H, Rahman M, Rogers RD. Where are ionic liquid strategies most suited in the pursuit of chemicals and energy from lignocellulosic biomass? *Chemical Communications*. 2011;47:1405-21.
- [22] Ngo HL, LeCompte K, Hargens L, McEwen AB. Thermal properties of imidazolium ionic liquids. *Thermochimica Acta*. 2000;357:97-102.
- [23] Fredlake CP, Crosthwaite JM, Hert DG, Aki S, Brennecke JF. Thermophysical properties of imidazolium-based ionic liquids. *Journal of Chemical and Engineering Data*. 2004;49:954-64.
- [24] Huddleston JG, Visser AE, Reichert WM, Willauer HD, Broker GA, Rogers RD. Characterization and comparison of hydrophilic and hydrophobic room temperature ionic liquids incorporating the imidazolium cation. *Green Chemistry*. 2001;3:156-64.
- [25] Lee SH, Dang DT, Ha SH, Chang WJ, Koo YM. Lipase-catalyzed synthesis of fatty acid sugar ester using extremely supersaturated sugar solution in ionic liquids. *Biotechnology and Bioengineering*. 2008;99:1-8.
- [26] Crosthwaite JM, Muldoon MJ, Dixon JK, Anderson JL, Brennecke JF. Phase transition and decomposition temperatures, heat capacities and viscosities of pyridinium ionic liquids. *Journal of Chemical Thermodynamics*. 2005;37:559-68.
- [27] Katagiri J, Borjigin S, Yoshioka T, Mizoguchi T. Formation and decomposition of tetrafluoroborate ions in the presence of aluminum. *Journal of Material Cycles and Waste Management*. 2010;12:136-46.
- [28] Friedl A, Padouvas E, Rotter H, Varmuza K. Prediction of heating values of biomass fuel from elemental composition. *Analytica Chimica Acta*. 2005;544:191-8.
- [29] Bridgeman TG, Jones JM, Shield I, Williams PT. Torrefaction of reed canary grass, wheat straw and willow to enhance solid fuel qualities and combustion properties. *Fuel*. 2008;87:844-56.
- [30] Bridgeman TG, Jones JM, Williams A, Waldron DJ. An investigation of the grindability of two torrefied energy crops. *Fuel*. 2010;89:3911-8.

- [31] Antal M, Simkovic I, Ebringerova A, Micko MM. New aspects in cationization of lignocellulose materials .4. modification of aspen wood meal with quarternary ammonium groups. *Journal of Applied Polymer Science*. 1986;31:621-5.
- [32] Li C, Zheng M, Wang A, Zhang T. On-pot catalytic hydrocracking of woody biomass into chemicals over supported carbide catalysts: simultaneous conversion of cellulose, hemicellulose and lignin. *Energy & Environmental Science*. 2011.
- [33] Radmanesh R, Courbariaux Y, Chaouki J, Guy C. A unified lumped approach in kinetic modeling of biomass pyrolysis. *Fuel*. 2006;85:1211-20.
- [34] Phanphanich M, Mani S. Impact of torrefaction on the grindability and fuel characteristics of forest biomass. *Bioresource Technology*. 2011;102:1246-53.
- [35] Kosmulski M, Gustafsson J, Rosenholm JB. Thermal stability of low temperature ionic liquids revisited. *Thermochimica Acta*. 2004;412:47-53.
- [36] Meine N, Benedito F, Rinaldi R. Thermal stability of ionic liquids assessed by potentiometric titration. *Green Chemistry*. 2010;12:1711-4.
- [37] Seeberger A, Andresen AK, Jess A. Prediction of long-term stability of ionic liquids at elevated temperatures by means of non-isothermal thermogravimetric analysis. *Physical Chemistry Chemical Physics*. 2009;11:9375-81.
- [38] Prins MJ, Ptasiński KJ, Janssen F. Torrefaction of wood - Part 2. Analysis of products. *Journal of Analytical and Applied Pyrolysis*. 2006;77:35-40.
- [39] Masia AAT, Buhre BJP, Gupta RP, Wall TF. Characterising ash of biomass and waste. *Fuel Processing Technology*. 2007;88:1071-81.
- [40] Whitehead JA, Zhang J, Pereira N, McCluskey A, Lawrance GA. Application of 1-alkyl-3-methyl-imidazolium ionic liquids in the oxidative leaching of sulphidic copper, gold and silver ores. *Hydrometallurgy*. 2007;88:109-20.
- [41] Chun S, Dzyuba SV, Bartsch RA. Influence of structural variation in room-temperature ionic liquids on the selectivity and efficiency of competitive alkali metal salt extraction by a crown ether. *Analytical Chemistry*. 2001;73:3737-41.
- [42] Bartsch RA, Chun S, Dzyuba SV. Ionic liquids as novel diluents for solvent extraction of metal salts by crown ethers. In: Rogers RD, Seddon KR, editors. *Ionic Liquids: Industrial Applications for Green Chemistry*. Washington: Amer Chemical Soc; 2002. p. 58-68.

## **Chapter 4 : Biomass torrefaction and CO<sub>2</sub> capture using mining wastes - A new approach for reducing greenhouse gas emissions of co-firing plants**

**Résumé** Une nouvelle combinaison de la torréfaction de la biomasse et de la séquestration du CO<sub>2</sub> a été explorée, combinaison dans laquelle la carbonatation des résidus miniers a été réalisée à des températures ambiantes. Le CO<sub>2</sub>, l'un des principaux gaz émis lors de la torréfaction de la biomasse lignocellulosique peut être piégé par dans des résidus miniers, résultant en un procédé de torréfaction à carbone négatif. Les fonctionnalités de la torréfaction comme condition *sine qua non* de l'efficacité de la co-combustion de la biomasse et du charbon pourraient donc être davantage améliorées en limitant les émissions globales de CO<sub>2</sub> du procédé. Pour tester ce concept, deux types différents de résidus miniers ultramafiques riches ont été introduits dans un réacteur de carbonatation installé en aval du réacteur de torréfaction et utilisé sous reflux total de gaz pour capturer le CO<sub>2</sub> émis. L'unité de torréfaction a été alimentée avec du bois de bouleau sec respectant le mode de torréfaction conventionnel et avec du bois de bouleau imprégné dans du liquide ionique afin d'accélérer le taux de dégradation des constituants du bois. L'effet de paramètres tels que la température de carbonatation, la saturation en eau des pores des résidus miniers, et les concentrations en monoxyde de carbone et en méthane dans le gaz émis sur l'absorption du CO<sub>2</sub> par les résidus miniers a été étudié systématiquement dans le but de jauger si un tel concept permettrait de stocker des quantités importantes de CO<sub>2</sub> émis lors de la torréfaction du bois.

**Abstract** A novel combination of biomass torrefaction and CO<sub>2</sub> sequestration was explored in which carbonation of mining residues was conducted near ambient temperatures. We report that CO<sub>2</sub> as one of the main gases evolved during torrefaction of lignocellulosic biomass can be trapped using cheap, abundant and already size-reduced mining residues resulting in a carbon-negative torrefaction process. Functionalities of torrefaction as a prerequisite step for an efficient biomass/coal co-firing could thus be further enhanced by curbing the overall process CO<sub>2</sub> emissions. To test this concept, two different Mg-rich ultramafic mining wastes were loaded in a carbonation reactor hyphenated downstream of a torrefaction reactor and operated under total gas reflux to capture the incipient CO<sub>2</sub>. The torrefaction unit was operated with birch wood according to conventional dry torrefaction as well as using ionic-liquid-impregnated torrefaction to increase birch wood constituents' torrefaction rate. The effect of some important parameters such as carbonation temperature, residue pore water saturation, and carbon monoxide and methane concentrations on mining residues CO<sub>2</sub> uptake was studied systematically to assess if such a tandem concept would enable displacement and storage of sizeable amounts of CO<sub>2</sub> emitted by torrefaction.

## 4.1. Introduction

Coal combustion for electricity generation is regarded as one of the most significant sources of greenhouse gas emissions [1]. In 2010, *ca.* 46% of world's electricity demand was generated from coal combustors while coal-based plants contributed *ca.* 70% of CO<sub>2</sub> emissions [2]. In Canada, nearly 80% of CO<sub>2</sub> emissions related to electricity generation (11.5% of Canada's total CO<sub>2</sub> emissions) are ascribed to coal-fired plants [3]. Fractional substitution of coal with biomass as a renewable energy source, *i.e.*, normally viewed as CO<sub>2</sub> neutral in energy conversion systems, is an appealing option to curb CO<sub>2</sub> emissions [4]. In this regard, biomass co-firing with coal is contemplated as a realistic option to alleviate the incidence of coal in electricity generation in existing coal-fired plants while requiring small capital investments for retrofitting [5]. In addition to the decrease in coal consumption, co-firing is anticipated to mitigate NO<sub>x</sub> and SO<sub>2</sub> emissions thus presenting biomass as a sustainable candidate source for electricity production [6-8]. Efficient and economic coal/biomass co-firing for energy production is hampered by the limited biomass energy contribution which is less than 10% in the majority of currently operated co-firing plants [9]. The most common hurdles are (though not limited to): 1) low energy density of biomass (as compared to coal) due to the large moisture and oxygen contents cause flame instabilities in the combustion chambers [6], 2) low biomass flowability and fluidization properties leading to difficulties in feeding biomass into combustors [10], 3) rigidity and mechanical strength of biomass structure attributed to the long crystalline cellulose fibers intertwined with non-crystalline hemicellulose resulting in higher grinding energy requirements and reducing grinding efficiency of coal-biomass feeds [11].

Torrefaction as a pretreatment technique is proposed as a retrofit measure to alter biomass properties and accommodate its application in co-firing plants [10]. Torrefaction consists of a mild pyrolysis of biomass at temperatures below 300°C in an oxygen-deprived headspace. Torrefaction, being a thermal O-removal process, increases energy density of treated biomass to achieve heating values nearing those of coal [11-13]. Furthermore, torrefaction promotes partial depolymerization/decomposition of cellulose and hemicellulose. This contributes to reduce fibers length and mechanical stability hence ameliorating biomass grindability properties [10,14,15]. Furthermore, torrefied biomass exhibits more uniform

physicochemical properties, *e.g.*, superior flowability and fluidization properties than raw biomass, making it more amenable for co-firing [10, 16]. Different torrefaction processes, *e.g.*, dry torrefaction [12,17,18], wet torrefaction [19,20] and ionic-liquid (IL) assisted torrefaction [21] have been investigated to enhance biomass properties. Decomposition of hemicellulose, cellulose and lignin fractions of biomass subjected to above torrefaction processes could release some low calorific-value gases such as carbon dioxide, water and some types of organic acids, such as formic and acetic acids [22]. Depending on the type of biomass and torrefaction conditions (temperature and treatment time), up to 30% of carbon can be released in the form of CO<sub>2</sub> [22].

Although biomass is a CO<sub>2</sub>-neutral source of energy, a torrefaction process hyphenated with capture of its evolved CO<sub>2</sub> gas could constitute an appealing option for co-firing plants to reduce their net CO<sub>2</sub> emissions. Furthermore, due to the importance of mitigating CO<sub>2</sub> emissions into the atmosphere, recent studies predict that the net negative greenhouse gas emissions from bioenergy with carbon capture and storage plants could be as much as 10<sup>9</sup> metric tons of CO<sub>2</sub> per year near 2050. This emphasizes the importance of intercepting CO<sub>2</sub> streams in future bioenergy-based plants [23]. In this regard, a combined continuous torrefaction and carbonation process is investigated in this study for trapping the CO<sub>2</sub> formed during torrefaction as a negative net CO<sub>2</sub> emission torrefaction process. The proposed CO<sub>2</sub> trapping process is based on the carbonation at nearly ambient temperature and pressure of cheap, easily-accessible, already-mined and pre-ground ore residues and tailings [24-27]. In particular, those consisting of mafic/ultramafic mining wastes, due to their high Mg content (up to 20 wt.%), are known to be very reactive with CO<sub>2</sub> [28]. Recently, our group studied the ability of ultramafic mining residues to directly capture CO<sub>2</sub> under ambient conditions and outlined the enhanced rate of carbonation under anoxic and low liquid saturation environments [29,30]. The carbonation reactions led to the formation of stable carbonate minerals such as nesquehonite and dypingite [30]. These findings suggest a possibility to combine biomass torrefaction with CO<sub>2</sub> fixation and whereby CO<sub>2</sub> produced during torrefaction could be trapped over moistened mining residues. The fact that the entire chain proceeds anoxically is also advantageous for the carbonation of residues as their carbonation activity was shown to decay in the presence of oxygen [29].

To study the possibility of on-stream biomass torrefaction and carbonation of mining residues, an assembly consisting of a hyphenated torrefaction-carbonation reactor was designed. The carbonation potential of two types of ultramafic tailing residues was assessed by testing streams of CO<sub>2</sub> produced during dry and ionic-liquid torrefaction of birch wood. The study's aim specifically addressed the impact of carbonation temperature, residues pore water saturation, and CO and methane composition of the evolving torrefaction gas on the carbonation rate of the mining residues.

## **4.2. Experimental**

### **4.2.1. Materials preparation**

To investigate the potential of ultramafic mining residues for capturing CO<sub>2</sub> from a torrefaction gas, two samples were used 1) chrysotile mining residues (CMR) received from the Black Lake Mine tailings (Thetford Mines, Québec, Canada) and 2) nickel mine residues (NMR) obtained from the exit of the defibering process of Royal Nickel Corporation's Dumont Nickel project pilot plant (Amos, Québec, Canada). The samples received were in two separate sealed 25 liters containers to avoid the contact of the residues with air during their transportations. The mining residue samples were then sieved to isolate particles smaller than 1.5 mm to be used for the carbonation experiments. Powder X-ray diffraction analysis of the two samples revealed the presence of chrysotile and lizardite as major minerals along with minor components such as magnetite, brucite, albite, chlorite, talc, phlogopite and wustite. The native brucite content, one of the active minerals for carbonation, was ca. 2.94 wt% and 10.9 wt% in CMR and NMR, respectively. Detailed information about these residues is available elsewhere [29,30]. Prior to experiments, the (porous) residue samples were moistened with water to achieve up to ca. 50% liquid saturation.

Isothermal torrefaction studies were performed using birch, an abundant wood biomass source from Québec forests. Before the experiments, the as-received tiny sheets of birch wood samples (the sample had no bark) were cut into small pieces to obtain woodchips in the 2-4 mm size range. The proximate analysis of birch wood showed the presence of 5.5% of humidity. The volatiles, fixed carbon and ash content of the samples were 89.4%, 9.8%

and 0.7% on a dry basis, respectively. The same batch of birch wood is used for all the torrefaction experiments performed in this study and the CHNS analysis performed on the samples proved the homogeneity of the birch wood samples. Birch wood torrefaction was performed using two different processes. In the first series of experiments, non-pretreated birch samples were torrefied at 260°C for 60 min, referred here to as dry torrefaction. At 260 °C, all the biomass constituents such as hemicellulose, cellulose and lignin are torrefied leading to an appropriate estimation of CO<sub>2</sub> production from the birch torrefaction. The rate of biomass torrefaction at 260 °C is not also very high leading to the good control over the torrefaction experiments and their repeatability in the term of torrefaction mass yield and CO<sub>2</sub> production rate during torrefaction. In a second series, birch wood samples were impregnated with 1-ethyl-3-methyl imidazolium trifluoromethanesulfonate ionic liquid (IL) at 60°C ([Emim][OTf], Sigma Aldrich, purity >98 %) and then torrefied at 260°C for 30 min. Impregnation of biomass with ionic liquids has been shown to enhance the rate of cellulose torrefaction at temperatures lower than 300°C [21]. Consequently, the torrefaction of IL-impregnated birch wood was carried out to evaluate the extent of carbon dioxide production associated with this process. The final mass ratio of absorbed IL to birch was around 2.

#### **4.2.2. Experimental assembly**

The biomass samples were torrefied in a fixed-bed reactor (Figure 4-1). The bench scale biomass torrefaction unit consisted of a stainless steel fixed-bed reactor (internal diameter 0.34 cm, length 70 cm) placed inside an induction coil. For each experiment, one gram of dry or IL-impregnated biomass sample was held atop of a steel grid located in the middle of a stainless steel tube to act as a support for the biomass bed. The reactor was heated through a 30 cm long coil connected to a 18 kW induction power supply for heating the stainless steel tube *via* an AC magnetic field then heating in turn the biomass layer through radiation and conduction. The biomass bed temperature was raised from the ambient to a target temperature of 260±0.1°C and kept there for specified time durations.

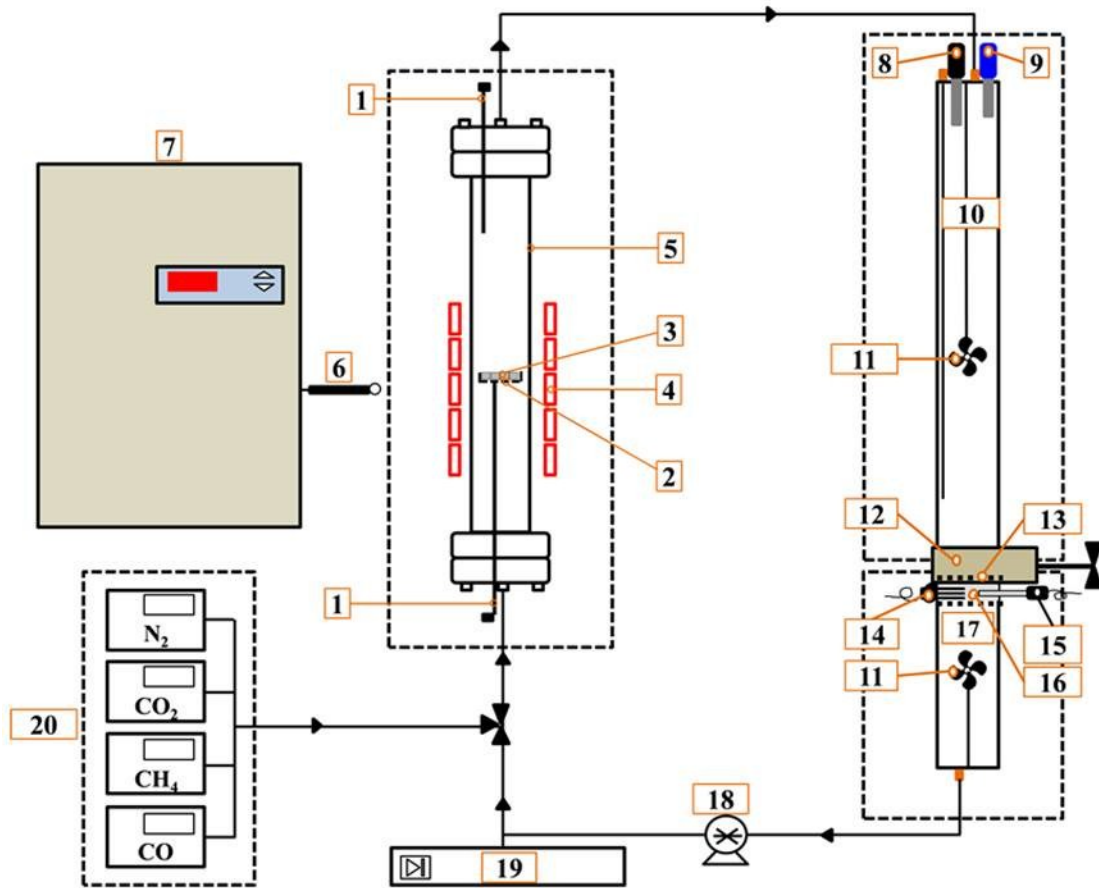


**Figure 4-1.** Schematic of experimental torrefaction-carbonation assembly. (1) K-type thermocouple (2) stainless steel mesh (3) birch sample holder (4) induction coil (5) stainless steel torrefaction reactor (6) pyrometer (7) induction power supply (8) CO<sub>2</sub> probe (9) hygrometer-thermocouple (10) carbonation upper compartment (11) electrical fan (12) gate (13) stainless steel filter (14) TDR probe (15) pH probe (16) residue bed holder (17) carbonation lower compartment (18) peristaltic pump (19) micro-GC (20) mass flowmeters

The gas exiting from the torrefaction reactor was directed towards the top of a carbonation reactor (cylindrical tube, 5.8 cm internal diameter) where carbonation took place through a 1.2 cm thick layer of mining residues. The carbonation column consisted of two compartments: an upper headspace occupying *ca.* 75% of the column volume, the mining residue bed and a lower compartment. The CO<sub>2</sub> concentration, gas humidity and temperature in upper compartment were hygrometer-thermocouples (HMT333 moisture-temperature transmitter, Vaisala). To homogenize the gas composition in both upper and lower compartments, each was gently mixed with a dedicated electrical fan. The bed characteristics, *i.e.*, its temperature, pore water pH and ionic conductivity during carbonation were also monitored as a function of time. A multi-task time-domain

reflectometer (TDR) probe (DELTA-T WET-2-K1, Hoskin Scientific) was inserted laterally in the residue layer for on-line monitoring of liquid saturation, bulk ionic conductivity (of solid, extra- and intra-porous water) and bed temperature. A pH probe (8616AQ, Hanna instruments) was also used to register the instantaneous residue pore-water pH.

The gas exiting the bottom of the carbonation column was recirculated to the torrefaction reactor by means of a peristaltic pump (Figure 4-1). Due to the slow reaction rates of both torrefaction and mineral carbonation reactions, the torrefaction gas was circulated between the two reactors to provide longer contact times between mining residues and CO<sub>2</sub> to enable its fixation. Before entering the torrefaction reactor, a sample of gas was taken by an Agilent micro-GC 3000 to quantify the concentrations of CO, CH<sub>4</sub>, H<sub>2</sub> and CO<sub>2</sub>. To start-up the tandem torrefaction-carbonation, biomass and water partially-saturated (50%) mining residue samples were first loaded in the torrefaction and carbonation reactors, respectively. Afterwards, the whole assembly was purged under nitrogen stream (1 L/min) to remove pre-existing oxygen and carbon dioxide. Once micro-GC and CO<sub>2</sub> probe O<sub>2</sub> and CO<sub>2</sub> signals were below detection limits, gas circulation and torrefaction reactor heat-up were initiated.

After test completion, the torrefied birch wood removed from the steel grid was dried at 110°C. In the case of IL-impregnated birch wood, the solid biomass was first mixed with water and immersed in an ultrasound bath at 60°C to separate IL from birch wood. The samples then were placed on a filter paper and washed with approximately 200 mL of distilled water using vacuum filtration. The solid recovered was dried in an oven at 110°C. The solid products obtained after torrefaction were analyzed to quantify their properties after thermal treatment. The solid products were weighed to obtain their mass yield ( $Y_M = \text{\%mass solid product/mass feed}$ ) after torrefaction. The C, H, N, S contents of the samples were also measured using an elemental analyzer (Fisons EA 1108CHNS). All measurements were repeated twice and their averages were reported. The higher heating value (HHV) of the samples before and after torrefaction were determined using a relationship based on carbon, hydrogen, oxygen, sulfur, nitrogen and ash content of biomass suggested by Channiwala et al. [31] where:

$$\text{HHV (kJ/g)} = \{0.3491 \times \text{C}\} + \{1.1783 \times \text{H}\} + \{0.1005 \times \text{S}\} - \{0.1034 \times \text{O}\} - \{0.0151 \times \text{N}\} - \{0.0211 \times \text{Ash}\}$$

With C, H, S, O, N and Ash representing carbon, hydrogen, sulfur, oxygen, nitrogen and ash mass percentages, respectively. Using the solid product HHV, the energy density ( $e = \text{HHV solid product}/\text{HHV feed}$ ) and energy yield ( $Y_e = e \cdot Y_M$ ) of the solids were also obtained. To investigate the effect of torrefaction on the samples hydrophobicity, equilibrium moisture content (EMC) analysis was also performed on the torrefied samples. EMC of raw and torrefied biomass samples were obtained by putting 300 mg samples in a vapor-saturated environment controlled at 25°C.

### 4.3. Results and discussion

#### 4.3.1. Analysis of torrefaction products

To determine the extent of torrefaction, the solid torrefaction products were thoroughly analyzed. The mass yield of solid products of the IL and dry torrefied birch were 73.2% and 75.1 %, respectively, which lie within the expected range for torrefaction (Table 4-1). Due to the considerably accelerated [Emim][OTf]-mediated torrefaction rate resulting in a lower mass yield of torrefied solid product, IL-impregnated birch was torrefied for a shorter time (30 min) compared to its dry torrefaction (60 min). As seen in Table 4-1, both IL-impregnated and dry-treated torrefied birch exhibited increased HHV showing improvements in birch energy density after torrefaction. The carbon content in the as-received birch (47.9 wt%) increased to 51.8 wt% and 48.8 wt% for dry and IL-impregnated torrefied sample, respectively (Table 4-1). Also, the carbon content of dry-torrefied birch exceeded that of IL-impregnated birch. Detection of 0.5 wt% of sulfur in the washed and dried IL-torrefied birch samples indicated that nearly 4 wt% of IL resisted the washing step and kept trapped inside the solid structure of the torrefied product. IL leftover in the torrefied birch reduces its HHV since [Emim][OTf] carbon represents 32.3%.

**Table 4-1** . Ultimate analysis (wt%), mass yield, higher heating value and energy yield of as-received and torrefied birch.

Samples	C	H	N	S	O	Ash	Mass yield ( $Y_M$ , %)	Energy Yield ( $Y_e$ , %)	HHV (kJ/g)
As received birch	47.9	6.1	0.02	0	45.3	0.7	.....	100	19.2
Dry torrefied	51.8	6.03	0.14	0	41.2	0.8	75.1	81.7	20.9
[Emim][OTf] torrefied	48.8	6.1	0.37	0.5	42.8	0.5	73.2	75.4	19.8

Resting the IL carbon contribution from that of IL-torrefied birch boosts torrefied birch carbon content to 49.5 wt% which is still lower than that of dry torrefied birch. IL-impregnated torrefied wood had considerably higher rates of decomposition though this was counterbalanced by a slight loss in quality of torrefied solid product in comparison to classical dry torrefaction. The EMC values of IL-impregnated and dry torrefied birch were, respectively, 30% and 40% lower as compared to as-received birch. The slightly higher moisture uptake of IL-treated birch was due to the [Emim][OTf] hydrophilic nature possibly compensating for the breakage of hydroxyl groups which promote hydrophobic surface during torrefaction [32].

#### 4.3.2. Carbonation-free torrefaction

Two blank experiments were performed in the torrefaction-carbonation assembly to monitor the concentrations of CO<sub>2</sub>, CO, CH<sub>4</sub> and H<sub>2</sub> produced during dry torrefaction and IL-impregnated torrefaction of 1 g of birch in the absence of mining residues. CO<sub>2</sub> concentration during dry torrefaction of birch increased over time leading to its build-up in the setup as measured in upper and lower carbonation compartments (Figure 4-2).

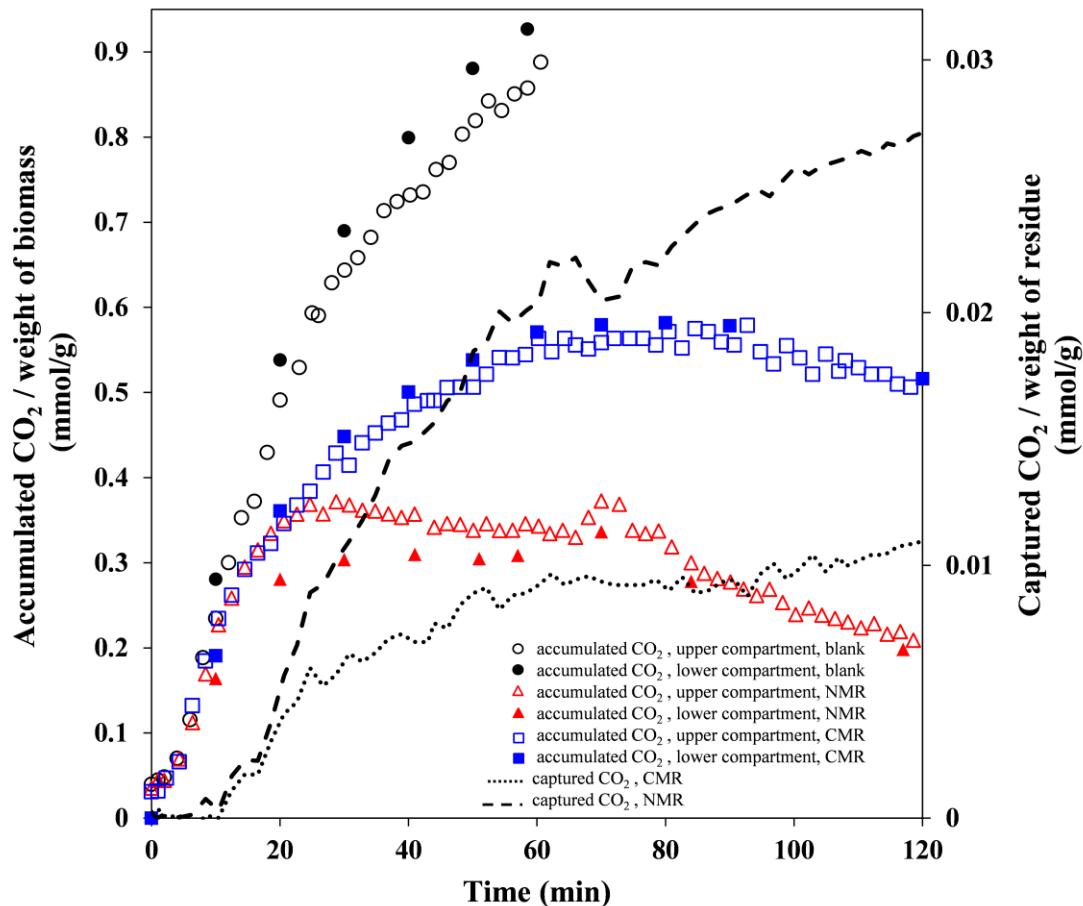


**Figure 4-2.** Time evolution of accumulated (left y-scale) and captured (right y-scale) CO<sub>2</sub> during birch dry torrefaction at 260°C. The marginal differences in CO<sub>2</sub> compositions in upper (empty symbols) and lower (filled symbols) compartments is worthy of notice.

Torrefaction at 260°C featured an early fast CO<sub>2</sub> production lasting 20 min where 58 % of CO<sub>2</sub> was produced. Fast hemicellulose decomposition starting at near 220°C, was likely the cause of such considerable CO<sub>2</sub> release in the first 20 min of torrefaction [33]. However, cellulose and lignin are also decomposed slowly along with hemicellulose leading to the production of  $9 \times 10^{-3}$  mol/g of CO<sub>2</sub> in 60 min. This amounted only to 16.2% of the carbon lost by birch during dry torrefaction. Besides carbon dioxide, carbon release also took place in the form of condensable hydrocarbons, *e.g.*, acid formic and acetic [22], CO and CH<sub>4</sub>. The rate of CO production was almost constant during blank test torrefaction (Figure 4-3 a) and its amount at the end of torrefaction contributed 40% of that of carbon dioxide ( $0.33 \times 10^{-3}$  mol/g; Figure 4-3 c).

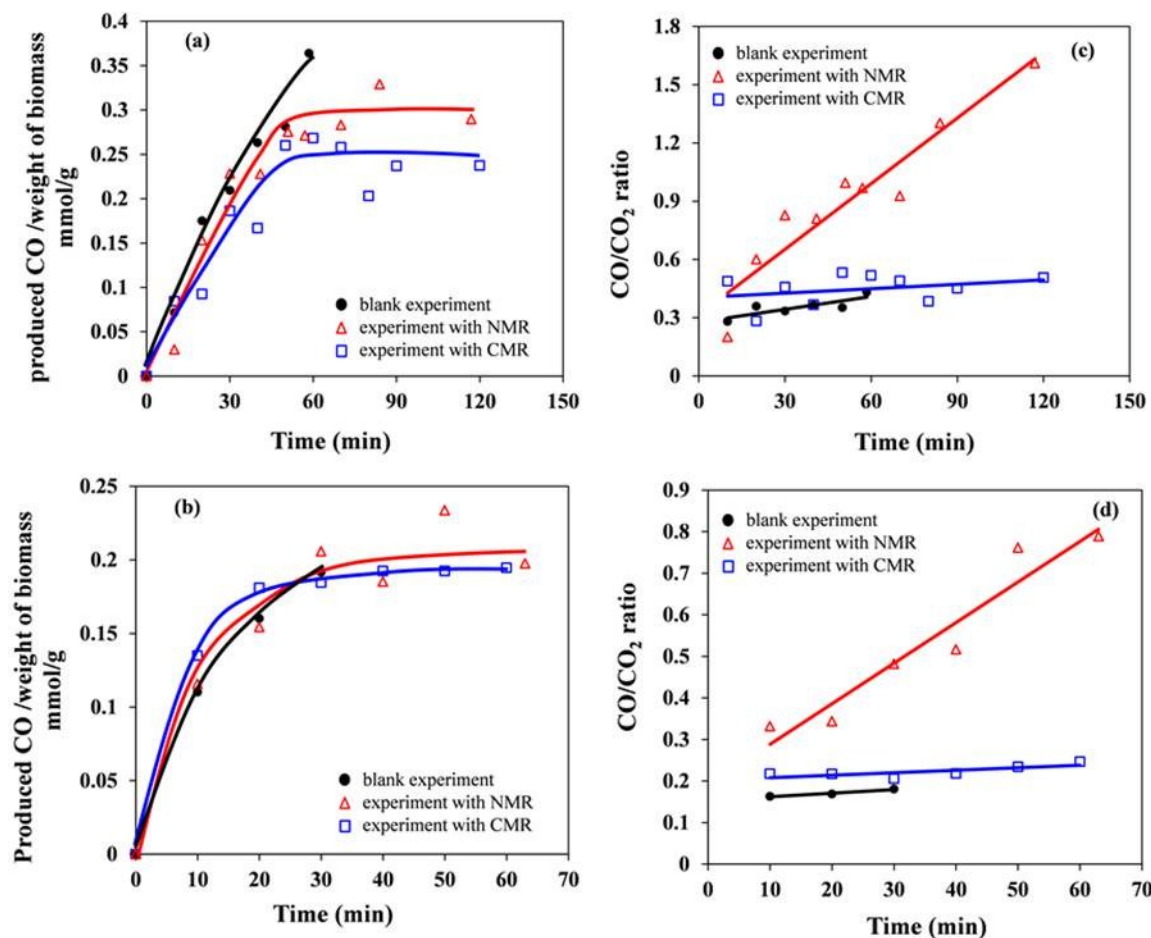


**Figure 4-3.** Time evolution of accumulated CO during a) dry birch torrefaction b) IL-impregnated birch torrefaction. Time evolution of CO/ CO<sub>2</sub> mole ratio during c) dry birch torrefaction d) IL-impregnated birch torrefaction

The profile of carbon dioxide production during the blank experiment of [Emim][OTf] impregnated birch torrefaction is presented in Figure 4-4. Torrefaction was performed at 260°C for the duration of 30 min. Torrefaction of IL-impregnated birch also showed a fast release of carbon dioxide over the first 10 min followed by a gentler rate up to 30 min. The rate of cellulose decomposition was stimulated by [Emim][OTf] at 260°C. This translated into CO<sub>2</sub> production ( $1.1 \times 10^{-3}$  mol/g) in 30 min outpacing by 20% that produced in 60 min by birch dry torrefaction. Independent thermal treatments of [Emim][OTf] at [21] 260°C unveiled neither CO<sub>2</sub> production nor IL thermal degradation confirming that CO<sub>2</sub> produced originated solely from birch decomposition. The release of CO vis-à-vis CO<sub>2</sub> was quite marginal, *i.e.*,  $0.19 \times 10^{-3}$  mol/g (Figure 4-3 b) which was 47.5% less than that produced during birch dry torrefaction (Figure 4-3 a). However, the proportional changes in the amounts of CO and CO<sub>2</sub> led to almost constant CO/CO<sub>2</sub> ratio for dry and IL-impregnated

torrefaction of birch alike (Figure 4-3 c,d). Likewise, no methane production was observed during torrefaction of IL-impregnated birch.

#### 4.3.3. Coupled torrefaction-carbonation

CO<sub>2</sub> evolution in the torrefaction-carbonation assembly after CMR and NMR were loaded in the carbonation reactor and birch dry torrefaction enabled is shown in Figure 4-2. Carbonation of CMR and NMR residues started almost 10 min after the onset of torrefaction. Such short delay was attributed to diffusion limitation of CO<sub>2</sub> in the residue pore water before reacting with the leached magnesium. The NMR carbonation rate outpaced that of CMR under identical conditions. The unreacted CO<sub>2</sub> in the presence of NMR peaked around  $0.37 \times 10^{-3}$  mol/g at 25 min of torrefaction. This was almost 36% lower than in the blank carbonation-free experiment demonstrating that both CO<sub>2</sub> production and sequestration were occurring simultaneously. Although CO<sub>2</sub> is still produced in the torrefaction reactor, the rate of carbonation was higher than the rate of CO<sub>2</sub> production leading to the decrease of CO<sub>2</sub> concentration in the tandem assembly. Up to 60 min torrefaction time (Figure 4-2), almost 62% of carbon dioxide produced was sequestered within the NMR samples. After this time period, birch torrefaction was suddenly quenched while the gas stream in the assembly was recirculated and depletion of CO<sub>2</sub> solely due to carbonation at ambient temperature was monitored. As seen in Figure 4-2, gaseous CO<sub>2</sub> was depleting very fast as no carbon dioxide was coming from the torrefaction reactor. It was estimated that 0.34% of NMR magnesium was carbonated in 2 h to displace 42% of the produced CO<sub>2</sub>. The rate of CMR carbonation was slower than the rate of CO<sub>2</sub> production in the torrefaction reactor. After 60 min torrefaction, CO<sub>2</sub> concentration was 35.9% lower than that in the blank experiment and only 0.17% of CMR magnesium was carbonated in 2 h. Residue carbonation also led to an increase of CO/CO<sub>2</sub> ratio (Figure 4-3 c) due to both CO<sub>2</sub> sequestration and continuous CO generation (Figure 4-3 a). The CO/CO<sub>2</sub> ratio obtained using NMR exceeded that obtained with CMR (Figure 4-3 c).

Carbonation of [Emim][OTf]-torrefied birch in the presence of CMR and NMR is shown in Figure 4-4. In these series of experiments, torrefaction lasted 30 min before the torrefaction reactor was quenched keeping gas recirculation for another 30 min NMR and CMR carbonation period.

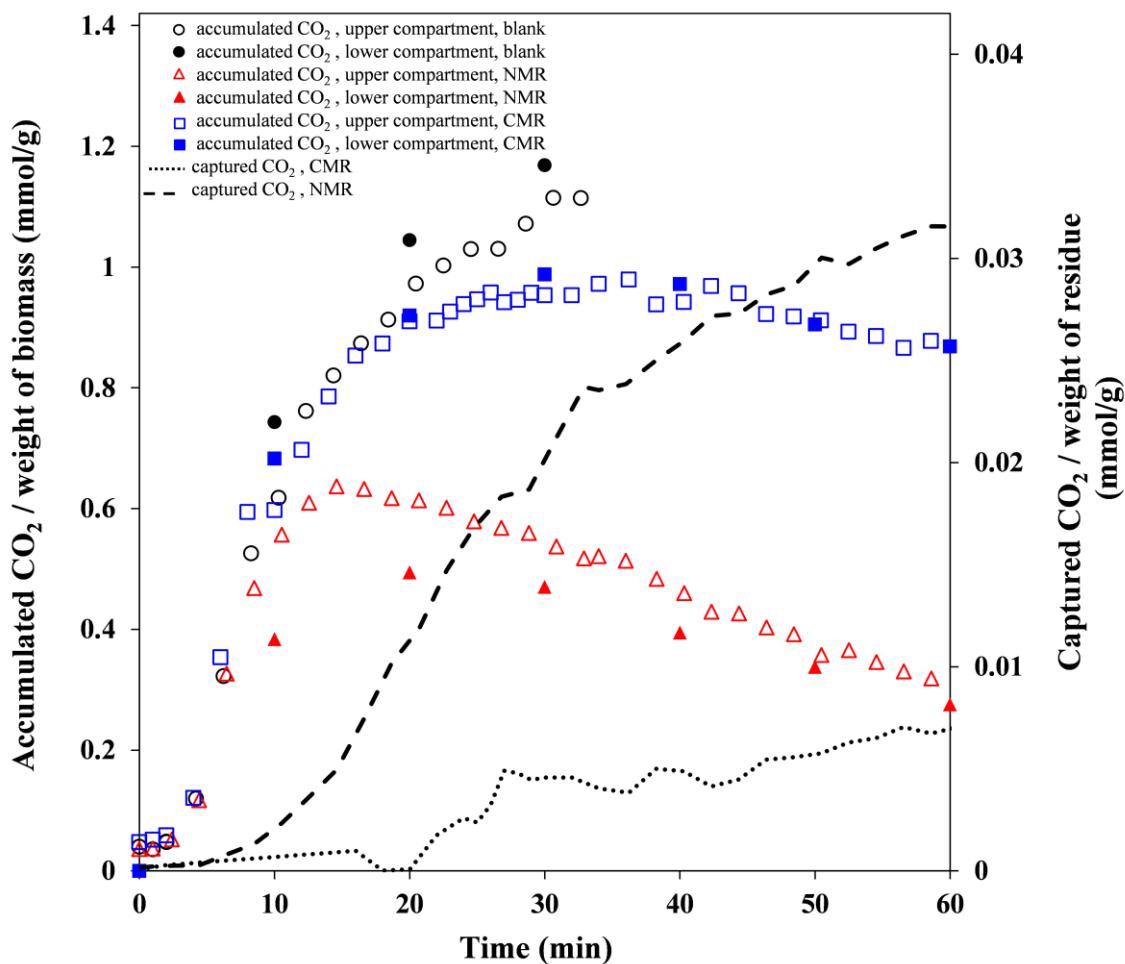


**Figure 4-4.** Time evolution of accumulated (left y-scale) and captured (right y-scale) CO<sub>2</sub> of the torrefaction of IL-impregnated birch at 260°C. Differences in CO<sub>2</sub> compositions in upper (empty symbols) and lower (filled symbols) compartments reveal strong carbonation reactivity of residues

Carbonation of NMR started after 5 min. The large difference between 10 to 30 min in CO<sub>2</sub> concentrations from upper and lower compartments of the carbonation column is an indicator of fast NMR carbonation. CMR carbonation pattern was similar to that observed during birch dry torrefaction. CO<sub>2</sub> accumulated after 30 min of experiment using CMR was 15% lower than that of the blank carbonation-free test. Yet, by letting carbonation to proceed after 30-min torrefaction, the CO<sub>2</sub> content in the assembly reduced to  $0.87 \times 10^{-3}$  mol/g corresponding to the capture of 22% of the total of CO<sub>2</sub> produced. Magnesium involved in the carbonation reaction using CMR and NMR during IL-torrefaction of birch amounted only to 0.11% and 0.4%, respectively.

A special attention is paid in this study to reduce the experimental errors resulting from the coupling of torrefaction and carbonation reactors. The temperature and the residence time of birch wood in the torrefaction reactor was controlled ( $260 \pm 0.1$  °C) so that the mass yield of IL assisted and dry torrefied birch wood samples varied by less than 1% for different experiments. The birch wood samples, all taken from the same batch, showed similar CHNS contents which enhanced the repeatability of the torrefaction experiments. The variation in the amount of produced carbon dioxide is also less than 2.5% for the torrefaction experiments repeated at 260 °C for IL assisted and dry torrefied birch wood samples. Furthermore, although the CMR and NMR samples used at different carbonation experiments were picked from the same batches of residues, the heterogeneity of residues could lead to some differences in their extent of CO<sub>2</sub> sequestration. Assima et al. [29,30] investigated the effect of heterogeneity of CMR and NMR residues on the extent of CO<sub>2</sub> sequestration at the different CO<sub>2</sub> concentrations. The carbonation experiments performed with NMR residue showed that the heterogeneity of this sample could lead to less than 0.6% difference in its extent of CO<sub>2</sub> sequestration. This value was higher for CMR (nearly 2.1%).

#### **4.3.4. Origin of residue carbonation activity**

The superior activity of NMR compared to CMR is attributed to the higher content of native brucite in the former [30] (10.9 wt% and 2.94 wt%, respectively). Brucite is dissolving rapidly in the pore water, liberating magnesium ions which were promptly bounded with dissolved CO<sub>2</sub>. Chrysotile, and to a lesser extent lizardite, at their contact with water also led to the leaching of additional Mg ions [30]. In the presence of dissolved CO<sub>2</sub> species, the leached Mg is precipitated in the form of magnesium carbonates under alkaline medium according to the following reactions [30].

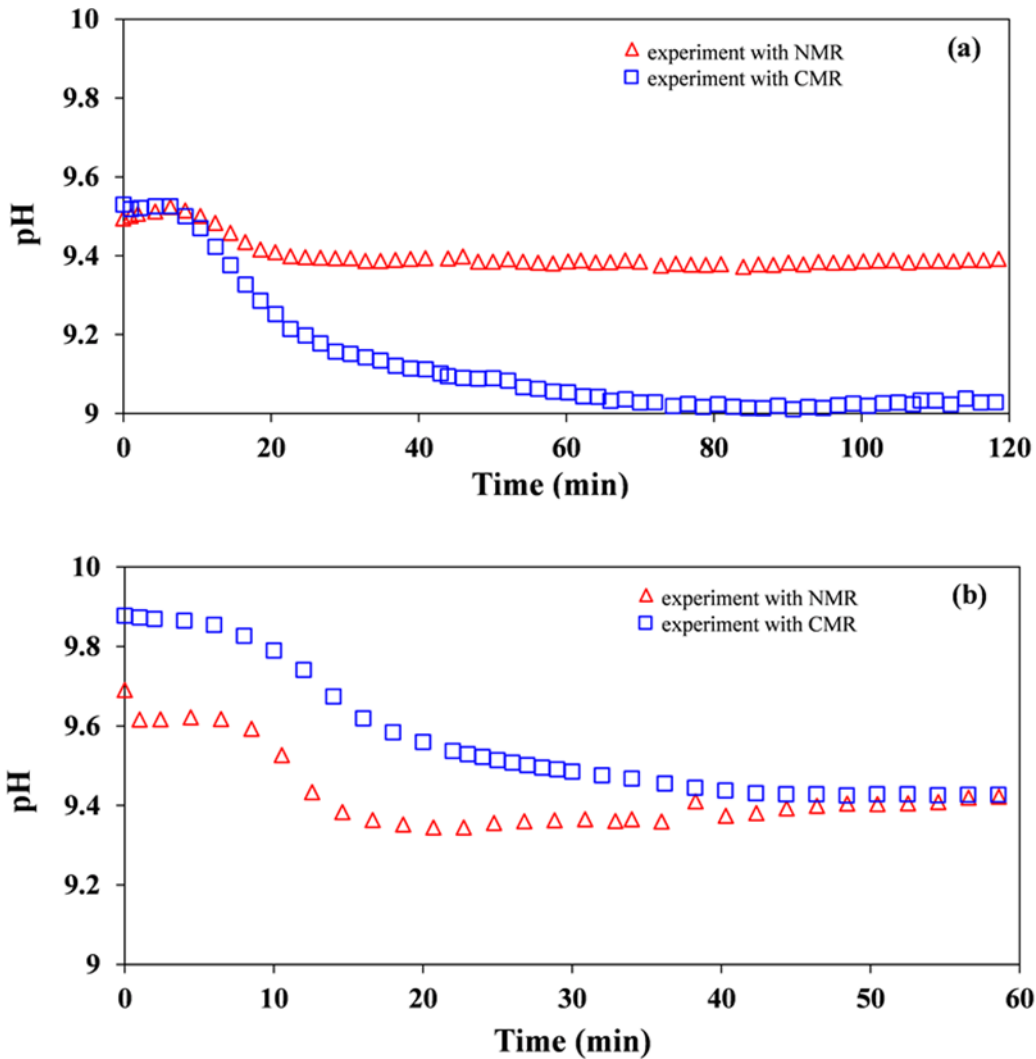
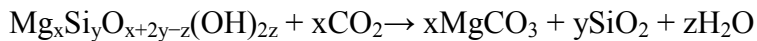
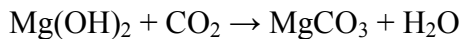


**Figure 4-5.** pH profiles versus time during a) dry birch torrefaction b) IL-impregnated birch torrefaction



The initial pH of both NMR and CMR pore water was in the range of 9.5 to 10 (Figure 4- 5 a,b) due to residue dissolution, and especially brucite, in the pore water. The pH of both media began to drop 5 min after torrefaction was started. The drop in pH of NMR during torrefaction was lower than with of CMR. Also, the pH of NMR reached a plateau in less than 20 min while a steady decrease of pH for CMR was observed during the whole 60 min of torrefaction. This pH decrease is attributed to the dissolution of CO<sub>2</sub> in pore water [29]. The brucite-rich NMR sample led to a less pronounced pH drop since enough brucite was

dissolved producing sufficient amount of hydroxide to compensate for the acidity generated by CO<sub>2</sub> dissolution. The contribution of both dissolved and leached ionic species could be also seen through the trend of ionic conductivities shown in Figure 4-6 a,b. The continuous dissolution of CO<sub>2</sub> as well as Mg leaching led to the observed increase in ionic conductivity of the moistened residues. However, the increase in CMR ionic conductivity exceeded that of NMR. This could be attributed to the higher rate of Mg carbonation with NMR leading to the formation and precipitation of MgCO<sub>3</sub> subsequently resulting in less ionic species in NMR pore water than CMR. The unchanged liquid saturation level during carbonation is worthy of notice (Figure 4-6 a,b).

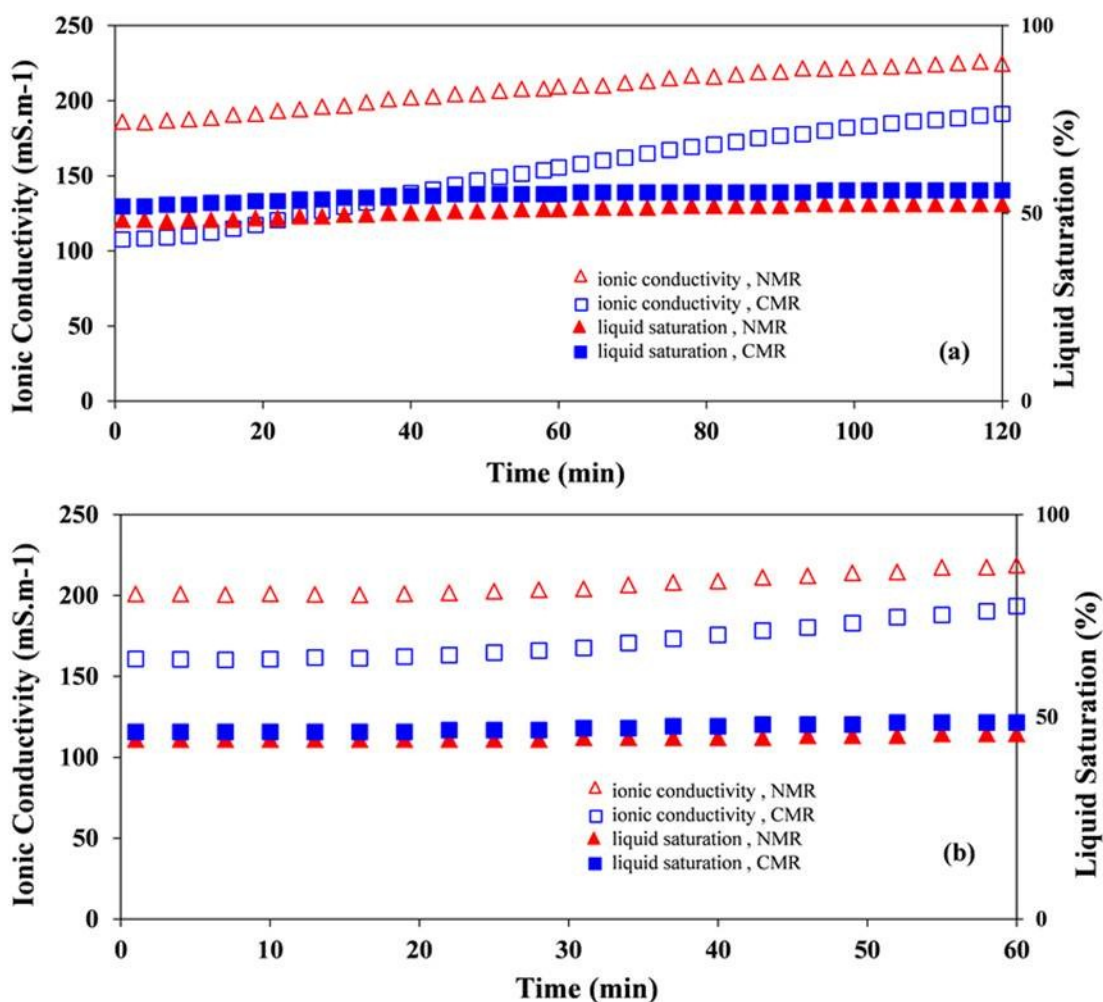


**Figure 4-6.** Profiles of ionic conductivity and liquid saturation versus time during a) dry birch torrefaction b) IL-impregnated birch torrefaction

#### 4.3.5. Effect of CO and CH<sub>4</sub> on residue carbonation

Carbon monoxide and methane built up in the recirculating gas during torrefaction-carbonation. To investigate the effect of increasing CH<sub>4</sub> and CO concentrations on the rate of carbonation, further studies were performed by contacting NMR with two simulated torrefaction gases having different CO and CH<sub>4</sub> contents. In the first experiment, the upper carbonation compartment was filled with a gas mixture composed of 3.23 / 1.57 / 0.52 mole% of CO<sub>2</sub>, CO and CH<sub>4</sub>, respectively in N<sub>2</sub> gas, while the lower compartment was initially purged with pure nitrogen. Another experiment was performed with a mixture richer in CO and CH<sub>4</sub> by filling the upper compartment with a gas mixture consisting composed of 3.13 / 9.2 / 3.15 mole% of CO<sub>2</sub>, CO and CH<sub>4</sub>, respectively in N<sub>2</sub> gas. At t = 0, the upper compartment gas contacted with the NMR bed by opening the separation gate (Figure 4-1) between the two compartments and recirculating the gas using a peristaltic pump. The CO<sub>2</sub> concentration in the upper and lower compartments was monitored for 1 h using two CO<sub>2</sub> probes. The trend of CO<sub>2</sub> concentration is shown in Figure 4-7 where the sequestered CO<sub>2</sub> was determined by subtracting the instantaneous CO<sub>2</sub> amount from the initial amount of carbon dioxide. As can be observed in Figure 4-7, the rate of carbonation within NMR was barely affected by the CO and CH<sub>4</sub> composition in the reacting gas. The difference observed on the amount of carbonation sequestered under various carbon monoxide and methane contents could be attributed to the tiny difference in the initial CO<sub>2</sub> concentration of the reacting gas mixtures [29,30].

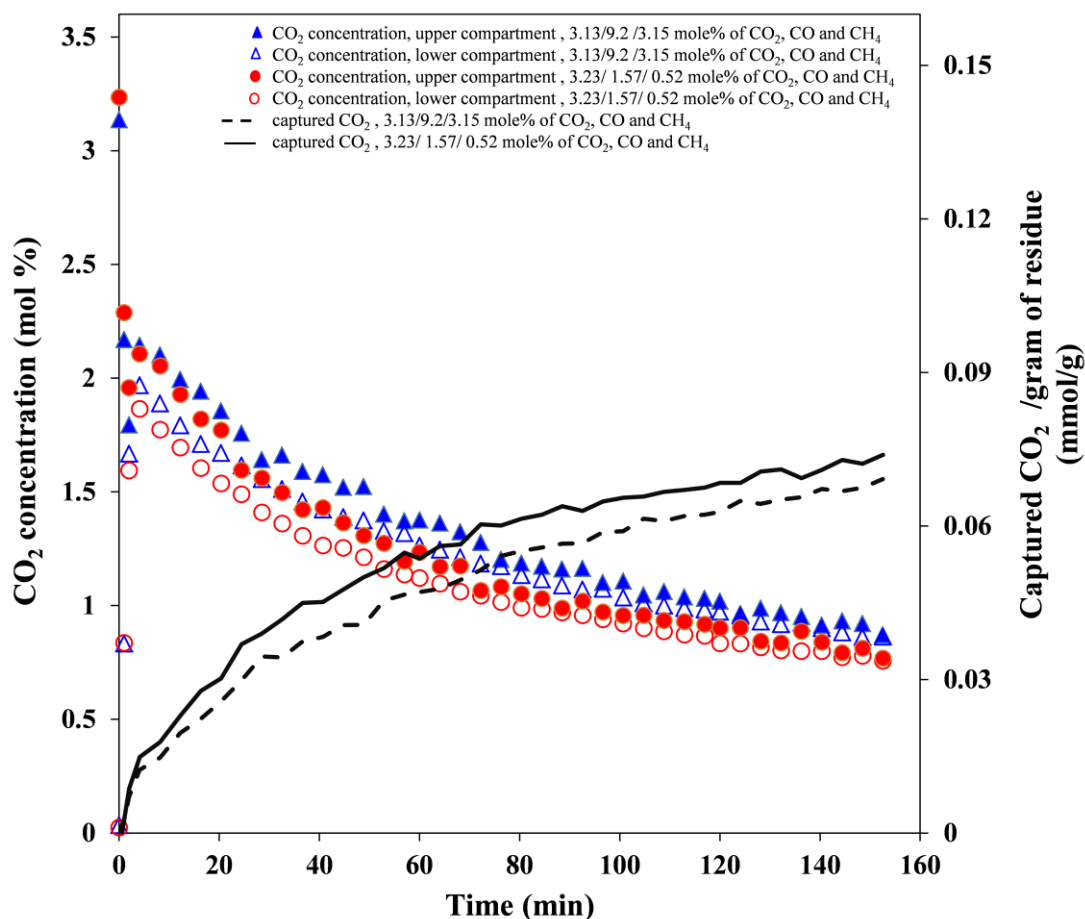


**Figure 4-7.** Effect of CO and methane content on CO<sub>2</sub> instantaneous concentration and amount of captured CO<sub>2</sub> using NMR

#### 4.3.6. Effect of temperature on residue carbonation

The effect of temperature on the rate of carbonation was also investigated. Nearly 8 g of pre-watered NMR samples (liquid saturation = 50%) was placed on a steel mesh and the torrefaction gas was passed through the residue bed. The torrefaction gas was produced by dry torrefaction of one gram of birch samples for 60 min and NMR carbonation was carried out at three different temperatures of 25°C, 45°C and 65°C. Blank experiments performed without NMR residue showed production of ca.  $0.95 \times 10^{-3}$  mol of CO<sub>2</sub> after 60 min of dry torrefaction (Figure 4-8). NMR carbonation at 25°C reduced considerably the amount of CO<sub>2</sub> in the assembly during torrefaction. At the end of torrefaction, the amount of CO<sub>2</sub> accumulated in the assembly was  $0.59 \times 10^{-3}$  mol, a reduction of 38% in the amount of accumulated CO<sub>2</sub> corresponding to almost 0.70% of carbonated Mg at 25°C.

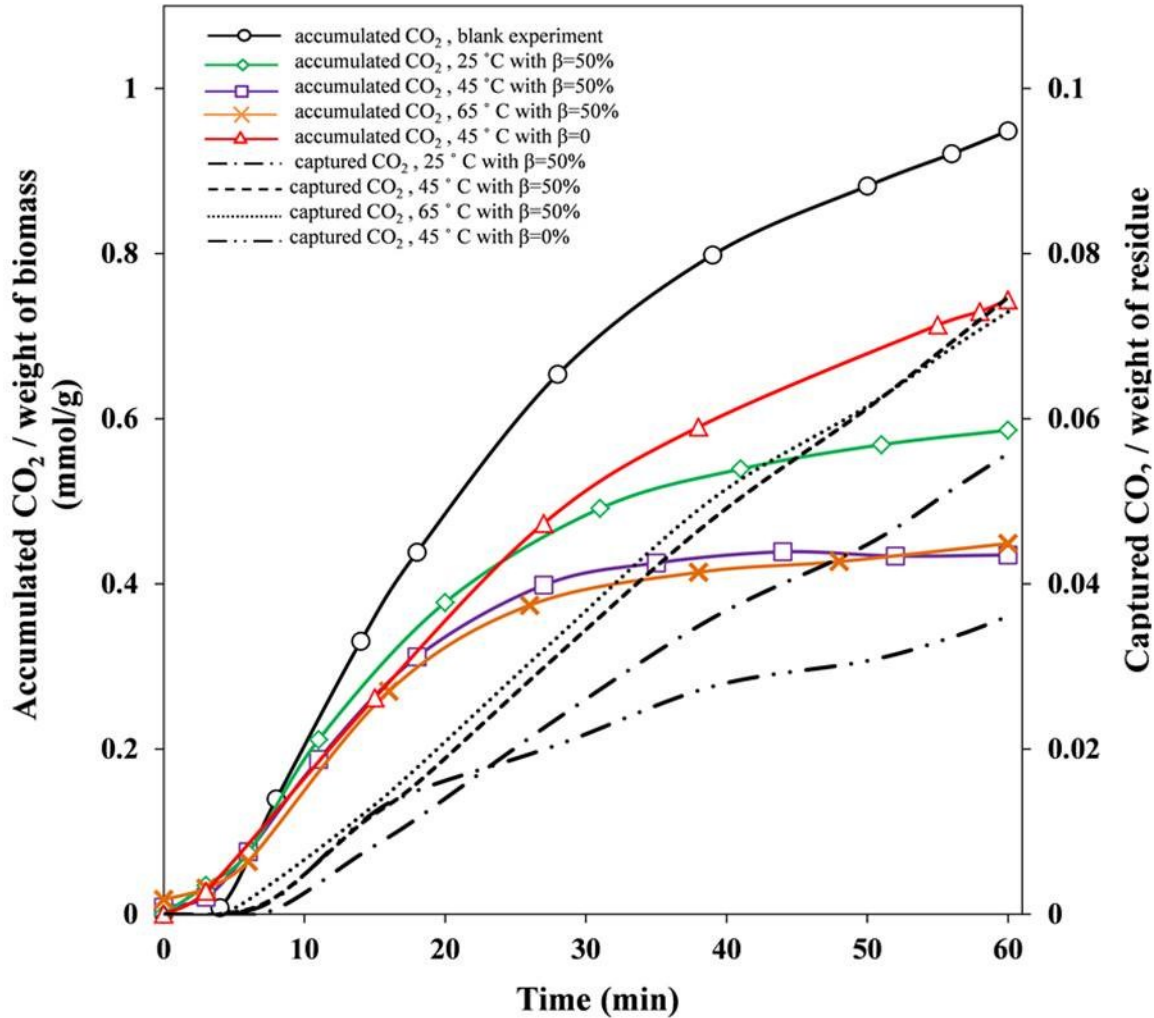


**Figure 4-8.** Effect of temperature on accumulated and captured CO<sub>2</sub> versus time during dry birch torrefaction in the presence of NMR (liquid saturation  $\beta = 50\%$ )

Carbonation at 45°C lowered CO<sub>2</sub> accumulated to  $0.43 \times 10^{-3}$  mol after 60 min (Figure 4-8) corresponding to carbonation of almost 55% of carbon dioxide produced during torrefaction and 0.93% of residue Mg. Increasing temperature to 65°C did not translate into significant gain in the extent of carbonation with a final accumulated CO<sub>2</sub> in the assembly equal to  $0.45 \times 10^{-3}$  mol. The amount of pore water of NMR sample after one hour of carbonation at 65°C was reduced by 65% while carbonation at 45°C resulted in the evaporation of only 20% of pore water. Evaporation and reduction of the amount of leached Mg at 65°C could be a reasonable explanation to the limited observed carbonation reactivity. The importance of pore water on carbonation was therefore investigated by performing carbonation tests at 45°C without adding at all water to the NMR at the beginning of carbonation test. The rate of carbonation was considerably lower for the dry

NMR at 45°C (Figure 4-8). The accumulated carbon dioxide in the assembly was around  $0.74 \times 10^{-3}$  mol and was considerably higher than that when the residue was moistened at 50% liquid saturation. The presence of some humidity in the torrefaction gas and consequently capillary condensation of water could lead to the limited Mg and CO<sub>2</sub> dissolution which resulted to the observed low reactivity of the dry NMR samples.

#### 4.4. Conclusion

The concept of simultaneous torrefaction and CO<sub>2</sub> sequestration using mining residues was investigated in this study. The use of mining residues led to a considerable reduction in the amount of CO<sub>2</sub> produced by torrefaction. Approximately 62% and 22% of the CO<sub>2</sub> emitted was captured with nickel and chrysotile mining residues, respectively. This discrepancy in carbonation was ascribed to the difference in their mineralogical composition, especially their different contents in brucite. The rate of carbonation was also shown to be highly dependent to temperature, residue pore water and CO<sub>2</sub> composition. Increasing carbonation temperature improved significantly CO<sub>2</sub> uptake. However, under elevated carbonation temperatures, a regular watering of mining residues is required to compensate for the evaporated pore water. Furthermore, capturing CO<sub>2</sub> could increase the concentration of reactive non-condensable gases such as CH<sub>4</sub> and CO which could be burned along with the condensable gases for improved process heat integration. The results obtained in this study showed a good potential of the combined torrefaction and mineral carbonation suggesting that the local torrefaction plants could be built close to the mining residue tailings, especially the ones rich in free brucite, to sequester the produced CO<sub>2</sub> from the torrefaction plants. The CO<sub>2</sub> sequestration in the local torrefaction plants could partly compensate the high CO<sub>2</sub> emission from coal combustion. Considering that the mining residues are abundant and already crushed, they could present a cheap solution for CO<sub>2</sub> sequestration. Bearing in mind that the torrefaction process is performed at 200-300 °C, the required energy for heating the mining residues to 40-50 °C (to increase the carbonation rate) could also be provided by the flue gas generated in the torrefaction plant. The torrefied biomass in the local torrefaction plants could be then pelletized and be transported to the co-firing plants for further mixing with coal in combustors.

## 4.5. References

- [1] Roy J, Sarkar P, Biswas S, Choudhury A. Predictive equations for CO<sub>2</sub> emission factors for coal combustion, their applicability in a thermal power plant and subsequent assessment of uncertainty in CO<sub>2</sub> estimation. *Fuel*. 2009;88:792-8.
- [2] The outlook for energy: a view to 2040. [www.exxonmobil.com/energyoutlook](http://www.exxonmobil.com/energyoutlook); 2013.
- [3] Canada's emissions trends 2012. Environment Canada; 2012.
- [4] McIlveen-Wright DR, Huang Y, Rezvani S, Mondol JD, Redpath D, Anderson M, et al. A Techno-economic assessment of the reduction of carbon dioxide emissions through the use of biomass co-combustion. *Fuel*. 2011;90:11-8.
- [5] Tillman DA. Biomass cofiring: the technology, the experience, the combustion consequences. *Biomass & Bioenergy*. 2000;19:365-84.
- [6] Sami M, Annamalai K, Wooldridge M. Co-firing of coal and biomass fuel blends. *Progress in Energy and Combustion Science*. 2001;27:171-214.
- [7] Demirbas A. Sustainable cofiring of biomass with coal. *Energy Conversion and Management*. 2003;44:1465-79.
- [8] Li J, Yang WH, Blasiak W, Ponzio A. Volumetric combustion of biomass for CO<sub>2</sub> and NO<sub>x</sub> reduction in coal-fired boilers. *Fuel*. 2012;102:624-33.
- [9] Basu P, Butler J, Leon MA. Biomass co-firing options on the emission reduction and electricity generation costs in coal-fired power plants. *Renewable Energy*. 2011;36:282-8.
- [10] Li J, Brzdekiewicz A, Yang WH, Blasiak W. Co-firing based on biomass torrefaction in a pulverized coal boiler with aim of 100% fuel switching. *Applied Energy*. 2012;99:344-54.
- [11] van der Stelt MJC, Gerhauser H, Kiel JHA, Ptasiński KJ. Biomass upgrading by torrefaction for the production of biofuels: A review. *Biomass & Bioenergy*. 2011;35:3748-62.
- [12] Medic D, Darr M, Shah A, Potter B, Zimmerman J. Effects of torrefaction process parameters on biomass feedstock upgrading. *Fuel*. 2012;91:147-54.
- [13] Uemura Y, Omar WN, Tsutsui T, Yusup SB. Torrefaction of oil palm wastes. *Fuel*. 2011;90:2585-91.
- [14] Phanphanich M, Mani S. Impact of torrefaction on the grindability and fuel characteristics of forest biomass. *Bioresource Technology*. 2011;102:1246-53.
- [15] Repellin V, Govin A, Rolland M, Guyonnet R. Energy requirement for fine grinding of torrefied wood. *Biomass & Bioenergy*. 2010;34:923-30.
- [16] Bridgeman TG, Jones JM, Shield I, Williams PT. Torrefaction of reed canary grass, wheat straw and willow to enhance solid fuel qualities and combustion properties. *Fuel*. 2008;87:844-56.

- [17] Pimchuai A, Dutta A, Basu P. Torrefaction of agriculture residue to enhance combustible properties. *Energy & Fuels*. 2010;24:4638-45.
- [18] Deng J, Wang GJ, Kuang JH, Zhang YL, Luo YH. Pretreatment of agricultural residues for co-gasification via torrefaction. *Journal of Analytical and Applied Pyrolysis*. 2009;86:331-7.
- [19] Hoekman SK, Broch A, Robbins C. Hydrothermal carbonization (HTC) of lignocellulosic biomass. *Energy & Fuels*. 2011;25:1802-10.
- [20] Yan W, Hastings JT, Acharjee TC, Coronella CJ, Vasquez VR. Mass and energy balances of wet torrefaction of lignocellulosic biomass. *Energy & Fuels*. 2010;24:4738-42.
- [21] Sarvaramini A, Gravel O, Larachi F. Torrefaction of ionic-liquid impregnated lignocellulosic biomass and its comparison to dry torrefaction. *Fuel*. 2013;103:814-26.
- [22] Prins MJ, Ptasiński KJ, Janssen F. Torrefaction of wood - Part 2. Analysis of products. *Journal of Analytical and Applied Pyrolysis*. 2006;77:35-40.
- [23] L. Milne J, B. Field C. Assessment report from the GCEP workshop on energy supply with negative carbon emissions. 2012.
- [24] Pronost J, Beaudoin G, Tremblay J, Larachi F, Duchesne J, Hebert R, et al. Carbon sequestration kinetic and storage capacity of ultramafic mining waste. *Environmental Science & Technology*. 2011;45:9413-20.
- [25] Pronost J, Beaudoin G, Lemieux JM, Hebert R, Constantin M, Marcouiller S, et al. CO<sub>2</sub>-depleted warm air venting from chrysotile milling waste (Thetford Mines, Canada): Evidence for in-situ carbon capture from the atmosphere. *Geology*. 2012;40:275-8.
- [26] Bea SA, Wilson SA, Mayer KU, Dipple GM, Power IM, Gamazo P. Reactive transport modeling of natural carbon sequestration in ultramafic mine tailings. *Vadose Zone Journal*. 2012;11.
- [27] Wilson SA, Dipple GM, Power IM, Thom JM, Anderson RG, Raudsepp M, et al. Carbon dioxide fixation within mine wastes of ultramafic-hosted ore deposits: examples from the Clinton Creek and Cassiar chrysotile deposits, Canada. *Economic Geology*. 2009;104:95-112.
- [28] Larachi F, Daldoul I, Beaudoin G. Fixation of CO<sub>2</sub> by chrysotile in low-pressure dry and moist carbonation: Ex-situ and in-situ characterizations. *Geochimica Et Cosmochimica Acta*. 2010;74:3051-75.
- [29] Assima GP, Larachi F, Beaudoin G, Molson J. CO<sub>2</sub> sequestration in chrysotile mining residues-implication of watering and passivation under environmental conditions. *Industrial & Engineering Chemistry Research*. 2012;51:8726-34.
- [30] P. Assima G, Larachi F, Beaudoin G, Molson J. Dynamics of carbon dioxide uptake in chrysotile mining residues- effect of mineralogy and liquid saturation. *International Journal of Greenhouse Gas Control*. 2013;12:124-35.
- [31] Channiwala SA, Parikh PP. A unified correlation for estimating HHV of solid, liquid and gaseous fuels. *Fuel*. 2002;81:1051-63.

[32] Peng JH, Bi HT, Lim CJ, Sokhansanj S. Study on Density, Hardness, and Moisture Uptake of Torrefied Wood Pellets. *Energy & Fuels*. 2013;27:967-74.

[33] Yang HP, Yan R, Chen HP, Lee DH, Zheng CG. Characteristics of hemicellulose, cellulose and lignin pyrolysis. *Fuel*. 2007;86:1781-8.



## **Chapter 5 : Integrated biomass torrefaction - chemical looping combustion as a method to recover torrefaction volatiles energy**

**Résumé** La combinaison de la torréfaction de la biomasse et de la combustion en boucle chimique (CBC) a été expérimentalement étudiée. Le concept consiste à brûler les composants volatils issus de la torréfaction à l'aide de l'oxyde de fer utilisé comme transporteur solide d'oxygène et au moyen duquel le gaz de combustion, essentiellement constitué de CO<sub>2</sub> et de vapeur d'eau, est recirculé dans le réacteur de torréfaction pour intégration thermique. En outre, le gaz de combustion CBC dépourvu d'azote et d'oxygène, permet de récupérer du CO<sub>2</sub> pur afin de le capturer ou de le séquestrer, établissant ainsi une intégration pour la torréfaction à empreinte CO<sub>2</sub> négative dans des installations de co-combustion dans le cadre de la réduction des émissions de gaz à effet de serre. Du bois de bouleau a été torréfié à des températures variant entre 260°C et 300°C et les composants volatils résultant de la torréfaction ont été brûlés entre 400 et 600°C sur de l'oxyde de fer transporteur solide d'oxygène convertissant jusqu'à 99% de carbone volatil en CO<sub>2</sub>. La stabilité du transporteur d'oxygène dans la combustion des volatils de torréfaction et dans l'appauvrissement en oxygène au cours de la séquence CBC ont été évalués en termes de désactivation du matériau, de la production du CO et d'hydrogène. L'accumulation de CO<sub>2</sub> et de vapeur d'eau dans le gaz de recirculation ainsi que leur incidence sur les propriétés du produit solide torréfié a été quantifiée en termes de masse et de rendement énergétique, la teneur en humidité à l'équilibre et la broyabilité du bois de bouleau torréfié.

**Abstract** Hyphenation of biomass torrefaction to chemical looping combustion (CLC) was studied experimentally. The concept consists of burning the torrefaction volatiles using iron oxide as solid oxygen carrier whereby the CLC flue gas, mostly non-diluted CO<sub>2</sub> and steam, is recirculated to the torrefaction reactor for heat integration. Also, being deprived of nitrogen and oxygen, the CLC flue gas allows pure CO<sub>2</sub> to be recovered and further captured or sequestered thus setting a frame for a negative net CO<sub>2</sub> torrefaction in co-firing plants to reduce greenhouse gas emissions. Birch wood was torrefied between 260°C and 300°C and the resulting volatiles were burned over iron oxide solid oxygen carriers between 400°C and 600°C converting up to 99% of volatile carbon into CO<sub>2</sub>. Oxygen carrier stability for burning torrefaction volatiles and oxygen depletion during CLC were assessed vis-à-vis deactivation, and CO and hydrogen production. Also, the buildup of CO<sub>2</sub> and water vapor in the recirculating torrefaction gas and their incidence on the properties of torrefied solid product were quantified in terms of mass and energy yields, equilibrium moisture content and grindability of the torrefied birch wood.

## 5.1. Introduction

Coal combustion in the electricity generation plants is considered as one of the most important sources of greenhouse gas emission [1]. Replacing coal with biomass as a renewable CO<sub>2</sub>-neutral energy source in energy conversion systems could be an option to reduce net CO<sub>2</sub> production [2]. However, raw biomass as a fuel features some drawbacks such as low calorific value due to its high moisture and oxygen contents [3,4], high grinding energy requirement due to its rigidity and mechanical strength [5,6], and low flowability and fluidization properties leading to difficulties in feeding it into boilers [7]. Improving these biomass properties via torrefaction is envisioned as a prerequisite step to adapt biomass properties to those of a fuel for efficient coal/biomass co-firing [7]. Torrefaction increases the energy density of biomass by reducing its oxygen content leading to a torrefied biomass product with heating values nearing those of coal [5,8,9]. Furthermore, torrefaction promotes partial depolymerization/decomposition of cellulose and hemicellulose reducing the fibers length and mechanical stability and resulting in improved grinding properties [7,10,11].

Biomass torrefaction is performed at temperatures below 300°C which prompts partial decomposition of hemicellulose, cellulose and lignin biomass constituents [7,12]. Decomposition is accompanied with the release of condensable and non-condensable volatiles such as CO<sub>2</sub>, CO, CH<sub>4</sub>, H<sub>2</sub>O and some hydrocarbon oxygenates (acetic, formic and lactic acids) [13]. In the usual industrial torrefaction practices, the produced volatiles are burned with air in a combustion unit and the hot flue gas is routed toward the pre-drying and torrefaction segments to pick up directly or indirectly its heat content [14,15]. Ideally well-designed torrefaction processes are thermally self-sufficient. That is, if apart from the heat released from the combustion of the torrefaction gases, no additional energy make-up is necessary to ensure their operation [15]. Direct contact of flue gas with biomass during torrefaction could be an efficient way for the heat to transfer to the biomass. However, the presence of residual O<sub>2</sub> in the flue gas could lower the efficiency of biomass torrefaction by burning a fraction of the biomass itself [14,16]. Furthermore, air consisting overwhelmingly of inert N<sub>2</sub> results in the handling of large flue gas volumes which translate into increased investments in terms of piping and ancillary equipment [14,16].

In recent years, the concept of chemical looping combustion (CLC) has been widely studied as a promising alternative for fossil fuel combustion while preventing dilution issues of the flue gas [17-19]. In this concept, the required oxygen for fuel combustion into CO<sub>2</sub> and water is supplied by a solid oxygen carrier such that after oxidation a N<sub>2</sub>-free flue gas is obtained. The concept is implemented in two interconnected reactors with one performing the fossil combustion/solid oxygen carrier reduction while in the other the solid carrier regeneration/oxidation by air takes place [17,18]. However in practice, both spatial [17,18] and temporal segmentations [20] are possible by enabling the solid oxygen carrier either to circulate between two reactors or exposed, in a stationary manner, to periodic oxidative/reductive cycles within the same reactor. The N<sub>2</sub>-free flue gas leaving the combustion reactor could be further processed to remove water and the remaining CO<sub>2</sub> could be captured, sequestered or used for other applications.

To the best of our knowledge, no work has been reported to evaluate whether integration of torrefaction with CLC of torrefaction volatiles is advantageous or not. In the present work the potential of this combination was studied. The gas evolved during torrefaction was routed to a CLC reactor in which the acid hydrocarbons, CO, CH<sub>4</sub> and H<sub>2</sub> are burned at the contact with a solid oxygen carrier and without oxygen gas. The CLC hot flue gas stream, consisting of CO<sub>2</sub> and water, or a fraction of it could be recycled to the upstream torrefaction unit to transfer heat for the torrefaction of the solid biomass particles. This concept is believed to have two main advantages over existing processes. First, the hot flue gas being O<sub>2</sub>-deprived will present no risk of burning biomass during torrefaction. Second, preliminary condensation and separation of water from the CLC flue gas will lead to a pure CO<sub>2</sub> stream which could be captured via physical or chemical solvents in a conventional gas-liquid scrubber [21,22] or directly sequestered in mining residues via dry or wet carbonation [23-25]. As biomass is CO<sub>2</sub>-neutral energy source, a negative net CO<sub>2</sub> emission from torrefaction could be very appealing for mitigating CO<sub>2</sub> emissions in the atmosphere in the future bioenergy co-firing plants hyphenated with carbon capture and storage plants [26].

## **5.2. Experimental**

### **5.2.1. Materials**

Isothermal torrefaction studies were performed using birch, an abundant woody biomass sample from Québec forests. Before the experiments, the as received tiny sheets of birch wood samples were cut into small pieces to obtain woodchips in the size range of 2-4mm. The proximate analysis of the birch wood showed the presence of 5.5% of humidity. The volatiles, fixed carbon and ash content of the samples were 89.4%, 9.8% and 0.7% on dry basis, respectively.

The oxygen carrier used in this study was an iron oxide powder prepared from pure iron metal powder (Atlantic Equipment Engineering, AEE) with 99.9% purity and particle size < 149  $\mu\text{m}$ . Iron oxide is considered as an inexpensive and environmentally safe compared to the other solid oxygen carriers such as nickel and cobalt oxides [27]. Prior to experiments, the iron powder samples were calcined in air for 3 hours at 600°C to form oxide particles.

### **5.2.2. Experimental setup**

The schematic diagram of the experimental assembly is shown in Figure 5-1. The experimental setup mainly consists of two connected torrefaction and chemical looping combustion reactors. Birch wood torrefaction was performed in a stainless steel tube (ID. 34 mm, length 70 cm) placed inside an induction coil while the samples were held atop of a steel grid located in the tube's middle. The torrefaction temperature was controlled by a fiber optic pyrometer connected to a temperature controller to meter the induction-heater power. Temperature was also measured through a K type thermocouple inserted in the center of the biomass layer. The difference in temperature between the bed and tube surface never exceeded 5°C in steady-state conditions. The gas exiting the torrefaction tube was transferred to a CLC stainless steel tube (ID. 10 mm, length 40 cm) from the top via a heated tube preventing volatiles condensation during transit. This latter was located in a vertical electrically heated furnace equipped with a PID temperature controller and a K type thermocouple for CLC temperature control. The combustion gas exiting the CLC reactor

was sent to an ice water cold trap to separate the remaining volatiles from the gas before samples were analyzed using Agilent micro GC 3000 for their CO, CH<sub>4</sub>, H<sub>2</sub> and CO<sub>2</sub> composition.

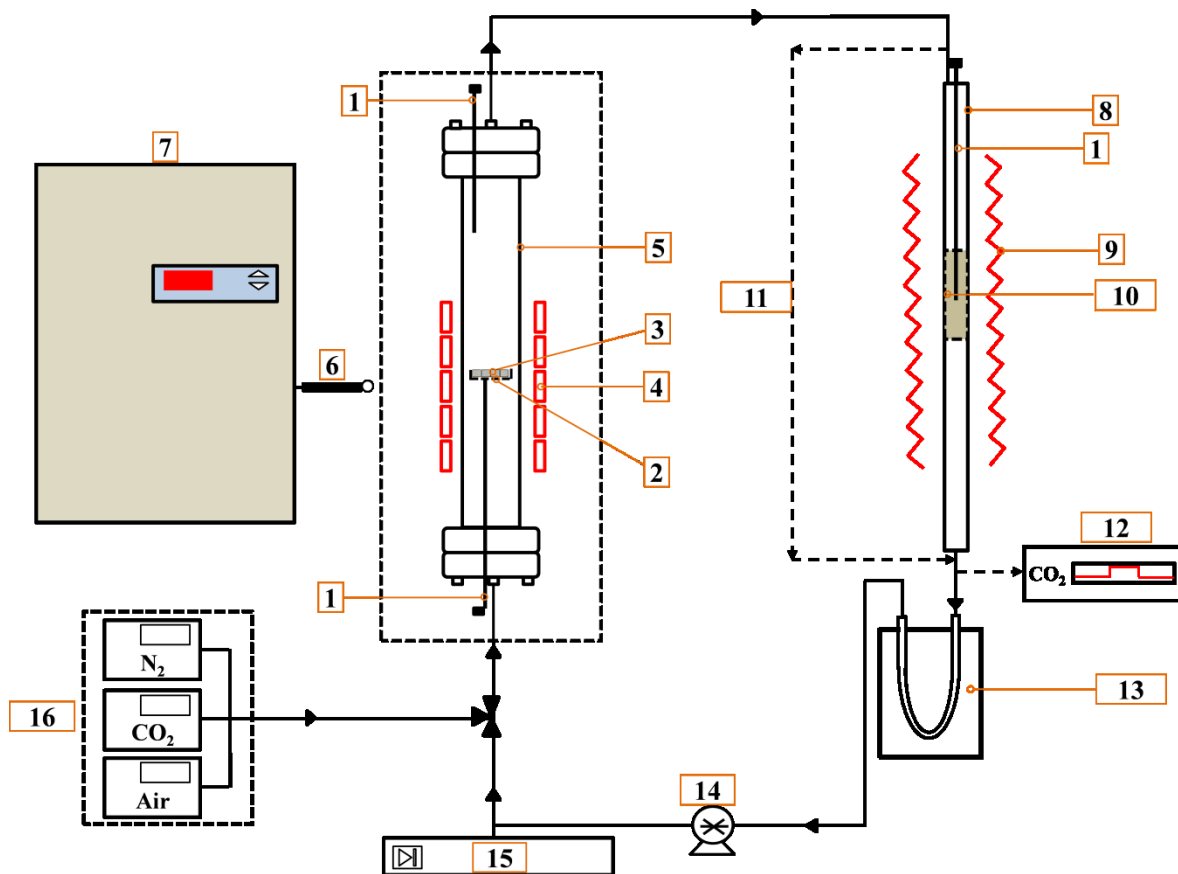


**Figure 5-1.** The schematic of experimental torrefaction-chemical looping combustion assembly: (1) K type thermocouple (2) stainless steel mesh (3) birch sample (4) induction coil (5) stainless steel torrefaction reactor (6) pyrometer (7) induction heater power supply (8) chemical looping combustion reactor (9) electric heater (10) iron/iron oxide fixed bed (11) CLC shortcut line (12) CO<sub>2</sub> infrared detector used during iron oxide regeneration (13) cold trap (14) peristaltic pump (15) micro GC (16) mass flow meters.

The following procedure was applied for performing simultaneous torrefaction and CLC experiment: initially 500 mg of birch wood and 10 g of iron oxide particles were loaded in the middle of torrefaction and CLC reactors, respectively. Next, the CLC reactor was heated to the desired temperature and kept there for 30 min to stabilize its temperature. Afterwards, the entire assembly was purged with N<sub>2</sub> (CO<sub>2</sub>, or mixture thereof) at 1 L/min to get rid of remnant gaseous oxygen. After oxygen was below micro GC detection limit, gas recirculation in the torrefaction-CLC assembly was resumed and torrefaction reactor

temperature was raised from ambient to either 260°C or 300°C and kept there for 60 and 20 min durations, respectively. The concentration of CO<sub>2</sub>, CO, H<sub>2</sub> and CH<sub>4</sub> accumulated in the assembly was measured every 5 to 6 minutes using micro GC. In some of the experiments referred to blank experiments the CLC reactor was bypassed and the volatiles released from the torrefaction reactor were headed directly to the cold trap without any further combustion in the CLC. These experiments were performed to investigate the accumulation of CO, CO<sub>2</sub>, CH<sub>4</sub> and H<sub>2</sub> in the assembly during the birch wood torrefaction and in the absence of CLC.

A regeneration cycle was started at the end of the test where the solid oxygen carrier was regenerated at 600 °C using oxygen (5% O<sub>2</sub> in N<sub>2</sub>) as an oxidant to burn the carbon deposits that formed on the surface of iron oxide particles. CO<sub>2</sub> evolved during regeneration was monitored online using an infrared CO<sub>2</sub> detector to quantify the amount of deposited carbon in each combustion cycle. Finally, the dry torrefied birch wood was removed from the steel grid and then weighed to obtain its mass yield ( $Y_M = \text{\%mass solid product/mass feed}$ ). The C, H, N, S contents of the samples were obtained using an elemental analyzer (Fisons EA 1108CHNS). All measurements were repeated twice and their averages reported. The higher heating value (HHV) of the samples before and after torrefaction was determined using a relationship obtained by Channiwala et al. [28] based on carbon, hydrogen, oxygen, sulfur, nitrogen and ash content of biomass. Using the solid product HHV, the energy density ratio ( $e = \text{HHV solid product/HHV feed}$ ) and energy yield ( $Y_e = e \cdot Y_M$ ) were also determined.

Acetic acid is an oxygenated hydrocarbon forming during biomass torrefaction [13,29]. Therefore, acetic acid was used as a model torrefaction volatile compound to assess the long-time stability for the combustion of torrefaction-formed volatiles and the possible effect of deactivation on the distribution of CLC gas products for the iron oxide oxygen carrier. Although acetic acid is only one of the constituents of torrefaction volatiles, application of acetic acid as a model torrefaction volatile compound for long time stability tests has some advantages over the volatiles released from the direct birch torrefaction. First, the concentration and flow rate of volatiles releasing from the birch torrefaction could change with time while the concentration and flow rate of acetic acid as a model

torrefaction volatile was controlled leading to the accurate calculation of its conversion over time during the long time stability tests. Furthermore, the CH<sub>4</sub>, CO and H<sub>2</sub> compounds produced during the birch torrefaction are difficult to be distinguished from them produced due to the lack of oxygen on the solid oxygen carrier. Consequently for these series of experiments 100 mL/min N<sub>2</sub> stream was saturated with acetic acid vapors by bubbling it through a temperature-controlled acetic acid pool. During the combustion cycle, the acid-saturated stream was contacted with 10 g of pre-oxidized iron particles at 600°C in the CLC reactor and the concentrations of CO<sub>2</sub>, CO, H<sub>2</sub>, CH<sub>4</sub>, oxygen and acetic acid were monitored. Likewise, when the combustion activity of the oxygen carrier declined enough, the combustion cycle was switched to a regeneration cycle by sweeping 200 mL/min of oxidizing gas stream (5%O<sub>2</sub> in N<sub>2</sub>) during which the concentrations of CO, CO<sub>2</sub> and O<sub>2</sub> were registered.

The properties of torrefied birch as affected by steam and CO<sub>2</sub> in the torrefaction reactor were compared by conducting birch torrefaction in a 80:20 (mol.%) CO<sub>2</sub>:water mixture and under N<sub>2</sub> environment. These properties were the mass and energy yield, higher heating value, CHO content of torrefied samples, humidity uptake and grindability of torrefied samples. The humidity uptake of torrefied and raw birch samples was measured under various relative humidity environments. A total of six saturated salt solutions with different equilibrium humidity at 30°C were prepared: 7.38% (KOH solution), 11.28 % (LiCl solution), 43.17% (K<sub>2</sub>CO<sub>3</sub> solution), 75.09% (NaCl solution), 83.62% (KCl solution) and 97.08% (K<sub>2</sub>SO<sub>4</sub> solution) [30]. 100 mg of raw and torrefied birch samples, first dried in an oven at 105°C, were placed in flasks containing aforementioned saturated salt solutions. The flasks were kept for one week in a temperature-controlled oven at 30°C while the samples weight change due to humidity uptake was measured daily. Samples reached equilibrium after almost four days. Samples with > 3270 µm initial size were loaded in the grinding chamber in a ball mill operated at 500 rpm speed with balls of 15 mm diameter to determine grindability of torrefied and raw samples. To ensure similar conditions for the different biomass samples, an equal volume of biomass was loaded in the milling chamber. The samples were ground for 30 min and the final samples obtained were sieved with a series of sieves of mesh sizes 3270, 2000, 850 and 355 µm.

## 5.3. Results and discussion

### 5.3.1. Torrefied solid produced in torrefaction-CLC closed assembly

Table 5-1 shows the results of elemental analysis, mass and energy yields and higher heating value of raw birch and torrefied birch samples at 260°C and 300°C for 60 min and 20 min. The mass yield of samples torrefied at 260°C and 300°C were, respectively, around 76 % and 64 %, reflecting enhanced torrefaction rates with increased temperature despite a correspondingly shortened contact time. Torrefaction increased considerably the carbon content in the torrefied birch at the expense of hydrogen and oxygen contents. This reflected in atom ratio reductions from H/C = 1.54 and O/C = 0.72 for birch to H/C = 1.38 and O/C = 0.62 for birch torrefied at 260°C and to H/C = 1.33 and O/C = 0.58 for birch torrefied at 300°C. The decrease in H/C and O/C ratios led to 7.3% and 10.2% increase in HHV of birch torrefied at 260°C and 300°C, respectively. Although torrefaction increases birch HHV, the energy yield of torrefied birch at 260°C and 300°C was 81.8% and 71.4%, respectively, in accordance with partial loss of biomass energy during torrefaction. Such energy yield loss of the resulting torrefied solid is attributed to the release of carbon and hydrogen during torrefaction. On a dry wood basis, birch torrefaction at 260°C led to the respective release of 13.1% and 22.1% of total carbon and hydrogen in the form of condensable and non-condensable gases. These levels were boosted at 300°C torrefaction to 24 % and 34.8 % for carbon and hydrogen, respectively.

**Table 5-1.** Ultimate analysis, mass yield, higher heating value and energy yield of as received and torrefied birch.

Samples	C	H	N	S	O	Ash	Mass yield ( $Y_M$ ,%)	Energy Yield ( $Y_{es}$ ,%)	HHV (kJ/g)
As received birch	47.6	6.1	0	0	45.6	0.7	.....	100	18.7
Torrefied birch (260°C, 60 min)	51.2	5.9	0	0	42.1	0.8	76.2	81.8	20.1
Torrefied birch (300°C, 20 min)	52.7	5.8	0	0	40.7	0.8	64.8	71.4	20.6

### 5.3.2. Gases released in torrefaction-CLC closed assembly

Torrefaction of birch without circulating volatile gas through the CLC reactor was referred to as blank experiment which is represented with black diamond symbols in Figures 5-(2-5). These Figures show that nearly 17.1 % and 13.2 % of total release carbon (obtained from the subtraction of carbon content of each sample before and after torrefaction on the dry basis) was in the form of CO<sub>2</sub> (Figure 5-2 a,b), 7 % and 6.5 % as CO (Figure 5-3 a,b), virtually no hydrogen (Figure 5-4 a,b), and 0.3 % and 0.2 % as CH<sub>4</sub> (Figure 5-5 a,b), respectively, at 260°C and 300°C. Consequently, the balance of the released carbon from the torrefied birch wood at 260°C and 300°C, respectively, contributed 75 % and 80 % of the total released carbon in the form of condensable volatiles.

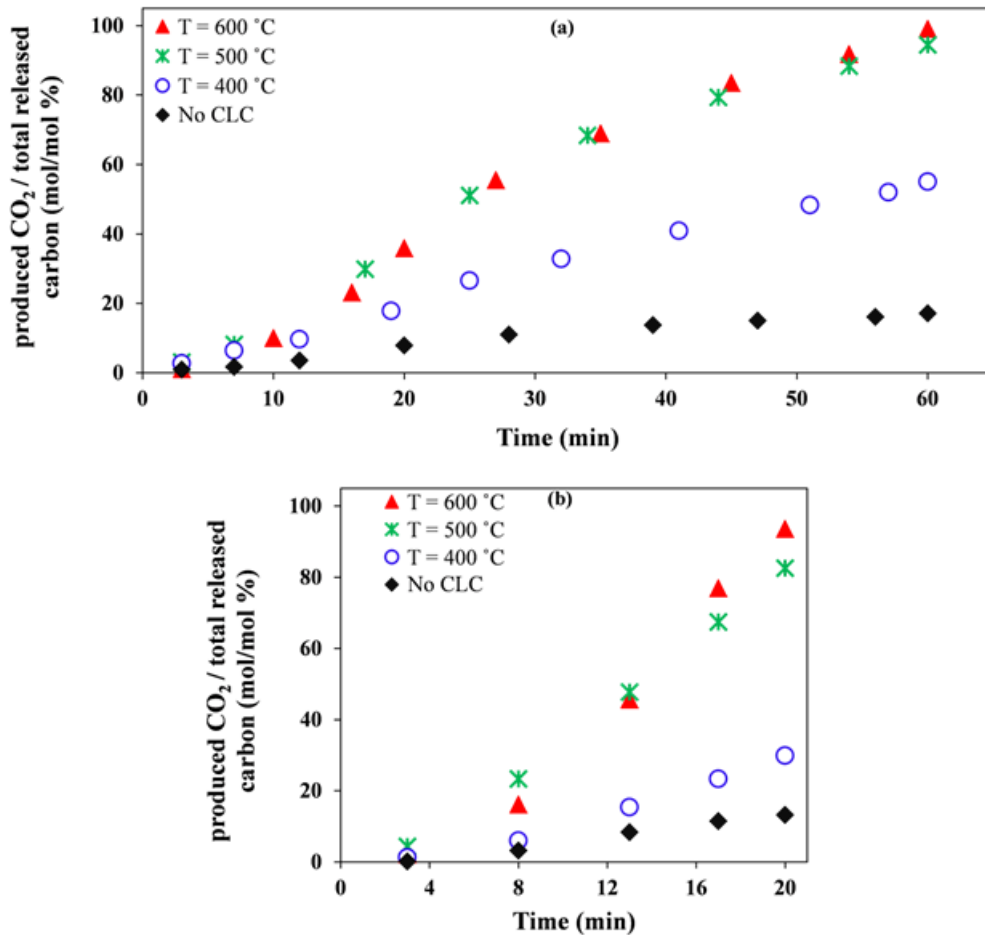


**Figure 5-2.** CO<sub>2</sub> accumulation profiles during the torrefaction of 500 mg of birch at 260°C (a) and 300°C (b) for different combustion temperatures in the torrefaction-CLC assembly.

Combustion of, and energy recovery from, the condensable volatiles is accompanied with production of CO<sub>2</sub>. Figure 5-2 a,b shows the trends of CO<sub>2</sub> production and accumulation in the torrefaction-CLC assembly during the separate torrefaction of birch wood at 260°C and 300°C and further combustion of the volatiles at 400°C, 500°C and 600°C in the CLC reactor. As can be seen, the CO<sub>2</sub> concentration in the assembly increased with time due to simultaneous production of CO<sub>2</sub> from the torrefaction section and the combustion of volatiles in the CLC section. The torrefaction of birch at 260°C and 300°C and further combustion of volatiles at 400°C led to the conversion of 55.1% and 29.9% of total released carbon to CO<sub>2</sub>, respectively. CO<sub>2</sub> levels reached correspondingly 94.5% (99.1%) and 82.5% (93.6%) of total released carbon at 500°C (600°C) combustion temperature. For the same CLC temperature, the extent of volatiles combustion was higher the lower the torrefaction temperature, although volatiles combustion increases conversion to CO<sub>2</sub> using iron oxide particles the higher the CLC temperature. Torrefaction of birch wood at 300°C being much faster than at 260°C was likely to produce some tar compounds [13] with more thermally stable structure than some acid oxygenated hydrocarbons such as acetic acid and formic acid known to be formed at low temperature torrefaction.

Figures 5-(3-5) show the respective trends of CO, H<sub>2</sub> and CH<sub>4</sub> production and accumulation in the torrefaction-CLC assembly as non-condensable gases produced during birch torrefaction. A large amount of CO was produced and accumulated during blank experiments contributing *ca.* 7 % and 6.6% of total released carbon from the torrefied birch at 260 °C and 300 °C, respectively (Figure 5-3 a,b). The accumulated CO in the assembly slightly increased in the experiments performed with CLC reactor at 400°C for the torrefied birch at 260°C and 300 °C. The partial decomposition of volatiles passed through the CLC could produce some CO leading to the observed increase of the CO concentration in the assembly. However, increasing CLC temperature to 500 °C considerably reduced the amount of CO accumulated in the assembly as it was oxidized into CO<sub>2</sub> through the iron oxide bed. At 600°C, CO contributed less than 2 % of total released carbon from the birch wood torrefied at 260 °C and 300 °C. The trend of H<sub>2</sub> production and accumulation in the assembly was somehow different from that of CO. Blank torrefaction at 260°C was virtually exempt of H<sub>2</sub> production unlike at 300°C whereby tiny H<sub>2</sub> amounts were formed. Also, the contacting of torrefaction volatiles with iron oxide at 400°C produced small

amounts of hydrogen (Figure 5-4 a) in accordance with the cracking of some volatiles in the CLC reactor.

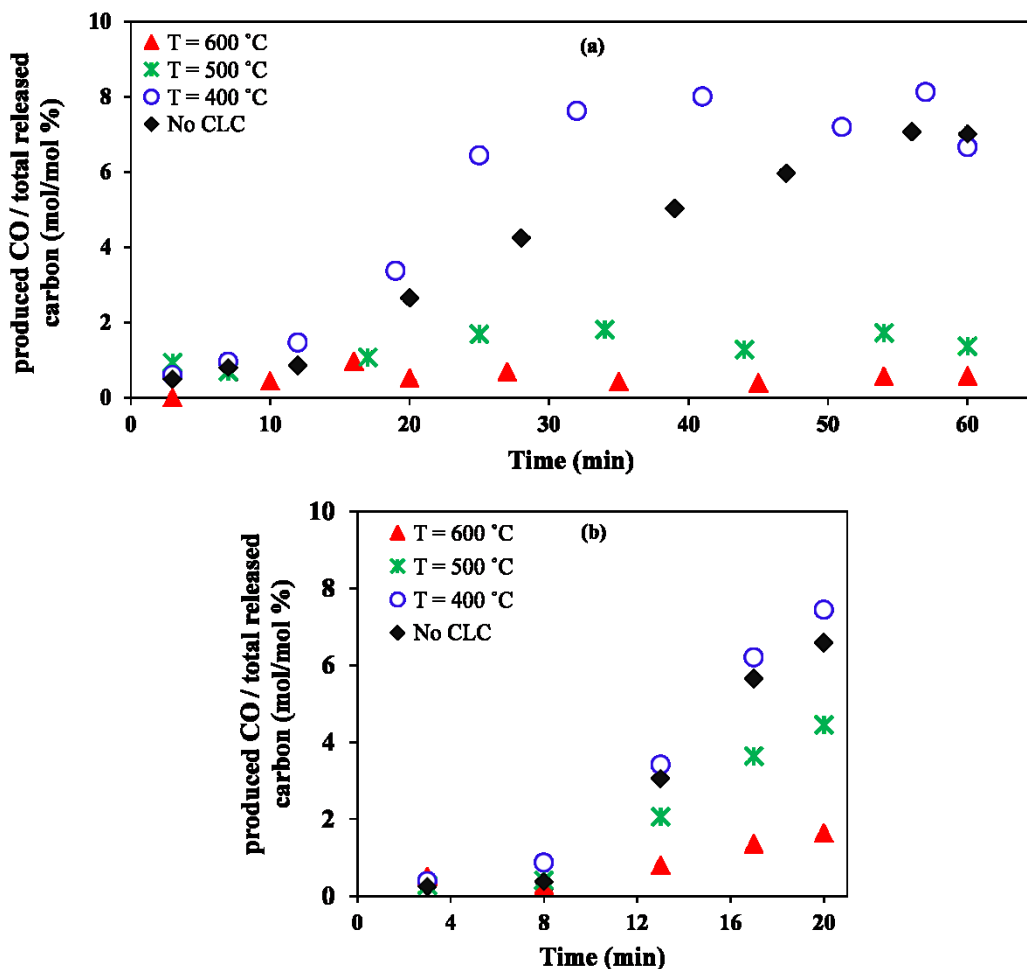


**Figure 5-3.** CO accumulation profiles during the torrefaction of 500 mg of birch at 260°C (a) and 300°C (b) for different combustion temperatures in the torrefaction-CLC assembly.

However, H<sub>2</sub> concentration declined with increased CLC temperature likely due to its oxidation to water (Figure 5-4 a,b). As a result, the accumulated H<sub>2</sub> in the assembly due to the birch torrefaction at 300 °C was less than 0.23% of total released hydrogen atoms (obtained from the subtraction of hydrogen content of each sample before and after torrefaction on the dry basis) from the torrefied biomass while no H<sub>2</sub> is observed in the assembly during the birch torrefaction at 260 °C and with the CLC performing at 500 °C and 600 °C. Unlike the low CH<sub>4</sub> production in blank torrefaction, contacting volatiles with iron oxide CLC bed led to an increase in methane composition in the torrefaction-CLC assembly. For instance at 600°C, the amount of accumulated CH<sub>4</sub> was, respectively, 2.5%

and 2.2% of total released carbon of birch torrefied at 260°C and 300°C. Even if CH<sub>4</sub> could form via volatiles cracking over iron oxide particles, activity of the latter was not sufficient to completely oxidize the produced methane.

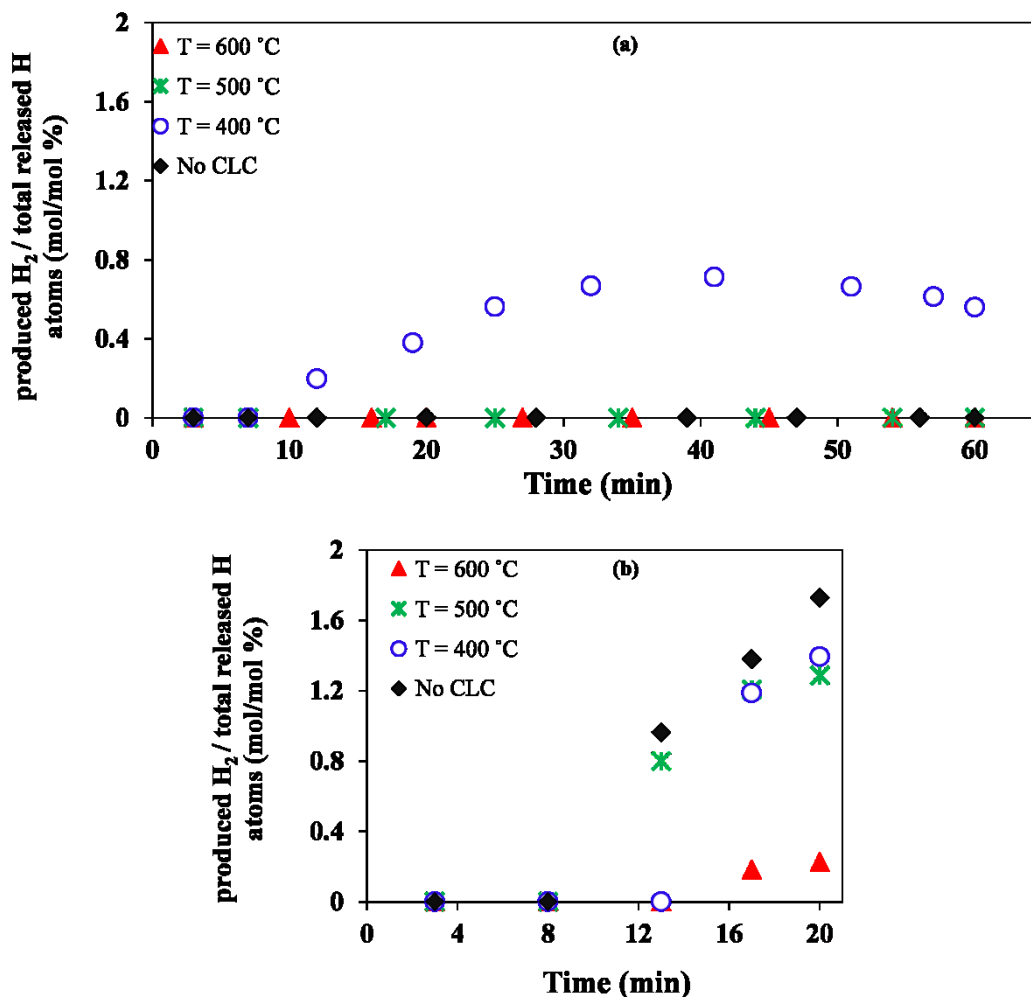


**Figure 5-4.** H<sub>2</sub> accumulation profiles during the torrefaction of 500 mg of birch at 260°C (a) and 300°C (b) for different combustion temperatures in the torrefaction-CLC assembly.

At completion of each simultaneous torrefaction-CLC experiment, regeneration was performed to evaluate the amount of deposited carbon as well as to monitor oxygen consumption of the CLC reactor. Maximum carbon deposition was observed for CLC experiments performed at 500°C. Torrefaction of birch at 260°C and 300°C and further combustion of their volatiles at 500°C CLC temperature led to carbon deposition on the surface of iron oxide particles contributing ca. 3.4% and 2.6% of the total released carbon.

The deposited carbon on the surface of iron oxide particles in the CLC reactor operating at 400°C and 600°C was less than 1.2%.

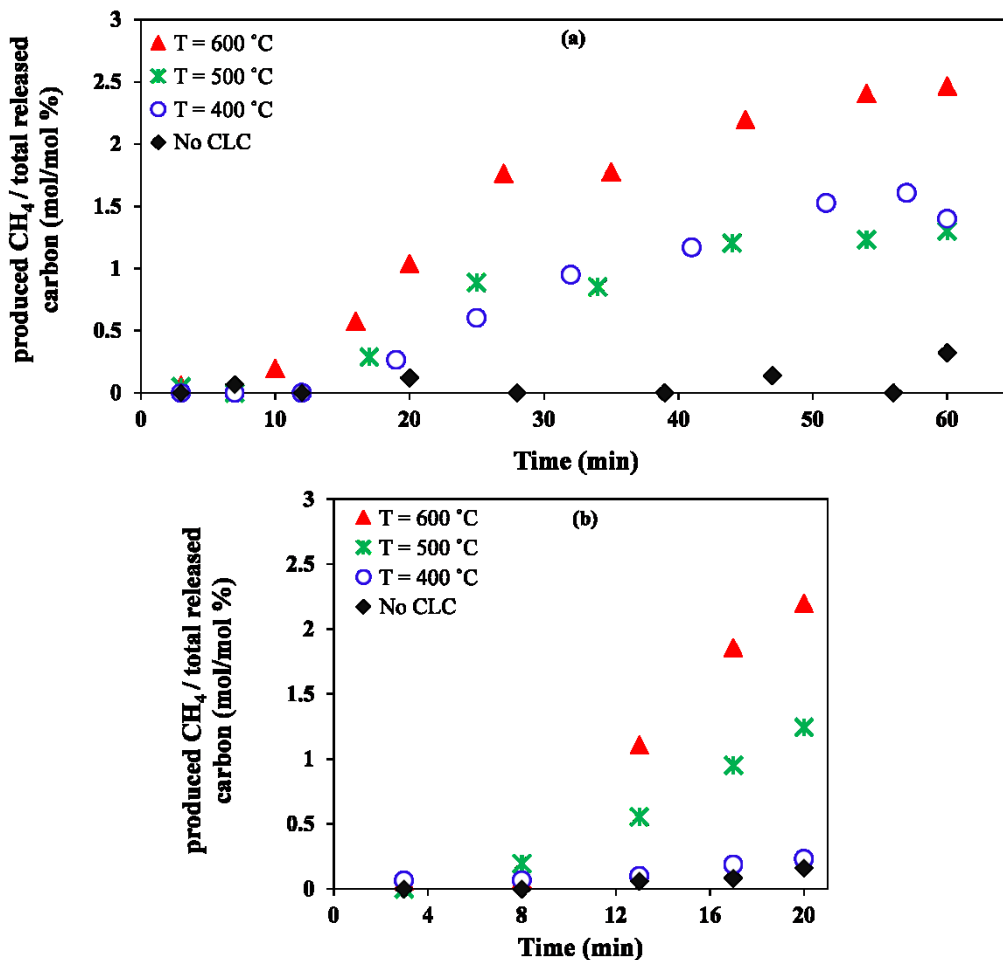


**Figure 5-5.** CH<sub>4</sub> accumulation profiles during the torrefaction of 500 mg of birch at 260°C (a) and 300°C (b) for different combustion temperatures in the torrefaction-CLC assembly.

Five successive torrefaction/combustion cycles followed by oxide regenerations were performed to assess whether or not the activity of iron oxide particles for burning of volatiles was affected in the long run. Birch wood samples were torrefied at 260°C for 1 h with CLC reactor operating at 600°C. Figure 5-6 shows the trends of CO<sub>2</sub> production and accumulation during simultaneous torrefaction and combustion as well as the oxygen concentration during the regeneration steps. CO<sub>2</sub> production and accumulation during the five cycles followed almost an identical pattern with no considerable decrease in iron oxide activity for combustion of volatiles in the CLC reactor.

To investigate if the presence of high CO<sub>2</sub> concentrations could influence the activity of iron oxide particles in the CLC reactor for the oxidation of volatiles, an experiment was performed with a mixture 50%:50% of CO<sub>2</sub> and N<sub>2</sub>, 500 mg of birch wood sample torrefied at 260°C for 1 h and 10 g of iron oxide oxygen carriers preheated and operated at 600°C. The results showed that the presence of initial CO<sub>2</sub> did not affect the activity of iron oxide particles for combustion of volatiles. Almost 97.6 % of the released carbon was found in the form of CO<sub>2</sub>. No hydrogen and very small amount of methane were detected. The amount of accumulated CO in the assembly, slightly larger in the presence of CO<sub>2</sub>, is easily rationalized in terms of reverse Boudouard reaction limiting oxidation of iron oxide particles and consequently resulting in the release of CO.

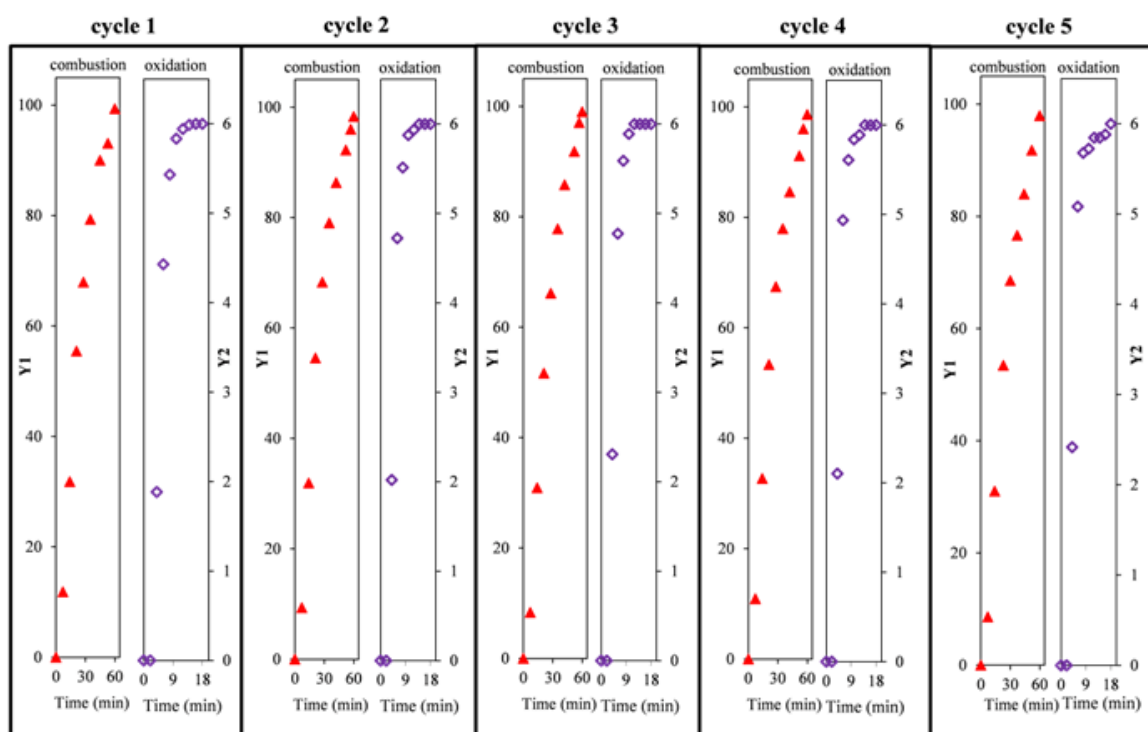


**Figure 5-6.** Profile of CO<sub>2</sub> production and oxygen consumption during five cycles of torrefaction/combustion and oxidation/regeneration of iron oxides. Torrefaction and CLC temperatures were, respectively, 260°C and 600°C. Red triangle = % released carbon converted to CO<sub>2</sub>. Purple diamond = O<sub>2</sub> concentration exiting CLC reactor during oxidation/regeneration. Initial O<sub>2</sub> concentration during oxidation was 6 mol% for N<sub>2</sub> flow-rate of 200 mL/min. Y1= produced CO<sub>2</sub>/total released carbon (mol/mol%), Y2 = oxygen concentration (mole%).

### 5.3.3. Long term stability

Product gas distribution during combustion in CLC reactor of model acetic acid is shown in Figure 5-7 a. During the first 90 min of acetic acid combustion through iron oxide oxygen carrier particles, CO<sub>2</sub> concentration was highest. Concomitantly, low CO and CH<sub>4</sub> concentrations were detectable while no residual acetic acid was detected at the CLC reactor outlet confirming complete acid conversion.

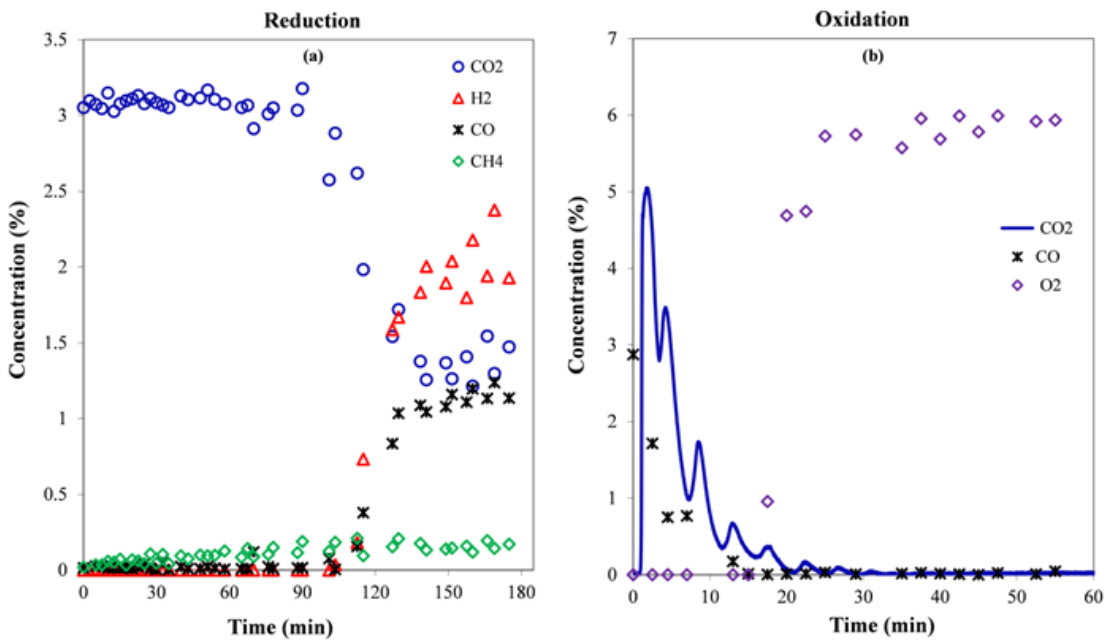


**Figure 5-7.** Gas products' distribution as a function of time during the reduction and oxidation steps of iron oxide at 600°C with acetic acid model torrefaction volatile. Acetic acid concentration during reduction was 1.6 mol.% and N<sub>2</sub> flow-rate was 100 mL/min, initial O<sub>2</sub> concentration during oxidation was 6 mol.% and N<sub>2</sub> flow-rate was 200 mL/min.

Almost 97 % of incident carbon was converted into CO<sub>2</sub> showing that the oxygen carrier function was active during this period. Later on, the exit CO<sub>2</sub> concentration began a decline while that of CO started to rise as did hydrogen though this latter went undetected before 90 min. Yet, no acetic acid was observed in the exit stream. This indicates that acetic acid thermally cracked over the surface of iron oxide particles. However, due to oxygen lack, CO<sub>2</sub> and water production was hampered at the expense of CO and H<sub>2</sub> accumulation. Scrutiny of the carbon mass balance revealed that after 90 min, large amounts of carbon should have been deposited over iron oxide particles. Reduction in the formation of H<sub>2</sub>, CO and CH<sub>4</sub>, and carbon deposit correlates with reduction in the duration of CLC combustion

and resumption of regeneration of the oxygen carriers. Figure 5-7 b illustrates the time evolution of oxygen, CO and CO<sub>2</sub> concentrations during oxidation. As can be seen, CO and CO<sub>2</sub> concentration peaks were observed upon switching CLC reactor into an O<sub>2</sub>-containing feed. CO<sub>2</sub> and CO concentration showed that almost 11.1 % of incident carbon introduced to the CLC reactor during the combustion period converted into carbon deposits on the oxygen carrier particles. Carbon deposition was mostly the result of fading activity of the oxygen carrier after 90 min combustion period. Oxygen concentration during the first 15 min of oxidation cycle was almost zero due to the burning of carbon deposits and oxidation of the oxygen carrier. However, after this time period the oxygen concentration increased progressively in the outlet gas, reaching a constant level indicative of completion of the oxidation step.

#### **5.3.4. Effect of torrefaction environment on properties of torrefied solid product**

Studies addressing the effect of torrefaction environment due to water vapor or CO<sub>2</sub> on the properties of torrefied solid products are to the best of our knowledge are very limited. Eseltine et al. [31] investigated the torrefaction of juniper and Mesquite samples under N<sub>2</sub> and CO<sub>2</sub> atmospheres using thermogravimetric analyzer and the weight loss of their samples was higher in the CO<sub>2</sub> atmosphere than the N<sub>2</sub> environment and the difference in the weight loss of CO<sub>2</sub> torrefied biomass and N<sub>2</sub> torrefied biomass was up to 4% at 300 °C. The effect of presence of CO<sub>2</sub> and water in the torrefaction reactor on the weight loss and properties of solid birch samples is also studied in this work. Birch wood torrefaction was therefore carried out under pure N<sub>2</sub> and water/CO<sub>2</sub> (20%/80%) atmospheres at 260°C for 60 min and 300°C for 25 min. The torrefied product mass yield, energy yield, equilibrium moisture content (EMC) and grindability were determined for each condition. The elemental analysis results of the torrefied samples are summarized in Table 5-2.

**Table 5-2.** Ultimate analysis, mass yield, higher heating value and energy yield of torrefied birch at different residence time and temperatures and under N<sub>2</sub> and water/CO<sub>2</sub> atmospheres.

Sample	C	H	N	S	O	Ash	Mass yield (Y <sub>M</sub> ,%)	Energy Yield (Y <sub>e</sub> ,%)	HHV (kJ/g)
Torrefied birch (260°C, N <sub>2</sub> , 60 min)	51.5	5.9	0	0	41.9	0.7	75.6	81.5	20.2
Torrefied birch (300°C, N <sub>2</sub> , 25 min)	53.7	5.8	0	0	39.6	0.9	61.0	68.6	21.1
Torrefied birch (260°C, water/CO <sub>2</sub> , 60 min)	51.7	5.9	0	0	41.6	0.8	76.6	83.3	20.4
Torrefied birch (300°C, water/CO <sub>2</sub> , 25 min)	54.2	5.8	0	0	39.1	0.9	61.5	69.8	21.3

The mass yields of birch torrefied at 260°C under N<sub>2</sub> and water/CO<sub>2</sub> environments were 75.6% and 76.6%, respectively. These decreased at 300°C to 61% and 61.5%, respectively. The mass yields of torrefied birch appeared to be virtually unaffected by whether the torrefaction atmosphere was N<sub>2</sub> or water/CO<sub>2</sub> while the results published by Eseltine et al. [31] showed higher weight loss of their biomass samples in CO<sub>2</sub> environment. We also performed several birch wood torrefaction experiments under CO<sub>2</sub> and N<sub>2</sub> atmospheres in the thermogravimetric (TG) analyzer to verify if the results obtained using the fixed bed reactor are supported by the experiments performed in TG which is an ideal reactor with a good control over the sample temperature. The experiments performed in TG were divided into the torrefaction experiments performed at 300 °C for 25 minutes and the torrefaction experiments performed at 260 °C for 60 minutes under N<sub>2</sub> and CO<sub>2</sub> atmospheres. Each experiment is carried twice to ensure its repeatability. As can be observed in Figure 5-8, the presence of CO<sub>2</sub> or N<sub>2</sub> atmospheres on the rate of birch torrefaction is ignorable and the birch wood mass loss during torrefaction is slightly lower in the presence of CO<sub>2</sub> than N<sub>2</sub>, which is also confirming the results we obtained by the fixed bed reactor. Effect of CO<sub>2</sub> on the rate of biomass torrefaction could be dependent on the type of biomass and the ash content of the samples. The juniper and Mesquite samples used by Eseltine et al. [31] have higher amount of ash content than the birch sample we used in this study. Furthermore the hemicellulose, cellulose and lignin content of the samples could be different and especially the structure of hemicellulose could change at different samples leading to the observed differences in the torrefaction rate of the biomass samples in the two studies. By similarly, samples torrefied under water/CO<sub>2</sub> had slightly higher carbon content, HHV and energy

yield than those torrefied in N<sub>2</sub> environment. It is plausible that torrefaction temperature being not high enough, reactions between CO<sub>2</sub> (or steam) and solid birch wood keep relatively slow whereby water and CO<sub>2</sub> are viewed as inert agents in birch wood torrefaction. As a matter of fact, temperatures as high as 600-800°C would be required to trigger significant reactivity between CO<sub>2</sub>, water and birch wood sample via the Boudouard water-gas reactions [32,33].

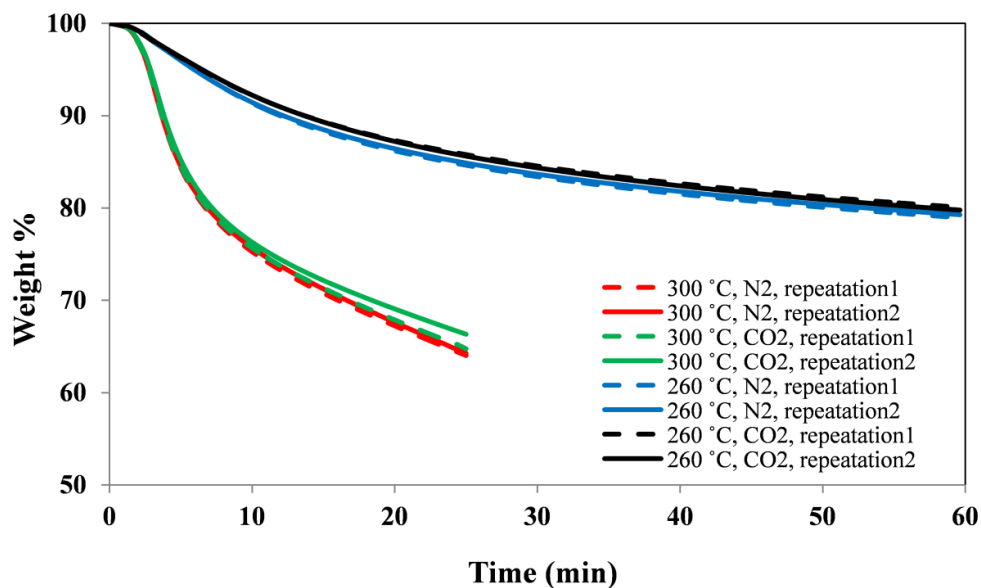


**Figure 5-8.** Mass yield of birch wood torrefied at 260 °C and 300 °C in the thermogravimetric analyzer and under N<sub>2</sub> and CO<sub>2</sub> atmospheres.

The dependence of EMC of the torrefied samples on relative humidity and thermal treatment is illustrated on Figure 5-9. The EMC of the samples at each specific relative humidity is calculated as below:

$$EMC (\%) = \frac{(W_s - W_d)}{W_s} * 100$$

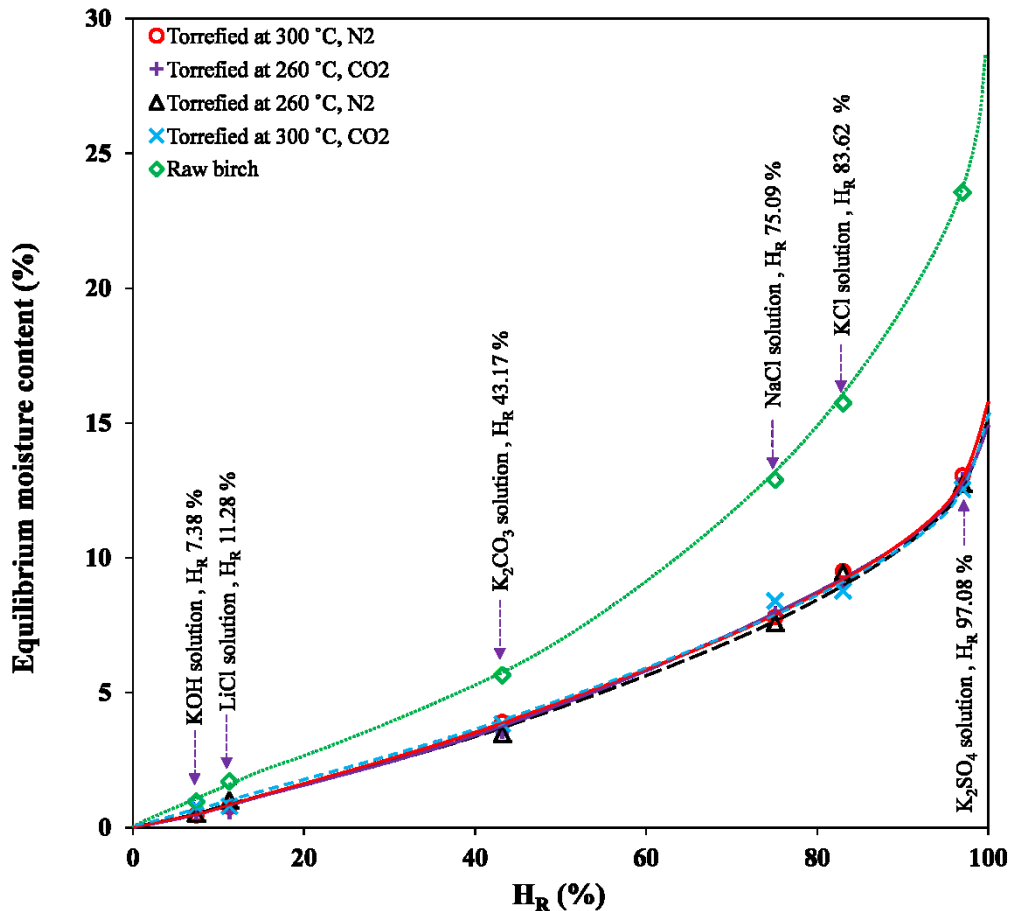


**Figure 5-9.** EMC of raw and torrefied birch under water/ $\text{CO}_2$  and  $\text{N}_2$  environments. The relative humidity ( $H_R$ ) prevailing for each salt solution is shown on x axis, lines show trends.

Where in this equation  $W_e$  is the weight of the birch wood at equilibrium at each specified humidity and  $W_d$  is the weight of dry sample. As can be observed in this Figure, torrefaction considerably decreased EMC of the torrefied samples as compared to raw birch whichever the prevailing relative humidity,  $H_R$ . EMC of torrefied birch under  $\text{N}_2$  and water/ $\text{CO}_2$  at  $H_R = 97.1\%$  was ca. 45% less than that of non-treated birch emphasizing the considerable impact of thermal treatment on reducing wood humidity uptake. However, the EMC of the four torrefied samples at  $260^\circ\text{C}$  and  $300^\circ\text{C}$  in the water/ $\text{CO}_2$  and  $\text{N}_2$  environments at different relative humidity were very close to each other. Although the samples torrefied at  $300^\circ\text{C}$  had smaller mass yield than those torrefied at  $260^\circ\text{C}$ , the results show that the extent of birch torrefaction at  $260^\circ\text{C}$  was enough to remove ample amounts of polar hydroxyl and carboxyl groups and yield similar moisture uptake patterns. The removal of hydroxyl and carboxyl groups of biomass during torrefaction reduces

considerably the amount of bonded water in the biomass structure. Figure 5-9 shows that at  $H_R < 43.17\%$  the EMC of torrefied and raw samples increases almost linearly with increasing the relative humidity.

At low relative humidity the dominant mechanism of water uptake in the biomass is the adsorption through the formation of strong bonds to the biomass network leading to the formation of bonded water [34]. However by increasing the relative humidity specially at  $H_R > 90\%$ , the capillary condensation leads to the formation of some non-bonded water in the biomass cavities [35] leading to the exponential shape increase in the equilibrium humidity uptake by increasing relative humidity (Figure 5-9). Acharjee et al. [34] have investigated the effect of thermal pretreatment on its equilibrium moisture content of Loblolly pine and they concluded that the content of non-bonded water is independent of thermal treatment.

Figure 5- 10 shows the sieved particle size distribution of raw and torrefied birch samples at 260°C and 300°C and under  $N_2$  and water/ $CO_2$  environments after milling. Obviously, torrefied birch samples exhibit quite different size distribution than raw birch. Almost 90% of raw birch after 30 min milling did not pass the largest mesh size (3270  $\mu m$ ). The rigidity and mechanical strength of the biomass structure is attributed to the long crystalline cellulose fibers linked through the non-crystalline hemicellulose which results in its higher grinding energy requirement [5]. Torrefied birch samples, on the contrary, offered superior grindability by showcasing lesser mechanical strength and were more fragile as evidenced by the large proportions of fines after sieving. More than 25.7% and 28.77% of the grinded birch wood torrefied at 260°C for 60 minutes in  $N_2$  and  $CO_2$ /water atmospheres, respectively, pass through 850  $\mu m$  sieve whereas those for torrefied birch at 300 °C for 25 minutes were 48% and 42%, respectively showing that the samples torrefied at 300°C have better grinding properties than those torrefied at 260°C. The partial depolymerization/decomposition of cellulose and hemicellulose during torrefaction reduces the fibers length and mechanical stability of biomass and as a result improves its grinding properties [7,10,11]. Although the grindability of torrefied birch at 260 °C and under  $CO_2$ /water was slightly better than that under  $N_2$  environment, this trend was not observed

for the torrefied birch at 300 °C and the grindability of the torrefied birch under N<sub>2</sub> atmosphere was superior to that under CO<sub>2</sub>/water environment.

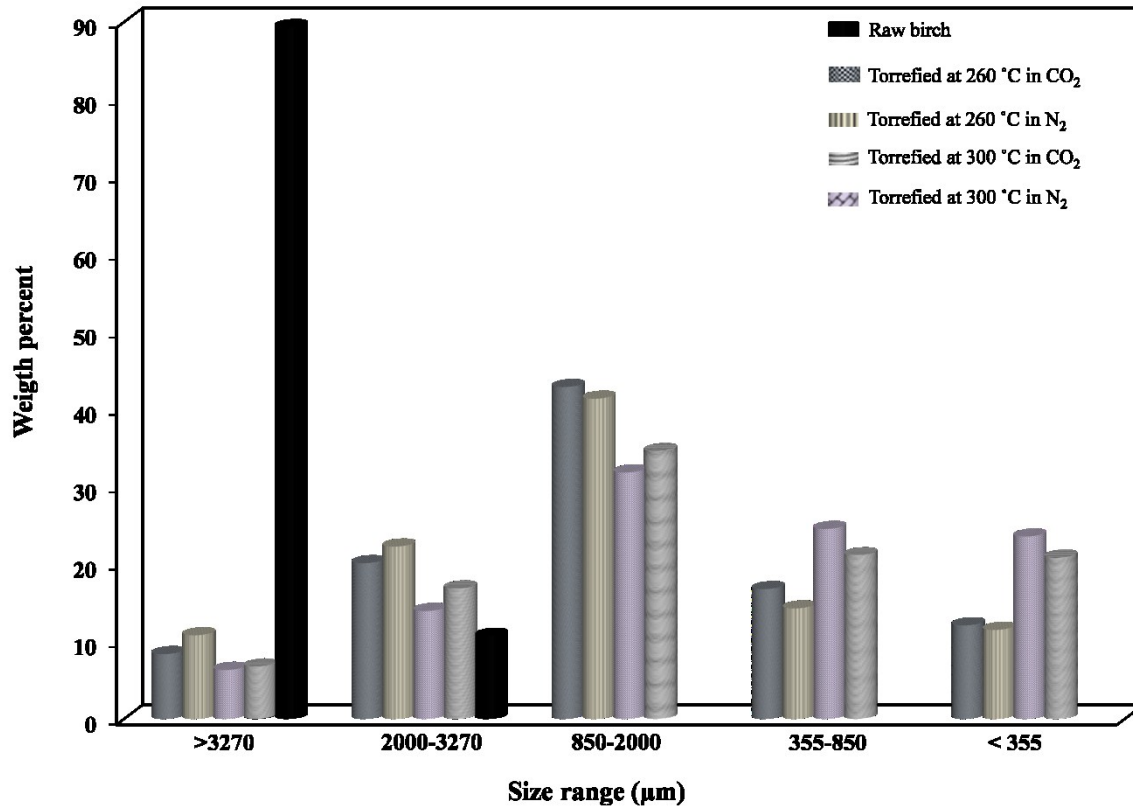


**Figure 5-10.** Weight-based particle size distribution of ground raw and torrefied birch under water/CO<sub>2</sub> and N<sub>2</sub> environments.

## 5.4. Conclusion

A new concept of biomass torrefaction and volatile combustion in a chemical looping combustion (CLC) reactor using iron oxide particles was examined in this study. Birch wood as model biomass sample was torrefied in a fixed bed reactor at 260°C and 300°C and the volatiles resulting from torrefaction were burned over iron oxide solid oxygen carriers in a CLC reactor. Different CLC temperatures were tested and up to 99 % of the carbon released during birch torrefaction was found in the form of CO<sub>2</sub> at 600°C. The long-time stability of iron oxide particles for burning the torrefaction volatiles was investigated using acetic acid as a model volatile compound of biomass torrefaction. The lack of oxygen on the solid oxygen carrier could lead to the production of considerable amounts of CO and H<sub>2</sub> and also deposition of deactivating carbon on the surface of iron oxides. Examination of the effect of CO<sub>2</sub> and water in the torrefaction atmosphere on the properties of torrefied solid product revealed that these agents could increase slightly the HHV and energy yield of torrefied birch wood while they had no considerable effect on the mass yield and equilibrium moisture content of the obtained solid.

## 5.5. References

- [1] Roy J, Sarkar P, Biswas S, Choudhury A. Predictive equations for CO<sub>2</sub> emission factors for coal combustion, their applicability in a thermal power plant and subsequent assessment of uncertainty in CO<sub>2</sub> estimation. *Fuel*. 2009;88:792-8.
- [2] McIlveen-Wright DR, Huang Y, Rezvani S, Mondol JD, Redpath D, Anderson M, et al. A Techno-economic assessment of the reduction of carbon dioxide emissions through the use of biomass co-combustion. *Fuel*. 2011;90:11-8.
- [3] Chen WH, Kuo PC. Torrefaction and co-torrefaction characterization of hemicellulose, cellulose and lignin as well as torrefaction of some basic constituents in biomass. *Energy*. 2011;36:803-11.
- [4] Pimchuai A, Dutta A, Basu P. Torrefaction of agriculture residue to enhance combustible properties. *Energy & Fuels*. 2010;24:4638-45.
- [5] van der Stelt MJC, Gerhauser H, Kiel JHA, Ptasiński KJ. Biomass upgrading by torrefaction for the production of biofuels: A review. *Biomass & Bioenergy*. 2011;35:3748-62.
- [6] Ohliger A, Forster M, Kneer R. Torrefaction of beechwood: A parametric study including heat of reaction and grindability. *Fuel*. 2013;104:607-13.
- [7] Li J, Brzdekiewicz A, Yang WH, Blasiak W. Co-firing based on biomass torrefaction in a pulverized coal boiler with aim of 100% fuel switching. *Applied Energy*. 2012;99:344-54.
- [8] Medic D, Darr M, Shah A, Potter B, Zimmerman J. Effects of torrefaction process parameters on biomass feedstock upgrading. *Fuel*. 2012;91:147-54.
- [9] Sarvaramini A, Gravel O, Larachi F. Torrefaction of ionic-liquid impregnated lignocellulosic biomass and its comparison to dry torrefaction. *Fuel*. 2013;103:814-26.
- [10] Phanphanich M, Mani S. Impact of torrefaction on the grindability and fuel characteristics of forest biomass. *Bioresource Technology*. 2011;102:1246-53.
- [11] Repellin V, Govin A, Rolland M, Guyonnet R. Energy requirement for fine grinding of torrefied wood. *Biomass & Bioenergy*. 2010;34:923-30.
- [12] Bridgeman TG, Jones JM, Shield I, Williams PT. Torrefaction of reed canary grass, wheat straw and willow to enhance solid fuel qualities and combustion properties. *Fuel*. 2008;87:844-56.
- [13] Prins MJ, Ptasiński KJ, Janssen F. Torrefaction of wood - Part 2. Analysis of products. *Journal of Analytical and Applied Pyrolysis*. 2006;77:35-40.
- [14] Koppejan J, Sokhansanj S, Melin s, Madrali S. status overview of torrefaction technologies. IEA bioenergy task 32 report December 2012.
- [15] Uslu A, Faaij APC, Bergman PCA. Pre-treatment technologies, and their effect on international bioenergy supply chain logistics. Techno-economic evaluation of torrefaction, fast pyrolysis and pelletisation. *Energy*. 2008;33:1206-23.

- [16] C.P. K. Overview of international development in torrefaction. Kema report, [www.kema.com2011](http://www.kema.com2011).
- [17] Hossain MM, de Lasa HI. Chemical-looping combustion (CLC) for inherent CO<sub>2</sub> separations-a review. *Chemical Engineering Science*. 2008;63:4433-51.
- [18] Adanez J, Abad A, Garcia-Labiano F, Gayan P, de Diego LF. Progress in chemical-looping combustion and reforming technologies. *Progress in Energy and Combustion Science*. 2012;38:215-82.
- [19] Moldenhauer P, Ryden M, Lyngfelt A. Testing of minerals and industrial by-products as oxygen carriers for chemical-looping combustion in a circulating fluidized-bed 300 W laboratory reactor. *Fuel*. 2012;93:351-63.
- [20] Iliuta I, Leclerc A, Larachi F. Allothermal steam gasification of biomass in cyclic multi-compartment bubbling fluidized-bed gasifier/combustor - New reactor concept. *Bioresource Technology*. 2010;101:3194-208.
- [21] Gazzani M, Macchi E, Manzolini G. CO<sub>2</sub> capture in integrated gasification combined cycle with SEWGS - Part A: Thermodynamic performances. *Fuel*. 2013;105:206-19.
- [22] Hasib-ur-Rahman M, Larachi F. CO<sub>2</sub> capture in Alkanolamine-RTIL blends via carbamate crystallization: route to efficient regeneration. *Environmental Science & Technology*. 2012;46:11443-50.
- [23] Assima GP, Larachi F, Beaudoin G, Molson J. CO<sub>2</sub> sequestration in chrysotile mining residues-implication of watering and passivation under environmental conditions. *Industrial & Engineering Chemistry Research*. 2012;51:8726-34.
- [24] Assima G P, Larachi F, Beaudoin G, Molson J. Dynamics of carbon dioxide uptake in chrysotile mining residues- effect of mineralogy and liquid saturation. *International Journal of Greenhouse Gas Control*. 2013;12:124-35.
- [25] Pronost J, Beaudoin G, Tremblay J, Larachi F, Duchesne J, Hebert R, et al. Carbon Sequestration Kinetic and Storage Capacity of Ultramafic Mining Waste. *Environmental Science & Technology*. 2011;45:9413-20.
- [26] L. Milne J, B. Field C. Assesment report from the GCEP workshop on energy supply with negative carbon emissions. 2012.
- [27] Abad A, Mattisson T, Lyngfelt A, Johansson M. The use of iron oxide as oxygen carrier in a chemical-looping reactor. *Fuel*. 2007;86:1021-35.
- [28] Channiwala SA, Parikh PP. A unified correlation for estimating HHV of solid, liquid and gaseous fuels. *Fuel*. 2002;81:1051-63.
- [29] Boateng AA, Mullen CA. Fast pyrolysis of biomass thermally pretreated by torrefaction. *Journal of Analytical and Applied Pyrolysis*. 2013;100:95-102.
- [30] Greenspan L. Humidity fixed-points of binary saturated aqueous-solutions. *Journal of Research of the National Bureau of Standards Section a-Physics and Chemistry*. 1977;81:89-96.

- [31] Eseltine D, Sankar Thanapal S, Annamalai K, Ranjan D. Torrefaction of woody biomass (Juniper and Mesquite) using inert and non-inert gases. *Fuel*. 2013;113:379-88.
- [32] Khalil R, Varhegyi G, Jaschke S, Gronli MG, Hustad J. CO<sub>2</sub> gasification of biomass chars: a kinetic study. *Energy & Fuels*. 2009;23:94-100.
- [33] Moon J, Lee J, Lee U, Hwang J. Transient behavior of devolatilization and char reaction during steam gasification of biomass. *Bioresource technology*. 2013;133:429-36.
- [34] Acharjee TC, Coronella CJ, Vasquez VR. Effect of thermal pretreatment on equilibrium moisture content of lignocellulosic biomass. *Bioresource Technology*. 2011;102:4849-54.
- [35] Venkates.A. Sorption of aqueous and nonaqueous media by wood and cellulose. *Chemical Reviews*. 1970;70:619-637.

## **Chapter 6 : Fe/Mg silicate mining residues as solid oxygen carriers for chemical looping combustion of torrefaction volatiles**

**Résumé** La torréfaction de la biomasse lignocellulosique est un traitement fréquemment employé afin d'augmenter la densité énergétique du produit solide préalablement à sa conversion thermochimique. Dans la présente étude, la faisabilité d'un tel procédé dans lequel l'énergie requise est fournie par la combustion des gaz volatils libérés alors que le dioxyde de carbone produit est subséquemment capturé dans un puits permanent est investiguée dans un objectif de valorisation des résidus miniers. L'utilisation de minéraux broyés, abondants et abordables, en tant que transporteurs d'oxygène pour la combustion en boucle chimique (CBC) ainsi qu'en tant que puits de carbone pour la carbonatation minérale en combinaison avec la torréfaction a été investiguée. Les résidus miniers utilisés sont des silicates de type chrysotile et lizardite riches en fer (17,3% massique) provenant de la récupération du nickel. Une pré-calcination à l'air à 700°C a permis d'augmenter la fraction en fer extra-réseau des minéraux jusqu'à 66%, principalement sous forme d'hématite comme l'a révélé la spectroscopie de Mössbauer. De tels transporteurs d'oxygène ont ensuite été testés dans un procédé de torréfaction-CBC en absence d'air avec recirculation des gaz dans une plage de température entre 500°C et 700°C afin de brûler les gaz volatils libérés pendant la torréfaction du bois de bouleau entre 260°C et 300°C. Jusqu'à 96% du carbone libéré par le bouleau torréfié sous forme de volatils a été converti en CO<sub>2</sub> dans le lit de CBC, soulignant la capacité du résidu à brûler les gaz volatils de torréfaction. Le résidu a finalement été testé dans une configuration de torréfaction-CBC-carbonatation avec recirculation des gaz afin de brûler les gaz volatils de torréfaction et de capturer le CO<sub>2</sub> pur à différentes températures de torréfaction, de CBC et de carbonatation.

**Abstract** Torrefaction of woody biomass is a thermal treatment often used to increase biomass energy density prior to its thermochemical conversion. The feasibility of integrated torrefaction where the energy required for torrefaction is provided from the burning of its self-released volatiles while the resulting carbon dioxide is subsequently captured in a permanent sink is an original avenue which was investigated in this study from the point of view of mining residues valorization. The use of abundant, cheap and comminuted minerals as solid-oxygen carriers for chemical looping combustion (CLC) and as carbon sinks for mineral carbonation in combination with torrefaction of woody biomass was studied. The mining residue consisted of iron-rich (17.3 wt. %) post-nickel recovery chrysotile/lizardite silicate minerals. Air pre-calcination of the mineral at 700°C helped boosting the extra-framework iron fraction up to 66%, mainly in the form of hematite as evidenced from Mössbauer spectroscopy. Such calcined oxygen carrier was then tested in *airless* torrefaction-CLC tied configuration under gas recirculation over the temperature range 500-700°C to burn the volatiles released during the torrefaction of birch at 260-300°C. Up to 96% of the carbon released from the torrefied birch as volatiles was converted in the CLC bed into CO<sub>2</sub> highlighting the residue ability for burning torrefaction volatiles. The residue was finally tested in a torrefaction-CLC-carbonation configuration under gas recirculation for burning the torrefaction volatiles and capturing the produced carbon dioxide for various torrefaction, CLC and carbonation temperatures.

## 6.1. Introduction

Lignocellulosic biomass waste residues, gifted with a seductive appeal as a source of renewable, sustainable and carbon-neutral energy, are opposed to fossil fuels as a rival green option [1]. As a fuel, however, raw biomass has the drawbacks of having low calorific value, high moisture content and O/C ratio, and a penalizing grinding energy [2-6]. Torrefaction, also referred to as mild pyrolysis, is a thermal pre-treatment which, applied to solid biomass, improves its properties as a fuel. Biomass torrefied in an inert atmosphere at temperatures ranging from 200°C to 300°C leads to a solid product with lowered moisture, superior hydrophobic character, higher energy density, and softer requirements in terms of grinding energy, all making torrefaction a process to upgrade biomass into a more suitable fuel [7-16].

Biomass decomposition during torrefaction leads to the release of volatiles composed of non-condensable, *e.g.*, CO<sub>2</sub>, CO, CH<sub>4</sub>, H<sub>2</sub>, and condensable, *e.g.*, water, oxygenated hydrocarbons: acetic, formic and lactic acids, etc., products [17]. In industrial torrefaction, volatiles are burnt in air combustors and the hot flue gas is directed toward biomass drying and torrefaction chambers to provide them with the needed energy [18,19]. However, the presence of residual oxygen in the flue gas contributes to the partial burning of biomass in the torrefaction chamber thus reducing the efficiency of torrefaction process [20]. A concept to circumvent recourse to air combustion of volatiles has recently been proposed by our group from combining biomass torrefaction and chemical looping combustion (CLC) for the *airless* burn-off of the torrefaction volatiles [21]. In this concept, torrefaction volatiles are burnt using a solid oxygen carrier while the combustion flue gas, consisting mostly of non-diluted CO<sub>2</sub> and steam, is recirculated to the torrefaction reactor for heat integration [21]. Another gain from such concept is the negative net CO<sub>2</sub> torrefaction in co-firing plants to reduce greenhouse gas emissions as a (N<sub>2</sub>- and O<sub>2</sub>-free) CLC flue gas and to allow recovery of pure CO<sub>2</sub> amenable to capture or sequestration [21].

A wide range of different transition metals combined with inert porous supports have been synthesized and tested as solid oxygen carriers in chemical looping combustion of methane and solid fuels [22,23]. However, these solid oxygen carriers are costly and may not be suitable for torrefaction [24] especially on account of the low-profitability margin of this

process. A recent status overview of torrefaction technologies revealed that replacing coal with torrefied biomass pellets could slightly relieve process costs in comparison to using non-torrefied feeds [18]. To maintain such marginal benefits, one should consider, beside reactivity to burn oxygenated hydrocarbons, the additional costs that might be imposed to the whole process. Due to its environmental compatibility and low price, in comparison with other metal oxides such as nickel and manganese oxides, iron oxide was recognized as a solid oxygen carrier apposite for burning the volatiles produced during torrefaction [21, 23]. Along the same line of thought, exploitation of abundant, cheap and already comminuted iron-rich minerals could be considered as even more economical should such mining waste exhibit a potential as solid oxygen carriers for burning torrefaction volatiles in a CLC reactor. Our group evaluated several iron-containing magnesium silicates for catalytic steam cracking of biomass tar model compounds, and ambient and high-pressure dry and wet mineral carbonations for these materials also possess, owing to magnesium, the ability to form solid carbonates [25-31].

This study aims at evaluating the feasibility of integrated torrefaction where the energy required for torrefaction could be provided from the burning of its self-released volatiles while the resulting carbon dioxide could be subsequently captured in a permanent sink. Therefore, the potential of post-nickel recovery mining residues from a nickel recovery mine project (Raglan mines, Xstrata Nickel, Nunavik, Québec, Canada) rich in chrysotile/lizardite and magnetite were tested as solid oxygen carrier for combustion of biomass derived volatiles during torrefaction and for mineral carbonation as carbonatable materials. Torrefaction of birch wood samples was used to illustrate experimentally the integration between a torrefaction reactor, a chemical looping combustion reactor and a carbonation reactor. The solid oxygen carrier capability was characterized with regard to the mining waste crystalline structure, iron oxidation states and coordinations in the as-received, pre-calcined and regenerated states for CLC applications. The possibility of mineral carbonation using the spent mining residues in a carbonation reactor hyphenated to CLC reactor was also investigated.

## 6.2. Experimental

### 6.2.1. Materials characterization and preparation

The torrefaction tests were performed using birch, an abundant woody biomass from Québec forests. Prior to the experiments, the as-received sample sheets of birch wood were cut into small woodchip pieces 2 to 4 mm in size. The proximate analysis of birch wood showed the presence of 5.5% of humidity. The volatiles, fixed carbon and ash content of the samples were 89.4%, 9.8% and 0.7% on dry basis, respectively.

The solid-oxygen carrier investigated in this study is an iron-containing silicate mineral obtained from the Raglan mine after nickel recovery (Xstrata Nickel, Nunavik, Québec). The as-received mining residue was in the form of fine agglomerates. It was broken and sieved to isolate the 100-250  $\mu\text{m}$  fraction which, referred to as Raglan mining residue (RMR), was used in all our tests. Elemental sample analysis (Table 6-1) using X-ray fluorescence (XRF) revealed iron as the most preponderant RMR element (17.3 wt. %). Such a level of iron certainly vouches for the potential of RMR as a cheap naturally-occurring oxygen-carrier which we will contemplate for chemical looping combustion (CLC) integration with a torrefaction operation to airlessly burn the torrefaction volatiles. Along with iron, Mg and Si are also found widely in the sample (13.8 and 16.5 wt. %, respectively). The concentration of some minor impurities in the RMR samples such as Ca, K, Al, Cr and Na are also given in Table 6-1.

**Table 6-1.** wt. % of main constitutive elements of RMR (Raglan mine, Québec) *via* XRF analysis

Analyte	Si	Mg	Fe	Ca	K	Cr	Ni	Al	Na	Ti
Raglan mine residue, wt%	16.5	13.8	17.3	1.1	0.10	0.18	0.15	0.17	0.30	0.08

RMR samples were prepared prior to each experiment by calcination under air for 3 h at 700°C to maximize extra-framework iron at the highest oxidation state. The air-calcined RMR underwent changes of its crystalline structures, porosity, and iron oxidation states and coordinations. These changes were assessed through characterization tests using X-ray powder diffraction (XRPD), N<sub>2</sub> adsorption/desorption BET measurements and <sup>57</sup>Fe Mössbauer spectroscopy for the as-received and calcined RMR, and the used RMR after

five oxidation/reduction cycles in CLC.

### **6.2.2. Experimental setup**

The experimental setup used for simultaneous biomass torrefaction and CLC (or airless combustion) of torrefaction volatiles consisted of two stainless steel tubular reactors in battery interconnected to each other through heated tubes (Figure 6-1). Prior to conducting hyphenated torrefaction-CLC tests, the CLC-reactor was first brought to its desired temperature set point, from 500°C to 700°C, and the entire assembly was swept with N<sub>2</sub> to purge oxygen out of it. Torrefaction of 500 mg of birch wood was then carried out at two temperatures, 260°C and 300°C, between 20 and 60 min by placing the torrefaction reactor in the bore of an induction heating coil (Figure 6-1). The temperature of the torrefaction reactor was controlled by a fiber optic pyrometer connected to a temperature controller for metering the induction-heater power. Temperature was also measured through a K type thermocouple inserted in the center of the biomass layer. The difference in temperature between the bed and reactor surface never exceeded 5°C in steady-state conditions. The volatiles thus produced in the torrefaction reactor were flowed to, and converted in, the CLC reactor across a 6-g layer of pre-calcined RMR. The CLC reactor was located in a vertical electrically heated furnace equipped with a PID temperature controller and a K type thermocouple for CLC temperature control. Torrefaction-CLC experiments were followed by a regeneration step using air where the amount of carbon deposited on the surface of oxygen carrier was determined through measuring the CO<sub>2</sub> gas generated during this step. Blank torrefaction tests were also performed after disconnecting the CLC branch to measure the accumulation of CO, CO<sub>2</sub>, CH<sub>4</sub> and H<sub>2</sub> in the assembly during birch wood torrefaction. Sintering and agglomeration of iron oxides are potential detrimental factors [23] to CLC catalytic activity of RMR samples. Therefore, tests for assessing catalyst activity upkeep were also carried out by operating the mining residues for several oxidation/reduction cycles.

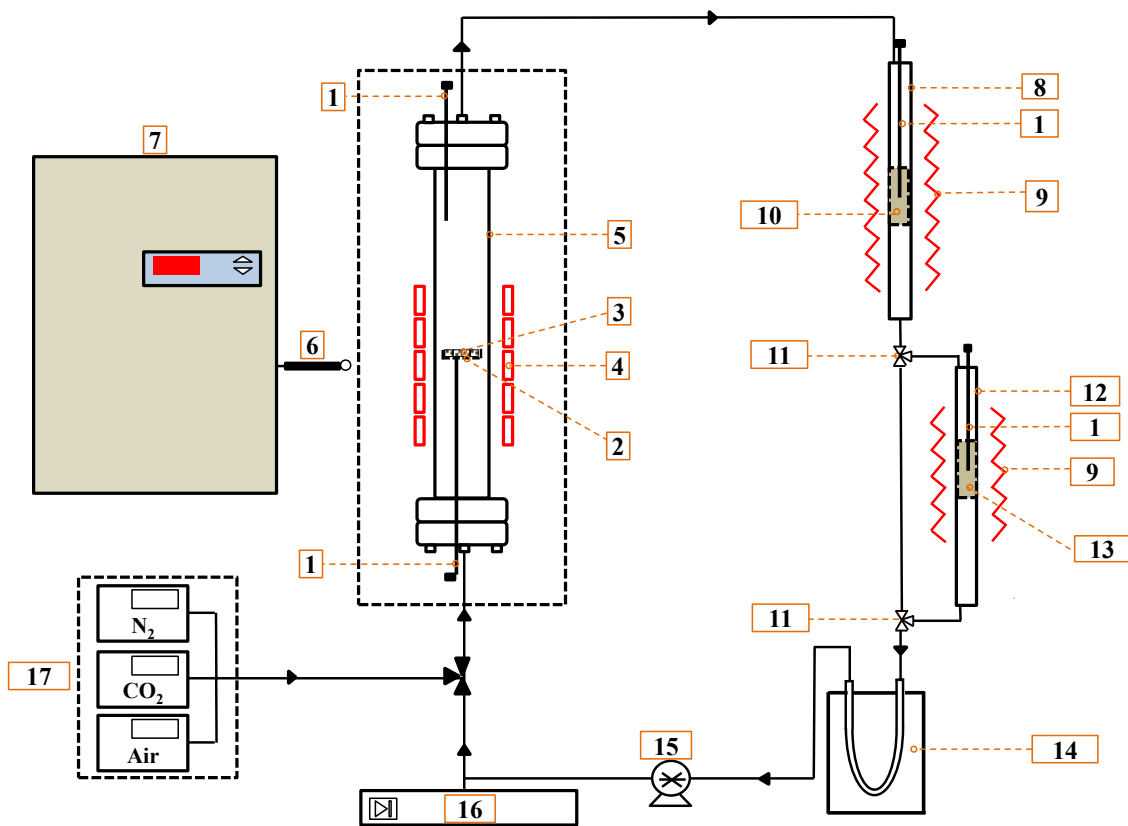


**Figure 6-1.** Schematic of the experimental torrefaction-chemical looping-carbonation assembly: (1) K type thermocouple (2) stainless steel mesh (3) birch sample (4) induction coil (5) stainless steel torrefaction reactor (6) pyrometer (7) induction heater power supply (8) chemical looping combustion reactor (9) electric heater (10) fixed bed of RMR solid oxygen carrier (11) three way valve (12) carbonation column (13) carbonation fixed-bed of RMR spent residue (14) cold trap (15) peristaltic pump (16) micro GC (17) mass flow meters

Another RMR component worth exploiting is its high magnesium content whereby carbonation to capture the post-CLC CO<sub>2</sub> stream would be an enticing addition to a three-level integrated strategy involving the same RMR material in torrefaction-CLC-carbonation. Therefore, the spent RMR was tested for carbonation at ambient pressure and moderate temperatures to contemplate the potential for CO<sub>2</sub> sequestration in conjunction with a combined torrefaction-CLC process. Approximately 25 g of calcined spent RMR used during 5 oxidation/reduction cycles in the CLC reactor was loaded in a third fixed-bed carbonation reactor placed downstream of CLC where RMR carbonations were performed at 25°C, 50°C and 70°C (Figure 6-1). These carbonation temperatures were controlled by electrically heating the carbonation column walls. Prior to carbonation, samples of spent calcined RMR were pre-watered to achieve liquid pore saturations around 50%. Watering is

indeed prerequisite to enable leaching of magnesium ions from the forsterite and brucitic structures and to allow prompt bounding to dissolved CO<sub>2</sub> in the form of magnesium carbonates.[30] The amount of CO<sub>2</sub> thus sequestered in the spent RMR samples was obtained by subtracting the amount of CO<sub>2</sub> that built up in the recirculating gas stream through the torrefaction-CLC and torrefaction-CLC-carbonation circuits. More specifically, these circuits were implemented according to two scenarios. In the first, the gas effluents leaving the CLC reactor was directly passed through a cold trap and, before being recirculated back to the torrefaction reactor, was analyzed every 5 min using Agilent micro GC 3000 for the determination of CO, CH<sub>4</sub>, H<sub>2</sub> and CO<sub>2</sub> contents. In the second, there was a desire to assess whether or not a carbonation step using spent NMR samples was also possible near ambient conditions. For this purpose, the post-CLC gas effluents were sent to a carbonation reactor (see Figure 6-1), and subsequently to the cold trap and micro-GC before to be recirculated to the torrefaction reactor as in the first scenario.

After an experiment was completed, the dry torrefied birch wood was weighted to obtain its mass yield ( $Y_M = \text{\%mass solid product/mass feed}$ ). The C, H, N, S contents of the samples were also obtained using an elemental analyzer (Fisons EA 1108CHNS). Carbon and hydrogen, being part of the torrefaction volatiles, were estimated upon subtraction of C and H contents of samples, on the dry basis, before and after torrefaction. The carbon content thus determined was compared to that accumulated as CO<sub>2</sub> in the torrefaction-CLC assembly to evaluate the RMR efficiency as a solid oxygen carrier. The sample higher heating value (HHV) before and after torrefaction was also estimated by means of the correlation given by Channiwala et al. [32] Using the solid product HHV, the energy density ratio ( $e = \text{HHV solid product/HHV feed}$ ) and energy yield ( $Y_e = e Y_M$ ) were also determined.

## **6.3. Results and discussions**

### **6.3.1. RMR characterization**

The X-ray diffraction patterns of RMR, as-received (a) and calcined at 700°C (b)—prior to its CLC testing— and the residue after exposure to five oxidation/reduction cycles (c) are shown in Figure 6-2. The main crystalline phases present in the as-received material are chrysotile ( $2\theta = 12^\circ, 24.3^\circ, 36.6^\circ$ ), lizardite ( $2\theta = 12.2^\circ, 24.5^\circ, 35.9^\circ$ ) and magnetite ( $2\theta =$

35.6°). The free iron oxide component, in magnetite form, is a potential for the residue to constitute a low-cost CLC solid oxygen carrier. Dehydroxylation of the serpentine phase under air calcination of RMR at 700°C resulted in the formation of forsterite ( $\text{Mg}_2\text{SiO}_4$ ,  $2\theta = 36.5^\circ$ ) and chlorite ( $\text{Mg}_6\text{Si}_4\text{O}_4\text{O}_{10}(\text{OH})_8$ ,  $2\theta = 12.1^\circ$ ) crystalline structures (Figure 6-2). RMR air-calcination, by oxidizing magnetite, also led to hematite formation ( $\alpha\text{-Fe}_2\text{O}_3$ ,  $2\theta = 33.2^\circ$ ). With the forsterite peaks completely overshadowing those of magnetite, it is uncertain, based on XRPD, to intuit how deep magnetite oxidation was run.

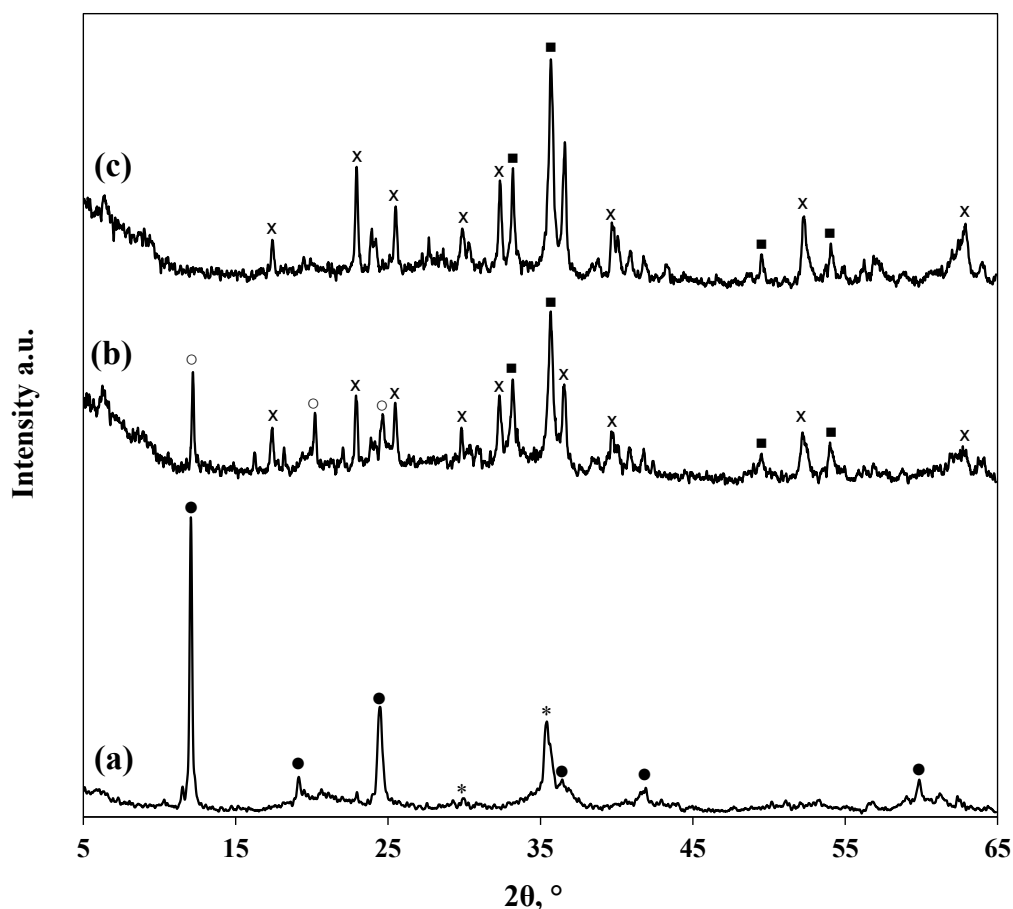


**Figure 6-2** . X-ray powder diffraction patterns of (a) as-received RMR; (b) RMR calcined under air at 700°C; (c) calcined RMR used during five oxidation/reduction cycles at 700°C. (●) chrysotile and lizardite, (○) chlorite, (x) forsterite, (\*) magnetite

The hematite peaks in the calcined RMR, overreaching those of forsterite, might also suggest that extraction of intra-framework iron from the serpentine bilayer structures would also have contributed to the build-up of hematite by the air-calcination step. These aspects will be later thoroughly addressed using Mössbauer spectroscopic characterizations. The X-

ray diffractogram of the residue after exposure to five oxidation/reduction cycles showed a pattern almost similar to the air-calcined one, except for the fading of chlorite peaks.

The BET surface area and pore volume of as-received RMR were  $4.2 \text{ m}^2/\text{g}$  and  $0.018 \text{ cm}^3/\text{g}$ , respectively. Those numbers are considerably lower than the ones measured for chrysotile [26] ( $19.9 \text{ m}^2/\text{g}$  and  $0.043 \text{ cm}^3/\text{g}$ ) and lizardite [33] ( $33.7 \text{ m}^2/\text{g}$  and  $0.148 \text{ cm}^3/\text{g}$ ) alone. The presence of collectors, such as carbonodithioic acid (xanthate potassium isobutyl), used in the upstream nickel flotation units of the Raglan ores and left in the residues are believed to be the reason why the BET and pore volume of as-received RMR were so low [34]. Therefore, calcination under of RMR at  $700^\circ\text{C}$  not only resulted in serpentines dehydroxylation but in the decomposition (starting near  $300^\circ\text{C}$ ) and burn-off of the collector leftovers too, leading likely to a slight boost of BET surface area ( $8.05 \text{ m}^2/\text{g}$ ) and pore volume ( $0.033 \text{ cm}^3/\text{g}$ ) of calcined RMR. Further calcination of RMR in the CLC reactor led to a small decrease in its surface area. The surface area and pore volume of RMR barely changed afterwards in subsequent CLC tests, respectively,  $7.96 \text{ m}^2/\text{g}$  and  $0.043 \text{ cm}^3/\text{g}$ .

The Mössbauer characteristics of the as-received and air-calcined RMR, and the CLC tested air-calcined RMF are summarized in Table 6-2. The two sextets in the Mössbauer spectrum of the as-received RMR are characteristic of magnetite iron. The sextet with an isomer shift of  $0.69 \text{ mm/s}$  and hyperfine field of  $46.4 \text{ T}$  represents octahedral  $\text{Fe}^{3+}$  and  $\text{Fe}^{2+}$ . The second sextet with an isomer shift of  $0.26 \text{ mm/s}$  and hyperfine field of  $49.6 \text{ T}$  is characteristic of tetrahedral  $\text{Fe}^{3+}$  in magnetite. Nearly 24% of iron in the as-received RMR belongs to magnetite while the rest is distributed as intra-framework octahedral ferric (51%) and octahedral ferrous (24%) as distinguished by their two quadruple doublets. RMR air calcination profoundly altered iron oxidation and coordination alike in the samples. Almost 66% of iron turned into  $\text{Fe}^{3+}$  as  $\alpha\text{-Fe}_2\text{O}_3$  (hematite) as observed by the emergence of three sextets (isomer shifts of  $0.37 \text{ mm/s}$ ,  $0.37 \text{ mm/s}$ ,  $0.36 \text{ mm/s}$ ) and respective hyperfine fields ( $51.4 \text{ T}$ ,  $49.5 \text{ T}$ ,  $45.2 \text{ T}$ ), Table 6-2. Calcination of RMR led to the disappearance of octahedral  $\text{Fe}^{2+}$  and its further oxidation to  $\text{Fe}^{3+}$ . Nearly 34 % of iron in the calcined RMR was octahedral  $\text{Fe}^{3+}$  as concluded from the observation of two quadruple doublets with isomer shifts of  $0.31 \text{ mm/s}$  and  $0.35 \text{ mm/s}$  and corresponding quadrupole splitting of  $1.5$

mm/s and 0.88 mm/s. The Mössbauer spectrum of the CLC tested air-calcined RMF was not much different in terms of Fe coordination and oxidation from the air-calcined RMR (Table 6-2).

**Table 6-2.** Isomer shift ( $\delta$ ), quadrupole splitting ( $\Delta$ ), hyperfine field ( $B_{hf}$ ) and relative areas of the components used to fit the as-received and calcined RMR and used RMR in five oxidation/reduction cycles

Catalyst	Iron assignment	$\delta$ (mm/s)	$\Delta$ (mm/s)	$B_{hf}$ (T)	Area (%)
a/r Raglan mine residue	Magnetite $Fe^{3+}$ , tetrahedral	0.26	0	49.6	10
	Magnetite $Fe^{2+}$ , $Fe^{3+}$ , octahedral	0.69	0	46.4	14
	Chrysotile/ lizardite $Fe^{+2}$ , octahedral	1.15	2.7	0	24
	Chrysotile/ lizardite $Fe^{+3}$ , octahedral	0.374	0.645	0	51
Raglan mine residue, air-calcined at 700°C during 3 hours before using in CLC	Hematite $Fe^{3+}$ , octahedral	0.37	-0.20	51.4	31
	Hematite $Fe^{3+}$ , octahedral	0.37	-0.20	49.5	18
	Hematite $Fe^{3+}$ , octahedral	0.36	-0.19	45.2	17
	$Fe^{3+}$ , octahedral (in Mg silicate)	0.31	1.5		17
	$Fe^{3+}$ , octahedral (in Mg silicate)	0.35	0.88		17
Raglan mine residue, air-calcined, after five cycles in CLC at 700°C	Hematite $Fe^{3+}$ , octahedral	0.37	-0.19	51.4	32
	Hematite $Fe^{3+}$ , octahedral	0.35	-0.11	49.2	15
	Hematite $Fe^{3+}$ , octahedral	0.33	-0.19	45.2	19
	$Fe^{3+}$ , octahedral (in Mg silicate)	0.30	1.6		17
	$Fe^{3+}$ , octahedral (in Mg silicate)	0.36	0.91		17

### 6.3.2. Biomass torrefaction - RMR CLC

Experiments were first performed in a closed loop assembly to investigate the performance of calcined RMR as solid oxygen carrier for combustion of volatiles during torrefaction of woody biomass. The performance of solid oxygen carrier for combustion of volatiles was investigated by monitoring the accumulated  $CO_2$  concentration in the assembly. The volatiles passing through a CLC reactor were burnt over the surface of calcined RMR leading to the formation of  $H_2O$  and  $CO_2$ . This latter amount of  $CO_2$  was compared to the total carbon released in the form of volatiles from birch wood during torrefaction to assess the  $CO_2$  portions stemming directly out of torrefaction and from the burn-off of oxidizable volatiles. Table 6-3 shows the results of elemental analysis, mass yield and energy yield of birch wood before and after torrefaction at 260°C for 60 min and 300°C during 20 min. The mass yield of birch wood samples torrefied at 260°C and 300°C were 76% and 64%,

respectively. Torrefaction, as expected, led to a decrease of H/C and O/C ratios of birch wood. Torrefaction at 260°C released 13.1% and 22.1% of its total carbon and hydrogen as condensable and non-condensable gases with CO<sub>2</sub>, H<sub>2</sub>O, CO, H<sub>2</sub>, CH<sub>4</sub>, and some acid oxygenated compounds as the typical volatile compounds [17]. These proportions climbed, respectively, to 24% carbon and 34.8% hydrogen by increasing torrefaction temperature to 300°C. The blank torrefaction experiments performed while disabling the CLC reactor showed that nearly 17.1 % and 13.2 % of released carbon was in the form of CO<sub>2</sub> (Figure 6-3 a,b), 7 % and 6.5 % as CO (Figure 6-4 a,b) and 0.3 % and 0.2 % as CH<sub>4</sub> (Figure 6-5 a,b), respectively, at 260°C and 300°C. Consequently, the balance of the released carbon from the torrefied birch wood at 260°C and 300°C, respectively, contributed to 75 % and 80 % of the total released carbon in the form of condensable volatiles.

**Table 6-3:** Ultimate analysis, mass yield and energy yield of as-received and torrefied birch

Samples	C (wt%)	H (wt%)	N (wt%)	S (wt%)	O (wt%)	Ash (wt%)	Mass yield ( $Y_M$ ,%)	Energy Yield ( $Y_e$ ,%)
As-received birch	47.6	6.1	0	0	45.6	0.7	.....	100
Torrefied birch (260 °C, 60 min)	51.2	5.9	0	0	42.1	0.8	76.2	81.8
Torrefied birch (300 °C, 20 min)	52.7	5.8	0	0	40.7	0.8	64.8	71.4

Hyphenation of CLC and torrefaction reactors followed by RMR air-calcined activation led to increased CO<sub>2</sub> concentrations in the assembly due to the oxidation of volatiles passing through RMR layer as illustrated in Figure 6-3 a,b for different CLC reactor temperatures at two torrefaction temperatures. For example CLC run at 500° led to CO<sub>2</sub> in the assembly to reach up to 70.6% and 62.6% of the total volatiles carbon released during birch torrefaction at 260°C and 300°C, respectively (Figure 6-3 a,b). Increasing CLC temperature increased the fraction of volatiles converted to carbon dioxide. At 700°C almost 96.1% and 94.36% of total released carbon from the biomass torrefied, respectively, at 260°C and 300°C was in the form of CO<sub>2</sub> (Figure 6-3 a,b) confirming the activity of RMR as a solid oxygen carrier for burning the torrefaction volatiles.

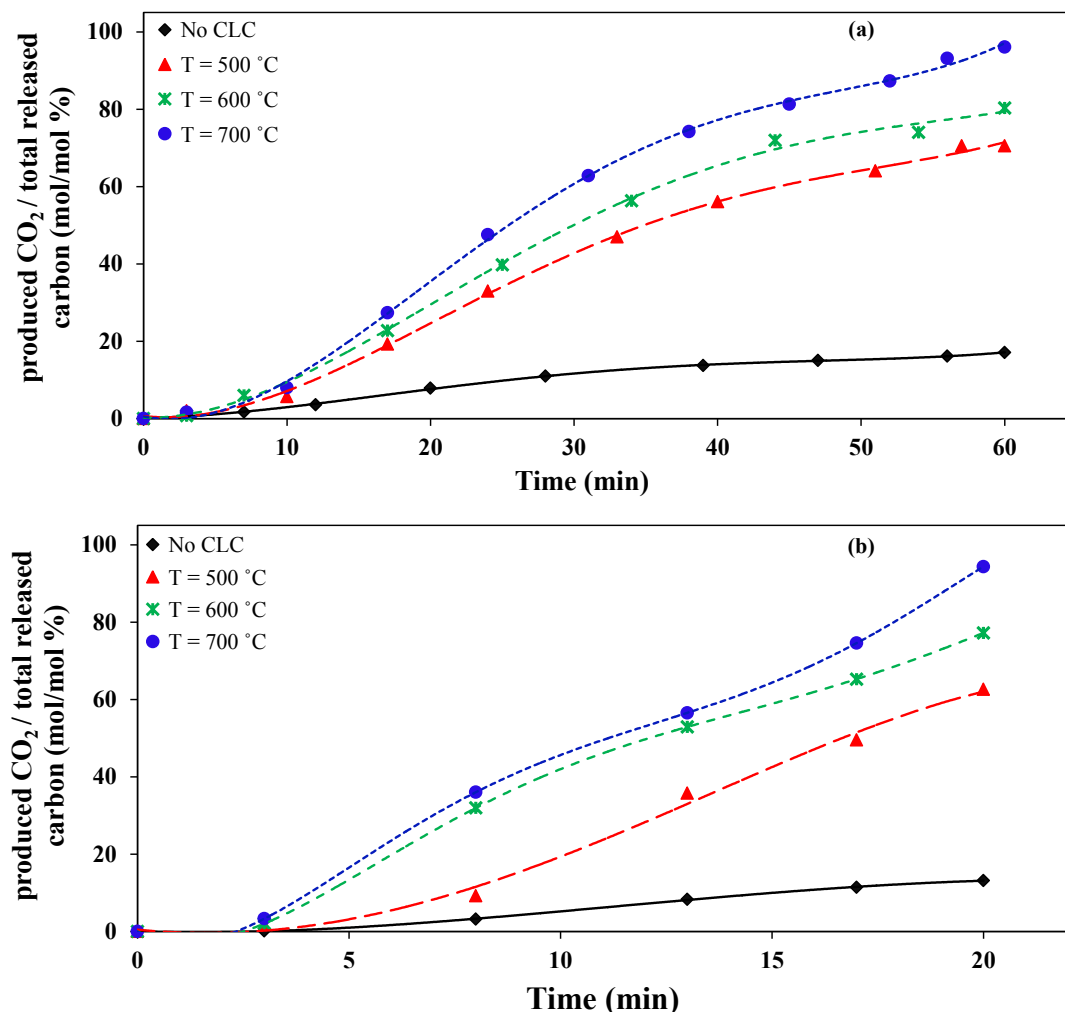


**Figure 6-3** . CO<sub>2</sub> accumulation profile in the assembly during torrefaction of 500 mg of birch at 260°C (a) and 300°C (b) for different CLC temperatures.

Oxidation of volatiles in the CLC reactor also contributed in depleting, as expected, carbon monoxide (Figure 6-4 a,b) at the expense of CO<sub>2</sub>. For instance, at a CLC temperature equal 700°C, CO contributed less than 0.5% of the total carbon released. However, in the case of methane (Figure 6-5 a,b), the trend differed from that of CO and CO<sub>2</sub> both in terms of torrefaction and CLC temperatures. The CLC reactor operating at 500°C could lead to the conversion of up to 1.5% and 2.5% of released carbon in the form of methane. The produced methane could be due to the cracking of organic compounds over the surface of RMR while, at such low CLC temperature, its activity as a solid oxygen carrier was not sufficient to then convert methane to CO<sub>2</sub>. Increasing CLC temperature to 700°C increased stimulated this latter activity function of RMR leading on the contrary to a reduction in

accumulated  $\text{CH}_4$ .

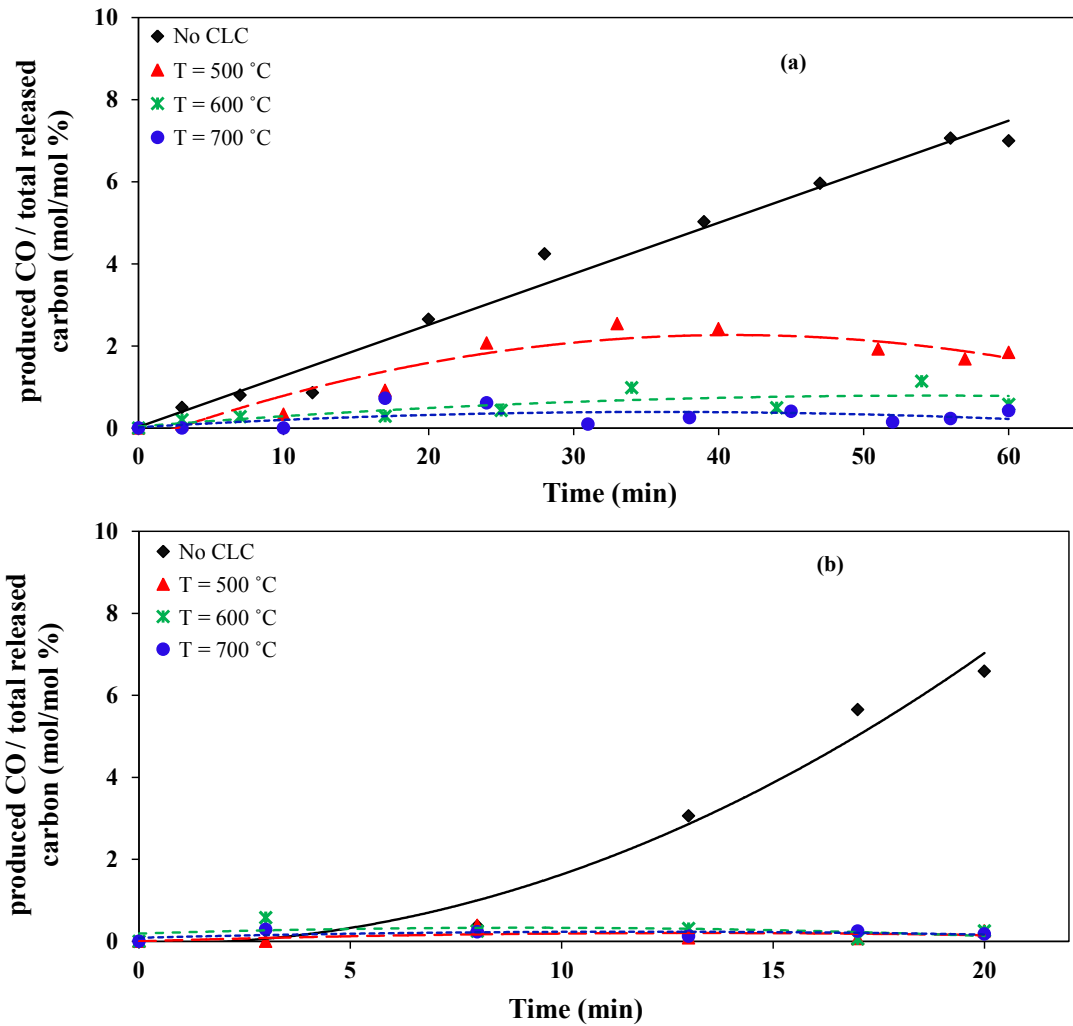


**Figure 6-4.** CO accumulation profiles in the assembly during torrefaction of 500 mg of birch at 260°C (a) and 300°C (b) for different CLC temperatures.

Cracking organic compounds inside the CLC reactor could also lead to the formation of  $\text{H}_2$ . Blank torrefaction at 260°C while disabling CLC (Figure 6-6 a) revealed no formation of  $\text{H}_2$ . This unlike the small amount of  $\text{H}_2$  measured after the CLC reactor brought at 500°C was combined with the torrefaction reactor operating at 260°C. Cracking of organic compounds was likely at the origin of such hydrogen release which was not anymore detected after rising the CLC temperature at 600°C and 700°C (Figure 6-6 a) and presumably ascribed to hydrogen accelerated oxidation into water. Torrefaction of birch at 300°C produced some  $\text{H}_2$  (Figure 6-6 b) while its concentration increased in the presence

with RMR in the CLC reactor operating at 500°C. However, by increasing the CLC temperature, hydrogen concentration decreased in the reactor leading to the formation of some water.

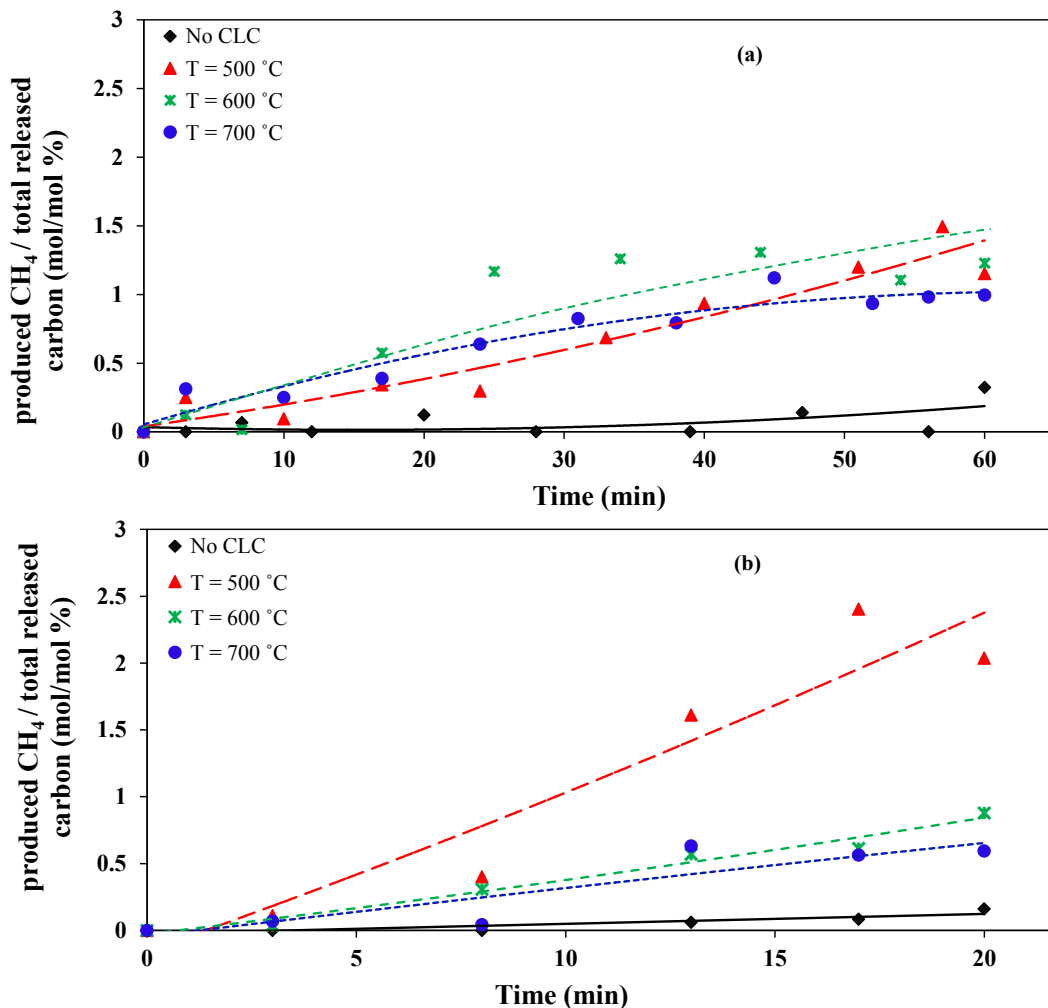


**Figure 6-5.** CH<sub>4</sub> accumulation profiles in the assembly during torrefaction of 500 mg of birch at 260°C (a) and 300°C (b) for different CLC temperatures.

The cracking of oxygenated hydrocarbons over the surface of RMR oxygen carrier could lead to the formation of some deposited carbon. The largest amount of deposited carbon was observed when the CLC was operating at 500°C. The amount of deposited carbon on the RMR was ca. 3.1% and 3.6% of the total released carbon for the biomass torrefied at 260°C and 300°C, respectively. Increasing the CLC temperature reduced carbon deposits formation, resulting at a CLC temperature 700°C in ca. 1.4% and 1.6% of total released

carbon at 260°C and 300°C torrefaction temperatures. The oxidation/reduction cycles of RMR revealed very minor activity losses through sintering of hematite particles. Figure 6-7 shows that RMR materials used after five consecutive cyclic operations underwent almost no activity loss for burning the oxidizable volatile components issued from torrefaction.

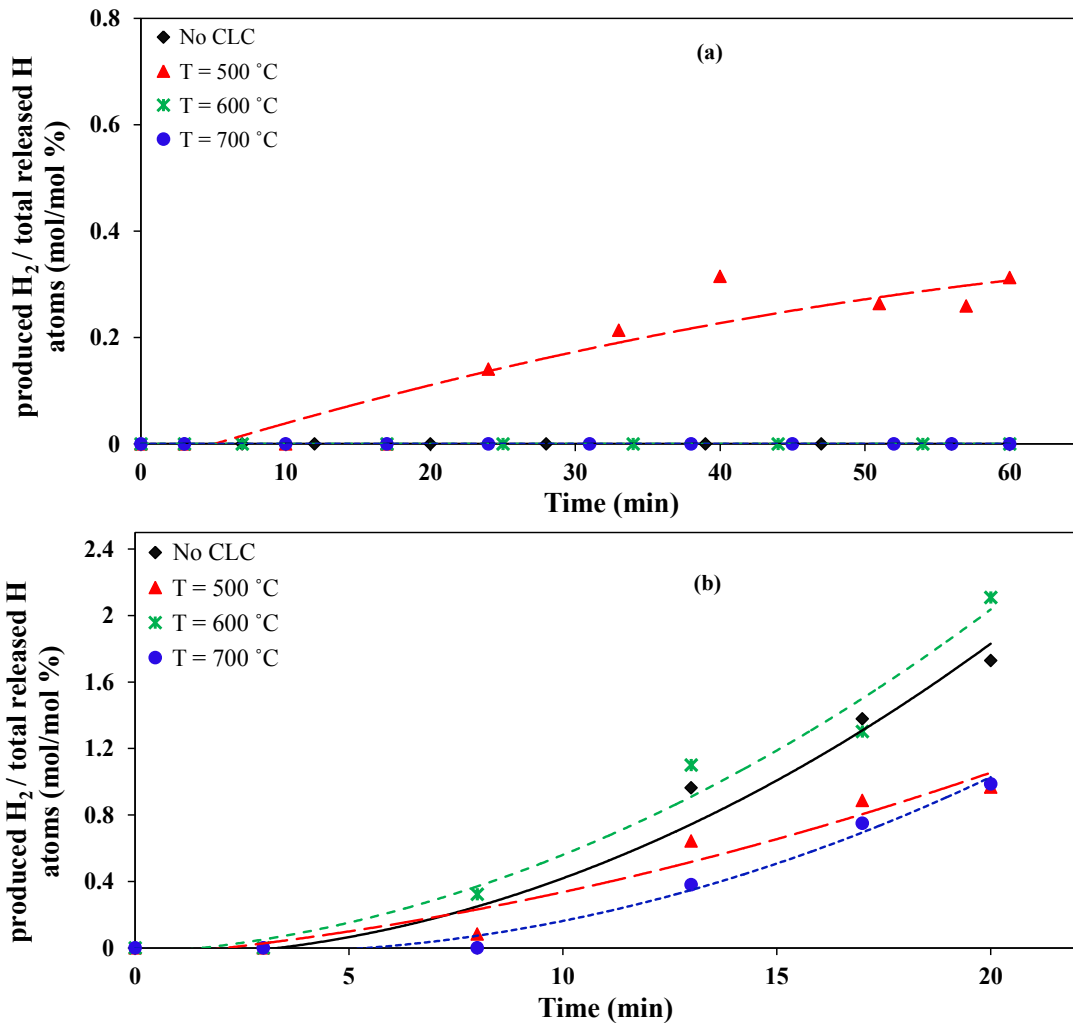


**Figure 6-6.** H<sub>2</sub> accumulation profiles in the assembly during torrefaction of 500 mg of birch at 260°C (a) and 300°C (b) for different CLC temperatures.

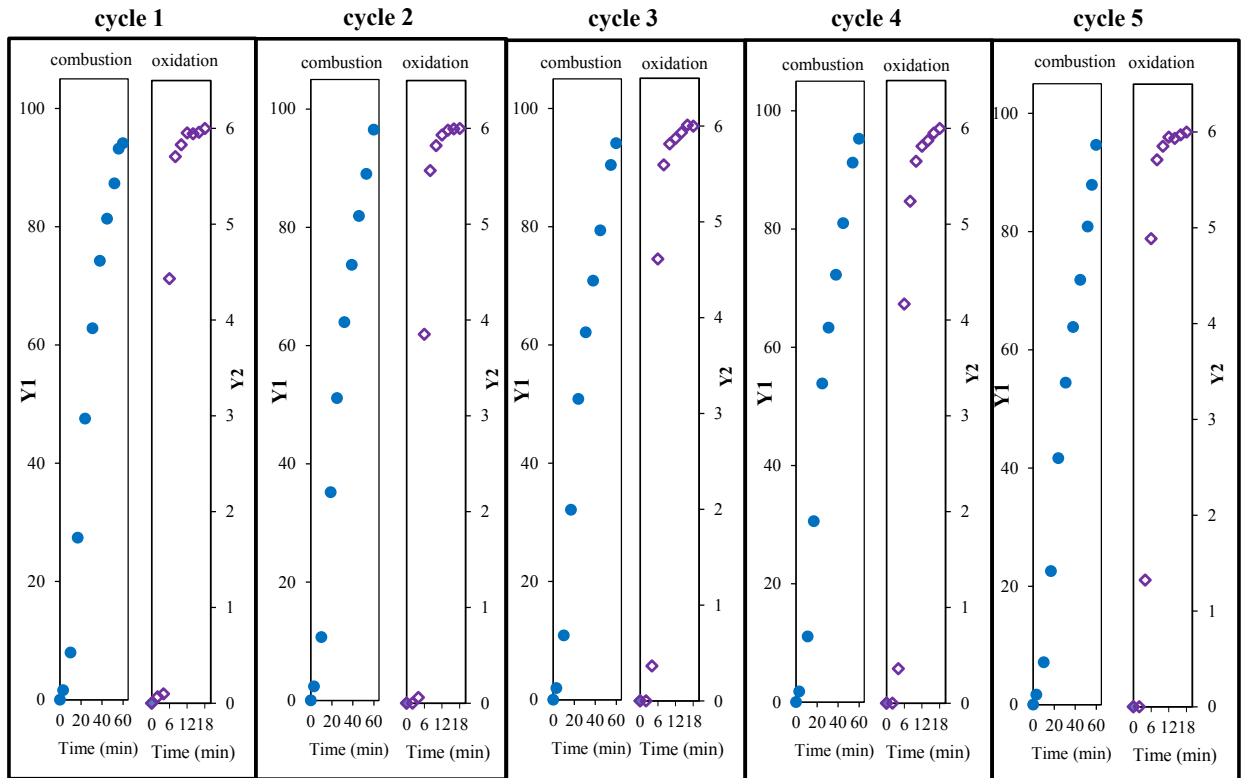


**Figure 6-7.** Profiles of CO<sub>2</sub> production and oxygen consumption during five cycles of torrefaction/combustion and oxidation /regeneration of RMR. Temperatures of torrefaction and CLC reactors were 260°C and 700°C, respectively. Blue circles are mol% of released carbon converted to CO<sub>2</sub> and accumulated in assembly. Purple diamonds are mol% of oxygen exiting CLC reactor during oxidation/regeneration step. Initial oxygen mol% during oxidation step was 6 mol% and nitrogen flow-rate 200 mL/min. Y1: produced CO<sub>2</sub>/total released carbon (mol/mol%), Y2: oxygen concentration (mol%).

### 6.3.3. Biomass torrefaction - RMR CLC - carbonation

The trend of CO<sub>2</sub> accumulation in the assembly with or without RMR as carbonation medium is depicted in Figure 8. As could be observed in this Figure, the CO<sub>2</sub> accumulation in the assembly was the highest in the experiment performed without RMR residue in the carbonation column. The experiment performed without RMR residue showed the production and accumulation of almost 2.4 mmol CO<sub>2</sub> in the assembly after 60 min of torrefaction (Figure 6-8). However, the carbonation reactions in the presence of 50% saturated RMR residues at 25°C reduced the amount of CO<sub>2</sub> accumulated in the assembly during torrefaction. At the end of torrefaction, the amount of CO<sub>2</sub> accumulated in the assembly was 2.1 mmol showing a reduction of 11% in the amount of accumulated CO<sub>2</sub> corresponding to the carbonation of 0.18% of total Mg at 25°C.

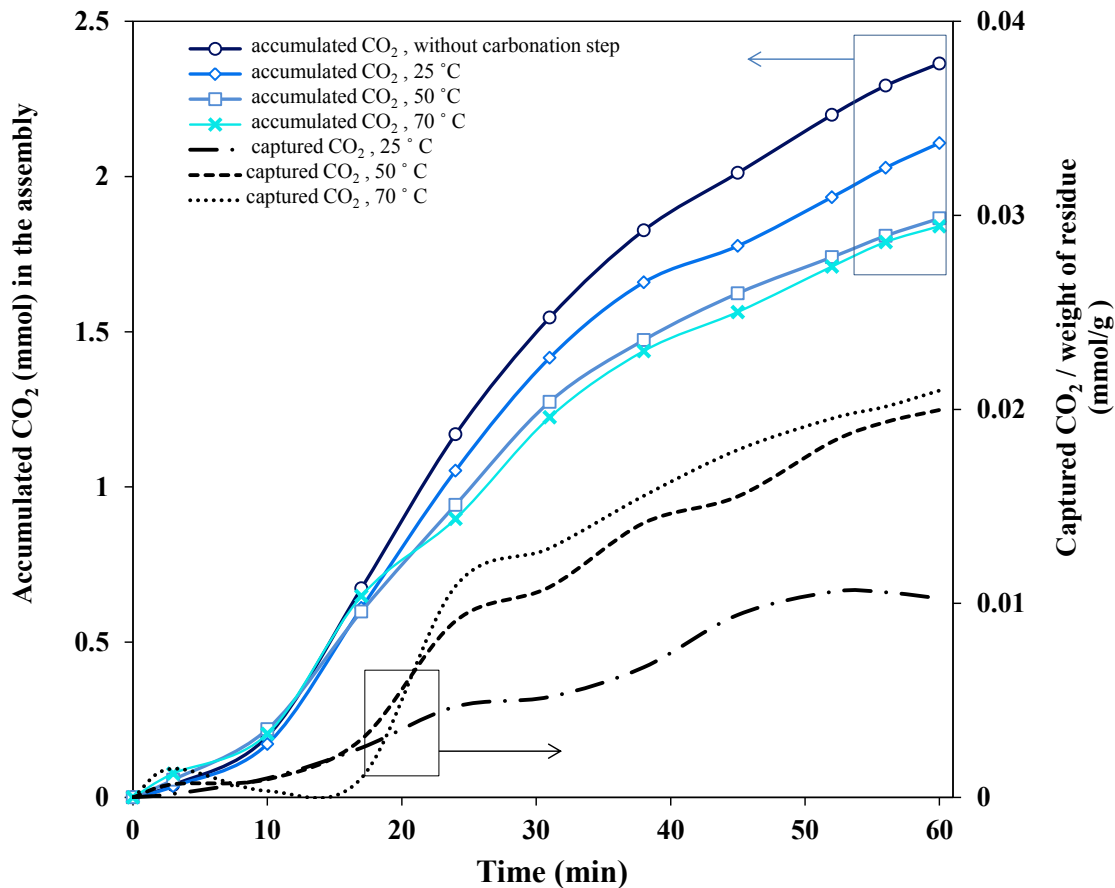


**Figure 6-8.** Accumulated and captured CO<sub>2</sub> versus time during dry birch torrefaction at 260°C in the presence of RMR carbonation bed at different temperatures.

The reactivity of RMR for carbonation is found to be lower than that of some other mining residues we have already tested [30]. This could be probably due to the low or negligible free Mg content in the form of brucite in this residue as revealed from the XRD pattern shown in Figure 2. However, the contact of forsterite with water could lead to the leaching of some Mg. The leached Mg is reacting with dissolved CO<sub>2</sub> leading to the formation and precipitation of magnesium carbonates [29, 30]. As illustrated in Figure 8, the rate of RMR carbonation at the beginning of torrefaction is low which could be attributed to diffusion limitations of CO<sub>2</sub> in the residue pore water before reacting with the leached magnesium. Increasing carbonation temperature to 50°C improved carbonation rate leading to an accumulation of 1.86 mmol of CO<sub>2</sub> in the assembly after 60 min. This was equivalent to displacing 21% in 60 min of produced carbon dioxide during torrefaction requiring only 0.35% Mg of total Mg present in the carbonation reactor. Increasing the carbonation

temperature to 70°C only marginally affected the CO<sub>2</sub> accumulated after 1 h compared to carbonation at 50°C. Although it is expected that carbonation rate increases with temperature, the increased rate of water evaporation from residue and the decreasing CO<sub>2</sub> solubility in water both contribute to reduce the amount of leached Mg and as a consequence carbonation reactivity. The percentages of water estimated to have evaporated at 50°C and 70°C during RMR carbonation were estimated to be 33% and 76% of the initial water pore saturation poured through the carbonation bed at the beginning of the torrefaction experiments. Meanwhile, the CO<sub>2</sub> solubility at 50°C and 70°C decreased, respectively, by 48% and 70% with respect to their level at 25°C (respectively, 319 ppm and 185 ppm versus 609 ppm) [35]. These figures could explain the limited carbonation reactivity of the sample at 70°C.

## 6.4. Conclusion

An iron-containing magnesium silicate mining residue from a nickel recovery mine project (Raglan mines, Xstrata Nickel, Nunavik, Québec, Canada) was tested in integrated with torrefaction to burn torrefaction volatiles from a woody biomass (birch) and then to carbonate the produced CO<sub>2</sub>. Hence, the mining residues were explored as a cheap oxygen carrier, owing to iron, in a chemical looping combustion (CLC) reactor and as a sink for carbonates, owing to magnesium, in a carbonation reactor connected to a torrefaction reactor. Although the as-received mining residue had only 24% of its iron in the form of magnetite, its pre-calcination led to the extraction of intra-framework iron from the residue crystalline structure and the conversion of 66% of iron to hematite to act as an oxygen carrier for burning the torrefaction volatiles. The residue was tested in a torrefaction-CLC combination for burning the torrefaction volatiles at different torrefaction and combustion temperature. It was found that up to 96% of the carbon released as volatiles was converted into CO<sub>2</sub>. Further, cycling the residue over up to 5 reduction/oxidation periods showed its potential as a stable oxygen carrier for burning torrefaction volatiles. The potential of the residue for the sequestration of CO<sub>2</sub> released during the process was also tested and a low carbonation activity by the residue was observed. The residue was finally tested in a torrefaction-CLC-carbonation combination for burning the torrefaction volatiles and capturing the produced carbon dioxide for different temperatures for torrefaction, CLC and carbonation.

## 6.5. References

- [1] The outlook for energy: a view to 2040. [www.exxonmobil.com/energyoutlook](http://www.exxonmobil.com/energyoutlook); 2013.
- [2] Wang C, Peng J, Li H, Bi XT, Legros R, Lim CJ, et al. Oxidative torrefaction of biomass residues and densification of torrefied sawdust to pellets. *Bioresource Technology*. 2013;127:318-25.
- [3] Hoekman SK, Broch A, Robbins C. Hydrothermal carbonization (HTC) of lignocellulosic biomass. *Energy & Fuels*. 2011;25:1802-10.
- [4] van der Stelt MJC, Gerhauser H, Kiel JHA, Ptasinski KJ. Biomass upgrading by torrefaction for the production of biofuels: A review. *Biomass & Bioenergy*. 2011;35:3748-62.
- [5] Bridgeman TG, Jones JM, Williams A, Waldron DJ. An investigation of the grindability of two torrefied energy crops. *Fuel*. 2010;89:3911-8.
- [6] Repellin V, Govin A, Rolland M, Guyonnet R. Energy requirement for fine grinding of torrefied wood. *Biomass & Bioenergy*. 2010;34:923-30.
- [7] Sarvaramini A, P. Assima G, Larachi F. Dry torrefaction of biomass – Torrefied products and torrefaction kinetics using the distributed activation energy model. *Chemical Engineering Journal* 2013. p. 498-507.
- [8] Sarvaramini A, Gravel O, Larachi F. Torrefaction of ionic-liquid impregnated lignocellulosic biomass and its comparison to dry torrefaction. *Fuel*. 2013;103:814-26.
- [9] Patel B, Gami B, Bhimani H. Improved fuel characteristics of cotton stalk, prosopis and sugarcane bagasse through torrefaction. *Energy for Sustainable Development*. 2011;15:372-5.
- [10] Bridgeman TG, Jones JM, Shield I, Williams PT. Torrefaction of reed canary grass, wheat straw and willow to enhance solid fuel qualities and combustion properties. *Fuel*. 2008;87:844-56.
- [11] Li J, Brzdekiewicz A, Yang WH, Blasiak W. Co-firing based on biomass torrefaction in a pulverized coal boiler with aim of 100% fuel switching. *Applied Energy*. 2012;99:344-54.
- [12] Boateng AA, Mullen CA. Fast pyrolysis of biomass thermally pretreated by torrefaction. *Journal of Analytical and Applied Pyrolysis*. 2013;100:95-102.
- [13] Chang S, Zhao Z, Zheng A, He F, Huang Z, Li H. Characterization of products from torrefaction of sprucewood and bagasse in an auger reactor. *Energy & Fuels*. 2012;26:7009-17.
- [14] Peng JH, Bi HT, Lim CJ, Sokhansanj S. Study on Density, Hardness, and Moisture uptake of torrefied wood pellets. *Energy & Fuels*. 2013;27:967-74.
- [15] Medic D, Darr M, Shah A, Rahn S. Effect of Torrefaction on water vapor adsorption properties and resistance to microbial degradation of corn stover. *Energy & Fuels*. 2012;26:2386-93.
- [16] Peng JH, Bi HT, Sokhansanj S, Lim JC. A study of particle size effect on biomass torrefaction and densification. *Energy & Fuels*. 2012;26:3826-39.

- [17] Prins MJ, Ptasiniski KJ, Janssen F. Torrefaction of wood - Part 2. Analysis of products. *Journal of Analytical and Applied Pyrolysis*. 2006;77:35-40.
- [18] Koppejan J, Sokhansanj S, Melin s, Madrali S. Status overview of torrefaction technologies. IEA bioenergy task 32 report December 2012.
- [19] Uslu A, Faaij APC, Bergman PCA. Pre-treatment technologies, and their effect on international bioenergy supply chain logistics. Techno-economic evaluation of torrefaction, fast pyrolysis and pelletisation. *Energy*. 2008;33:1206-23.
- [20] C.P. K. Overview of international development in torrefaction. Kema report, [www.kema.com2011](http://www.kema.com2011).
- [21] Sarvaramini A, Larachi F. Integrated biomass torrefaction-chemical looping combustion as a method to recover torrefaction volatiles energy. *Fuel*. 2014;116:158-67.
- [22] Mattisson T, Lyngfelt A, Cho P. The use of iron oxide as an oxygen carrier in chemical-looping combustion of methane with inherent separation of CO<sub>2</sub>. *Fuel*. 2001;80:1953-62.
- [23] Hossain MM, de Lasa HI. Chemical-looping combustion (CLC) for inherent CO<sub>2</sub> separations-a review. *Chemical Engineering Science*. 2008;63:4433-51.
- [24] Leion H, Lyngfelt A, Johansson M, Jerndal E, Mattisson T. The use of ilmenite as an oxygen carrier in chemical-looping combustion. *Chemical Engineering Research & Design*. 2008;86:1017-26.
- [25] Sarvaramini A, Larachi F. Mossbauer spectroscopy and catalytic reaction studies of chrysotile-catalyzed steam reforming of benzene. *Journal of Physical Chemistry C*. 2011;115:6841-8.
- [26] Sarvaramini A, Larachi F. Catalytic oxygenless steam cracking of syngas-containing benzene model tar compound over natural Fe-bearing silicate minerals. *Fuel*. 2012;97:741-50.
- [27] Assima GP, Larachi F, Beaudoin G, Molson J. CO<sub>2</sub> sequestration in chrysotile mining residues-implication of watering and passivation under environmental conditions. *Industrial & Engineering Chemistry Research*. 2012;51:8726-34.
- [28] P. Assima G, Larachi F, Molson J, Beaudoin G. Accurate and direct quantification of native brucite in serpentine ores—New methodology and implications for CO<sub>2</sub> sequestration by mining residues. *Thermochimica Acta* 2013. p. 281-91.
- [29] P. Assima G, Larachi F, Beaudoin G, Molson J. Dynamics of carbon dioxide uptake in chrysotile mining residues- effect of mineralogy and liquid saturation. *International Journal of Greenhouse Gas Control*. 2013;12:124-35.
- [30] Sarvaramini A, Assima GP, Beaudoin G, Larachi F. Biomass torrefaction and CO<sub>2</sub> capture using mining wastes- A new approach for reducing greenhouse gas emissions of co-firing plants. *Fuel*. 2014;115:749-57.
- [31] Larachi F, Daldoul I, Beaudoin G. Fixation of CO<sub>2</sub> by chrysotile in low-pressure dry and moist carbonation: Ex-situ and in-situ characterizations. *Geochimica Et Cosmochimica Acta*. 2010;74:3051-75.

[32] Channiwala SA, Parikh PP. A unified correlation for estimating HHV of solid, liquid and gaseous fuels. *Fuel*. 2002;81:1051-63.

[33] O'Connor WK, Dahlin DC, Nilsen DN, Gerdemann SJ, Rush GE, Penner LR, et al. Continuing studies on direct aqueous mineral carbonation for CO<sub>2</sub> sequestration. 27th International technical Conference On Coal Utilization and Fuel Systems, Clear Water. Florida.

[34] Lotter NO, Bradshaw DJ. The formulation and use of mixed collectors in sulphide flotation. *Minerals Engineering*. 2010;23:945-51.

[35] Carroll JJ, Slupsky JD, Mather AE. The solubility of carbon-dioxide in water at low-pressure. *Journal of Physical and Chemical Reference Data*. 1991;20:1201-9.



## **Chapter 7 : Mössbauer spectroscopy & catalytic reaction studies of chrysotile-catalyzed steam reforming of benzene**

**Résumé** Le chrysotile, un phyllosilicate d'hydroxide de magnésium ferrifère d'origine naturelle et retrouvé dans les mines et dans les résidus miniers provenant du sud du Québec, a été testé pour son potentiel en tant que catalyseur pour le craquage du goudron en gazéification à la vapeur de la biomasse. Incrustés dans le minerai de chrysotile, les impuretés de magnétite ont été ciblées en tant que source des propriétés de craquage catalytique du goudron du matériau. L'activité de reformage à la vapeur du chrysotile a été investiguée à l'aide de benzène en tant que composé modèle du goudron à différentes températures, différentes vitesses spatiales horaires gazeuses et différents prétraitements du catalyseur. L'activité du chrysotile calciné à l'air (converti en forsterite contenant de l'hématite) a été comparée à son équivalent en contenu de fer d'un catalyseur d'olivine. De la spectroscopie de Mössbauer combinée à des études de réduction à température programmée, au rendement en gaz de synthèse (*syngas*) et aux conversions du benzène ont permis de d'identifier le rôle des différents états d'oxydation ainsi que des environnements de coordination du fer en tant que fonction des conditions de prétraitement du catalyseur. Les résultats de l'étude ont été mis en perspective en termes du déportement du fer et de la surface spécifique BET du minerai dans le but d'expliquer l'augmentation par un facteur de près de cinq de la conversion du benzène et du rendement en *syngas* du chrysotile par rapport à l'olivine pour des vitesses spatiales horaires gazeuses, des températures et des tailles de particules similaires.

**Abstract** Chrysotile, a naturally-occurring iron-bearing magnesium hydroxide phyllosilicate found in mine and milling residue heaps from southern Québec was tested for its potential use as a tar-cracking catalyst in biomass steam gasification. Interspersed within the chrysotile mineral, magnetite impurities were recognized to confer tar-cracking catalytic properties to the material. Chrysotile steam-reforming activity was probed using benzene model tar compound at various temperatures, gas hourly space velocities and catalyst pretreatments. The activity of air-calcined chrysotile (converted to hematite-containing forsterite) was benchmarked against that of olivine catalyst with nearly equal iron content. Mössbauer spectroscopy combined with temperature programmed reduction studies, syngas yield and benzene conversion responses enabled recognizing the role of the various oxidation states and coordination environments of iron as a function of pretreatment conditions of the catalyst. The study's findings were rationalized in terms of iron deportment and BET specific surface area of the minerals to explain the fivefold increase of benzene conversion and syngas yield of chrysotile over olivine for similar gas hourly *mass* space velocities, temperatures and particle sizes.

## 7.1. Introduction

The need for non-fossil energy alternatives is increasingly shifting industry's focus towards inedible (lignocellulosic) biomass residues as a potential renewable energy source. Gasification is one such thermochemical route sought for converting biomass into biosyngas – a precursor to biofuels or biochemical [1]. Accumulation of heavy condensable polycyclic hydrocarbon volatiles, i.e., primary and secondary tar aerosols, during the gasification of biomass is known to exact serious operational problems. As high quality and competitive biosyngas must be tar-free ( $< 0.5 \text{ g/Nm}^3$ ), extensive research is being conducted to limit its formation, either by operating the process at very high temperature ( $> 1100^\circ\text{C}$ ) to thermally crack tars, or by using reforming (or tar-cracking) catalysts [2-9].

The extent and scale at which gasification is practiced industrially makes catalytic cracking of biomass-released tars relying on cheap naturally-occurring minerals an appealing option. Hence, cheap and abundant iron-bearing silicate catalysts such as olivine have been applied successfully in pilot-scale gasifiers for cracking tars [10]. It was established that olivine's tar-cracking catalytic activity correlates both with the coordination environment and content of iron in the material. More specifically, olivine with higher content in *reducible* iron leads to improved tar cracking activity [11]. Yet, iron in the olivine natural structure is poorly reducible primarily because it lies predominantly as intra-framework divalent cation. Calcination of olivine at high temperature ( $> 900^\circ\text{C}$ ) is hence implemented as a prerequisite step to the formation of free reducible extra-framework  $\text{Fe}^{3+}$ -bearing iron oxides. Extraction of  $\text{Fe}^{2+}$  from the olivine lattice through calcination and formation therefrom of reducible hematite- or magnetite-borne  $\text{Fe}^{3+}$  bestow on olivine its tar-cracking activity [12].

The mining activity in Thetford Mines (Québec, Canada) since its inception in 1878 led to the accumulation of approximately 2 billion tonnes of serpentized milling/mining residues where chrysotile is abundant and is naturally entwined with magnetite [13]. These large accumulations of iron-bearing magnesium silicate minerals present in residue heaps are worth investigating for chrysotile may constitute a regional low-cost alternative catalyst to olivine in supplying biomass-steam gasification plants nearby the mining sites for converting inedible lignocellulosic residues into biosyngas or for power generation.

In the present study, the focus is on the serpentinic polymorph chrysotile as this was recently tested for its carbonation potential for CO<sub>2</sub> capture and sequestration [14]. Chrysotile, Mg<sub>3</sub>Si<sub>2</sub>O<sub>5</sub>(OH)<sub>4</sub>, is a nanotubular (self-reeled) bilayer hydrous phyllosilicate formed by hydrothermal fluids during the hydration of mafic/ultramafic rocks. Its basic structure consists of tetrahedral [SiO<sub>4</sub>]<sup>4-</sup> silicate sheets attached to trioctahedral [Mg<sub>3</sub>O<sub>2</sub>(OH)<sub>4</sub>]<sup>2-</sup> brucitic-like sheets through common apical oxygen atoms [14]. As for olivine, Mg partial substitution with iron in the chrysotile lattice is not uncommon. Furthermore, owing to the magnetic signature of the as-received mineral, the material also contains extra-framework iron through intergrown magnetite. Therefore, the occurrence of iron in the native mineral samples is foreseen to confer tar-cracking catalytic properties to chrysotile. We propose hence to assess in this study the chrysotile steam-reforming catalytic activity for a model-tar compound which we will benchmark with respect to the catalytic response of an olivine loaded with approximately the same amount of iron. Benzene selection as a representative biomass model-tar compound is widely accepted in the literature [15-18], therefore this molecule was chosen in our study for the same purpose.

## 7.2. Experimental

The chrysotile residue, originating from Thetford Mines (Québec) was sieved to isolate the fraction 212-300 μm (65-48 mesh Tyler sieves) for the catalytic study. No attempt was made to isolate chrysotile out of the residue matrix so that designation as chrysotile henceforth refers to the raw (native or as-received) mineral. Despite chrysotile fluffy and fibrous aspect, the size range of the sieved fibers was fit for fixed-bed catalytic tests requiring no further dilution with inert solids. N<sub>2</sub> adsorption isotherms of native chrysotile were measured on a Micromeritics TRISTAR 3000 at 77 K and residual pressures down to 10<sup>-5</sup> Torr. As-received chrysotile is a relatively porous mineral with a measured BET surface area amounting to 19.9 m<sup>2</sup>/g. Elemental analysis of the raw chrysotile obtained through X-ray fluorescence analysis (Table 7-1) revealed the presence, apart from the main chrysotile constitutive elements (Mg and Si), of Fe and Al as dominant elemental contaminants, and other minority contaminations, Ca, K, Cr, Mn and Na. The computed Mg/Si atomic ratio is 1.444. This is 3.7% less than the theoretical chrysotile stoichiometric ratio despite traces of free brucite, Mg(OH)<sub>2</sub>, were objectified through X-ray powder

diffraction. The total iron loading in chrysotile is 4.2 wt%. Ignoring, as a first approximation, the brucitic Mg toll calls for Fe(intra-framework)/Si ratio equal to 0.056 suggesting a maximum substitution of ca. 39 intra-framework Fe<sup>2+</sup> cations for every 1,000 Mg<sup>2+</sup> ions. This is tantamount to an upper limit of 49.2% of iron potentially incorporable into the chrysotile lattice.

The chrysotile catalytic activity was benchmarked with respect to an olivine catalyst supplied by Minelco which was extracted from mines in Greenland. It was sieved to isolate the fraction 250-425 μm (60-35 mesh Tyler sieves). The as-received olivine had a BET surface area equal 0.2 m<sup>2</sup>/g and a total iron loading of 6.4 wt%. The as-received olivine constitutive analytes are also given in Table 7-1.

**Table 7-1:** wt % of analytes constitutive of raw chrysotile (Thetford Mines, Québec) and olivine (Greenland) <sup>a</sup>Lost on ignition

Analyte	SiO <sub>2</sub>	MgO	Fe <sub>2</sub> O <sub>3</sub>	CaO	K <sub>2</sub> O	Cr <sub>2</sub> O <sub>3</sub>	MnO	Al <sub>2</sub> O <sub>3</sub>	Na <sub>2</sub> O	LOI <sup>a</sup>	Total
chrysotile	39.71	38.46	6.02	0.50	0.14	0.11	0.10	0.67	0.030	13.20	98.94
olivine	41.37	47.72	9.15	0.19	0.08	0.19	0.12	0.72	0.010	-	99.55

The steam-reforming catalytic activities of chrysotile and olivine were compared using benzene as a biomass model-tar compound. Benzene is known to be among the most stable constituents of biomass-derived tar [19]. Furthermore, benzene is thermally stable so that thermal cracking –whether in the presence or not of H<sub>2</sub> and/or steam– is minor below 900°C [20]. Consequently, benzene cracking at temperatures not in excess of 900°C would be representative of the sole catalytic activity of the mineral being tested. Some of the reactions involved in steam reforming of benzene are as follows:



The experimental setup for benzene catalytic reforming consists of a stainless steel (SS) fixed-bed reactor (i.d. 34 mm, length 70 cm) and a concentric quartz tube (i.d. 30 mm,

length 70 cm) adjusted within the steel tube to avert metal-benzene contacting. The catalyst is held atop of a quartz grid (40-90  $\mu\text{m}$  pore diameter) welded in the middle of the quartz tube to act as a gas distributor. The reactor is heated through a 30 cm long coil connected to a 18 kW induction power supply for heating the stainless steel tube via AC magnetic field then heating in turn the catalyst layer through radiation and conduction. The SS tube temperature is controlled by a fiber optic pyrometer connected to a temperature controller to meter the induction-heater power. Temperature is also measured through a ceramic-shielded K type thermocouple inserted in the center of the catalyst bed. The difference between the bed temperature and SS tube surface never exceeded 5°C.

The effect of steam/carbon (mole) ratio (S/C) on the activity of our chrysotile and olivine samples was assessed in preliminary tests. It was found that the catalytic activity of calcined chrysotile and olivine marginally responded to changes in S/C ratios ranging from 1 to 6. Therefore, a constant steam/carbon mole ratio = 1.05 was used in this study. A similar lack of dependence of activity to S/C ratio was reported for the steam reforming of naphthalene over calcite at  $S/C > 1$  [21], of toluene over Ni/olivine catalyst at  $S/C > 2$  [22], and of benzene over dolomite at  $S/C > 1$  [15].

A stream of  $\text{N}_2$  saturated with benzene (16 g/ $\text{Nm}^3$ ) and steam ( $S/C = 1.05$ ) was fed upwardly through the fixed-bed reactor. Gas products' concentrations ( $\text{CO}$ ,  $\text{CO}_2$ ,  $\text{H}_2$  and  $\text{CH}_4$ ) and benzene were quantified using micro-gas chromatography (Agilent 3000A, Agilent Technologies) and the yield of products and benzene conversion were obtained at 210 s time intervals during 1 h runs. The carbon balance was completed by burning off in-situ the coke deposited on the catalyst surface which was quantified on-line using an infrared  $\text{CO}_2$  detector. The carbon mass balance was closed up to within 5%.

Prior to the catalytic tests, native chrysotile and olivine were calcined, alternatively under air or  $\text{N}_2$  streams, for at least 2 h at 900°C at a flow rate of 200 mL/min (20°C, 1 atm). This temperature is high enough to ensure complete dehydroxylation and amorphisation of chrysotile and thence its recrystallization into forsterite and enstatite [14]. For post-mortem characterizations of calcined (or spent) materials, the catalysts were subsequently quenched in-situ under air or  $\text{N}_2$  from 900°C to 250°C then to 50°C, respectively, at 130 and 40 K/min cooling rates and a flow rate 5000 mL/min (20°C, 1

atm). The quench rates were deemed fast enough to freeze the crystalline structure of the materials so that their off-line characterizations would still reflect their states at the catalytic conditions.

To help interpreting the observed benzene steam-reforming catalytic activity, ex-situ X-ray powder diffraction (XRPD),  $^{57}\text{Fe}$  Mössbauer spectroscopy, temperature-programmed reduction (TPR) under a stream of hydrogen and transmission electron microscopy (TEM) tests were performed both on native and calcined chrysotile and olivine samples. The crystalline phases in presence and the catalyst structural modifications due to calcination were identified by XRPD on a Siemens D5000 X-ray powder diffractometer using a  $\text{Cu K}\alpha$  radiation ( $\lambda = 1.54059 \text{ \AA}$ ) generated at 40 kV and an emission current of 30 mA. The distribution of iron, the species mainly responsible for the catalytic activity, in different coordinations and oxidation states in the as-received and calcined materials was estimated through room temperature  $^{57}\text{Fe}$  Mössbauer spectroscopy using a 50 mCi  $^{57}\text{CoRh}$  source on a conventional Mössbauer spectrometer operated in a sine mode. The Mössbauer spectra were fitted to a sum of Lorentzian lines using a non-linear least-squares minimization routine. The atomic percentages of the various iron entities with respect to the total iron (quantified through X-ray fluorescence analysis) were taken to be equal to their corresponding Mössbauer absorption areas [23]. Both as-received and calcined catalysts were submitted to temperature-programmed reductions in the fixed-bed reactor.  $\text{H}_2\text{-N}_2$  mixtures (3.04 vol.% of  $\text{H}_2$ ) at a flow rate of 300 mL/min ( $20^\circ\text{C}$ , 1 atm) were fed through a 2 g catalyst layer in a prograde heating mode up to  $950^\circ\text{C}$  at a programmed heating rate of 15 K/min and  $\text{H}_2$  uptake was monitored via micro-gas chromatography at 100 s time intervals. Transmission electron microscopy (TEM) images were obtained for chrysotile and olivine samples using a JEOL JEM-1230 electron microscope after the samples were dispersed in methanol and a drop of the suspension was deposited on the formvar coated nickel grid. The size of hematite islands formed on the surface of calcined chrysotile and olivine was correlated to the sintering phenomenon.

## 7.3. Results & discussion

### 7.3.1. X-ray powder diffraction patterns

Figure 7-1 (a&b) shows the XRPD patterns of native and air-calcined chrysotile. X-ray powder diffraction of raw chrysotile shows the main peaks of chrysotile at  $2\theta = 12^\circ$ ,  $24.3^\circ$  and  $36.6^\circ$  along with the main peak of  $\text{Fe}_3\text{O}_4$  phase at  $2\theta = 35.6^\circ$ .

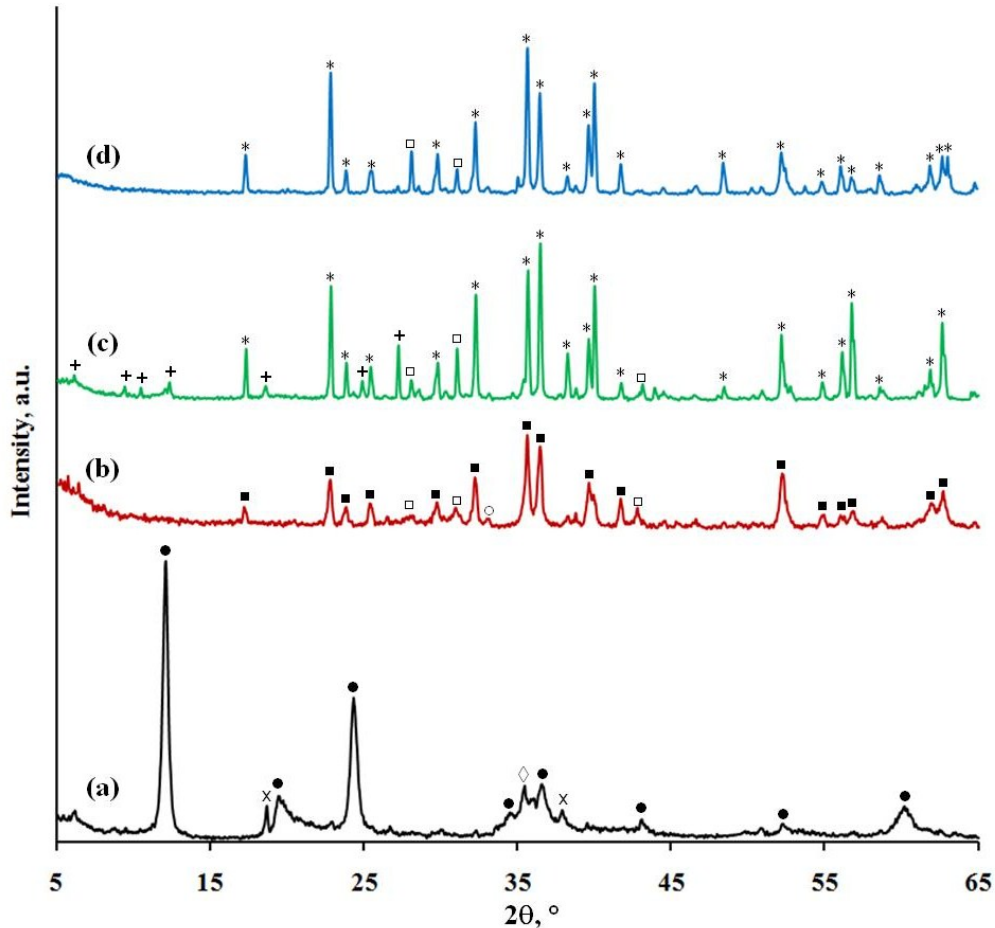


**Figure 7-1.** X-ray powder diffraction patterns of (a) raw chrysotile (b) chrysotile calcined with air at  $900^\circ\text{C}$  (c) raw olivine (d) olivine calcined with air at  $900^\circ\text{C}$ . (●) chrysotile, (◇) magnetite, (▪) forsterite, (□) enstatite, (○) hematite, (x) brucite, (\*) olivine, (+) serpentinite impurities in olivine.

Calcination at  $900^\circ\text{C}$  obliterated the structure of chrysotile and led to the formation of new silicate crystalline phases, enstatite ( $\text{MgSiO}_3$ ,  $2\theta = 28.2^\circ$ ) and forsterite ( $\text{Mg}_2\text{SiO}_4$ ,  $2\theta = 35.6^\circ$  and  $36.5^\circ$ ), and of crystalline hematite ( $2\theta = 33.2^\circ$ ). The XRPD patterns of raw and air-calcined olivine are shown in Figure 7-1 (c&d). The main diffraction peaks associated

with the olivine crystalline phase peak up at  $2\theta = 35.7^\circ$  and  $36.5^\circ$  and are close, as expected, to the forsterite main peaks ( $\text{Mg}_2\text{SiO}_4$ ,  $2\theta = 35.6^\circ$  and  $36.5^\circ$ , Figure 7-1 b). Serpentine impurities, such as chlorite ( $\text{Mg}_6\text{Si}_4\text{O}_{10}(\text{OH})_8$ ), talc ( $\text{Mg}_3\text{Si}_2\text{O}_5(\text{OH})_2$ ) and enstatite ( $\text{MgSiO}_3$ ), were mingled with the as-received olivine as detected from the XRPD patterns (Figure 7-1 c). Calcination in air at  $900^\circ\text{C}$  of olivine led to the decomposition of chlorite and talc possibly into enstatite and forsterite; the latter being hardly distinguishable from olivine (Figure 7-1 d).

### 7.3.2. $^{57}\text{Fe}$ Mössbauer spectroscopy

A total of five samples were run at ambient temperature: three chrysotile samples and two of olivine. Iron oxide was found in all of the chrysotile samples while firing the olivine sample in air led to the formation of some iron oxide. A summary of the fitting results is given in Table 7-2 in terms of isomer shift ( $\delta$ ), quadrupole splitting ( $\Delta$ ), hyperfine field ( $B_{\text{hf}}$ ) and relative areas of the components used to fit the chrysotile and olivine spectra shown in Figure 7-2.

The Mössbauer spectra of raw chrysotile, and chrysotile calcined in air and  $\text{N}_2$ , are shown in Figure 7-2 (a-c), respectively. The Mössbauer spectrum of raw chrysotile (Figure 7-2 a) consists of two sextets and three quadruple doublets. The observed sextets with isomer shifts  $\delta = 0.27$  and  $0.67$  mm/s and hyperfine fields  $B_{\text{hf}} = 49$  and  $46.1$  T are characteristic of octahedral  $\text{Fe}^{2+}$ , and octahedral and tetrahedral  $\text{Fe}^{3+}$  coordinations evocative of magnetite ( $\text{Fe}_3\text{O}_4$ ). In the native chrysotile, 64 % of iron is assigned to magnetite foreseeing “catalytic” accessibility of a large portion of iron in the raw material. The balance, i.e., 36%, corresponds to iron incorporated into the chrysotile lattice. This is less than the previous upper-limit estimate implying that Mg, in an intergrown crystalline brucite phase, and some Al, incorporated in the chrysotile lattice, would contribute for the lesser Fe substitution. The observed quadruple doublet with isomer shift  $\delta = 1.12$  mm/s and quadrupole splitting  $\Delta = 2.85$  mm/s connote with the occurrence of octahedral  $\text{Fe}^{2+}$  replacing magnesium in the trioctahedral layer of chrysotile<sup>24</sup> and contributing for 21 % of iron. Also, intra-framework  $\text{Fe}^{3+}$  was present in the chrysotile backbone in tetrahedral (7 %) and octahedral (8 %) coordinations as identified, respectively, through the isomer

shifts of 0.25 and 0.37 mm/s and quadrupole splitting of 0.41 and 1.00 mm/s [24].

**Table 7-2:** Isomer shift ( $\delta$ ), quadrupole splitting ( $\Delta$ ), hyperfine field ( $B_{\text{hf}}$ ) and relative areas of the components used to fit the chrysotile and olivine spectra shown in Figure 7-2.

Catalyst	Iron assignment	$\delta$ (mm/s)	$\Delta$ (mm/s)	$B_{\text{hf}}$ (T)	Area (%)
a/r chrysotile	Magnetite $\text{Fe}^{3+}$ , tetrahedral	0.27	0.00	49.0	26
	Magnetite $\text{Fe}^{2+}$ , $\text{Fe}^{3+}$ , octahedral	0.67	0.03	46.1	38
	Chrysotile $\text{Fe}^{2+}$ , octahedral	1.12	2.85	0.00	21
	Chrysotile $\text{Fe}^{3+}$ , tetrahedral	0.25	0.41	0.00	7
	Chrysotile $\text{Fe}^{3+}$ , octahedral	0.37	1.00	0.00	8
chrysotile, air-calcined	Hematite $\text{Fe}^{3+}$ , octahedral	0.382	-0.176	51.6	51
	$\text{Fe}^{2+}$ , octahedral	1.11	3.06	0.00	2
	$\text{Fe}^{3+}$ , octahedral	0.11	2.00	0.00	8
	$\text{Fe}^{3+}$ , octahedral	0.34	0.95	0.00	20
	Hematite solid-solution $\text{Fe}^{+3}$ , octahedral	0.37	0	43.7	18
chrysotile, $\text{N}_2$ -calcined	Magnetite $\text{Fe}^{3+}$ , tetrahedral	0.30	0.01	49.3	32
	Magnetite $\text{Fe}^{2+}$ , $\text{Fe}^{3+}$ , octahedral	0.68	0.03	45.9	26
	$\text{Fe}^{2+}$ , octahedral	1.12	2.99	0.00	21
	$\text{Fe}^{2+}$ , octahedral	0.8	2.3	0.00	6
	$\text{Fe}^{3+}$ , octahedral	0.49	0.84	0.00	15
a/r olivine	Olivine $\text{Fe}^{2+}$ , octahedral	1.136	3.003	0.00	100
olivine, air-calcined	Olivine $\text{Fe}^{2+}$ , octahedral	1.133	3.002	0.00	88
	Superparamag. hematite $\text{Fe}^{3+}$ , octahedral	0.44	0.62	0.00	6
	Hematite $\text{Fe}^{3+}$ , octahedral	0.32	0.00	51.0	6

Oxidative calcination of chrysotile at 900°C led to hematite forms as revealed by the inception of two sextets and three quadruple doublets in the Mössbauer spectrum (Table 7-2, Figure 7-2 b). Nearly half the iron (51 %) was assigned to  $\alpha\text{-Fe}_2\text{O}_3$  as objectified in the Mössbauer spectrum from the sextet isomer shift at 0.382 mm/s and a hyperfine field of 51.6 T. The air-calcined chrysotile displayed an extra sextet, contributing another 18 % of iron, with an isomer shift (0.37 mm/s) close to that of hematite but having a hyperfine field (43.7 T) that is considerably lower. Incorporation of aluminum into the hematite structure is known to reduce the hyperfine field of hematite [25]. It is probable in our case that Al and Mg might have diffused during oxidative calcination into some iron oxide particles leading to solid-solution hematite particles producing an extra sextet with lower hyperfine field than pure hematite. Oxidative calcination of chrysotile at 900°C also led to massive oxidation of intra-framework  $\text{Fe}^{2+}$ . Only 2 % of iron was left as an octahedrally-coordinated  $\text{Fe}^{2+}$  ( $\delta = 1.11$  mm/s and  $\Delta = 3.06$  mm/s) in the nascent forsterite structure after chrysotile amorphisation and dehydroxylation as revealed above from the XRD pattern. Intra-framework octahedrally-coordinated ferric cations, contributing for 28 % of the total iron,

were fitted with two quadruple doublets ( $\delta = 0.34$  and  $0.11$  mm/s and  $\Delta = 0.95$  and  $2.00$  mm/s). Hence despite the mineral transformations during calcination, of the original intra-framework iron barely 6 % was exoriated towards the intergrown iron oxides. This suggests that mainly magnetite is involved in the formation of the hematite forms.

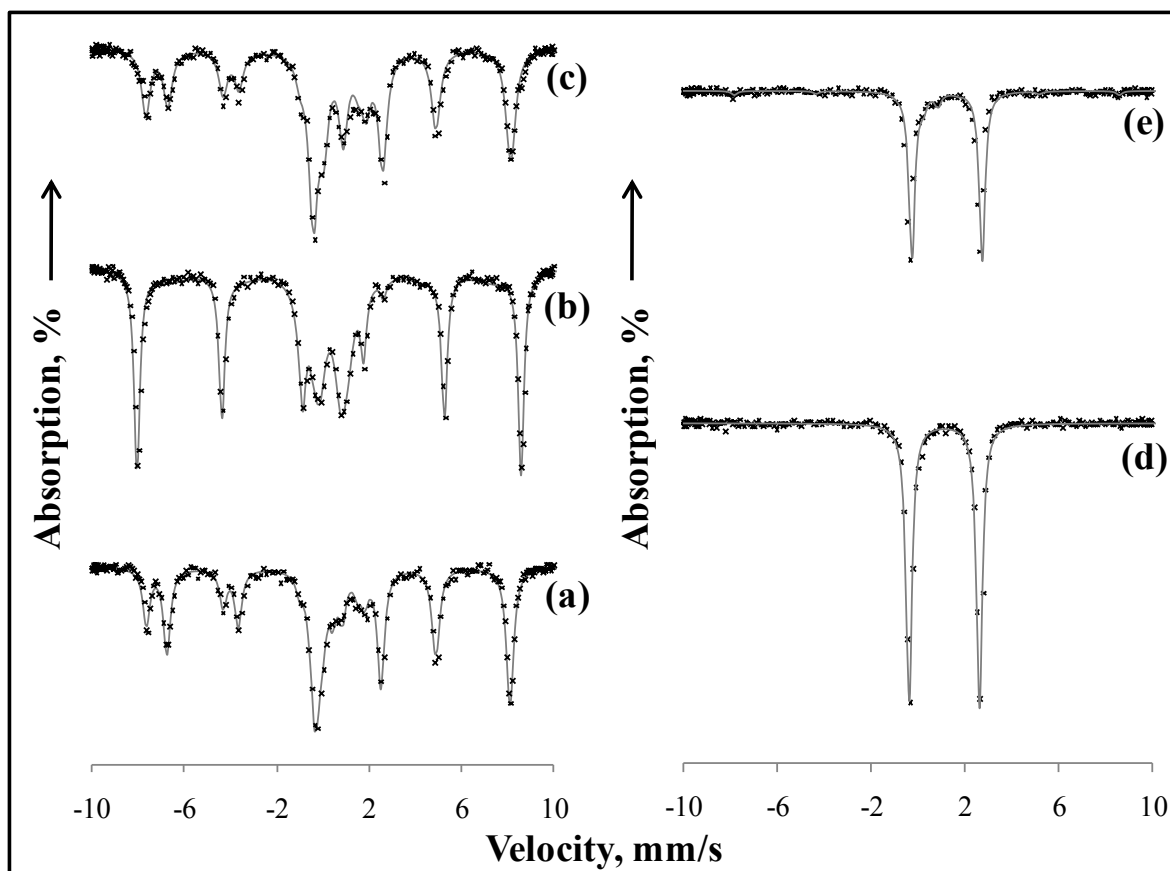


**Figure 7-2.** Room-temperature  $^{57}\text{Fe}$  Mössbauer spectra of (a) raw chrysotile. (b) chrysotile calcined for 2 h in air at  $900^\circ\text{C}$ . (c) chrysotile calcined for 2 h in  $\text{N}_2$  at  $900^\circ\text{C}$  (d) raw olivine. (e) olivine calcined for 2 h in air at  $900^\circ\text{C}$ .

The Mössbauer spectrum of  $\text{N}_2$ -calcined chrysotile at  $900^\circ\text{C}$  is shown in Figure 7-2 c. Unlike native chrysotile, iron present as magnetite dropped to 58 % which would imply a fraction of iron (6 %) in the native magnetite has migrated into the forsterite structure during calcination. The relative amount of the octahedrally-coordinated  $\text{Fe}^{2+}$  in forsterite is similar to that in the native chrysotile (i.e., 21 %). It is, on the other hand, considerably far off the one in air-calcined chrysotile (2 %) emphasizing the role the calcination environment plays on the oxidation state of intra-framework iron in forsterite. 15 % of iron

in the N<sub>2</sub> calcined chrysotile was also in the form of ferric iron with isomer shift of 0.49 mm/s and quadrupole splitting of 0.84 mm/s which are similar to the Mössbauer features of octahedral ferric iron in orthopyroxene [26]. Incorporation of iron in the crystalline structure of dehydroxylated chrysotile also led to 6 % of octahedrally-coordinated Fe<sup>2+</sup> ( $\delta = 0.8$  mm/s and  $\Delta = 2.3$  mm/s) similar to octahedral Fe<sup>2+</sup> in synthesized olivine [27].

Figure 7-2 (e&d) represent the Mössbauer spectra of raw and air-calcined olivine. The Mössbauer spectrum of raw olivine depicts a single quadruple doublet ( $\delta = 1.136$  mm/s and  $\Delta = 3.003$  mm/s) assigned to Fe<sup>2+</sup> ions in the olivine structure. Despite iron-loading in the native olivine slightly exceeds that in the as-received chrysotile, only intra-framework ferrous is featured in olivine.

Mössbauer spectroscopy of calcined olivine confirms rejection of iron from the olivine lattice due to oxidation at 900°C with inception of intergrown free iron oxides. Air-calcined olivine gave rise to a sextet ( $\delta = 0.32$  mm/s and  $B_{hf} = 51.0$  T) and a quadruple doublet ( $\delta = 0.44$  mm/s and  $\Delta = 0.62$  mm/s) aside of the main quadruple doublet stemming from the non-oxidized Fe<sup>2+</sup> in the olivine structure that accounts for 88 % of the total iron. The sextet features Fe<sup>3+</sup> in  $\alpha$ -Fe<sub>2</sub>O<sub>3</sub> and represents 6 % of total iron whilst the quadruple doublet was assigned to Fe<sup>3+</sup> contributing for an extra 6 % and occurring in a super paramagnetic hematite [28]. Disparities in hematite particle sizes, the incipience of which within the olivine matrix, may be that part of them reflect a non-super paramagnetic state contributing to a sextet, while another part, the very small particles, would be super-paramagnetic as evidenced by the quadruple doublet [12].

### 7.3.3. Temperature-programmed reduction

Iron reducibility in chrysotile was assessed via TPR tests carried out on air- and N<sub>2</sub>-calcined chrysotile, as well as on olivine. H<sub>2</sub> consumption rates are plotted in Figure 7-3 as a function of ramp temperature. Clearly, H<sub>2</sub> consumption of air-calcined chrysotile outweighs the one corresponding to N<sub>2</sub>-calcined chrysotile. Integrating the area underneath the TPR curve (after dividing by the heating rate) for the air-calcined chrysotile was in accordance with reducing almost 97 % of the total iron present in chrysotile from ferric to metallic iron – According to the Mössbauer assignments (Table 7-2), 98 % of the iron in

air-calcined chrysotile was labelled as  $\text{Fe}^{3+}$ . Similarly,  $\text{H}_2$  consumption for  $\text{N}_2$ -calcined chrysotile was only enough to reduce the iron present in the magnetite phase (ca. 58 %, Table 7-2) to  $\text{Fe}^0$  in addition to partial reduction of  $\text{Fe}^{3+}$  to  $\text{Fe}^{2+}$ .

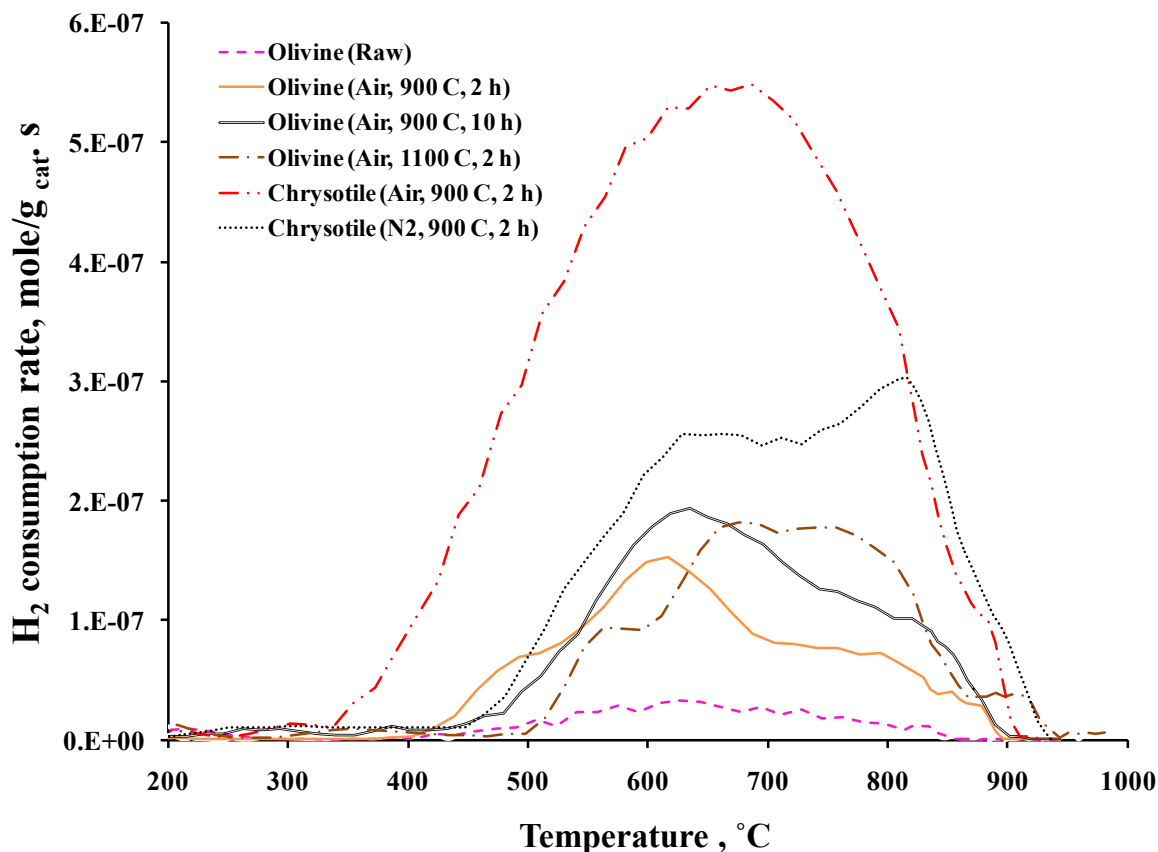


**Figure 7-3.** Hydrogen consumption rates (in  $\text{mol}(\text{H}_2)/\text{g}_{\text{cat}}/\text{s}$ ) as a function of ramp temperature in temperature-programmed reduction tests of native and calcined chrysotile and olivine samples.

Mössbauer spectroscopy combined with TPR reveal also that chrysotile air-calcination led to the transformation of octahedral  $\text{Fe}^{2+}$  in the forsterite lattice –an otherwise difficult to reduce species as observed in the case of olivine– into a ferric iron located in more reducible crystalline forms (hematite and solid-solution hematite). However chrysotile  $\text{N}_2$ -calcination left ca. 21 % as ferrous iron in the forsterite structure (Table 7-2) reflecting in decreased hydrogen consumption (Figure 7-3) and in lesser reducibility in comparison with chrysotile air-calcination. Availability of highly-reducible iron will certainly impact the catalyst activity since the reduction of iron by means of *autogenously* hydrogen, produced due to gasification and reforming of tar, could lead to the formation of active metallic iron

to break the C-C and C-H bonds [11].

The reducibility of iron in native and air-calcined olivine was also monitored via TPR (Figure 7-3). Iron in raw olivine is barely reducible as mirrored by the resulting minor H<sub>2</sub> consumption. Hardly 2-3 % of iron in olivine would have been reduced though the presence of free reducible iron oxide in raw olivine went undetected by Mössbauer spectroscopy. Small amounts of iron may have been present as octahedral Fe<sup>2+</sup> in the XRPD-identified talc and chlorite impurities whose isomer shift and quadrupole splitting are indistinguishable from the olivine octahedral Fe<sup>2+</sup> ones [29]. Due to decomposition of these impurities during TPR, some reducible iron could be produced leading to minor H<sub>2</sub> consumption.

Air-calcination of olivine at 900°C for 2 h boosted H<sub>2</sub> consumption during TPR. H<sub>2</sub> consumption integrated from Figure 7-3 mirrors with a reduction of 14 % of iron from Fe<sup>3+</sup> to Fe<sup>0</sup>. This is very close to the Mössbauer spectroscopy assessment where ca. 12 % of iron is present as Fe<sup>3+</sup> in the regular and super-paramagnetic hematite forms, Table 7-2. Extending air calcination of olivine for 10 h at 900°C further increased the amount of reducible iron. In this case, H<sub>2</sub> consumption obtained from integration of the corresponding TPR curve mirrored with reduction of almost 21 % of Fe<sup>3+</sup> in hematite phase to metallic iron. Air-calcination of olivine at even longer times enabled extraction of more iron from the olivine lattice and formation of more reducible iron in the form of hematite [12].

The effect of calcination temperature on iron reducibility was also investigated. H<sub>2</sub> consumption for olivine calcined for 2 h at 1100°C outpaced the one at 900°C, Figure 7-3. It matched the reduction of ca. 21-24 % of iron present as Fe<sup>3+</sup> in hematite or magnetite phases for the air-calcined olivine at 1100°C. It is worth-reminding that around 1100°C a transition occurs from hematite to magnetite from a starting olivine material [30].

#### **7.3.4. Reaction tests**

Blank tests were carried out using silica sand as an inert material to evaluate benzene non-catalytic steam reforming at 850 and 900°C and to weigh up thermal and catalytic contributions in the presence of olivine and chrysotile. Thermal steam reforming mediated by sand at 850 and 900°C always led to less than 3 % conversion of benzene which is

mostly converted into coke atop of the silica surface.

**Table 7-3:** Catalyst calcination pre-treatment and various steam-reforming operating conditions, products' yields and benzene conversion over chrysotile and olivine

Run	Catalyst	Calcination			Operating condition		Products					Conversion (%)
		Calcination Agent	Temperature (°C)	Time (h)	Temperature (°C)	GHSV(m <sup>3</sup> /kg <sub>cat</sub> ·h)	Yield of H <sub>2</sub> (%)	Yield of CO (%)	Yield of CO <sub>2</sub> (%)	Yield of CH <sub>4</sub> (%)	Yield of Coke (%)	
1	Chrysotile	Air	900	2	900	8.46	71.6	45.8	21.5	1.1	0.5	64.2
2	Chrysotile	Air	900	2	900	24	42.7	15.9	17.6	0.6	0.6	31.1
3	Chrysotile	Air	900	2	850	8.46	44.7	16.5	20.3	0.4	0.6	37.2
4	Chrysotile	Air	900	2	850	24	31.4	8.3	14.8	0.2	0.5	23.1
5	Chrysotile	N <sub>2</sub>	900	2	900	8.46	59.2	32.2	18.3	1.0	0.6	52.5
6	Chrysotile	N <sub>2</sub>	900	2	850	8.46	37.9	13.3	17.3	1.0	0.5	31.2
7	Chrysotile	Air	1100	2	850	24	26.5	6.7	7.0	0.4	1.3	13.3
8	Olivine	Air	900	2	900	8.46	14.6	6.8	5.9	0.3	0.3	13.4
9	Olivine	Air	900	2	850	8.46	8.1	3.3	3.6	0.2	0.2	7.2
10	Olivine	Air	900	2	850	1.91	26.7	7.9	14.2	0.2	0.3	23.2
11	Olivine	Air	900	10	850	1.91	24.5	7.8	15.3	0.5	0.2	24.4
12	Olivine	Air	1100	2	850	1.91	26.4	8.7	16.1	0.6	0.2	24.7

Considerable activity for benzene steam reforming was observed using pre-calcined chrysotile. At 900°C, benzene conversion increased from 31.1 to 64.2 % while decreasing air-calcined chrysotile gas hourly space velocities from 24 to 8.46 m<sup>3</sup>/kg/h (runs 1&2, Table 7-3). Benzene conversion over air-calcined chrysotile was essentially lower at 850°C for the same gas hourly space velocities (runs 1&3, 2&4, Table 7-3). The large amount of reducible iron, as revealed by Mössbauer spectroscopy and TPR, on the surface of air-calcined chrysotile could be the main reason for the mineral activity for benzene cracking. The activity of N<sub>2</sub>-calcined chrysotile at 850 and 900°C is also investigated. Although the N<sub>2</sub>-calcined chrysotile had the same surface area as its air-calcined sibling (9 m<sup>2</sup>/g), activity of the former for the cracking of benzene at the same gas hourly space velocity and reactor temperature was lower than that of air-calcined mineral (runs 1&5, 3&6, Table 7-3). The presence of lesser amount of reducible iron with the N<sub>2</sub>-calcined chrysotile, as revealed from the TPR experiments, can be the main reason for the differences in activity between the air- and N<sub>2</sub>-calcined chrysotile. Long-term catalytic experiments were also performed using the calcined chrysotile to demonstrate its stability for benzene steam reforming.

Figure 7-4 shows the stable activity of calcined chrysotile for 22 h where the reactor temperature was cycled twice between 800°C and 900°C. The drop in catalyst activity was minor and the catalyst quickly retrieved its cruise conversion for the assigned temperatures back and forth from 800°C up to 900°C, then back down to 800°C and so forth.

Catalytic activity of calcined olivine for tar cracking has been related to the presence of extra-framework free iron oxide species on the surface of calcined olivine. Olivine with more free iron has shown more reducibility and activity for cracking tars [11]. Olivine oxidation at elevated temperature results in the decomposition of olivine impurities, such as Fe-bearing serpentinic antigorite, followed by the release of free iron oxides [11,12]. Abstraction of  $\text{Fe}^{2+}$  from the olivine lattice and its oxidation into  $\text{Fe}^{3+}$  also leads to the formation of crystalline hematite and paramagnetic  $\text{Fe}^{3+}$  as revealed by our Mössbauer spectroscopy results.

Under identical gas hourly mass space velocity, temperature and close equivalent particle diameters (runs 1&8, 3&9, Table 7-3), air-calcined chrysotile outperformed by up to a factor 5 air-calcined olivine in terms of benzene conversion and syngas yield. Despite nearing iron loadings, air-calcined chrysotile exhibited a BET surface area 41 times that of air-calcined olivine ( $0.22 \text{ m}^2/\text{g}$ ), in addition to much more extra-framework iron exposed from the former over the latter. Both features hence obviously concur to leaning in favor of the chrysotile superior performance.

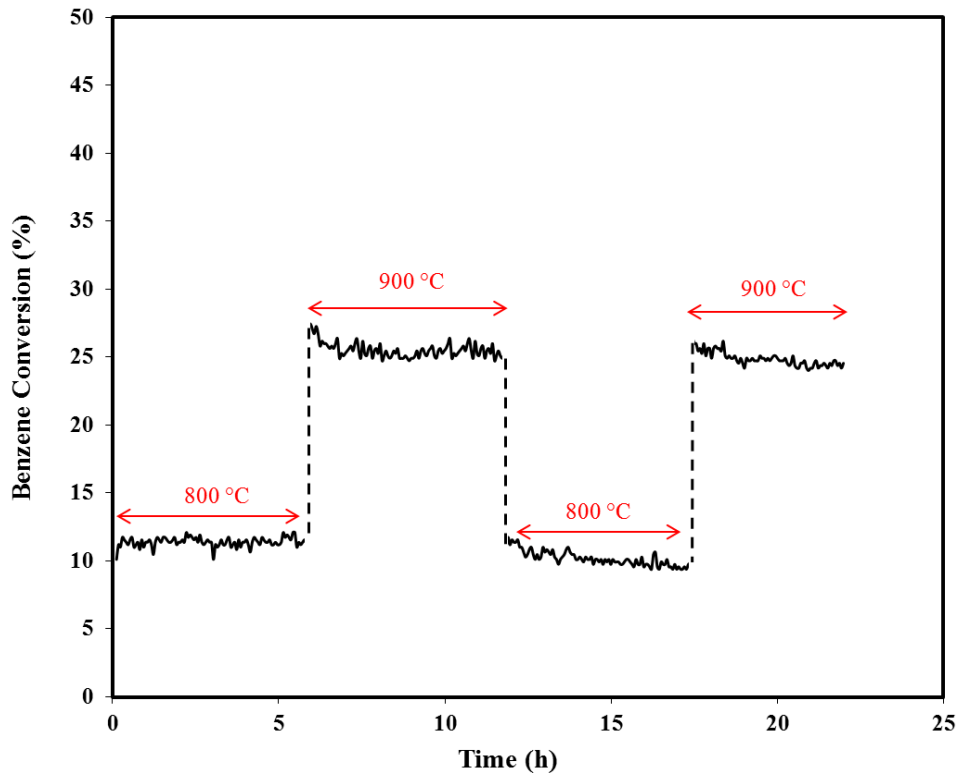


**Figure 7-4.** Activity tests of chrysotile during long-term runs (22 h) with cyclic benzene steam reforming between 800-900 °C, S/C =1.05, GHSV= 28.4 m<sup>3</sup>/(kg<sub>cat.</sub> h).

Devi et al. [12] tested olivine calcined from 1 to 20 h at 900°C and found that 10 h calcination time led to the maximum activity for naphthalene steam reforming. At 900°C, by increasing air-calcination time from 2 to 10 h for olivine (runs 10&11, Table 7-3), benzene conversion virtually stood still –increased by almost 1.2% barely distinguishable from thermal cracking effects– though air-calcined olivine for 10 h had shown 50-70% more reducibility. It may be speculated that sintering of the intergrown highly-dispersed super-paramagnetic hematite particles may be favored by the longer calcination times which would exclude access to the core Fe<sup>3+</sup> in the benzene steam-reforming catalysis. This is further supported by the fact that iron dispersion is physically limited by the low BET surface area of the material hence considerably stifling the activity of olivine. To verify that olivine’s low activity is indeed attributed to sintering during calcination of iron extracted from the olivine’s lattice, TEM images were taken for raw olivine as well as for olivine (air) calcined during 2 h and 10 h at 900°C. In accordance with the Mössbauer spectral results (a/r olivine, Table 7-2 & Figure 7-2 d), Figure 7-5 a featureless TEM image tends to

support the absence of coexisting iron oxide particles with raw olivine.

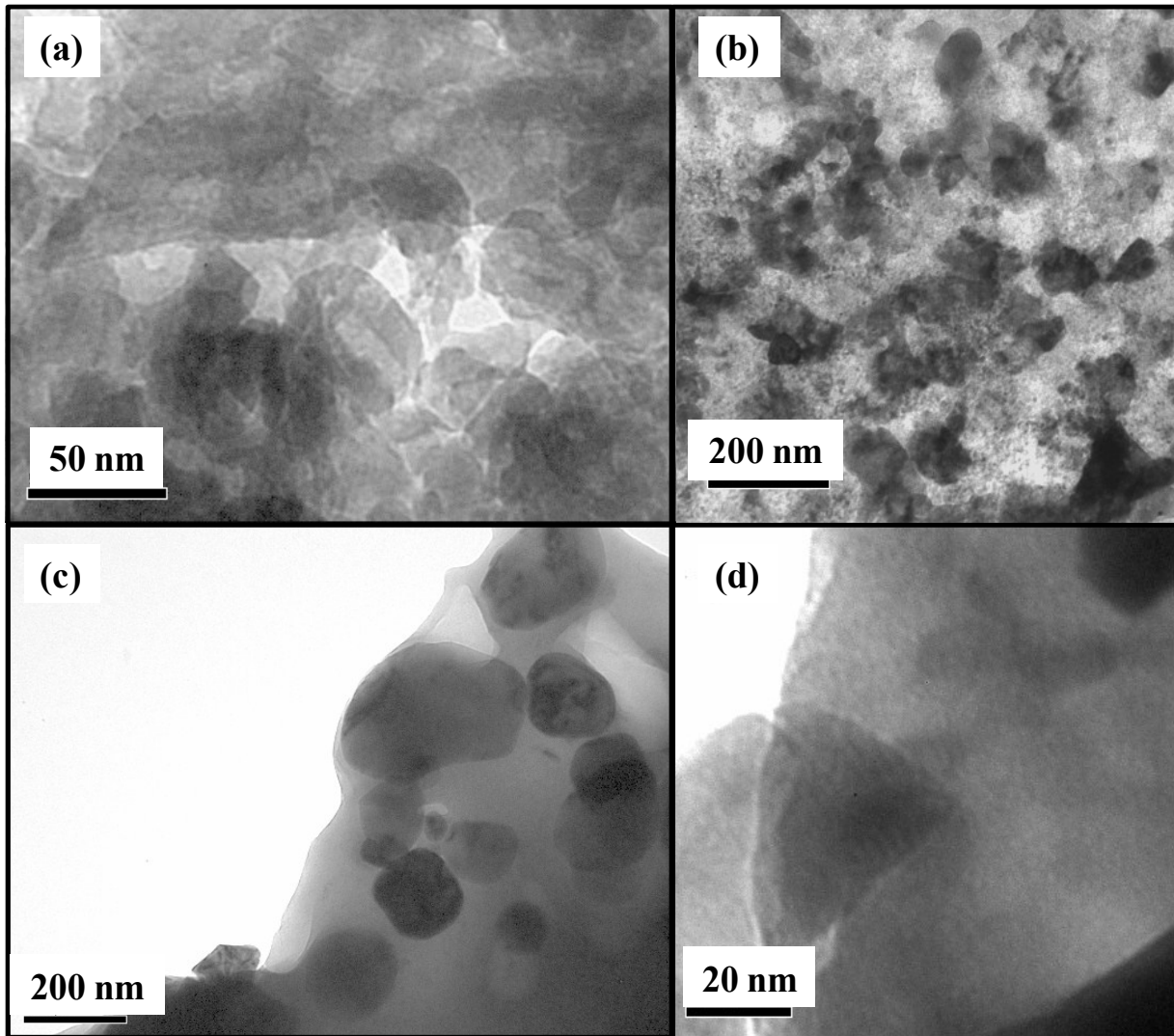


**Figure 7-5.** Transmission electron microscopy (TEM) images of (a) raw olivine, (b) olivine calcined for 2 h in air at 900°C, (c) olivine calcined for 10 h in air at 900°C, (d) chrysotile calcined for 2 h in air at 900°C.

A budding of dark granulous spots emerged after olivine calcination for 2 h at 900°C (Figure 7-5 b). The spots, which were ascribed to hematite on the surface of olivine, exhibit a wide particle size range centered on 80 nm. Extending the calcination time of olivine to 10 h led to considerable growth of the hematite islands (Figure 7-5 c) with further extractions of lattice iron and sintering of small hematite particles into coarser ones (average size > 100 nm). The average size of hematite particles formed on chrysotile surface after calcination during 2 h at 900°C was *ca.* 20-30 nm, and was considerably lower

than for calcined olivine (Figure 7-5 d). Therefore, the presence of hematite particles on the surface of chrysotile that are smaller than on olivine's confirm the larger iron oxide dispersion for the former, and consequently provide post-facto proof for calcined chrysotile superior activity over calcined olivine.

Similarly, increasing olivine calcination temperature from 900 to 1100°C (runs 11&12, Table 7-3) led to a boost in benzene conversion (1.5%) barely distinguishable from the concomitant thermal contribution. This is unlike the behavior of chrysotile which revealed a large drop in benzene conversion after subjection to a similar pre-treatment.

At 850°C, conversion of benzene over air-calcined chrysotile at 1100°C (13.3 %: run 7, Table 7-3) was remarkably less than that at 900°C (23.1 %: run 4, Table 7-3). This is likely ascribable to similar iron-oxide sintering effect, in addition to a BET surface area of calcined chrysotile at 1100°C equal 4.8 m<sup>2</sup>/g, i.e., nearly half that of calcined chrysotile at 900°C (9 m<sup>2</sup>/g).

Finally, the H<sub>2</sub>/CO ratio depends on the water gas shift reaction during steam reforming of benzene. This reaction is sensitive to steam vapor pressure and temperature. Since the water gas shift reaction is exothermic, lower temperature leads to higher ratio of H<sub>2</sub>/CO. As can be seen in Table 7-3, the H<sub>2</sub>/CO ratio is higher at lower reaction conversion (consequently water concentration is higher) and also when reaction temperature is 850°C (tests 6, 7 & 4 with chrysotile and 10, 11 & 12 with olivine). In the tests with more benzene conversion and consequently lower concentration of steam, the H<sub>2</sub>/CO ratio was considerably lower, see tests 1&3 in Table 7-3.

## 7.4. Conclusion

The activity of chrysotile was compared to olivine's for the steam-reforming of benzene, a biomass model-model compound, at equal gas hourly space mass velocities and comparable iron loadings at 850-900°C. Chrysotile's catalytic activity was related to its fair BET specific surface area and the considerable free iron oxides that coexist entwined with the chrysotile-containing residue originating from the mine and residue heaps from Thetford Mines. The activity of chrysotile was influenced by the pre-treatment environment (oxidative or non-oxidative). Air-calcined chrysotile was found to be considerably active, up to a fivefold increase in conversion and syngas yield, compared to olivine, no matter the type of pretreatment of the latter. Nearly 97 % of iron in the air-calcined chrysotile was in the form of reducible  $\text{Fe}^{3+}$ , as opposed to ca. 70 % in the  $\text{N}_2$ -calcined chrysotile, which could be the main reason for the former superior activity for benzene steam reforming. Increasing calcination temperature and time from 900 to 1100°C and from 2 to 10 h, led to the presence of more reducible free iron oxides over the calcined olivine. This, however, translated only in a tepid increase in activity of olivine. Sintering of dispersed hematite on the catalyst surface and limited iron dispersion, due to the low BET surface area of olivine, could be the main factors behind the lower activity of olivine in comparison with the air-calcined chrysotile.

## 7.5. References

- [1] Huber GW, Iborra S, Corma A. Synthesis of transportation fuels from biomass: Chemistry, catalysts, and engineering. *Chemical Reviews*. 2006;106:4044-98.
- [2] Pfeifer C, Rauch R, Hofbauer H. In-bed catalytic tar reduction in a dual fluidized bed biomass steam gasifier. *Industrial & Engineering Chemistry Research*. 2004;43:1634-40.
- [3] Swierczynski D, Courson C, Bedel L, Kiennemann A, Vilminot S. Oxidation reduction behavior of iron-bearing olivines ( $\text{Fe}_x\text{Mg}_{1-x}$ ) $_2\text{SiO}_4$  used as catalysts for biomass gasification. *Chemistry of Materials*. 2006;18:897-905.
- [4] Mastellone ML, Arena U. Olivine as a tar removal catalyst during fluidized bed gasification of plastic waste. *Aiche Journal*. 2008;54:1656-67.
- [5] Miyazawa T, Okumura K, Kunimori K, Tomishige K. Promotion of oxidation and reduction of rh species by interaction of rh and  $\text{CeO}_2$  over  $\text{Rh/CeO}_2/\text{SiO}_2$ . *Journal of Physical Chemistry C*. 2008;112:2574-83.
- [6] Swierczynski D, Libs S, Courson C, Kiennemann A. Steam reforming of tar from a biomass gasification process over Ni/olivine catalyst using toluene as a model compound. *Applied Catalysis B-Environmental*. 2007;74:211-22.
- [7] Virginie M, Courson C, Niznansky D, Chaoui N, Kiennemann A. Characterization and reactivity in toluene reforming of a Fe/olivine catalyst designed for gas cleanup in biomass gasification. *Applied Catalysis B-Environmental*. 2010;101:90-100.
- [8] Bampenrat A, Meeyoo V, Kitiyanan B, Rangsunvigit P, Rirksomboon T. Naphthalene steam reforming over Mn-doped  $\text{CeO}_2\text{-ZrO}_2$  supported nickel catalysts. *Applied Catalysis a-General*. 2010;373:154-9.
- [9] Li C, Suzuki K. Tar property, analysis, reforming mechanism and model for biomass gasification-An overview. *Renewable & Sustainable Energy Reviews*. 2009;13:594-604.
- [10] van der Meijden CM, van der Drift A, Vreugdenhil BJ. Experimental results from the allothermal biomass gasifier Milena. 15th European Biomass Conference, 7-11 May 2007, Berlin, Germany.
- [11] Kuhn JN, Zhao ZK, Felix LG, Slimane RB, Choi CW, Ozkan US. Olivine catalysts for methane- and tar-steam reforming. *Applied Catalysis B-Environmental*. 2008;81:14-26.
- [12] Devi L, Craje M, Thune P, Ptasinski KJ, Janssen F. Olivine as tar removal catalyst for biomass gasifiers: Catalyst characterization. *Applied Catalysis a-General*. 2005;294:68-79.
- [13] Cecchi E, Mercier G, Bergeron M. A feasibility study of carbochlorination of chrysotile tailings. *International Journal of Mineral Processing*. 2009;93:278-83.
- [14] Larachi F, Daldoul I, Beaudoin G. Fixation of  $\text{CO}_2$  by chrysotile in low-pressure dry and moist carbonation: Ex-situ and in-situ characterizations. *Geochimica Et Cosmochimica Acta*. 2010;74:3051-75.

- [15] Simell PA, Hirvensalo EK, Smolander VT. Steam reforming of gasification gas tar over dolomite with benzene as a model compound. *Industrial & Engineering Chemistry Research*. 1999;38:1250-7.
- [16] Park HJ, Park SH, Sohn JM, Park J, Jeon J-K, Kim S-S, et al. Steam reforming of biomass gasification tar using benzene as a model compound over various Ni supported metal oxide catalysts. *Bioresource Technology*. 2010;101:S101-S3.
- [17] Furusawa T, Miura Y, Kori Y, Sato M, Suzuki N. The cycle usage test of Ni/MgO catalyst for the steam reforming of naphthalene/benzene as model tar compounds of biomass gasification. *Catalysis Communications*. 2009;10:552-6.
- [18] Zhang R, Wang Y, Brown RC. Steam reforming of tar compounds over Ni/olivine catalysts doped with CeO<sub>2</sub>. *Energy Conversion and Management*. 2007;48:68-77.
- [19] Simell P, Kurkela E, Stahlberg P. In *advances in Thermochemical Biomass Conversion*; Bridgwater, A.V., Ed. London: Blackie Academic & Professional; 1994. p. 265-79.
- [20] Jess A. Mechanisms and kinetics of thermal reactions of aromatic hydrocarbons from pyrolysis of solid fuels. *Fuel*. 1996;75:1441-8.
- [21] Garcia X, Huttinger KJ. Steam gasification of naphthalene - catalyst - calcium-oxide. *Erdol & Kohle Erdgas Petrochemie*. 1990;43:273-81.
- [22] Swierczynski D, Courson C, Kiennemann A. Study of steam reforming of toluene used as model compound of tar produced by biomass gasification. *Chemical Engineering and Processing*. 2008;47:508-13.
- [23] Coey JMD, Venkatesan M, Fitzgerald CB, Douvalis AP, Sanders IS. Ferromagnetism of a graphite nodule from the Canyon Diablo meteorite. *Nature*. 2002;420:156-9.
- [24] Blaauw C, Stroink G, Leiper W, Zentilli M. Mossbauer analysis of some canadian chrysotiles. *Canadian Mineralogist*. 1979;17:713-7.
- [25] Fysh SA, Clark PE. Aluminous hematite - a Mossbauer study. *Physics and Chemistry of Minerals*. 1982;8:257-67.
- [26] Annersten H, Olesch M, Seifert FA. Ferric iron in ortho-pyroxene - Mossbauer spectroscopic study. *Lithos*. 1978;11:301-10.
- [27] Shinno I. A Mossbauer study of ferric iron in olivine. *Physics and Chemistry of Minerals*. 1981;7:91-5.
- [28] Sanchez LC, Arboleda JD, Saragovi C, Zysler RD, Barrero CA. Magnetic and structural properties of pure hematite submitted to mechanical milling in air and ethanol. *Physica B-Condensed Matter*. 2007;389:145-9.
- [29] Aramu F, Maxia V, Delunas A. Mossbauer-spectroscopy of talc minerals. *Nuovo Cimento Della Societa Italiana Di Fisica D-Condensed Matter Atomic Molecular and Chemical Physics Fluids Plasmas Biophysics*. 1989;11:891-6.
- [30] Gualtieri AF, Gemmi M, Dapiaggi M. Phase transformations and reaction kinetics during the

temperature-induced oxidation of natural olivine. *American Mineralogist*. 2003;88:1560-74.



## **Chapter 8 : Catalytic oxygenless steam cracking of syngas-containing benzene model tar compound over natural Fe-bearing silicate minerals**

**Résumé** Dans le but d'identifier une source minérale abondante et abordable pour la gazéification à la vapeur de la biomasse, l'activité de reformage à la vapeur de deux minerais de silicate ferrifères d'origine naturelle contenant du chrysotile et de la lizardite ont été investigués à l'aide de benzène en tant que composé modèle du goudron mélangé à du *syngas* simulé à différentes compositions en H<sub>2</sub>, CO, CO<sub>2</sub>, CH<sub>4</sub> et vapeur d'eau. Le fer intra et extra-structural abondant et enlacé parmi ces silicates a révélé de remarquables propriétés de craquage catalytique à la vapeur. L'activité des minerais de silicate a été comparée avec celle de catalyseurs d'olivine communs pour le craquage de goudron à des températures, des contenus en fer et des tailles de particules semblables. La conversion du benzène des minerais de chrysotile et de chrysotile/lizardite s'est avérée quadruplée par rapport à l'olivine. Les activités vers la conversion du benzène et du méthane ainsi que vers la formation de coke se sont montrées très sensibles au ratio des gaz réducteurs (H<sub>2</sub> and CO) aux gaz oxydants (H<sub>2</sub>O and CO<sub>2</sub>) dans le *syngas* alors que la conversion du benzène des minerais de chrysotile et de chrysotile/lizardite a été quadruplée en comparaison avec celle de l'olivine. Les études de réaction ont été interprétées en fonction de l'état d'oxydation et de coordination du fer ainsi que de la réductibilité et de la taille des particules d'oxydes de fer telles que déterminées par spectroscopie de Mössbauer, réduction à température programmée (TPR) et microscopie électronique à transmission (TEM).

**Abstract** In a prospect of identifying cheap and abundant mineral sources for biomass catalytic steam gasification, the catalytic steam reforming activity of two naturally-occurring iron-bearing mineral silicate ores containing chrysotile and lizardite, was probed using benzene model-tar compound co-mixed with simulated syngas at varying H<sub>2</sub>, CO, CO<sub>2</sub>, CH<sub>4</sub> and steam compositions. Abundant intra-/extra-framework iron entwined within these silicates revealed remarkable steam cracking catalytic properties. The activity of the silicate ores was benchmarked against that of a common tar-cracking olivine catalyst at identical temperature, iron loading and particle size. Benzene conversion of chrysotile and chrysotile/lizardite ores exhibited up to a fourfold increase compared to olivine. Activity toward benzene and methane conversions, and coke formation were very sensitive to the ratio of reductive (H<sub>2</sub> and CO) to oxidative (H<sub>2</sub>O and CO<sub>2</sub>) gases in syngas whereas benzene conversion of chrysotile and chrysotile/lizardite ores exhibited up to a fourfold increase compared to olivine. The reaction studies were interpreted in light of iron oxidation state and coordination, and reducibility and particle size of iron oxides as determined using Mössbauer spectroscopy, temperature-programmed reduction (TPR) and transmission electron microscopy (TEM).

## 8.1. Introduction

Biomass as a carbon-neutral renewable energy source is increasingly receiving attention for the important role it is foreseen to play in the world's energy mix [1]. Gasification is a particularly attractive thermochemical process for converting biomass into biofuels and value-added chemicals or for power generation. Consisting of condensable aromatic and oxygenated hydrocarbons along with complex polycyclic aromatic hydrocarbons (PAH), tar which inescapably forms during gasification represents one of the perplexing problems to deal with in biomass gasification processes even for those operated at quite high temperature ( $>850\text{ }^{\circ}\text{C}$ ) [2]. Despite a rapidly climbing worldwide gasification capacity in terms of syngas generation in recent years, formation of excessive tar amounts remains a technological barrier to the implementation of commercial-scale biomass gasification technology as tar demands for appending costly gas cleaning operations [3]. Formation of  $0.5$  to  $100\text{ g/m}^3$  of tar, as reported in different biomass gasification processes, adds severe operational burdens such as fouling due to tar condensation downstream of the gasifier where temperatures below the tar dew point occur [4]. Hence, success in producing nearly tar-free syngas ( $< 0.5\text{ g/Nm}^3$ ) would be a remedy current research and development is striving to achieve.

One efficient method to discard tar from syngas is *via* catalytic hot gas cleanup whereby not only tar is converted at the gasifier temperature thus simplifying downstream wastewater treatment units, but also the carbon efficiency is increased with more syngas obtained from tar reforming [5]. Selection of cheap and active catalysts for tar cracking is still a critical task for developing feasible hot gas cleanup systems [3]. Naturally-occurring mineral catalysts as cheap and abundant source for tar cracking are increasingly contemplated for this task [6,7]. Iron-bearing silicate minerals such as olivine and chrysotile have been applied in laboratory- and pilot-scale reactors for cracking biomass derived tar or model tar compounds [8-12]. Studies on olivine and chrysotile unveiled the correlation existing between materials' tar cracking activity and availability of reducible iron within [11-13]. Oxidation of olivine at temperatures in excess of  $900^{\circ}\text{C}$  is a prerequisite for liberation of iron incorporated in the olivine crystalline structure and formation of free reducible iron [12-14]. The amount of reducible iron was found to increase by

extending the time and temperature of olivine oxidation [12,14]. A downside of extending oxidation time of olivine is sintering of iron oxide particles which is known to offset olivine tar cracking activity even with a rise in free reducible iron oxides over olivine surface [12]. As an ersatz to improve olivine activity toward tar cracking, iron precursors were impregnated on olivine surface leading to considerable enhancement in its activity for tar cracking and syngas yield [15]. Contrary to olivine which contains almost exclusively intra-framework iron, chrysotile has most of its iron in the form of inter-grown magnetite phases [12]. Iron was highly reducible in the calcined chrysotile leading to Fe oxide particles smaller in size with respect to calcined olivine. This translated into up to a fivefold increase in activity of calcined chrysotile over olivine irrespective of olivine pretreatment [12].

This study aims at evaluating the potential of naturally-occurring iron-containing magnesium silicate minerals for biomass catalytic steam gasification. Two ores were studied, namely, post-nickel extraction mining wastes from Raglan (Québec) rich in chrysotile/lizardite and magnetite as well as chrysotile from Thetford Mines (Québec). These catalysts were tested for cracking catalytically benzene (a biomass model tar compound) embedded in a simulated syngas environment to assess both 1<sup>st</sup>-order and higher-order coupling effects stemming from co-existing H<sub>2</sub>, CH<sub>4</sub>, CO, CO<sub>2</sub> and steam as in actual syngas-tar mixtures. The compositional incidence of the various syngas components on the catalytic activity for benzene cracking was investigated to highlight the conditions for achieving both optimum cracking activity and ability to minimize coke buildup, the important factors which had not been investigated by detail in the previous works on the iron bearing mineral silicates as tar cracking catalyst. The reaction studies were interpreted in light of iron oxidation state and coordination, and reducibility and particle size of iron oxides as determined using Mössbauer spectroscopy, temperature-programmed reduction (TPR) and transmission electron microscopy (TEM).

## **8.2. Experimental section**

The activity of three iron-containing silicate minerals for benzene reforming in the presence of simulated syngas was studied in this work. The mineral samples consisted of: a) Raglan mine residues (RMR) after nickel separation obtained from the Raglan Mine (Québec) b) Chrysotile obtained from Thetford Mines (Québec) and c) olivine from Greenland supplied

by Minelco. Samples were sized to the 100-250 micron range using mechanical vibratory sieves. The main constitutive elements of RMR, chrysotile and olivine were assayed using inductively coupled plasma optical emission spectroscopy (ICP-POE) and X-ray fluorescence (XRF). Mg, Si and Fe are the main constitutive elements of RMR, chrysotile and olivine (Table 8-1). Iron is highly abundant in RMR, respectively, 4.1 and 2.7 times more than in chrysotile and olivine, whereas Ca, K, Al, Cr and Na are present as minority elements in all three minerals.

**Table 8-1.** wt % of main constitutive elements of RMR (Raglan mine residues, Québec), chrysotile (Thetford Mines, Québec) and olivine (Greenland)

Analyte	Si	Mg	Fe	Ca	K	Cr	Ni	Al	Na	Ti
RMR, wt%	16.5	13.8	17.3	1.1	0.10	0.18	0.15	0.17	0.30	0.08
chrysotile, wt%	18.6	23.2	4.2	0.36	0.12	0.07	trace	0.31	0.02	trace
olivine, wt%	19.4	28.8	6.4	0.14	0.07	0.13	trace	0.34	0.01	trace

To investigate the activity of the three abovementioned catalysts for tar cracking, benzene is chosen as a biomass tar proxy due to its thermal stability [16] (thermal cracking occurs after 900°C) and abundance in biomass-released tars [17]. The minerals activity for catalytic cracking was tested by feeding a benzene-containing simulated syngas through a fixed-bed reactor packed with sieved silicate minerals. The mixtures consisted of benzene (16 g/Nm<sup>3</sup>) with steam (0-18 mole %), carbon dioxide (0-15 mole %), carbon monoxide (0-18 mole %), hydrogen (0-22 mole %) and methane (0-16.5 mole %). The reactor consisted of a catalyst-hosting concentric quartz tube (i.d. 30 mm, length 70 cm) slid inside a stainless steel (SS) tube (i.d. 34 mm, length 70 cm) to prevent metal-benzene contacting (Figure 8-1). Catalyst samples with amounts between 0.4 and 2 g were placed on the top of a quartz frit (40-90 µm pore diameter) located in the middle of the quartz tube to ensure an even distribution of the up-flowing gas. The bed temperature was varied in the range of 700-800°C through the heat supplied by an induction heater. The reactor was heated through a 30 cm long coil connected to a 18 kW induction power supply for heating the stainless steel tube via an ac magnetic field and heating in turn the catalyst layer through radiation and conduction. A detailed description of the catalytic setup can be found

elsewhere [12]. The concentrations of the different gas components were measured at the reactor outlet as a function of time by means of a micro-gas chromatograph (micro GC) (Agilent 3000A, Agilent Technologies). The carbon balance was evaluated by burning off in-situ the coke deposited on the catalyst surface. The on-line quantification was accomplished using an infrared CO<sub>2</sub> detector and the carbon mass balance was closed up to within 5%.

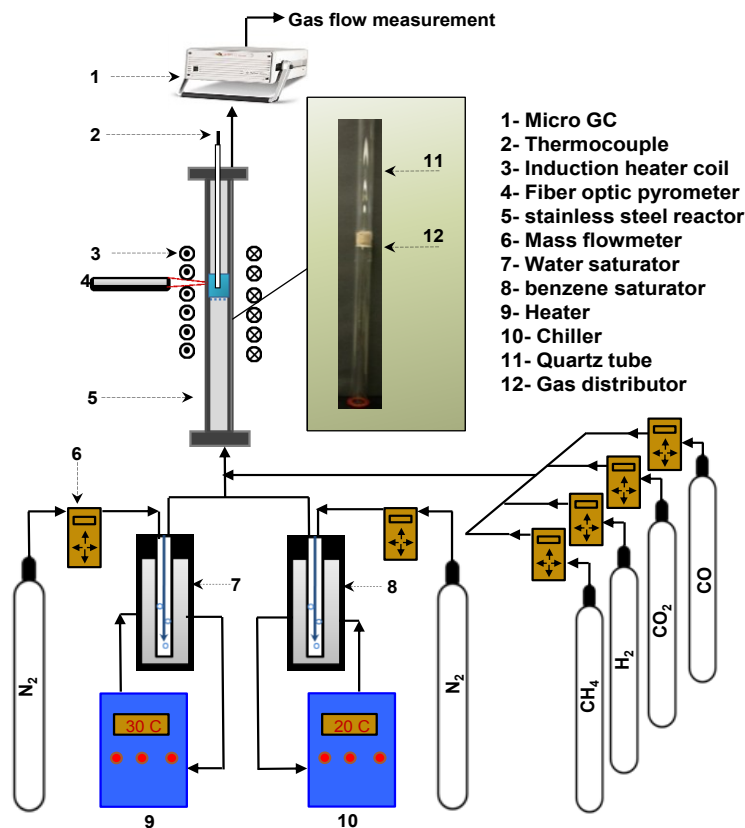


**Figure 8-1.** Schematic of experimental setup used for measuring the catalytic activity of RMR, chrysotile and olivine for benzene cracking in a simulated syngas

Prior to catalyst activity tests, the as-received RMR, chrysotile and olivine were calcined under air flow rate of 200 mL/min for 2 h at 900°C. This pretreatment led to a complete dehydroxylation and amorphisation of the serpentine phase in the samples followed by its recrystallization into forsterite and enstatite. The samples quenching rate (130 K/min) down to ambient temperature was deemed fast enough to assume that the high-temperature crystalline structures were preserved during cooling. Ex-situ phase identification of

crystalline phases of the samples, taken before and after calcination at 900°C, was performed through a Siemens D5000 X-ray powder diffractometer using a Cu K<sub>α</sub> radiation ( $\lambda = 1.54059 \text{ \AA}$ ) generated at 40 kV and an emission current of 30 mA.

N<sub>2</sub> adsorption/desorption isotherms of as-received and calcined RMR, chrysotile and olivine were obtained from a Micromeritics TRISTAR 3000 at 77 K and residual pressures down to 10<sup>-5</sup> Torr. The BET surface area (and pore volume) of RMR before and after calcination amounted to 4.2 m<sup>2</sup>/g (and 0.018 cm<sup>3</sup>/g) and 10.5 m<sup>2</sup>/g (and 0.045 cm<sup>3</sup>/g), respectively. The carbonodithioic acid (xanthate potassium isobutyl) collector left on the residue after the ore floatation treatment reduced the BET surface area and pore volume of as-received RMR. This acid decomposes at temperatures as high as 300°C and was removed during the catalyst calcination step at 900°C. The BET surface area (and pore volume) of chrysotile before and after calcination were 19.9 m<sup>2</sup>/g (and 0.043 cm<sup>3</sup>/g) and 9.02 m<sup>2</sup>/g (and 0.023 cm<sup>3</sup>/g), respectively. Olivine being a non-porous mineral had a surface area of 0.22 m<sup>2</sup>/g which is considerably lower than that of calcined RMR and chrysotile, irrespective of whether it was calcined or not.

A thermogravimetric analyzer (TG) (Perkin Elmer Lab System Diamond TGA-DTA) coupled with a mass spectrometer (MS) with quadrupole analyzer (Thermostar Prisma QMS200, Pfeiffer Vacuum) were used for monitoring the samples weight loss and release of H<sub>2</sub>O and CO<sub>2</sub> during calcinations. All the samples were submitted to prograde heating at 50°C/min under air flow (200 NmL/min) and held for 30 min at 900°C.

The distribution of iron, the species mainly responsible for the catalytic activity, in different coordination and oxidation states in the as-received and calcined minerals was assessed through room-temperature <sup>57</sup>Fe Mössbauer spectroscopy using a 50 mCi<sup>57</sup> CoRh source on a conventional Mössbauer spectrometer operated in a sine mode. The Mössbauer spectra were fitted to a sum of Lorentzian lines using a non-linear least-squares minimization routine. The atomic percentages of the various iron entities with respect to the total iron (quantified through elemental analysis) were taken to be equal to their corresponding Mössbauer absorption areas [18].

Reducibility of iron as the active phase for catalytic cracking was investigated through

temperature-programmed reduction (TPR) of the samples. H<sub>2</sub>-N<sub>2</sub> mixtures (3.04 vol% of H<sub>2</sub>) at a flow rate of 300 mL/min (20°C, 1 atm) were fed through the catalyst layer in a programmed heating mode up to 950°C at a programmed heating rate of 15 K/min and H<sub>2</sub> uptake was monitored via micro-gas chromatography at 100 s time intervals.

Visualizations from the surface of RMR, chrysotile and olivine samples was enabled *via* transmission electron microscopy (TEM) using a JEOL JEM-1230 electron microscope. It was achieved by suspending the samples in methanol and depositing a drop of the resulting suspension on the Formvar coated nickel grid to determine hematite island sizes on the surface of each sample.

## 8.3. Results & discussion

### 8.3.1. Catalyst characterization

**Ex-situ X-ray powder diffraction analysis** The X-ray powder diffraction (XRPD) pattern of as-received RMR showed the presence of serpentine phases such as chrysotile ( $2\theta = 12^\circ, 24.3^\circ, 36.6^\circ$ ) and lizardite ( $2\theta = 12.2^\circ, 24.5^\circ, 35.9^\circ$ ) as its main constituents (Figure 8-2). Magnetite was also observed in RMR evidenced by its main peak at  $2\theta = 35.6^\circ$ . Free iron oxides (magnetite) entwined within RMR can be regarded as a potential for an active catalyst for tar cracking purposes. Chrysotile and lizardite crystalline phases in the air-calcined RMR at 900°C for 2 h collapsed and were replaced by enstatite (MgSiO<sub>3</sub>,  $2\theta = 28.2^\circ$ ) and forsterite (Mg<sub>2</sub>SiO<sub>4</sub>,  $2\theta = 36.5^\circ$ ). Free iron oxide was observed in air-calcined RMR in the form of maghemite ( $\gamma$ -Fe<sub>2</sub>O<sub>3</sub>,  $2\theta = 35.7^\circ$ ) or hematite ( $\alpha$ -Fe<sub>2</sub>O<sub>3</sub>,  $2\theta = 33.2^\circ$ ). Calcination led to the transformation of magnetite in the as-received RMR to hematite, directly or *via* maghemite [19]. It is worthy of notice that transformation of maghemite to hematite was reported to occur at temperatures below 900°C [19]. However, the occurrence of RMR minority elements such as Al, Cr, and Ni, is likely to have required longer calcination time and higher temperature to fully convert maghemite into hematite [19]. The considerable increase in the overall XRPD intensity of free iron oxides (hematite and maghemite) for the calcined RMR suggests some extractions of in-situ iron from the serpentine phase to have taken place during calcination. Alteration of Fe coordination and distribution in calcined RMR was probed via Mössbauer spectroscopy to be discussed later

on. The XRPD patterns of as-received chrysotile material revealed that chrysotile and magnetite were its main crystalline phases [12]. Calcination under air of chrysotile at 900°C led to the collapse of chrysotile structure and formation of enstatite and forsterite. Formation of hematite both due to transformation of magnetite and extraction/oxidation of in-situ iron was also observed. Unlike the as-received chrysotile, almost no free iron oxides were found for raw olivine. Calcination of this latter led to the formation of enstatite and forsterite.

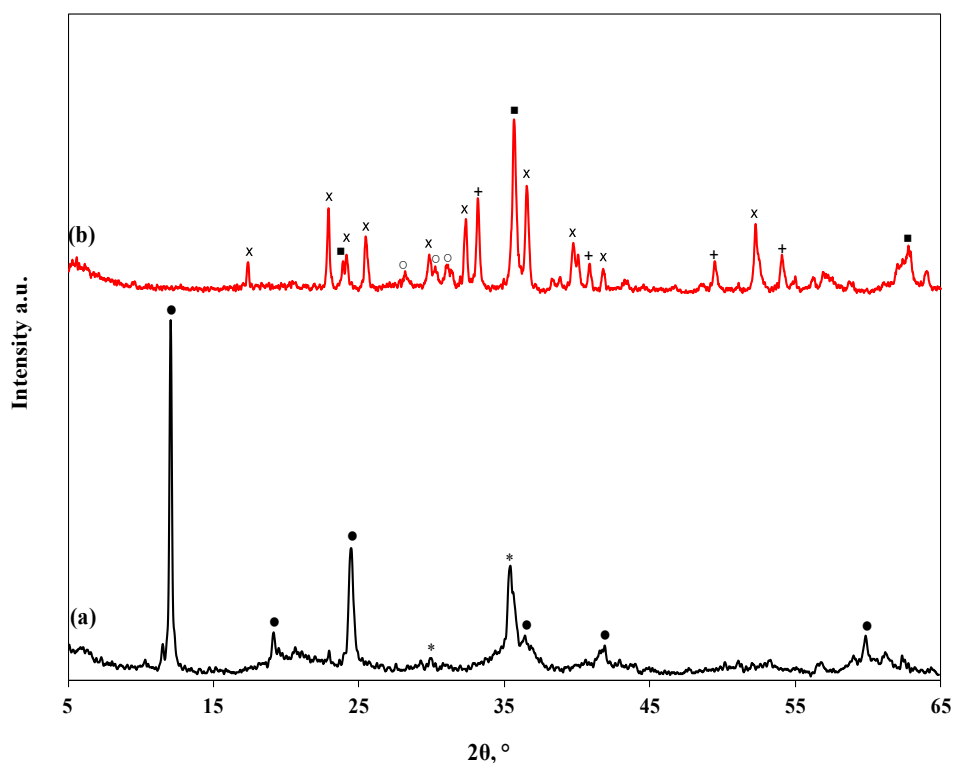


**Figure 8-2.** X-ray powder diffraction patterns of (a) as-received RMR (b) RMR calcined under air at 900 °C. (●) chrysotile and lizardite, (■) maghemite, (○) enstatite, (x) forsterite, (\*) magnetite, (+) hematite

**Tandem thermogravimetric analysis-mass spectrometry** Figure 8-3 illustrates the weight loss profile of RMR and chrysotile during calcination. The weight loss for both samples began after 120°C due to simultaneous release of water ( $m/z = 18$ ) and  $\text{CO}_2$  ( $m/z = 44$ ) as observed from MS (Figure 8-4). These species result from the decomposition of carbonodithioic acid collector and of native carbonates and desorption of physically bound

water. Spontaneous carbonation of serpentine residues at weathering conditions was shown to lead to several species such as hydromagnesite ( $\text{Mg}_5(\text{CO}_3)_4(\text{OH})_2 \cdot 4\text{H}_2\text{O}$ ), nesquehonite ( $\text{MgCO}_3 \cdot 3\text{H}_2\text{O}$ ), lansfordite ( $\text{MgCO}_3 \cdot 5\text{H}_2\text{O}$ ) [20] and other carbonates on the residue surface leading to the distinction of  $\text{CO}_2$  and  $\text{H}_2\text{O}$  signatures in MS due to calcination from 100 to 700°C [21]. Further water was also released as a result of RMR and chrysotile dehydroxylation after 600°C. The two distinguishable weight loss steps observed during dehydroxylation of RMR are probably due to coexisting lizardite and chrysotile being dehydroxylated at different rates. The former's occurring at temperatures higher than the later's [22], hence the broad temperature range required for RMR dehydroxylation (Figure 8-4). It is worthy of mention that the weight loss of olivine due to the decomposition of impurities during calcination was negligible (less than 0.1%).

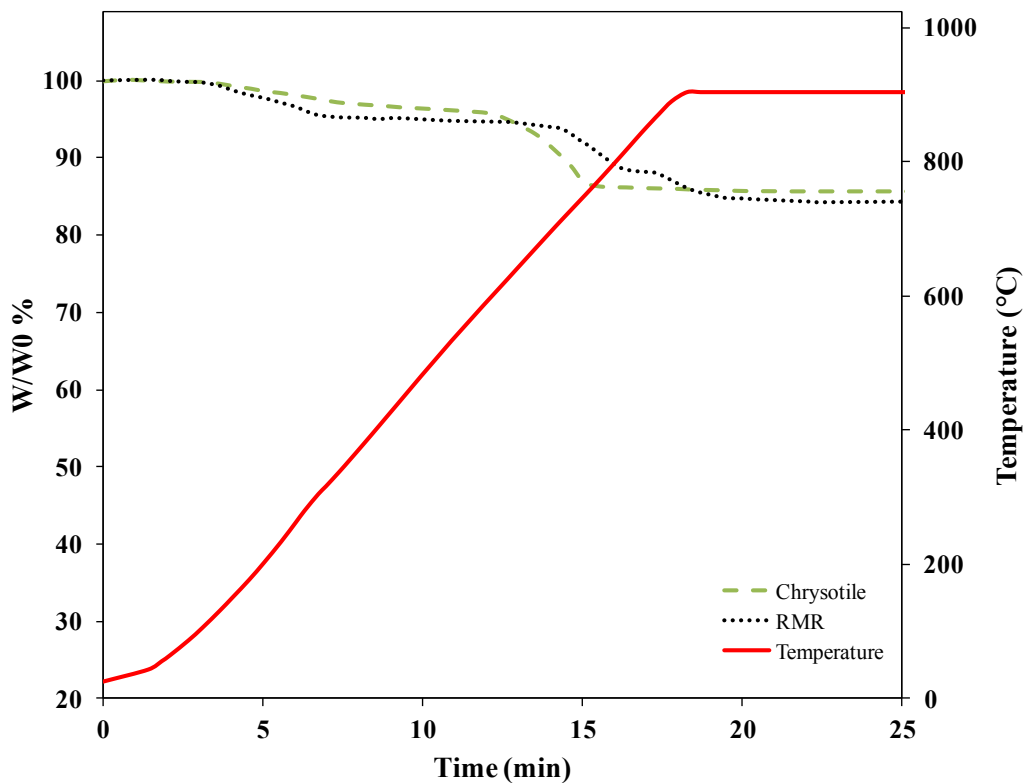


**Figure 8-3.** TG monitoring of RMR and chrysotile weight loss during calcination at 50°C heating rate

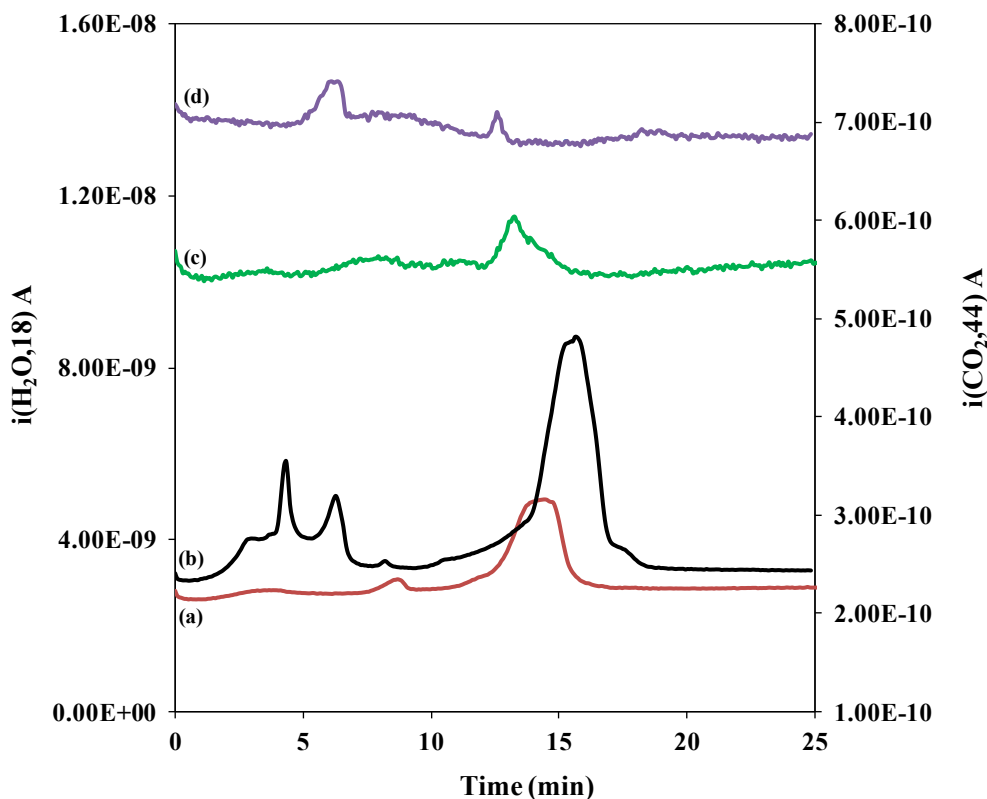


**Figure 8-4.** MS monitoring of positive ion currents (a)  $m/z=18$  ( $\text{H}_2\text{O}$ ) for chrysotile (b)  $m/z=18$  ( $\text{H}_2\text{O}$ ) for RMR, (c)  $m/z=44$  ( $\text{CO}_2$ ) for chrysotile and (d)  $m/z=44$  ( $\text{CO}_2$ ) for RMR, during air calcination at  $50^\circ\text{C}$  heating rate in TG

**Mössbauer spectroscopy** Mössbauer parameters of as-received RMR, chrysotile and olivine are summarized in Table 8-2. The Mössbauer spectrum of as-received RMR exhibited two sextets and two quadruple doublets. The two sextets are characteristic of iron in magnetite. The sextet with isomer shift of  $0.69\text{ mm/s}$  and hyperfine field of  $46.4\text{ T}$  represents octahedral  $\text{Fe}^{3+}$  and  $\text{Fe}^{2+}$ . Since the electron hopping between octahedral  $\text{Fe}^{2+}$  and  $\text{Fe}^{3+}$  is faster than the Mössbauer spectrum characteristic time ( $10^{-8}\text{ s}$ ), the Fe Mössbauer spectrum features an average valence of  $+2.5$  and only one spectrum for the two octahedral  $\text{Fe}^{3+}$  and  $\text{Fe}^{2+}$  cations [23]. The second sextet with isomer shift of  $0.26\text{ mm/s}$  and hyperfine field of  $49.6\text{ T}$  is characteristic of tetrahedral  $\text{Fe}^{3+}$  in magnetite. The two sextets contribute for 24% of iron in RMR located in magnetite. Consequently, 76% of iron was present as intra-framework iron distinguishable by two quadruple doublets. The more intense of two doublets had an isomer shift of  $0.374\text{ mm/s}$  and quadrupole splitting of  $0.645$

mm/s, and accounted for 51% of iron in RMR. A similar spectrum was reported for octahedral ferric doublet in chrysotile and lizardite [24,25]. The less intense quadruple doublet (isomer shift 1.15 mm/s and quadrupole splitting 2.75 mm/s) contributed for 24% of octahedral Fe<sup>2+</sup> iron akin to octahedral Fe<sup>2+</sup> in olivine and chrysotile structures [25]. In-situ iron was predictable from RMR elemental analysis as the Mg/Si atom ratio equal 0.964 in as-received RMR was far from theoretical chrysotile and lizardite Mg/Si ratio (1.5) suggesting a Mg in chrysotile and lizardite were replaced by iron. Unlike intra-framework iron rich RMR, most of iron in raw chrysotile (64%) belonged to magnetite. Intra-framework iron in chrysotile crystalline structure was in three forms: 1) octahedral Fe<sup>2+</sup> (21%), 2) octahedral Fe<sup>3+</sup> (8%) and 3) tetrahedral Fe<sup>3+</sup> (7%). Iron replaced octahedral Mg<sup>2+</sup> in the brucitic layer and tetrahedral Si<sup>4+</sup> in the silicate layer of chrysotile. For raw olivine, Mössbauer spectrum shows only one quadruple doublet (isomer shift 1.136 mm/s and quadrupole splitting 3.002 mm/s) which is characteristic of octahedral intra-framework ferrous iron.

**Table 8-2.** Isomer shift ( $\delta$ ), quadrupole splitting ( $\Delta$ ), hyperfine field ( $B_{hf}$ ) and relative areas of the components used to fit the spectra of the as-received RMR (Raglan mine residues, Québec), chrysotile (Thetford Mines, Québec) and olivine

Catalyst	Iron assignment	$\delta$ (mm/s)	$\Delta$ (mm/s)	$B_{hf}$ (T)	Area (%)
a/r RMR	Magnetite Fe <sup>3+</sup> , tetrahedral	0.26	0	49.6	10
	Magnetite Fe <sup>2+</sup> , Fe <sup>3+</sup> , octahedral	0.69	0	46.4	14
	Chrysotile/ lizardite Fe <sup>2+</sup> , octahedral	1.15	2.7	0	24
	Chrysotile/ lizardite Fe <sup>3+</sup> , octahedral	0.374	0.645	0	51
a/r chrysotile	Magnetite Fe <sup>3+</sup> , tetrahedral	0.27	0.00	49.0	26
	Magnetite Fe <sup>2+</sup> , Fe <sup>3+</sup> , octahedral	0.67	0.03	46.1	38
	Chrysotile Fe <sup>2+</sup> , octahedral	1.12	2.85	0.00	21
	Chrysotile Fe <sup>3+</sup> , tetrahedral	0.25	0.41	0.00	7
	Chrysotile Fe <sup>3+</sup> , octahedral	0.37	1.00	0.00	8
a/r olivine	Olivine Fe <sup>2+</sup> , octahedral	1.136	3.003	0.00	100

**Table 8-3.** Isomer shift ( $\delta$ ), quadrupole splitting ( $\Delta$ ), hyperfine field ( $B_{\text{hf}}$ ) and relative areas of the components used to fit the spectra of calcined RMR, chrysotile and olivine for 2h at 900°C

Catalyst	Iron assignment	$\delta$ (mm/s)	$\Delta$ (mm/s)	$B_{\text{hf}}$ (T)	Area (%)
RMR	Hematite $\text{Fe}^{3+}$ , octahedral	0.367	-0.23	51.9	56
air-calcined	Hematite solid-solution $\text{Fe}^{+3}$ , octahedral	0.30	0	47.3	22
	$\text{Fe}^{3+}$ , octahedral	0.34	1.01		22
Chrysotile	Hematite $\text{Fe}^{3+}$ , octahedral	0.382	-0.176	51.6	51
air-calcined	$\text{Fe}^{2+}$ , octahedral	1.11	3.06	0.00	2
	$\text{Fe}^{3+}$ , octahedral	0.11	2.00	0.00	8
	$\text{Fe}^{3+}$ , octahedral	0.34	0.95	0.00	20
	Hematite solid-solution $\text{Fe}^{+3}$ , octahedral	0.37	0	43.7	18
Olivine	Olivine $\text{Fe}^{2+}$ , octahedral	1.133	3.002	0.00	88
air-calcined	Superparamag. hematite $\text{Fe}^{3+}$ , octahedral	0.44	0.62	0.00	6
	Hematite $\text{Fe}^{3+}$ , octahedral	0.32	0.00	51.0	6

Calcination under air of RMR, chrysotile and olivine in air for 2h considerably altered iron oxidation and coordination in the samples. The Mössbauer parameters of calcined RMR, chrysotile and olivine are summarized in Table 8-3. Almost 56% of iron was present in the calcined RMR in the form of  $\text{Fe}^{3+}$  in  $\alpha\text{-Fe}_2\text{O}_3$  (hematite) or  $\gamma\text{-Fe}_2\text{O}_3$  (maghemite) corresponding to an isomer shift of 0.367 mm/s and hyperfine field of 51.9 T. Though maghemite and hematite were revealed from the XRPD of calcined RMR, the Mössbauer spectra of maghemite and hematite coincide at ambient temperature [26] making it difficult to quantify them separately. Presence of Al, Ca, Cr, Ni traces in RMR and their incorporation in hematite and maghemite structures during calcination could explain the occurrence of a sextet with isomer shift 0.3 mm/s and hyperfine field of 47.3 T representing 22% of the total iron. For example, Al impurities in the hematite and maghemite structure are known to decrease hematite and maghemite hyperfine field [27]. Calcination of RMR also led to the disappearance of octahedral  $\text{Fe}^{2+}$  in accordance with its oxidation as  $\text{Fe}^{3+}$ . Nearly 22% of iron was in the form of octahedral  $\text{Fe}^{3+}$  in the calcined sample with isomer shift of 0.34 mm/s and quadrupole splitting of 1.01 mm/s. RMR calcination at 900°C

increased the quadrupole splitting of  $\text{Fe}^{3+}$  doublet although the isomer shift remained relatively static. Calcination and dehydroxylation might increase the distortion of octahedral  $\text{Fe}^{3+}$  sites. As suggested by Rozenon et al. [28] increased distortions of octahedral  $\text{Fe}^{3+}$  correlated with increasing quadrupole splitting of  $\text{Fe}^{3+}$  sites.

Calcination of olivine led to the extraction of octahedral  $\text{Fe}^{2+}$  from lattice and formation of hematite particles as objectified by a sextet with isomer shift 0.32 mm/s and hyperfine field 51.0 T. Part of hematite particles, consisting of quite small particles, were also showing superparamagnetic properties as evidenced by the appearance of a quadruple doublet with isomer shift 0.44 mm/s and quadrupole splitting 0.62 mm/s. Formation of hematite grains within chrysotile matrix was also observed after calcination. Transformation of magnetite to hematite along with oxidation of most of in-situ  $\text{Fe}^{2+}$  led to ca. 69 % of iron in the form of hematite. Some 74 % of hematite iron featured pure hematite with isomer shift 0.382 mm/s and hyperfine field 51.6 T. The balance (26%) was due to a Mössbauer spectrum of impurities-incorporated hematite such as Ca and Al integration in the hematite structure after calcination. More details on the Mössbauer spectra of chrysotile and olivine are given in our previous work [12].

**Temperature-programmed reduction**  $\text{H}_2$  consumption of calcined RMR, chrysotile and olivine at  $15^\circ\text{C}/\text{min}$  heating rate is plotted against temperature in Figure 8-5. The reduction of iron oxides started near  $300^\circ\text{C}$  covering a broad temperature range until  $950^\circ\text{C}$ . The area under TPR curve (after dividing by heating rate) represents almost 87% reduction of ferric iron to metallic iron for the calcined RMR. This is compatible with the presence of 78% of free iron oxides in the form of pure and impurities-substituted hematite/maghemite as probed by Mössbauer spectroscopy while the rest as due to  $\text{H}_2$  reduction of some octahedral  $\text{Fe}^{3+}$  in the calcined RMR. Reduction of octahedral  $\text{Fe}^{3+}$  was also observed by TPR of calcined chrysotile while  $\text{H}_2$  consumption was an indication of almost 97% reduction of ferric iron to metallic iron. This ferric iron exists in three forms: pure hematite, impurities-substituted hematite and octahedral  $\text{Fe}^{3+}$ . Chrysotile and RMR calcination in air and subsequent transformation of their octahedral  $\text{Fe}^{2+}$  to octahedral  $\text{Fe}^{3+}$  increased iron reducibility in these samples. Previous experiments performed with  $\text{N}_2$ -calcined chrysotile revealed lower reducibility of iron in the sample as well [12].

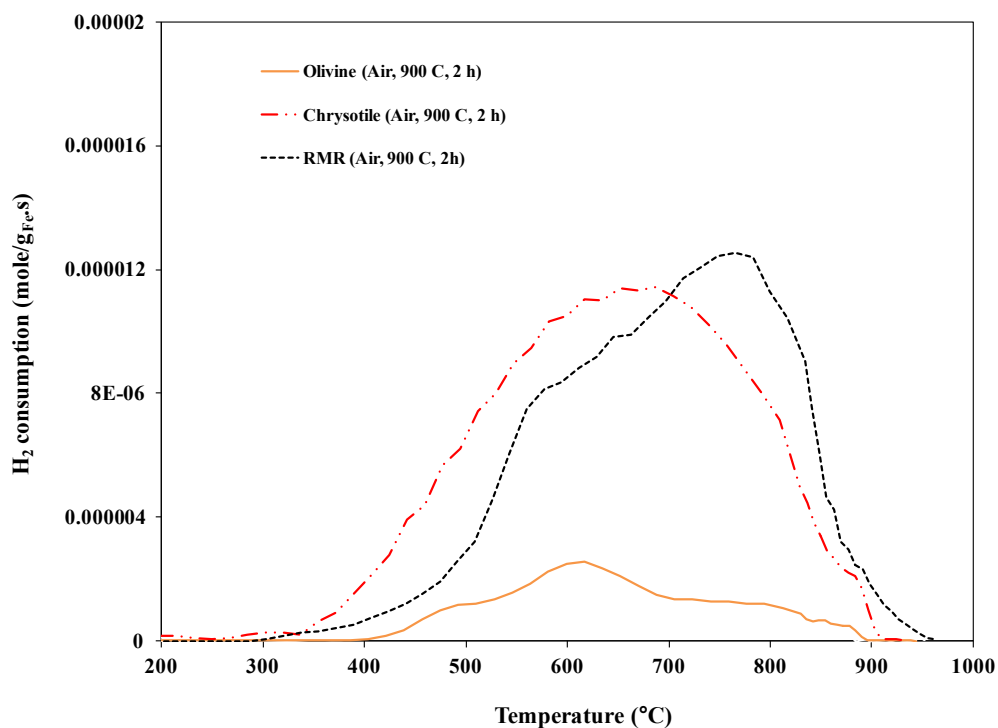


**Figure 8-5.** Hydrogen consumption rates (in mol(H<sub>2</sub>)/g<sub>Fe</sub>/s) as a function of ramp temperature in temperature-programmed reduction tests of calcined RMR, chrysotile and olivine samples

Iron is also present in as-received olivine mainly in the form of octahedral Fe<sup>2+</sup>. Olivine's low iron reducibility (*ca.* 2-3 % of iron) is mainly attributed to decomposition of iron bearing coexisting impurities such as talc and chlorite. However, calcination of olivine in air led to extraction of iron from olivine lattice and spreading of free iron oxides across olivine. Reducible iron to metallic iron in calcined olivine at 900°C for 2 h amounted to *ca.* 14 %. This is in agreement with the Mössbauer spectroscopy results which showed that calcined olivine contained almost 12% of iron in the form of ferromagnetic or superparamagnetic hematite. By extending the olivine calcination period and increasing temperature, iron reducibility was seen to increase due to extraction of more iron from the lattice and formation of free iron oxides [12]. Availability of reducible iron will positively influence catalyst activity since iron reduction by autogenous H<sub>2</sub> (produced during gasification and tar reforming) could lead to the formation of active metallic iron to mediate C-C and C-H bond cleavage [11].

**Transmission electron microscopy** Figure 8-6 a,b show, respectively, TEM images for RMR and chrysotile air-calcined at 900°C for 2 h. The black spots on calcined RMR, attributed to hematite, evidence large particle sizes with an average of 100 nm. Unlike calcined RMR, calcined chrysotile featured much finer hematite particles in the 20-30 nm range. In accordance with the Mössbauer results, no iron oxide particles were observed on the surface of raw olivine (Figure 8-6 c). However, after olivine calcination (at 900°C for 2 h), relatively large black spots with 80 nm average size were formed illustrating iron extraction from olivine lattice (Figure 8-6 d). Prolonging olivine calcination time to 10 h coarsened even further the size of black spots (average size > 100 nm) resulting both from more lattice iron extraction and sintering of hematite particle into coarser ones (Figure 8-6 e).

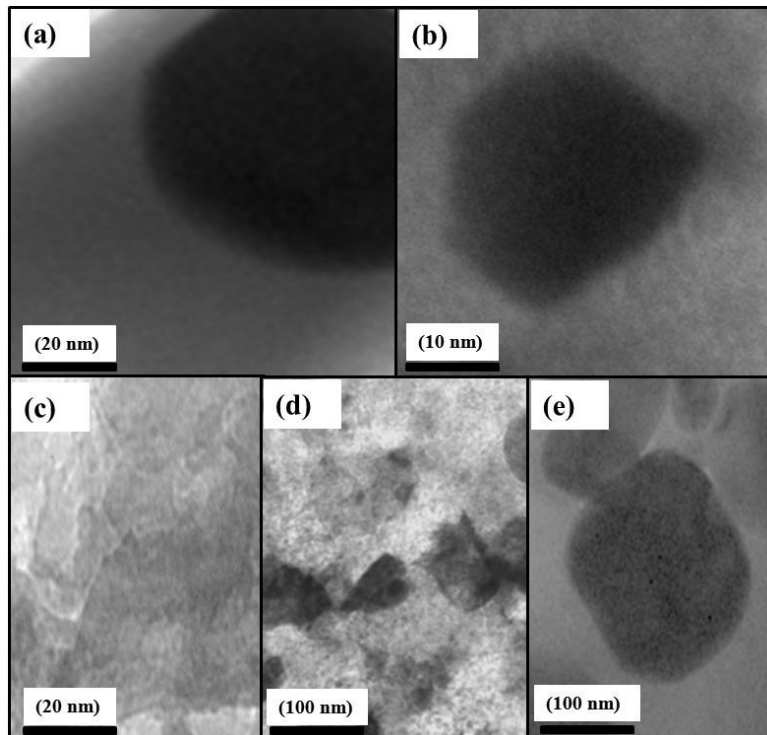


**Figure 8-6.** transmission electron microscopy (TEM) images taken of (a) calcined RMR for 2 h at 900 °C (b) calcined chrysotile for 2 h at 900 °C (c) raw olivine (d) calcined olivine for 2 h at 900 °C (e) calcined olivine for 10 h at 900°C

### 8.3.2. Comparison of RMR, chrysotile and olivine activity

Activities of calcined chrysotile, RMR and olivine for cracking of benzene in two different compositions of simulated syngas are compared under identical temperature, equivalent

particle size and the same iron loading. The syngas composition was chosen to coincide with the ranges typical of biomass steam gasification [29,30].

Benzene and methane conversion over calcined chrysotile, RMR and olivine are compared in Figure 8-7 a,b for two syngas compositions. Activity of chrysotile for benzene cracking is considerably higher than that of calcined RMR and olivine. In terms of benzene conversion, calcined chrysotile outperformed by up to a factor 4 and 2.5 calcined olivine and calcined RMR, respectively. Chrysotile activity for methane conversion was also noticeably higher, by up to a factor 7, than calcined RMR and olivine. The correlation between iron reducibility and higher activity of catalyst for tar cracking is well established [12-14]. After calcination at 900°C for 2 h, chrysotile and RMR hold 97% and 87% of reducible iron, respectively, whereas in olivine reducible iron accounts for 14%. In addition to highly reducible calcined chrysotile and RMR, they also exhibited a BET surface area 41 and 47 times larger than olivine, respectively. Although iron reducibility and BET surface area of calcined RMR and chrysotile are comparable, the average size of hematite particles for calcined chrysotile is typically 4 to 5 times lower than for calcined RMR and calcined olivine. Finer hematite particles, and thus superior dispersion (and reducibility) over the surface of calcined chrysotile aligns with this latter larger activity for benzene cracking in comparison to calcined RMR and olivine.

Olivine activity for benzene cracking slightly changed as calcination was extended from 2 h to 10 h while methane conversion was almost unchanged (Figure 8-7). A similar observation can be made regarding calcination temperature (results not shown). Increasing calcination time of olivine from 2 h to 10 h increased Fe reducibility by 50-70%. Correlatively, the average particle size of iron oxides on olivine surface augmented from 80 nm to 100<sup>+</sup> nm after calcination. Hence, sintering of inter-grown highly-dispersed superparamagnetic hematite particles due to longer calcination time (and/or higher temperature) might prevent access to core Fe<sup>3+</sup> in the benzene reforming catalyst.

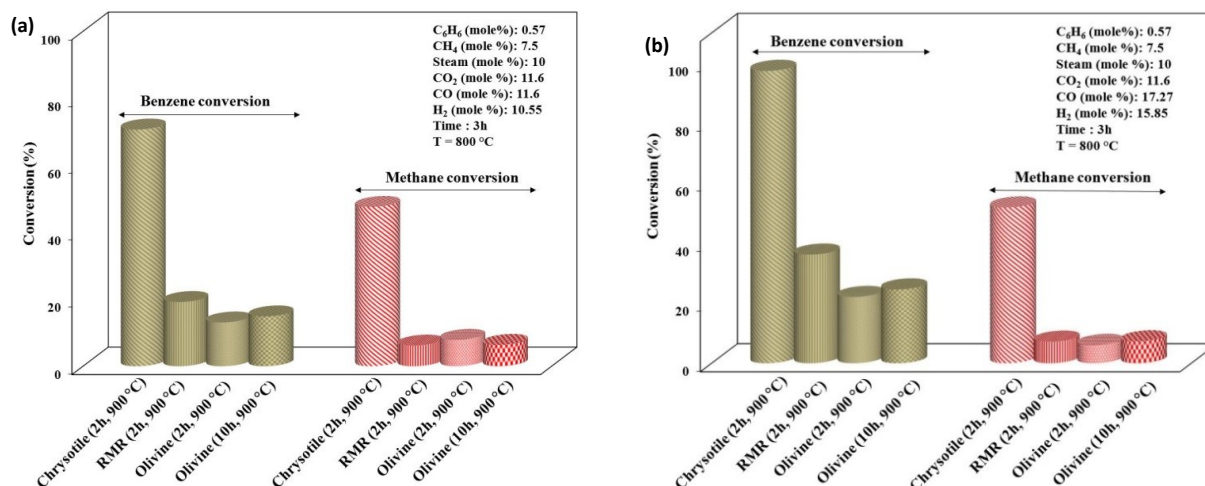


**Figure 8-7.** Comparison of Benzene and methane conversion by RMR, chrysotile and olivine at two different syngas concentrations

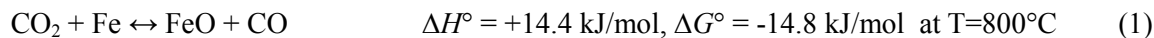
### 8.3.3. Parametric study of chrysotile activity

Chrysotile, among the above tested iron-bearing silicates at identical reactor iron loading, had the highest activity for benzene cracking in simulated syngas. Consequently, chrysotile was thoroughly tested against syngas varied compositions to achieve both optimum cracking activity and ability to minimize coke formation. For this purpose, benzene and methane reforming reactions were studied under: 1) dry reforming of benzene and methane in  $CO/CO_2/N_2$  mixtures and 2) steam reforming of benzene and methane in  $H_2/H_2O/N_2$  mixtures. Based on these dry and steam reforming studies, several experiments in presence of all syngas components were also designed.

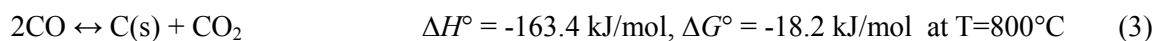
Prior to each case study, calcined chrysotile was reduced in-situ the reactor under  $H_2$  flow for 1 h at  $800^\circ\text{C}$  to form metallic iron, i.e., active phase for tar cracking.  $H_2$  inside the reactor was then purged with  $N_2$  and subsequently a specified gas mixture was injected. Formation of carbon on the surface of chrysotile was also examined by its burn-off in air and monitoring  $CO_2$  production rate with  $CO_2$  infrared detector.

**Dry reforming** In the first series of experiments,  $CO/CO_2/N_2$  mixtures with various proportions were introduced to the hot bed of reduced chrysotile.  $CO_2$  and  $CO$  concentrations were monitored for *ca.* 60 min *via* micro GC to identify the reactions taking place between chrysotile and the gas mixture. Feeding  $CO$ -free  $CO_2/N_2$  mixture to the reactor led to considerable drop in outlet  $CO_2$  concentration (Figure 8-8 a). Carbon dioxide

consumption manifests itself by CO formation and iron oxidation. Wüstite and magnetite were reported to form by oxidation of metallic iron through dissociation of CO<sub>2</sub> on iron and release of atomic oxygen [31]:



Formation of deposited carbon on chrysotile surface was also detected after passing CO/CO<sub>2</sub>/N<sub>2</sub> mixture through the hot bed (Figure 8-8 a). Increased CO/CO<sub>2</sub> ratios promoted carbon deposition on chrysotile as carburization in presence of metallic iron could lead to the formation of surface deposited carbon on chrysotile:



Carburization takes place by rapid surface dissociation of CO into carbon and oxygen atoms followed by reaction of atomic oxygen with CO. This latter reaction is the rate-determining step [32,33]:



Carburization is known to lead to the formation of iron carbides such as Fe<sub>3</sub>C, Fe<sub>2</sub>C along with some graphitic carbon as reportedly observed through Mössbauer spectroscopy and XRD [34]. It is worth mentioning that at 800°C, formation of iron carbonates such as siderite (FeCO<sub>3</sub>) is not thermodynamically favorable [35,36]. Although increasing the CO/CO<sub>2</sub> ratio could diminish chrysotile deactivation by oxidation of metallic iron, higher amounts of carbon deposit may have negative influence on chrysotile activity for tar cracking [5].

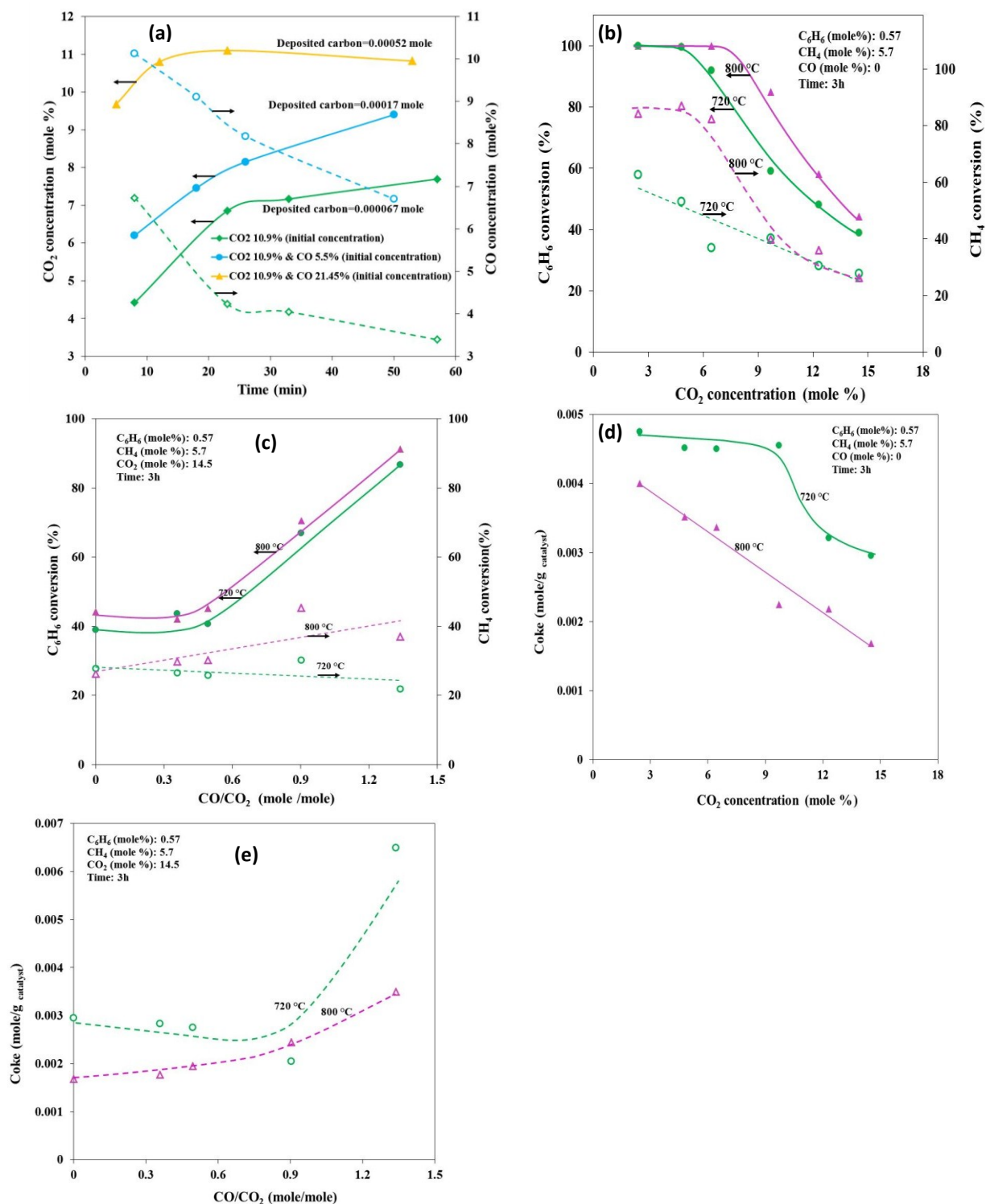
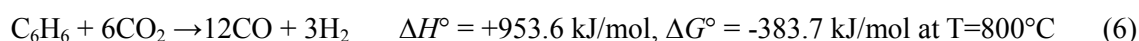
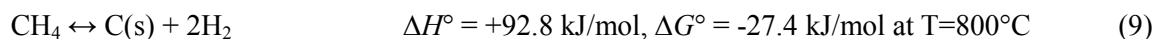


**Figure 8-8.** (a) CO and CO<sub>2</sub> concentration profile by passing mixtures of CO/CO<sub>2</sub>/N<sub>2</sub> through a reduced bed of chrysotile at 800 °C (b) benzene and methane conversion by chrysotile versus CO<sub>2</sub> concentration in C<sub>6</sub>H<sub>6</sub>/CH<sub>4</sub>/CO/CO<sub>2</sub>/N<sub>2</sub> mixture (c) benzene and methane conversion by chrysotile versus CO/CO<sub>2</sub> mole ratio in C<sub>6</sub>H<sub>6</sub>/CH<sub>4</sub>/CO/CO<sub>2</sub>/N<sub>2</sub> mixture (d) coke formation on chrysotile versus CO<sub>2</sub> concentration in C<sub>6</sub>H<sub>6</sub>/CH<sub>4</sub>/CO/CO<sub>2</sub>/N<sub>2</sub> mixture (e) coke formation on chrysotile versus CO/CO<sub>2</sub> concentration in C<sub>6</sub>H<sub>6</sub>/CH<sub>4</sub>/CO/CO<sub>2</sub>/N<sub>2</sub> mixture

Experiments conducted with C<sub>6</sub>H<sub>6</sub>/CH<sub>4</sub>/CO<sub>2</sub>/N<sub>2</sub> mixtures showed that by increasing CO<sub>2</sub> concentration in the mixture, methane and benzene conversions nose-dove steadily after remaining rather unchanged at low CO<sub>2</sub> concentrations (Figure 8-8 b). Oxidation of metallic iron at high CO<sub>2</sub> concentration decreases the number of available active sites for benzene and methane cracking. Addition of CO to C<sub>6</sub>H<sub>6</sub>/CH<sub>4</sub>/CO<sub>2</sub>/N<sub>2</sub> mixtures increased benzene conversion at CO/CO<sub>2</sub> ratios higher than 0.5 (Figure 8-8 c) by limiting oxidation of active metallic iron thus in turn preserving more active sites for dry reforming of benzene. However, conversion of methane in the mixture followed no special trend by increasing CO/CO<sub>2</sub> ratio. As seen in Figure 8-8 c, methane conversion at 720°C slowly decreased by increasing CO/CO<sub>2</sub> ratio while at 800°C its conversion slowly increased.



Under no CO, coke buildup diminished as mixtures were CO<sub>2</sub>-enriched (Figure 8-8 d). However, the rise in CO/CO<sub>2</sub> ratio within C<sub>6</sub>H<sub>6</sub>/CH<sub>4</sub>/CO<sub>2</sub>/CO/N<sub>2</sub> mixtures led to deposition of more coke on chrysotile at 800°C (Figure 8-8 e). Carbon deposition on the surface of chrysotile at 720°C started climbing for CO/CO<sub>2</sub> ratios > 0.9 (Figure 8-8 e). Carburization reactions at high CO/CO<sub>2</sub> ratio could increase carbon deposition on the surface of chrysotile. Promoting dissociation of benzene and methane on the surface of chrysotile due to the presence of more active metallic phase could be another reason for such increased amounts of coke on chrysotile.



Although coke deposition increased with increasing CO/CO<sub>2</sub> ratio, availability of additional non-oxidized iron sites thereof led to a considerable increase in benzene conversion in steady state conditions. Such benzene higher conversion was in accordance with the increased H<sub>2</sub> and CO composition measured online at the exit of reactor.

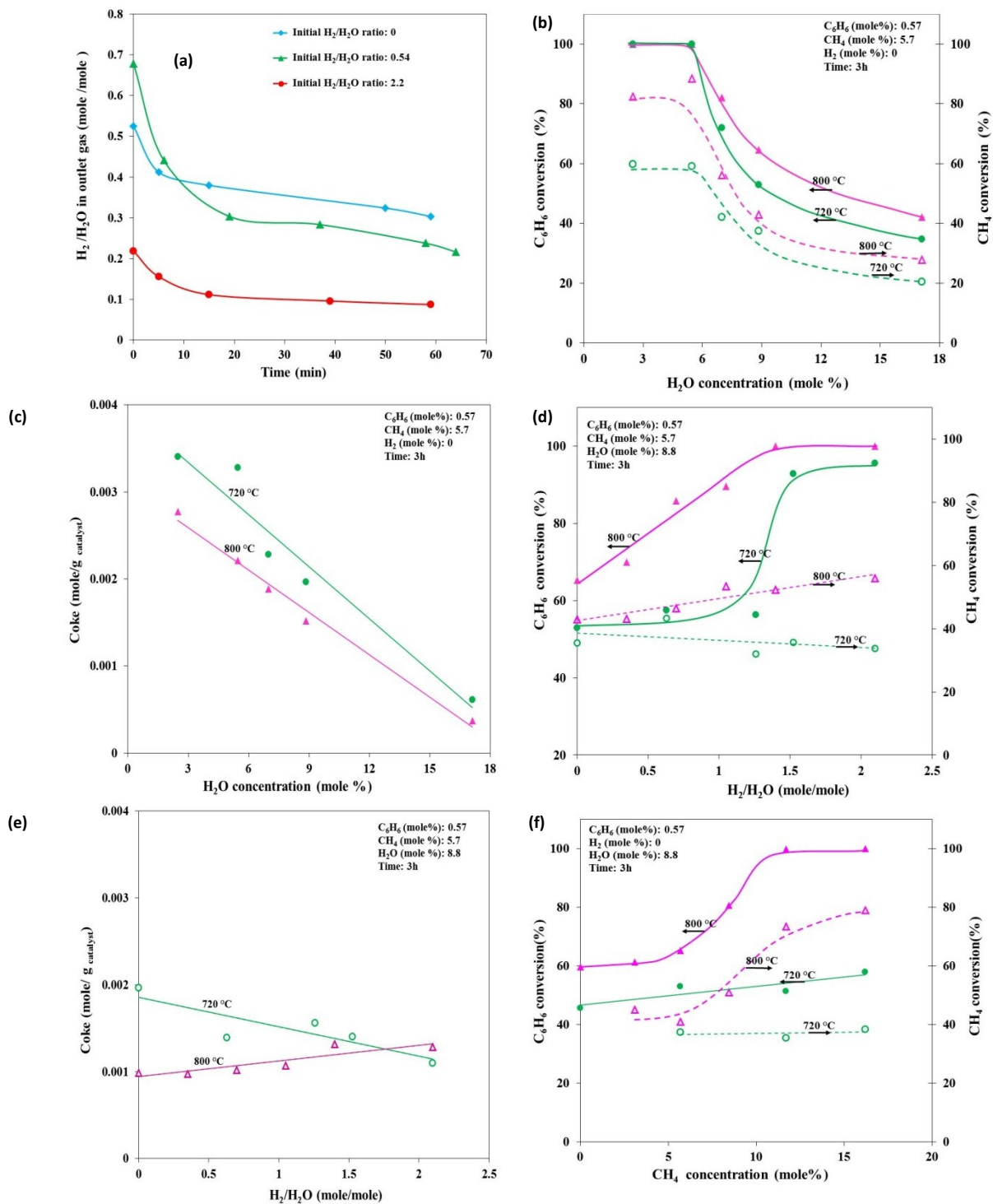
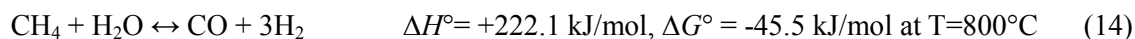
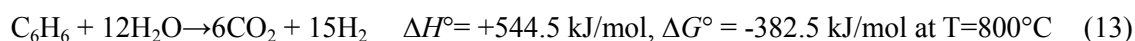


**Figure 8-9.** (a) H<sub>2</sub> production by passing mixtures of CO/CO<sub>2</sub>/N<sub>2</sub> through a reduced bed of chrysotile at 800 °C (b) benzene and methane conversion by chrysotile versus H<sub>2</sub>O concentration in C<sub>6</sub>H<sub>6</sub>/CH<sub>4</sub>/H<sub>2</sub>O/N<sub>2</sub> mixture (c) coke formation on chrysotile versus H<sub>2</sub>O concentration in C<sub>6</sub>H<sub>6</sub>/CH<sub>4</sub>/H<sub>2</sub>O/N<sub>2</sub> mixture (d) benzene and methane conversion by chrysotile at versus H<sub>2</sub>/H<sub>2</sub>O mole ratio in C<sub>6</sub>H<sub>6</sub>/CH<sub>4</sub>/H<sub>2</sub>/H<sub>2</sub>O/N<sub>2</sub> mixture (e) coke formation on chrysotile versus H<sub>2</sub>/H<sub>2</sub>O mole ratio in C<sub>6</sub>H<sub>6</sub>/CH<sub>4</sub>/H<sub>2</sub>/H<sub>2</sub>O/N<sub>2</sub> mixture (f) benzene and methane conversion by chrysotile versus CH<sub>4</sub> concentration in C<sub>6</sub>H<sub>6</sub>/CH<sub>4</sub>/H<sub>2</sub>O/N<sub>2</sub> mixture

**Steam reforming** Chrysotile metallic iron oxidation in H<sub>2</sub>/H<sub>2</sub>O environment is investigated by feeding H<sub>2</sub>/H<sub>2</sub>O/N<sub>2</sub> mixtures at various compositions. Metallic iron in chrysotile was oxidized by steam at 700-800°C leading to the production of H<sub>2</sub> (Figure 8-9a). As can also be seen, increasing inlet H<sub>2</sub>/H<sub>2</sub>O ratio reduced iron oxidation as confirmed by less hydrogen production at the reactor outlet.



The experiments showed that benzene and methane cracking in C<sub>6</sub>H<sub>6</sub>/CH<sub>4</sub>/H<sub>2</sub>/H<sub>2</sub>O/N<sub>2</sub> mixture followed qualitatively the same trend as that of C<sub>6</sub>H<sub>6</sub>/CH<sub>4</sub>/CO/CO<sub>2</sub>/N<sub>2</sub> mixture. Adding benzene and methane to H<sub>2</sub>/H<sub>2</sub>O/N<sub>2</sub> mixture led to benzene and methane steam reforming reactions taking place on chrysotile active metallic iron sites:



Similarly to dry reforming, increasing steam concentration in C<sub>6</sub>H<sub>6</sub>/CH<sub>4</sub>/H<sub>2</sub>O/N<sub>2</sub> mixture led to a drop in benzene and methane conversion (Figure 8-9 b). The rise in steam concentration decreases the number of available active sites for benzene and methane cracking by oxidizing metallic iron. Coke formation on chrysotile was also decreased by increasing steam concentration. Coke formation due to methane and benzene steam reforming was considerably lower compared to the dry reforming route (Figures 8-8 d, 8-9 c).

Increasing H<sub>2</sub> concentration in C<sub>6</sub>H<sub>6</sub>/CH<sub>4</sub>/H<sub>2</sub>/H<sub>2</sub>O/N<sub>2</sub> mixtures led to a continuous increase in benzene and methane conversion at 800°C. Benzene conversion started to increase by increasing H<sub>2</sub>/H<sub>2</sub>O ratio until it reached a maximum at H<sub>2</sub>/H<sub>2</sub>O = 1.5 (Figure 8-9 d). Addition of more H<sub>2</sub> is expected to reduce iron oxidation consequently providing more active sites for cracking of benzene and methane. However, increasing H<sub>2</sub>/H<sub>2</sub>O ratio at 720°C led to different trends of benzene and methane conversion (Figure 8-9 d). Benzene

conversion kept nearly constant at  $H_2/H_2O < 1.5$  beyond which it started to increase until to plateau at  $H_2/H_2O > 2$ . Methane conversion also had a very slight decrease at  $720^\circ\text{C}$  as  $H_2/H_2O$  ratio was increasing. Temperature is likely to have a significant effect on the cracking reactions, iron oxidation/reduction and coke formation. The amount of coke formed on chrysotile at  $800^\circ\text{C}$  was also gradually increasing by a rise in  $H_2/H_2O$  ratio while at  $720^\circ\text{C}$  the amount of coke was decreasing slowly (Figure 8-9 e). Coke formation due to reforming in  $H_2/H_2O$  environment was less active than in dry  $CO/CO_2$  reforming conditions (Figures 8-9 e, 8-8 e). The effect of rise in methane concentration on benzene and methane conversion is shown in Figure 8-9 f. Increasing methane concentration in the mixture increased benzene conversion.

**Benzene reforming in simulated syngas** Dry and steam reforming of benzene revealed that the ratio of reductive to oxidative gases in the reactor had considerable effect on benzene conversion over chrysotile. Benzene conversion in simulated syngas mixtures of  $C_6H_6/CH_4/CO_2/H_2O/CO/H_2/N_2$  was consequently dependent to the ratio of reductive gasses ( $H_2$  and  $CO$ ) to oxidative gases ( $H_2O$  and  $CO_2$ ). Figure 8-10 a shows that by increasing  $H_2$  concentration in simulated syngas, benzene conversion increased notably unlike methane conversion which kept virtually constant. By increasing the overall concentration of  $H_2$  and  $CO$  in the mixture, benzene and methane conversions increased (Figure 8-10 b). Hence, it is likely that increasing the ratio of reductive to oxidative gases improved chrysotile cracking activity by limiting oxidation of active iron sites. Coke formation on chrysotile was lower in the presence of (reductive gas)  $H_2$ . Although increasing  $CO$  concentration improved chrysotile activity for benzene cracking, the higher coke formation on chrysotile due to  $CO$  was remarkable.

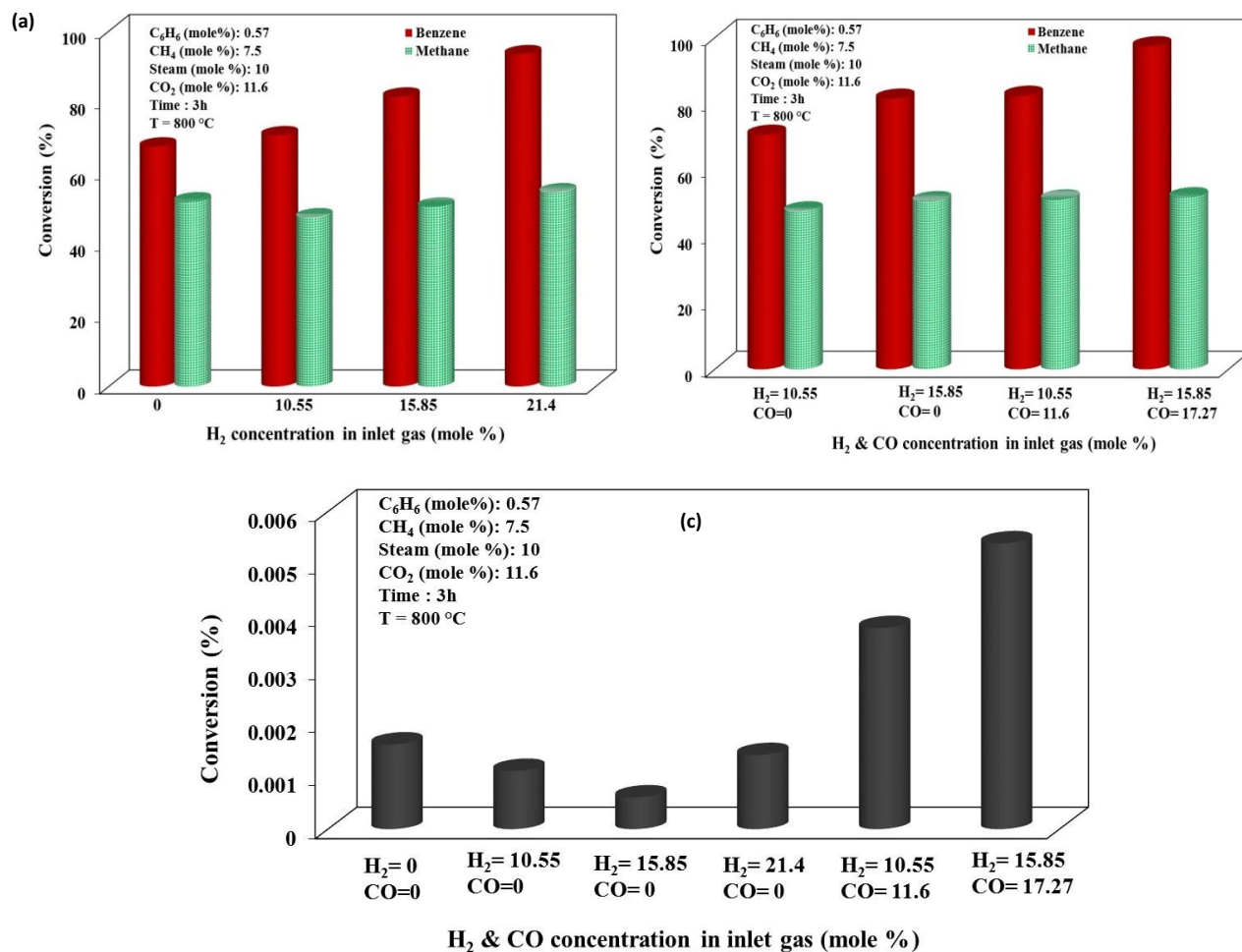


**Figure 8-10:** (a) benzene and methane conversion by chrysotile at 800 °C versus H<sub>2</sub> concentration (b) benzene and methane conversion by chrysotile at 800 °C versus CO and H<sub>2</sub> concentration (c) coke formation on the surface of chrysotile at 800 °C versus CO and H<sub>2</sub> concentrations

## 8.4. Conclusion

Investigations on the steam reforming activity of chrysotile, RMR and olivine were carried out using benzene, as a model tar compound, co-mixed with H<sub>2</sub>, CO, CO<sub>2</sub>, CH<sub>4</sub> and steam in simulated syngas. The activity of calcined chrysotile and RMR was compared to that of olivine for benzene steam-reforming at comparable iron loadings in a fixed-bed reactor at 800°C. Regardless of olivine's pretreatment, air-calcined chrysotile and RMR were found to be considerably active, with up to a fourfold and twofold increase in benzene conversion, respectively, compared to olivine. Chrysotile exhibited considerable activity for methane reforming in simulated syngas. Compared to olivine, this increased chrysotile and RMR activity was attributed to both higher surface area and reducibility of iron (97% and 87%, respectively). Sintering of iron oxide particles on the surface of olivine revealed by TEM, however, adversely affected olivine's catalytic activity. The presence of various components in the simulated syngas with different H<sub>2</sub>, CO, CO<sub>2</sub>, CH<sub>4</sub> and steam compositions on chrysotile activity for benzene cracking was also investigated. Increasing the mole fraction of reducing agents, i.e., H<sub>2</sub> and CO, and decreasing the fraction of oxidizing agents, e.g., CO<sub>2</sub> and H<sub>2</sub>O, in syngas resulted in increased benzene cracking activity of chrysotile. Furthermore, oxidation of metallic iron in the presence of oxidative agents such as H<sub>2</sub>O and CO was noted to reduce the activity of chrysotile for benzene cracking. Coke formation on chrysotile surface was dependent on syngas composition as an increase in H<sub>2</sub> concentration reduced coke formation while higher CO concentrations promoted higher amounts of coke.

## 8.4. References

- [1] Berndes G, Hoogwijk M, van den Broek R. The contribution of biomass in the future global energy supply: A review of 17 studies. *Biomass Bioenerg* 2003;25:1-28.
- [2] Devi L, Ptasinski KJ, Janssen F. A review of the primary measures for tar elimination in biomass gasification processes. *Biomass Bioenerg* 2003;24:125-40.
- [3] Xu CB, Donald J, Byambajav E, Ohtsuka Y. Recent advances in catalysts for hot-gas removal of tar and  $\text{NH}_3$  from biomass gasification. *Fuel* 2010;89:1784-95.
- [4] Milne TA, Evans RJ, Abatzoglou N. Biomass gasifier tars: their nature, formation, and conversion. National Renewable Energy Laboratory, US department of energy 1988.
- [5] Yung MM, Jablonski WS, Magrini-Bair KA. Review of catalytic conditioning of biomass-derived syngas. *Energ Fuel* 2009;23:1874-87.
- [6] Devi L, Ptasinski KJ, Janssen F, van Paasen SVB, Bergman PCA, Kiel JHA. Catalytic decomposition of biomass tars: Use of dolomite and untreated olivine. *Renew Energ* 2005;30:565-87.
- [7] Delgado J, Aznar MP, Corella J. Calcined dolomite, magnesite, and calcite for cleaning hot gas from a fluidized bed biomass gasifier with steam: Life and usefulness. *Ind Eng Chem Res* 1996;35:3637-43.
- [8] Pfeifer C, Rauch R, Hofbauer H. In-bed catalytic tar reduction in a dual fluidized bed biomass steam gasifier. *Ind Eng Chem Res* 2004;43:1634-40.
- [9] Rapagna S, Jand N, Kiennemann A, Foscolo PU. Steam-gasification of biomass in a fluidised-bed of olivine particles. *Biomass Bioenerg* 2000;19:187-97.
- [10] Mastellone ML, Arena U. Olivine as a tar removal catalyst during fluidized bed gasification of plastic waste. *AICHE J* 2008;54:1656-67.
- [11] Kuhn JN, Zhao ZK, Felix LG, Slimane RB, Choi CW, Ozkan US. Olivine catalysts for methane- and tar-steam reforming. *Appl Catal B-Environ* 2008;81:14-26.
- [12] Sarvaramini A, Larachi F. Mössbauer spectroscopy and catalytic reaction studies of chrysotile-catalyzed steam reforming of benzene. *J Phys Chem C* 2011;115:6841-8.
- [13] Swierczynski D, Courson C, Bedel L, Kiennemann A, Vilminot S. Oxidation reduction behavior of iron-bearing olivines ( $\text{Fe}_x\text{Mg}_{1-x}$ ) $_2\text{SiO}_4$  used as catalysts for biomass gasification. *Chem Mater* 2006;18:897-905.
- [14] Devi L, Craje M, Thune P, Ptasinski KJ, Janssen F. Olivine as tar removal catalyst for biomass gasifiers: Catalyst characterization. *Appl Catal A-Gen* 2005;294:68-79.
- [15] Virginie M, Courson C, Niznansky D, Chaoui N, Kiennemann A. Characterization and reactivity in toluene reforming of a Fe/olivine catalyst designed for gas cleanup in biomass gasification. *Appl Catal B-Environ* 2010;101:90-100.

- [16] Jess A. Mechanisms and kinetics of thermal reactions of aromatic hydrocarbons from pyrolysis of solid fuels. *Fuel* 1996;75:1441-8.
- [17] Simell P, Kurkela E, Stahlberg P. In advances in thermochemical biomass conversion; Bridgwater, A.V., Ed. London: Blackie Academic & Professional 1994. p. 265-79.
- [18] Coey JMD, Venkatesan M, Fitzgerald CB, Douvalis AP, Sanders IS. Ferromagnetism of a graphite nodule from the Canyon Diablo meteorite. *Nature* 2002;420:156-9.
- [19] Sidhu PS. Transformation of trace element-substituted maghemite to hematite. *Clay Clay Miner* 1988;36:31-8.
- [20] Wilson SA, Dipple GM, Power IM, Thom JM, Anderson RG, Raudsepp M, et al. Carbon dioxide fixation within mine wastes of ultramafic-hosted ore deposits: Examples from the Clinton Creek and Cassiar chrysotile deposits, Canada. *Econ Geol* 2009;104:95-112.
- [21] Dheilly RM, Sebaibi Y, Tudo J, Queneudec M. Importance of the presence of magnesia in limestone storage: carbonation of magnesium oxide and magnesium hydroxide. *Can J Chem* 1998;76:1188-96.
- [22] Viti C, Hirose T. Dehydration reactions and micro/nanostructures in experimentally-deformed serpentinites. *Contrib Mineral Petr* 2009;157:327-38.
- [23] Gorski CA, Scherer MM. Determination of nanoparticulate magnetite stoichiometry by Mössbauer spectroscopy, acidic dissolution, and powder X-ray diffraction: A critical review. *Am Mineral* 2010;95:1017-26.
- [24] Fuchs Y, Linares J, Mellini M. Mössbauer and infrared spectrometry of lizardite-1T from Monte Fico, Elba. *Phys Chem Miner* 1998;26:111-5.
- [25] Giacobbe C, Gualtieri AF, Quartieri S, Rinaudo C, Allegrina M, Andreozzi GB. Spectroscopic study of the product of thermal transformation of chrysotile-asbestos containing materials (ACM). *Eur J Mineral* 2010;22:535-46.
- [26] Goulart AT, Dejesus MF, Fabris JD, Coey JMD. Quantitative Mössbauer analysis of maghemite hematite mixtures in external applied-field. *Hyperfine Interact* 1994;83:451-5.
- [27] Fysh SA, Clark PE. Aluminous hematite - A Mössbauer study. *Phys Chem Miner* 1982;8:257-67.
- [28] Rozenson I, Bauminger ER, Hellerkallai L. Mössbauer -spectra of iron in 1-1 phyllosilicates. *Am Mineral* 1979;64:893-901.
- [29] Xu GW, Murakami T, Suda T, Matsuzawa Y, Tani H. Gasification of coffee grounds in dual fluidized bed: Performance evaluation and parametric investigation. *Energ Fuel* 2006;20:2695-704.
- [30] Gil J, Corella J, Aznar MP, Caballero MA. Biomass gasification in atmospheric and bubbling fluidized bed: Effect of the type of gasifying agent on the product distribution. *Biomass Bioenerg* 1999;17:389-403.
- [31] Nordhei C, Mathisen K, Safonova O, van Beek W, Nicholson DG. Decomposition of carbon dioxide at 500 °C over reduced iron, cobalt, nickel, and zinc ferrites: A combined XANES-XRD

Study. *J Phys Chem C*. 2009;113:19568-77.

[32] Wang Z, Yetter RA. Iron carburization in CO-H<sub>2</sub>-He Gases, Part I: Experiment. *Int J Chem Kinet* 2009;41:327-36.

[33] Kaspersma JH, Shay RH. Carburization of iron by co-based mixtures in nitrogen at 925°C. *Metall Mater Trans B* 1981;12:77-83.

[34] Hwang HS, Chung UC, Chung WS, Cho YR, Jung BH, Martin GP. Carburization of iron using CO-H<sub>2</sub> gas mixture. *Met Mater Int* 2004;10:77-82.

[35] Xuan SH, Chen MW, Hao LY, Jiang WQ, Gong XL, Hu Y, et al. Preparation and characterization of microsized FeCO<sub>3</sub>, Fe<sub>3</sub>O<sub>4</sub> and Fe<sub>2</sub>O<sub>3</sub> with ellipsoidal morphology. *J Magn Magn Mater* 2008;320:164-70.

[36] Miyano T, Klein C. Fluid behavior and phase-relations in the system Fe-Mg-Si-C-O-H - application to high-grade metamorphism of iron-formations. *Am J Sci* 1986;286:540-75.



## Chapter 9 : Conclusion and future work

### 9.1. Key contributions

In chapter **two**, we investigated the torrefaction of two woody samples (birch and aspen) and their main constituents, e.g., cellulose, xylan (hemicellulose representative) and lignin in a fixed-bed reactor at temperatures ranging from 240°C (mild torrefaction) to 280°C (severe torrefaction). The results of our study showed that torrefaction improves the energy density of biomass by reducing its hydrogen and oxygen contents. Hemicellulose was the most reactive component of biomass in the torrefaction conditions. Lignin also showed considerable activity under severe torrefaction and the mass yield of lignin was lower than that of cellulose under the same operating conditions. In addition, the increase in the heating value of lignin was more pronounced in comparison with that of cellulose showing that cellulose decomposition is involved with a release of some valuable tar compounds. The loss of hydroxyl and carboxyl groups of cellulose, xylan and lignin during torrefaction was also observed in the samples FTIR spectra; these losses led to 30-40 % reduction in humidity uptake of treated birch and aspen. A combined distributed activation energy model with a three parameter log-normal distribution function was also developed to fit the isothermal mass loss of cellulose, xylan and lignin during torrefaction at temperatures ranging from 240°C to 290°C. The developed model could fit the experimental results of xylan and lignin decomposition while it exhibited some under-prediction in the case of cellulose torrefaction. However, the model developed for birch and aspen torrefaction using the distributed activation energy models of xylan, cellulose and hemicellulose could fit the experimental results.

In chapter **three** it is demonstrated that the rate of biomass torrefaction could be enhanced through its impregnation with ionic liquids. Among the three different ionic liquids tested in this study, i.e. [Emim][OTf], [Emim][BF<sub>4</sub>] and [Hmim][NTf<sub>2</sub>], the first two ILs showed higher impact on the rate of biomass decomposition than [Hmim][NTf<sub>2</sub>]. This is attributed to the hydrophilic nature of [Emim][OTf], [Emim][BF<sub>4</sub>] and their interaction with hydrogen bonds in biomass which leads to the breakage of its polymeric structure and its

fast decomposition. It is also found that the cellulose decomposition rate is more affected by ILs than that of hemicellulose and lignin. Impregnation of cellulose by the hydrophilic ionic liquids reduced considerably its initial decomposition temperature and enhanced its decomposition rate. Ionic-liquid assisted torrefaction could increase the energy density of biomass. However, fast biomass decomposition produces some tars which could reduce the overall energy yield of torrefied samples.

In chapter **four** we proposed a novel combination of biomass torrefaction and CO<sub>2</sub> sequestration in which the carbonation of mining residues is performed near ambient temperature. The performed experimental study showed that considerable amount of CO<sub>2</sub> could be produced during biomass torrefaction which could be subsequently sequestered using Mg rich mining residues leading to a net negative CO<sub>2</sub> torrefaction process. The ultramafic mining residues containing considerable amount of Mg could represent cheap and abundant sources for CO<sub>2</sub> sequestration. Our study showed that the carbonation rate is dependent on several factors such as the nature of mining residues, carbonation temperature and residues water content. The mining residues containing higher amount of free brucite could have higher carbonation rate and yield than those having low free brucite content. The effect of temperature and residue pore water on the carbonation rate is also considerable. The presence of liquid water is essential for the dissolution of magnesium and its further carbonation with the dissolved carbonate ions. Increasing the carbonation temperature increases the rate of Mg leaching leading to the increased rate of carbonation. However, evaporation of pore water is increased by increasing the carbonation bed temperature which reduces magnesium dissolution. Carbonation temperatures around 45°C were found to be optimum for atmospheric pressure and close to ambient temperature carbonation conditions studied in this work.

In chapters **5 & 6** we showed that the chemical looping combustion (CLC) concept could be applied in biomass torrefaction process to recover the torrefaction volatile's energy. This combination will have two main advantages over the conventional processes in which an air combustor is used to recover volatiles energy. First, the flue gas which is recirculated to the torrefaction reactor will be oxygen-free and as a result there will be no risk of biomass burn out by oxygen. Second, the produced CO<sub>2</sub> during torrefaction will be N<sub>2</sub> free and

consequently it could be directly sequestered. However, the economic constraints involved with torrefaction process necessitate application of cheap oxygen carriers in this process. Iron oxide solid oxygen carriers, as cheap metal oxides, showed good efficiency to burn the torrefaction volatiles released during birch wood torrefaction at CLC temperatures around 600°C. Almost 99% of carbon released during biomass torrefaction was converted to CO<sub>2</sub> using iron oxide particles. In addition, iron oxides were active for volatiles burning during several successive oxidation/combustion cycles. The iron rich magnesium silicate mining residues could be also a source of cheap and abundant solid oxygen carriers for the combined torrefaction/chemical looping combustion. Although considerable proportion of iron in these types of residues could be found as intra-framework iron in the octahedral and tetrahedral magnesium silicate structure, calcination of mining residues prior to their application in a CLC reactor helps extraction of iron from the magnesium-silicate structure and formation of hematite. The calcined post-nickel recovery mining residue tested in this work as solid oxygen carrier showed high activity for cracking of biomass torrefaction volatiles. Up to 96% of carbon released from the torrefied birch was burnt to produce CO<sub>2</sub> in CLC at 700°C revealing the high capability of these mining residues for burning torrefaction volatiles.

In chapters 7 we showed that chrysotile as a naturally occurring iron bearing magnesium silicate could be active for cracking benzene as biomass model tar compound. We compared the activity of air-calcined chrysotile for steam reforming of benzene with that of olivine for equal gas hourly space mass velocity and comparable iron loading at temperatures ranging from 850°C to 900°C and over 5 fold increase in benzene conversion and syngas yield of chrysotile over olivine was observed. The superior activity of chrysotile compared to olivine was related to the former higher reducible iron content and the better dispersion of iron oxides on the chrysotile surface than olivine.

In chapters 8, we studied the steam reforming activity of three iron-bearing mineral silicates consisting of chrysotile, nickel mining residue and olivine for cracking of benzene model tar compound mixed with H<sub>2</sub>, CO, CO<sub>2</sub>, CH<sub>4</sub> and steam to simulate syngas environments. We also compared the activity of calcined chrysotile and nickel residues to that of olivine for benzene steam-reforming at comparable iron loadings in a fixed-bed reactor at 800°C.

Air-calcined chrysotile and nickel mining residue were found to be considerably active, with up to a fourfold and twofold increase in benzene conversion, respectively, compared to olivine. Chrysotile also had considerable activity for methane reforming in the simulated syngas. The higher activity of calcined nickel mining residue and chrysotile compared to olivine was attributed to their higher surface area and higher reducibility of iron in the samples compared to those in olivine. The concentration of different syngas species such as H<sub>2</sub>, CO, CO<sub>2</sub>, CH<sub>4</sub> and steam on the activity of the mentioned catalyst for cracking of benzene was also considerable. Increasing the mole fraction of reducing agents, i.e., H<sub>2</sub> and CO, and decreasing the fraction of oxidation agents, e.g., CO<sub>2</sub> and H<sub>2</sub>O, in syngas resulted in increased benzene cracking activity of chrysotile. Furthermore, oxidation of metallic iron in the presence of oxidative agents such as H<sub>2</sub>O and CO was noted to reduce the activity of chrysotile for cracking of benzene. Coke formation on chrysotile surface was dependent on the syngas composition as an increase in H<sub>2</sub> concentration reduces coke formation while higher CO concentrations give rise to higher amounts of coke.

## 9.2. Suggested future works

To sum up, the following suggestions could be recommended for future works to strengthen our understanding on this subject:

- *Studying the combined torrefaction/chemical looping volatiles combustion and CO<sub>2</sub> sequestration by mining residues in a continuous pilot scale unit.*

In this thesis, for the first time, the ideas of simultaneous torrefaction and chemical looping volatile combustion as well as the combined torrefaction and CO<sub>2</sub> sequestration by mining residues were introduced. The laboratory torrefaction, chemical looping combustion and carbonation reactors used consisted of fixed bed reactors and experiments were performed in batch or semi-batch conditions. However, there were several parameters which were not studied in this work due to the design of our reactors. Detailed study and scale up of the proposed combinations require development of a continuous pilot unit consisting of a torrefaction unit which produces continuously the solid and volatile products followed by a continuous CLC process having both combustion and regeneration steps simultaneously and finally sequestration of produced CO<sub>2</sub>. A continuous biomass torrefaction could be

performed in a fluidized bed torrefaction reactor while a continuous CLC operation needs a special design. The best design for a continuous CLC reactor would be by using two interconnected fluidized bed reactors in which the torrefaction volatiles are burned in a bubbling fluidized bed (fuel reactor) while the solid oxygen carriers are transferred continuously to an air reactor to be oxidized and regenerated. The oxidation reactor could be a riser in which the regenerated solid oxygen carriers are separated from air in a series of cyclones and they are then transferred to the fuel reactor. Using this design, the solid oxygen carrier is continuously oxidized in the air reactor and it can keep its activity for volatiles burning. Furthermore, the coke formed on the surface of solid oxygen carrier is also burned continuously in the air reactor leading to better performances for the oxygen carrier in the fuel reactor. Using this pilot unit, several important parameters which have been skipped in our investigation could be studied. One of these parameters is optimum operating temperatures of fuel and air reactors which were constrained independently in our work. As it is observed in chapters 5& 6, the temperature of CLC reactor could have an important effect on the activity of iron oxide oxygen carriers for burning the volatiles. However, the temperature of air and fuel reactor should be adjusted so that no external heat is used in the process while the solid oxygen carrier maintains its activity. The feed rate of biomass, the circulation rate of solid oxygen carrier between the fuel and air reactors and flow rate of air injected to the air reactor are among the parameters which should be adjusted to control the CLC temperature. Due to the continuous biomass torrefaction and volatiles burnout, the carbon from the torrefaction process is released as CO<sub>2</sub>. This latter could be sequestrated using brucite-rich mining residues. A fixed bed of mining residues could be designed after the CLC reactor to study different parameters involved in CO<sub>2</sub> fixation using mining residues. These parameters could be pressure drop in the carbonation column due to precipitation of carbonates as gas recirculation could take an important power-dissipation share, the effect of slow-down or passivation of residue carbonation, etc. Finally, the experimental data obtained here could be used for further simulation and design of an optimum process.

- *Studying the activity of chrysotile for cracking of biomass derived tar*

In the present thesis, the activity of chrysotile for benzene cracking as a biomass model tar compound was studied. Benzene is known as one of the hydrocarbons having high thermal stability due to its aromatic ring. Chrysotile showed considerable activity for benzene cracking as a stable hydrocarbon. However, biomass-derived tar could be composed of different classes of hydrocarbons. More than 300 different hydrocarbon species could be identified as entering in tar composition. The activity of chrysotile for cracking and reforming different tar compounds could be different. Different tar species could produce different types of deposited coke on the surface of catalyst and affect differently its activity. Consequently, it is also recommended to investigate the activity of chrysotile for cracking of biomass derived tar and to compare its activity with that of olivine. However, one should also consider the impact of gasification temperature and heating rate on the concentration and amount of different tar species produced during gasification. As a prospective suggestion, biomass gasification could be performed in a stainless steel reactor heated by an induction heater followed by the catalytic cracking of tar in a second catalytic reactor in which the chrysotile/olivine catalyst is loaded. Using induction heater, one can have good control over temperature and heating rate of biomass during its gasification. Furthermore, a wide range of heating rates from slow (a few degree per minutes) to fast heating rates (up to 200 °C/s) could be achieved by induction heaters which could simulate biomass gasification conditions in moving bed (slow-heating rate) and fluidized bed and entrained flow gasification reactors (fast-heating rate). Such study would require the development of a reliable tar measurement method to quantify the amount and concentration of different tar species before and after catalytic cracking.

- *Studying the impact of torrefaction on steam gasification of biomass*

Steam gasification of biomass is an efficient method to produce high hydrogen content synthesis gas. The thermal degradation of biomass in a steam gasifier takes place in two steps, the first step is biomass drying to remove the existing humidity of the biomass and second step is devolatilization. The gasification fuel having high moisture content could reduce the gasification temperature leading to reduced hydrogen production and increases the amount of tar produced. Biomass torrefaction could be a beneficial step for the steam gasifiers. In fact torrefaction reduces the physically and chemically absorbed water content

of biomass and it could improve the efficiency of steam gasification processes. Due to the reduced oxygen content of biomass during torrefaction, the synthesis gas could have higher yield of CO and H<sub>2</sub>. Torrefaction could also affect the amount and concentration of different constituents of tar which could affect the efficiency of tar cracking catalyst. No work is reported in the literature to investigate the effect of biomass torrefaction on the efficiency of steam biomass gasification process and thus it is suggested as part of the future perspectives.